KEK Report 2012-3
September 2012
A

Analysis of RF Magnetic Properties of Plane Magnetic Sheet:

Basis for Applications of Magnetic Alloys to RF Accelerating Cavities

Eizi EZURA and Masahito YOSHII

High Energy Accelerator Research Organization (KEK)
1-1 Oho, Tsukuba-shi, Ibaraki-ken, 305-0801, Japan

High Energy Accelerator Research Organization

KEK Reports are available from:

High Energy Accelerator Research Organization (KEK)
1-1 Oho, Tsukuba-shi
Ibaraki-ken, 305-0801
JAPAN

Phone: +81-29-864-5137
Fax: +81-29-864-4604
E-mail: irdpub@mail.kek.jp
Internet: http://www.kek.jp

Analysis of RF Magnetic Properties of Plane Magnetic Sheet:

Basis for Applications of Magnetic Alloys to RF Accelerating Cavities

Eizi EZURA and Masahito YOSHII

High Energy Accelerator Research Organization

1-1 Oho, Tsukuba-shi, Ibaraki-ken 305-0801, Japan

Abstract

RF magnetic properties of conductive plane magnetic sheets are analyzed to provide a basis for applications of magnetic alloy tapes to RF accelerating cavities. This paper reports on the effects of eddy current on the magnetic properties of the sheets when the frequency of the applied magnetic field increases up to RF frequencies. A nonuniform magnetic field distribution, formed within the sheet by eddy currents, is obtained by solving a field equation based on Maxwell's equations, which include conductivity and complex permeability. The resulting distribution is used to derive expressions for RF magnetic properties of the sheet, such as effective permeability, magnetic power loss, and Q-value.

KEY WORDS: RF cavity, magnetic alloy, magnetic sheet, magnetic field distribution, Q-value, magnetic energy, magnetic loss, loss factor, hysteresis loss, eddy-current loss, skin depth, magnetic cylinder, intrinsic permeability, effective permeability.

Contents

1. Introduction and Survey

1.1 Background

High energies and high beam intensities continue to be major goals in accelerator science. The drive for higher energies comes principally from high-energy particle physics, where the Large Hadron Collider (LHC) is leading the field. A complementary drive is toward higher beam power or luminosity, for example, spallation neutron source (SNS), Japan Proton Accelerator Research Complex (J-PARC), SuperKEKB, and the SuperB Factory to be built at the University of Rome. In novel proton accelerators, such as J-PARC and SNS, high-intensity proton beams and a variety of intense secondary particle beams are required to pursue frontier science in particle and nuclear physics, material science, life science, nuclear technology, and so on.

In proton synchrotrons, an effective method for meeting the increasing demand for higher beam intensity is to increase the repetition rate, which essentially requires a higher RF accelerating voltage. Since the space allocated for RF accelerating cavities is usually limited, this measure is only possible if there is a cavity that can produce a much higher accelerating gradient than that obtained with a conventional RF cavity. The widely used ferrite-loaded RF cavities can only attain an accelerating gradient of approximately 10 [kV/m]. This limitation comes mainly from an anomalous RF-loss mechanism termed *high-loss effect*, which is observed at high RF magnetic fields [1]. Another factor limiting the accelerating gradient is a cooling problem due to the rather low Curie temperature (100 to 200°C) of ferrites.

1.2 Birth of MA Cavity

In recent years, the development of highly permeable, soft magnetic alloys (MA) has been underway. The first attempt to apply MA materials to an accelerating cavity was made in CEA-LNS Saclay in the late 1980s to early 1990s. A test cavity loaded with cobalt-based amorphous alloy was built for MIMAS, the storage booster for the SATURNE II synchrotron [2][3]. The reason for building this cavity was to replace the two existing ferrite-loaded cavities with a single unit that affords the same performance in order to free up part of the ring for other instrumentation [3]. Although the work on this project slowed, the development of the cavity was continued for the Proton-Ion Medical Machine Study (PIMMS) at the European Organization for Nuclear Research (CERN) and for TERA, the Italian proton and light-ion synchrotron project for cancer therapy [4][5][6].

In Japan, the development of a MA-loaded cavity was started in the mid-1990s. Early in the development of RF cavities for the J-PARC, which was then called the

Japan Hadron Project (JHP) and later the Japan Hadron Facility (JHF), the properties of numerous magnetic materials, including ferrites and MAs, were measured[7][8]. Shunt resistance, which describes the accelerating gradient of the cavity, is proportional to a $\mu_p Qf$-product of the loaded magnetic core, where μ_p is the permeability in parallel circuit representation; Q, the quality factor; and f, the frequency. During the course of material surveying and research, it was found that the field dependence of the $\mu_p Qf$-product (hereafter, $\mu_p Qf$-value) of MA materials was drastically different from that of ferrites[9][10][11][12]. Although MAs exhibited lower $\mu_p Qf$-values than ferrites in low RF magnetic fields, even when the RF magnetic field was increased to levels well over 0.1 [T], the $\mu_p Qf$-value remained at almost the same level as that in the low magnetic fields. This is in striking contrast to the behavior of ferrite $\mu_p Qf$-values, which decrease rapidly as the RF magnetic field is increased and above around 0.01 [T] fall to values unsuitable for cavity applications. This remarkable feature of MA materials suggested the possibility of realizing a new high-accelerating-gradient cavity. Extensive measurements confirmed that amongst the MA materials that had been measured, an iron-rich nanocrystalline magnetic alloy had the highest $\mu_p Qf$-value and was best suited for RF cavity applications [13][14]. In this paper, we term this material *iron-rich nanocrystalline magnetic alloy* (hereafter, IRNC). IRNC is also called "Finemet", which is a registered trade name owned by Hitachi Metals, Ltd.

1.3 IRNC and MAs

Although Fe-based amorphous alloys can produce a large magnetic flux density, they have been used for low-frequency applications only due to their inferior soft magnetic properties in the high frequency range as compared to those of Co-based amorphous alloys. After extensive research and development, a new class of Fe-based soft magnetic alloys with nanoscale grains, IRNC, was developed by crystallization from amorphous precursors [15][16][17]. IRNC is prepared by annealing amorphous alloys consisting of Fe, Si, B, and small amounts of Cu and Nb under substantial crystallization. The structure comprises randomly oriented ultrafine crystals in the order of 10 [nm] and even finer crystal grains distributed in the remaining amorphous phase. IRNC has a very high saturation magnetic flux density (over 1.3 [T]), low magnetostriction, as well as superior soft magnetic properties. The mechanism whereby IRNC exhibits these excellent soft magnetic properties is not fully understood yet. However, it is suggested that this may be attributed to the decrease in local magnetic anisotropy due to reduced grain size and a decrease in magnetostriction as the result of cancellation between the crystals and the amorphous phase[15].

Most MA materials have moderate conductivity, which limits their usefulness in

high-frequency applications because of induced eddy currents. Power loss caused by eddy currents may exceed an acceptable level unless a magnetic object is made by laminating a very thin plate insulated electrically from its neighbors or by winding a very thin insulated tape. In accelerating cavity applications, an insulator-coated magnetic alloy tape of approximately 20 [μm] in thickness is wound into a toroidal core with a diameter of several tens of centimeters and heat-treated in an oven. The shunt resistance of an RF cavity is proportional to $\mu_p Qf \times \ln[\text{O.D.}/\text{I.D.}]$, where O.D. and I.D. denote the outer and inner diameters, respectively. This means that a larger O.D./I.D. makes shunt resistance higher and consequently leads to a higher accelerating gradient. Since MA cores are formed by winding, it is possible to fabricate large cores, with an O.D. greater than 1 [m]. This is a practical advantage over ferrites, whose ceramic nature makes them unsuitable for forming large cores because the cores are manufactured by pressing, with the size of the press being a limiting factor.

1.4 Characteristics of MAs in Cavity Applications

High-power measurements revealed that when the intensity of the RF field was varied over a wide range, IRNCs maintained a fairly high $\mu_p Qf$-value ($\simeq$5 [kΩ/m]) up to a magnetic field intensity of 0.2 [T], whereas the $\mu_p Qf$-value of ferrites was greatly reduced even at much lower field intensities [8][9][14]. It should be emphasized that 0.2 [T] is not the ultimate magnetic field that IRNCs can hold but the maximum field that could be attained by using the then available RF measurement system, which had limited power capacity. This indicated that IRNCs have the potential to produce an accelerating gradient much higher than can be attained with ferrites. In addition, the IRNCs' operations were quite stable even at very high magnetic fields because of their high heat resistance, based on a high Curie temperature of about 570℃.

Two distinctive features of IRNC material as seen from cavity applications are a high relative permeability and a low Q-value. High relative permeability compensates for a decreased $\mu_p Qf$-value due to a low Q-value and thereby helps to keep the cavity shunt resistance fairly high. Another advantage of the very high permeability of MAs is that accelerating structures can be much more compact than those loaded with ferrites. However, an applicable frequency range of MAs is limited due to eddy currents that make the relative permeability start to drop at a relatively low RF. A low Q-value of the core causes a broad cavity resonance, thereby making it possible for the cavity to operate over a wide frequency range without any cavity tuning system. The broad bandwidth of a low-Q cavity allows multi-harmonic RF operation, in which bunch properties can be manipulated, for instance, to reduce space-charge effects at injection, to match bunch shape and emittance between cascaded machines, and to avoid some

types of beam instabilities. A broad-bandwidth cavity is also suited to producing a pulsed sinusoid for barrier-bucket manipulations. In addition, a low-Q cavity has little memory of the beam that passed through it and, as a result, barely excites severe coupled-bunch instabilities. However, since the impedance of a low-Q cavity extends over a wide frequency range, the voltages at several revolution harmonics might be induced in the cavity and added to the accelerating voltage. To avoid the distortion of the accelerating voltage, which is much more serious at higher beam-current operation, the induced voltages must be compensated for by means of some kind of feedforward or feedback system.

The Q-value of the core can be increased by introducing a radial gap and controlled by a factor of more than 10 by changing the gap width. However, the $\mu_p Qf$-value or shunt resistance does not change much because the radial gap also reduces the effective permeability by an amount that almost cancels out the increase in Q-value. To summarize, the radial gap increases the effective Q-value while the shunt resistance R remains almost unchanged, which reduces R/Q. A low R/Q is beneficial with respect to beam instabilities and transient beam loading.

Regarding MA materials other than IRNC, tests of newly developed cobalt-based amorphous cores have been reported [18][19][20][21]. The permeability of the core was improved by adjusting the annealing temperature and by applying a magnetic field during heat treatment. The $\mu_p Qf$-value of the test cores with a 300 [mm] O.D. and 150 [mm] I.D. was found to be approximately 1.6–1.9 times as high as that of IRNC [19]. A prototype RF cavity loaded with 12 cores of 550 [mm] O.D. and 310 [mm] I.D. was installed and beam-tested in the Heavy Ion Medical Accelerator in Chiba (HIMAC) at the National Institute of Radiological Sciences (NIRS). In the beam test, the cavity showed good acceleration performances [21]. However, the procedure for manufacturing large size cores for RF cavity applications has not yet been established, and consequently, the shunt resistance of the core still depends significantly on the core size and annealing/manufacturing parameters [19][20].

Recently, to increase the accelerating voltage of J-PARC RF cavities, a new class of IRNC core has been developed, with a $\mu_p Qf$-value approximately twice that of conventional IRNC cores [22]. The increase in $\mu_p Qf$-value was achieved by introducing a new annealing method in which a magnetic field is applied during the crystallization process and by reducing the tape thickness from 18 [μm] to 13 [μm] [23].

1.5 Applications of MAs to RF Cavities

RF cavities loaded with MA cores (mostly IRNC cores) worked or have been working as RF accelerating cavities or as special purpose cavities at numerous institutes worldwide. The following is a brief survey of MA-loaded cavity applications.

(a) Cavities for High-Energy Physics

The first application of IRNC to RF cavities was made in collaboration between the High Energy Accelerator Research Organization (KEK) and Brookhaven National Laboratory (BNL). An MA-loaded cavity designed and built in KEK was successfully beam-tested in the alternating gradient synchrotron (AGS) at BNL in 1998. It was used as a barrier-bucket cavity to maximize the longitudinal bunching factor in a bucket-to-bucket beam transfer [24][25][26][27]. In 2000, a second harmonic RF system equipped with an MA-loaded cavity was installed in the KEK 12 [GeV] proton synchrotron (KEK-PS) to alleviate the space charge effects during the beam injection period [28][29]. Subsequently, in 2003, one of the ferrite-loaded cavities for the KEK-PS booster was replaced with a nonresonant MA-loaded cavity [30][31]. The new accelerating system, together with a new COD correction system, contributed to increasing the booster's average beam intensity by up to 40 [%].

At CERN, two MA-loaded cavities were built for a low-energy ion ring (LEIR) in collaboration with KEK. They cover a wide frequency range (0.35–5.0 [MHz]) without cavity tuning and allow multiharmonic operation [32][33]. Also at CERN, as part of the LHC injector upgrade program, an increase in the beam energy transferred from the proton synchrotron booster (PSB) to the proton synchrotron (PS) has been investigated as a possible upgrade scenario [34]. An RF cavity loaded with the abovementioned IRNC with an improved $\mu_p Qf$-value is being developed in order to increase the total accelerating voltage obtainable within the space allotted to the RF cavities [35]. In Fermilab, a 7.5 [MHz] single-gap RF cavity with five MA cores was built and tested as part of the Proton Driver Design Study [36]. The MA-loaded cavity was chosen to achieve the highest possible accelerating gradient and to reduce beam-loading effects. In addition, at Fermilab, a barrier RF system with an MA-loaded cavity was installed in the main injector to increase the luminosity of the Tevatron, which was shut down in September 2011 [37].

One of the fruitful applications of MA is an induction-accelerating cell, which was built in the KEK-PS to demonstrate the feasibility of realizing an induction synchrotron. The induction-accelerating system successfully captured an injected 500 [MeV] single proton-bunch by a barrier bucket, and succeeded in accelerating it up to 6 [GeV] [38] [39][40][41][42].

(b) Cavities for Medical-Use Synchrotrons

In the field of particle-beam therapy, MA-loaded cavities have been gaining a firm hold, because their suitability for untuned wideband operation is particularly favorable for medical-use synchrotrons characterized by a large RF swing between the injection energy and the top energy. In 1999, an MA-loaded cavity was installed in the HIMAC

at NIRS to accelerate carbon or heavier ions through a large frequency change of 1–8 [MHz] with an accelerating gradient of 50 [kV/m] [43][44] [45].

Stimulated by the remarkable results at HIMAC, medical-use synchrotrons equipped with MA-loaded cavities have been built and are operating at a large number of institutes, including the Proton Medical Research Center (PMRC) at the University of Tsukuba [46][47], the Wakasa-wan Energy Research Center (WERC)[48][49], and the M. D. Anderson Cancer Center (MDACC) at University of Texas [50].

(c) Cavities for FFAGs

MA-loaded cavities have also been successfully applied to fixed-field alternating gradient accelerators (FFAG). In KEK, the 1 [MeV] proof-of-principle (POP) FFAG came into operation in 2000, and in 2006, the larger 150 [MeV] FFAG, a prototype for proton therapy and neutron production, first accelerated protons up to 100 [MeV] at a repetition rate of 100 [Hz] [51][52][53][54]. Subsequently, it was relocated to the Center for Accelerator and Beam Applied Science at Kyushu University to promote both research and educational activities at the university [55]. Beam commissioning and pilot research in nuclear, medical, and life sciences are being carried out from 2011 to 2013 [56].

Another 150 [MeV] FFAG was built at the Kyoto University Research Reactor Institute (KURRI) to test accelerator-driven subcritical reactor (ADSR) operation [57][58]. The whole machine is a cascade of three FFAG rings, the beam of which was successfully accelerated up to 100 [MeV] in 2008 [59]. Also at KURRI, a project aiming at medical applications of FFAG accelerators is ongoing: an FFAG storage ring with energy/emittance recovery internal target (ERIT) has been constructed, which is intended to serve as an intense accelerator-based neutron source for boron neutron-capture therapy (BNCT) [60][61][62][63].

In France, a variable-energy (70–180 [MeV]) spiral-lattice FFAG equipped with two MA cavities was designed for a project, Recherche en ACCélérateurs et Applications Médicales (RACCAM) [64][65][66]. One aim of RACCAM is to show the feasibility of the application of FFAG beam to hadron therapy. FFAGs are also of interest for muon acceleration: at the Research Center for Nuclear Physics (RCNP) of Osaka University, a Phase Rotated Intense Slow Muon beam (PRISM) has been constructed, which aims to produce a high-quality and high-intensity muon beam by means of a phase rotating technique [67][68][69] [70].

(d) Others

The first application of IRNC in the field of accelerators was not to an RF cavity but to a longitudinal impedance tuner, which was planned at KEK in 1996 to mitigate the

longitudinal space-charge effects in the KEK-PS [71][72]. The tuner was designed to compensate for the longitudinal space-charge impedance (negative inductance) and consisted of three units, each having four MA cores with 340 [mm] O.D. and 140 [mm] I.D. The beam test performed in 1997 showed that the tuner effectively reduced the space-charge impedance and proved that IRNC has a very high tolerance to radiation [73][74].

A very short length (11.6 [cm]) beam chopper using three MA cores was developed for HIMAC and installed between the ion sources and the RFQ [75][76]. It operated stably at a chopping voltage of 5 [kV] with a rise and fall time of 10 [ns]. At the Center for Nuclear Study (CNS) at the University of Tokyo, an RF buncher using MA cut-cores was installed in the beam transport line of an ECR ion source HiECR [77][78][79]. The buncher operates in a wide frequency range (18–45[MHz]) without tuning and successfully formed bunched beams of H^{+}, O^{5+}, and Ar^{8+}.

1.6 Cavities for J-PARC

1.6.1 Progress of J-PARC

As mentioned in Section 1.2, the MA (IRNC)-loaded cavity was originally designed in the mid-1990s in collaboration between KEK and the Institute for Nuclear Study (INS) at the University of Tokyo* to meet the challenging requirements for J-PARC RF cavities. Since then, it has been developed in INS and KEK and later in the Japan Atomic Energy Agency (JAEA). The J-PARC was a large-scale project and accordingly it took a long time before the design was finalized and the project was officially approved. During this period, besides developing their own cavities for J-PARC, the J-PARC (JHF) group energetically led activities in applying MA to other machines. Because of their efforts, a number of MA-loaded cavities were developed and worked well in various machines. These cavities have demonstrated that both high accelerating gradient and large frequency swing are practically achievable.

The J-PARC rings are composed of a 3 [GeV] rapid cycling synchrotron (RCS) and a 50 [GeV] synchrotron of the main ring (MR), now operating at a phase-I energy of 30 [GeV]. Beam commissioning of the RCS started in October 2007. The first 3 [GeV] beam from the RCS was injected into the MR in May 2008, and user runs of the RCS started in December 2008 for the Materials and Life Science Facility (MLF). The MR proton beam reached the initial goal of 30 [GeV] in December 2008. In January 2009, the 30 [GeV] proton beam was successfully extracted from the MR and then transferred to the Hadron experimental hall. The first neutrino beam production was confirmed in April 2009 by observing the muons produced by the fast-extracted proton beam. In February 2010, the Tokai-to-Kamioka (T2K) collaboration detected the first neutrino

event at Super-Kamiokande, which is located 295 [km] away from Tokai. In the RCS, the beam intensity has been steadily increased and in November 2010 the beam power delivered to MLF went up to 200 [kW]. In the MR, the beam power to T2K beam line reached 145 [kW] in March 2011, shortly before the northeastern region of Japan was struck by a gigantic earthquake (officially called the Great Eastern Japan Earthquake) in which the J-PARC facility experienced considerable damage.

*In 1997, the High Energy Accelerator Research Organization (present KEK) was established by merging three laboratories: National Laboratory for High Energy Physics (old KEK) and two related institutions of the University of Tokyo, INS, and Meson Science Laboratory.

1.6.2 Build-up of Cavities

J-PARC was the first accelerator to use MA cavities on a large scale. Beam tests of the RCS started with 10 RF accelerating cavities, each loaded with 18 noncut MA cores. The cavity is equipped with a low-loss inductor and a vacuum capacitor, with both connected in parallel to the cavity in order to adjust its Q-value and resonance frequency [80][81][82]. To increase the beam-capture efficiency, a second-harmonic RF voltage is added to the fundamental one in the early stages of acceleration [83]. Application of the second harmonic voltage maximizes the longitudinal bunching factor and thereby alleviates the space-charge effect that causes capture efficiency to deteriorate. An eleventh RF accelerating cavity was added in December 2008, and since then, the RF system has been working very well. The beam energy of the linac will be upgraded in the fiscal year 2013 from a provisional value of 181 [MeV] to the design value of 400 [MeV]. At about that time, a twelfth RF cavity will be installed to provide a total accelerating voltage sufficient to accept the upgraded beam and to accelerate it up to 3 [GeV] [84].

Beam tests of the MR started with four RF accelerating cavities, each loaded with 18 radial-cut MA cores. A fifth RF accelerating cavity was added in August 2009 [84]. To reduce the space-charge effects that hamper increases in beam current, the first second-harmonic RF cavity was installed in August 2010, and shortly thereafter, a preliminary beam study using the second-harmonic cavity was performed [85]. By changing the tuning capacitors, the MR cavity is easily converted from the accelerating cavity to the second-harmonic cavity or vice versa. In October 2011, two more RF cavities were installed, and in December 2011, the first beam test after the earthquake began. At present, eight RF cavities are operational in the MR and the ninth (and last) cavity will be added during the 2012 summer shutdown [86].

In the near future, to achieve the target beam-power of 750 [kW], the MR repetition cycle will be reduced from the present 2.56 [s] to 1.28 [s] [87]. The RF voltage required

for this high repetition rate is much higher than the present total RF voltage. Since space for cavities is limited, the accelerating gradient of the cavity must be increased considerably to obtain the necessary RF voltage. As mentioned in Section 1.4, a new class of IRNC core has been developed, with a much higher $\mu_p Qf$-value than the present core. Production of real-size cores (80 [cm] in diameter) has been started after completion of various tests of the manufacturing system. The system is mainly composed of a large oven for annealing the core and a larger magnet that can hold the whole oven between its pole pieces and generate a high magnetic field with acceptable uniformity [88]. Newly designed RF cavities loaded with these cores are expected to attain the required RF voltage within the capacity of the present RF power amplifiers and to fit in the present space for cavities [88].

1.7 Outline of the Paper

The purpose of this paper is to give a detailed description of the RF magnetic properties of plane magnetic sheets made of lossy materials, such as soft magnetic alloys. Finite resistivity or nonzero conductivity of a material causes a flow of eddy current within the sheet, which plays an important role in determining the magnetic properties of the sheet. Throughout the analyses, complex permeability and nonzero conductivity are used so that the obtained results can be applied to any magnetic sheet having any value of $\tan\delta$ and conductivity.

The contents of the paper are organized into eight chapters. Chapter 2 reviews some fundamental equations of basic physical quantities, such as stored magnetic energy and magnetic power loss. From these equations, we obtain various expressions for magnetic properties of the sheet. We introduce two definitions of permeability—the intrinsic permeability and the effective permeability—which form the basic elements of the analyses in this paper.

In Chapter 3, approximate expressions for the AC magnetic properties of the sheet are derived on the assumption that the frequency of the applied magnetic field is much lower than RF frequencies. The derived expressions are useful for predicting the behavior of magnetic sheets when used at frequencies from very low to approximately 100 [kHz]. These expressions can also be used as the references to which the accurate expressions derived in the following chapters must reduce when the frequency is assumed to be much lower than RF frequencies.

Chapter 4 discusses the distribution of the magnetic field in the interior of the sheet, which is essentially formed under the influence of eddy currents. We obtain the field distribution by solving a field equation that is based on Maxwell's equations and governs the magnetic field inside the sheet. We derive an expression of skin depth for the magnetic sheet, which is applicable to all magnetic sheets because it includes $\tan\delta$

and conductivity. We give some numerical examples of the field distribution to show the way it changes as a function of frequency, material constants, and thickness of the sheet.

Chapter 5 briefly surveys the frequency characteristics of the intrinsic permeability, which is inherent in magnetization mechanisms and is therefore a material constant. The main sources of dispersion in the frequency response of intrinsic permeability are the relaxation and resonance absorption associated with magnetization processes. We describe two dispersion sources in some detail, namely, the relaxation in orientation of magnetic moments and the resonance of domain wall motion. Both effects usually appear in a relatively low RF range in which most proton-ring RF cavities operate.

In Chapter 6, we derive the effective permeability that characterizes the macroscopic magnetic properties of the sheet. It represents the relationship between the average magnetic flux density within the sheet and the applied magnetic field strength. To obtain the complex effective permeability, the real and imaginary parts of the magnetic field are separately integrated and averaged over the cross section of the sheet. The effective permeability of the sheet is determined mainly by eddy current, and hence, it depends on the frequency and sheet thickness as well as the material constants.

In Chapter 7, we derive expressions for the RF magnetic properties of the sheet using the magnetic field distribution obtained in Chapter 4 and its integrations given in Chapter 6. Here, we obtain the expressions for the stored magnetic energy, overall magnetic power loss, eddy-current loss, hysteresis loss, and Q-value of the sheet. We give some numerical examples of these magnetic properties to show how they depend on the material constants and thickness and how they change as the frequency is varied over a wide range.

Appendix A takes a fundamental approach to the subject of stored energy and derives the equation for the stored magnetic energy of a magnetic object when it is placed in a magnetic field. Appendix B expresses the magnetic power loss in terms of field quantities and verifies that the expression agrees precisely with the commonly used power loss defined by the product of voltage and current. Appendix C discusses the distribution of magnetic field within a solid magnetic cylinder made of a material having complex permeability and nonzero conductivity.

2. Basic Physical Quantities

In this chapter, we review some fundamental equations of basic physical quantities, such as stored magnetic energy and magnetic power loss. From these equations, we obtain expressions for various properties of magnetic materials under an alternating magnetic field.

2.1 Stored Magnetic Energy

Stored magnetic energy and magnetic power loss are important basic physical quantities of magnetic sheets. The quality factor, usually referred to as the Q-value, is another important quantity and is based on these two quantities. In this section, we review the expression for the stored energy of a magnetic object when it is placed in a magnetic field.

First, let $\mathbf{H}$ and $\mathbf{B}$ denote the magnetic field intensity and magnetic flux density in a medium, respectively. Then, the magnetic energy stored in a volume V is expressed (as derived in Appendix A) by

$$W_V = \int_V dv \int \mathbf{H} \cdot d\mathbf{B}, \tag{2.1}$$

where the symbol "$\cdot$" represents the scalar product of the two vectors $\mathbf{H}$ and $\mathbf{B}$ and $\int \mathbf{H} \cdot d\mathbf{B}$ represents the local density of the stored magnetic energy. If we assume that the relationship of $\mathbf{B}$ to $\mathbf{H}$ is linear and that the medium is isotropic, we can write $\mathbf{B} = \mu \mathbf{H}$, where μ is the permeability and is a constant if the medium is homogeneous. The energy given in eq. (2.1) then reduces (as shown in Appendix A) to

$$W_V = \frac{1}{2} \int_V \mathbf{H} \cdot \mathbf{B} \, dv. \tag{2.2}$$

Let us assume that a magnetic field has been established in a medium that is isotropic and homogeneous. A magnetic object is now introduced into the field, while the source of the field is maintained strictly constant. The energy stored in the object can be obtained from the change in energy of the system before and after the introduction of the object. If the magnetic properties of the medium and the object can be characterized by the permeability μ, the magnetic energy stored in the object is given by (Appendix A)

$$W_V = \frac{1}{2} \int_V \left(1 - \frac{\mu_1}{\mu_2} \right) \mathbf{H}_1 \cdot \mathbf{B}_2 \, dv, \tag{2.3}$$

where V is the volume occupied by the magnetic object; μ_1, the permeability of the medium outside the object; μ_2, the permeability of the object; $\mathbf{H}_1$, the magnetic field intensity in the medium before introducing the object; and $\mathbf{B}_2$, the magnetic flux density within the object. If the configuration of the field and object is such that the magnetic polarization in the object does not affect the field in the medium, the field intensity in the medium is independent of the presence or absence of the object. In this case, $\mathbf{H}_1$ in eq. (2.3) is also the field intensity in the medium after the object is introduced. If the medium is not magnetic or μ_1 is much lower than μ_2, such that the condition $\mu_1/\mu_2 \ll 1$ is satisfied, the second term in parentheses in eq.(2.3) can be ignored, and thus, W_V can be written as

$$W_V = \frac{1}{2} \int_V \mathbf{H}_1 \cdot \mathbf{B}_2 \, dv. \tag{2.4}$$

The condition $\mu_1/\mu_2 \ll 1$ is satisfied for almost all ordinary proton-ring RF cavities in which magnetic cores are placed in a nonmagnetic medium, such as air or water. Therefore, we conclude that eq.(2.4) can be used to calculate the stored magnetic energy of the cores.

If **H** and **B** change sinusoidally, they can be represented by

$$\mathbf{H}(r,t) = \mathbf{H}(r)\, e^{j\omega t} \quad \text{and} \quad \mathbf{B}(r,t) = \mathbf{B}(r)\, e^{j\omega t}, \tag{2.5}$$

where ω is the angular frequency of the field and r is the generalized position. The scalar product of **H** and **B** can be obtained from the ordinary product of **H*** (the complex conjugate of **H**) and **B**, instead of performing a vector operation. Expressing variables as a complex conjugate enables a much easier calculation because the time factors of **H*** and **B**, $e^{-j\omega t}$ and $e^{j\omega t}$ respectively, cancel each other out. We can easily show that the scalar product of **H** and **B** is equal to the real part of the ordinary product of **H*** and **B**:

$$\mathbf{H} \cdot \mathbf{B} = \mathrm{Re}\left[\mathbf{H}^* \mathbf{B}\right]. \tag{2.6}$$

Substituting eq. (2.6) into eq.(2.4), the average density of the magnetic energy stored in the object, W, becomes

$$W = \frac{1}{2V} \int_V \mathrm{Re}\left[\mathbf{H}_1^* \mathbf{B}_2\right] dv, \tag{2.7}$$

where V is the volume of the magnetic object; $\mathbf{H}_1$, the magnetic field intensity in the medium before introducing the object; and $\mathbf{B}_2$, the magnetic flux density within the object.

2.2 General Consideration of Magnetic Power Loss

In this section, we review the energy conservation law, from which we can obtain the magnetic power loss expressed in terms of field quantities. Consider an arbitrary region in which there exists an electric field **E** with electric flux density **D** and conducting current density **J**, and a magnetic field **H** with magnetic flux density **B**. The question is "How can the energy relationship be represented inside a region whose volume and surface area are V and S, respectively?"

By applying some mathematical operations to Maxwell's equations in differential form, the following expression is derived (Appendix B):

$$\oint_S (\mathbf{E}\times\mathbf{H})\cdot d\mathbf{a} + \int_V \mathbf{E}\cdot\mathbf{J}\, dv = -\int_V \left(\mathbf{E}\cdot\frac{\partial\mathbf{D}}{\partial t} + \mathbf{H}\cdot\frac{\partial\mathbf{B}}{\partial t}\right) dv. \qquad (2.8)$$

The result is essentially a power balance equation known as *Poynting's theorem*, after J. H. Poynting who first derived this equation. The customary interpretation of eq. (2.8) is as follows. The right-hand side represents the rate of decrease in electric and magnetic energy stored within the volume V. From the conservation law of energy, the loss of available stored energy must be accounted for by the sum of the energy loss within the volume and the outward energy flow across the volume's boundary surface S. Since the second term of the left-hand side is the power dissipated in Joule heat within the volume, the first term must be the power flow out of the closed surface S. The vector $\mathbf{S}=\mathbf{E}\times\mathbf{H}$ is termed the *Poynting vector*, which represents the magnitude of energy-flux flow [W/m^2] and direction of the energy flow.

Equation (2.8) is the general expression for all cases, because it is derived from Maxwell's equations without any assumptions. This theorem is one of the most fundamental and useful relationships of electromagnetic theory. In eq. (2.8), $\mathbf{H}\cdot\partial\mathbf{B}/\partial t$ is the only term concerned with magnetic power loss, and therefore, it must represent the overall magnetic power loss including all types of power loss originating from all mechanisms.

2.3 Overall Magnetic Power Loss

It follows from the Poynting's theorem given in eq. (2.8) that the average density of magnetic power loss in the volume, V, is given by

$$P_{m,g} = \frac{1}{V}\int_V \mathbf{H}\cdot\frac{\partial\mathbf{B}}{\partial t}\, dv. \qquad (2.9)$$

As mentioned above, this is the expression of magnetic power loss that includes all types of losses, such as hysteresis loss, eddy-current loss, magnetic after-effect loss, and

so on. Hence, by using eq.(2.9), we can, in principle, obtain the overall magnetic power loss, provided the distribution of **H** and **B** that reflects all of these losses is known and manageable. However, in practice, it is only when the magnetic field distribution is very simple that we can express the overall magnetic power loss analytically. Using the complex conjugate representation given in eq. (2.6), we can rewrite eq. (2.9) as

$$P_{m,g} = \frac{1}{V}\int_V \mathrm{Re}\left[\mathbf{H}^*\frac{\partial \mathbf{B}}{\partial t}\right] dv. \tag{2.10}$$

A commonly used measure of power loss is the rate at which energy is expended, that is, the time-averaged power loss, which is expressed in watts or joules per second. To calculate the time-averaged power loss, the integration in time over a period T is necessary, in addition to integration in space. If **H** and **B** are steady-state sinusoidal time-varying functions, the time integral over T simply produces a factor of $T/2$. Then, dividing the result of integration by T, we obtain P_m, the time-averaged overall power loss per unit volume given by

$$P_m = \frac{1}{2V}\int_V \mathrm{Re}\left[\mathbf{H}^*\frac{\partial \mathbf{B}}{\partial t}\right] dv. \tag{2.11}$$

Magnetic energy dissipation comes from the irreversibility inherent in magnetizing mechanisms. It shows up at the macroscopic scale through the area enclosed by a *B-H* or hysteresis loop. From eq. (2.1), the average density of magnetic energy loss in volume V in one hysteresis cycle is

$$\begin{aligned} P_{m,c} &= \frac{1}{V}\int_V dv \oint \mathbf{H}\cdot d\mathbf{B} \\ &= \frac{1}{V}\int_V dv \oint \mathrm{Re}\left[\mathbf{H}^* d\mathbf{B}\right]. \end{aligned} \tag{2.12}$$

Equation (2.12) is another expression of magnetic energy loss, and it also embraces all types of magnetic losses, since it is derived from the general stored magnetic energy expression (eq. (2.1)). If **H** and **B** are periodic functions of time with a period T, eq. (2.12) can be written as

$$P_{m,c} = \frac{1}{V}\int_V dv \int_0^T \mathrm{Re}\left[\mathbf{H}^*\frac{\partial \mathbf{B}}{\partial t}\right] dt. \tag{2.13}$$

Performing the time integral in eq. (2.13), we obtain

$$P_{m,c} = \frac{T}{2V}\int_V \mathrm{Re}\left[\mathbf{H}^* \frac{\partial \mathbf{B}}{\partial t}\right] dv. \tag{2.14}$$

Comparing eq. (2.14) with eq. (2.11), we can see a natural consequence that the magnetic energy loss per cycle (eq. (2.14) is equivalent to the magnetic energy loss per second (eq. (2.11) multiplied by the period T.

The power loss of a magnetic object placed in a magnetic field can be obtained in the same manner as used in Section 2.1. From eq. (2.11), the time-averaged overall magnetic loss per unit volume, P_m, is

$$P_m = \frac{1}{2V}\int_V \mathrm{Re}\left[\mathbf{H}_1^* \frac{\partial \mathbf{B}_2}{\partial t}\right] dv, \tag{2.15}$$

where $\mathbf{H}_1$ is the magnetic field intensity in the medium before introducing the object and $\mathbf{B}_2$ is the magnetic flux density within the object. Likewise, the overall magnetic loss per cycle per unit volume is given (from eq. (2.14)) by

$$P_{m,c} = \frac{T}{2V}\int_V \mathrm{Re}\left[\mathbf{H}_1^* \frac{\partial \mathbf{B}_2}{\partial t}\right] dv. \tag{2.16}$$

As stated before (below eq. (2.3)), if magnetic polarization of the object does not affect the field in the medium, $\mathbf{H}_1$ does not change even if the object is introduced.

In this section, two conventions are presented to express the magnetic power loss, namely, the energy loss per second (P_m) and the energy loss per cycle ($P_{m,c}$). Materials scientists usually use the energy loss per cycle because it is suited to basic materials research. On the other hand, engineers or users of magnetic materials prefer the energy loss per second because it is more convenient in practical use. As mentioned above, $P_{m,c} = P_m T$ ($=P_m/f$), where f is the frequency of the field. In this paper, we use P_m as a measure of magnetic power loss

2.4 Power Loss due to Eddy Current

2.4.1 Effects of Eddy Current

When the magnetic flux in a conductor changes with time, an electric field is generated in the plane at right angles to the direction in which the flux is changing, resulting in a flow of currents within the conductor. These currents are referred to as *eddy currents* and depend on the geometry of the conductor specimen, on its resistivity, and on the frequency of alternation of the field. Their directions always counteract the change in field that produced them. The net effect of the flow of eddy currents is to prevent the field from penetrating immediately to the interior of the conductor. When the applied

field varies fast, the field strength in the interior may never be more than a small fraction of the field strength at the surface. Thus, the eddy currents produce a nonuniform field distribution over the cross section of the conductor, a phenomenon referred to as the *skin effect*. The skin effect expresses the tendency of alternating current to flow near the surface of a conductor. This effect becomes more pronounced at higher frequencies and, in particular, at microwave frequencies, an electromagnetic field can only survive in very close vicinity to the surface.

A magnetic material also suffers from the skin effect if it has finite resistivity or nonzero conductivity. Because of limited penetration of the applied magnetic field, the magnetic flux density also decreases from the surface toward the interior. This leads to a reduction in the average magnetic flux density within the material and consequently causes a reduction in effective permeability.

2.4.2 Eddy-Current Loss

Power dissipated due to eddy currents is referred to as an *eddy-current loss*, which increases with a decrease in resistivity of magnetic material. We will see in Chapter 3 that in a low-frequency region where the influence of eddy currents is weak, the loss is precisely proportional to the reciprocal of resistivity. Ferrites that have been widely used in proton-ring RF cavities have high resistivity, and consequently, the eddy-current loss is insignificant compared to the hysteresis loss. On the other hand, the resistivity of magnetic alloys is considerably lower than that of ferrites, and as a result, the eddy-current loss of magnetic alloys is substantially higher than the hysteresis loss in the frequency range where most of the RF cavities for proton rings operate.

In principle, if the distribution of electric field induced within a magnetic object is known, the eddy-current loss can be calculated. For a magnetic object in which there is a time-varying magnetic flux density **B**, the following Faraday's law holds:

$$\oint_c \mathbf{E} \cdot d\mathbf{s} = -\frac{\partial}{\partial t} \int_S \mathbf{B} \cdot \mathbf{n}\, da, \tag{2.17}$$

where $\mathbf{n}$ is a unit vector whose direction is outwardly normal to the surface S. Basically, the law states that a changing magnetic field will induce an electric field. More specifically, the equation indicates that the line integral of electric field $\mathbf{E}$ along any closed path c is equal to the rate of decrease in the magnetic flux through any surface S spanning that path. Provided that the distribution of $\mathbf{B}$ is known, we can obtain the distribution of both the electric field and the eddy current within the object from eq. (2.17). The magnitude of the eddy current depends on the magnitude of $\mathbf{E}$ and the resistivity of the object. If $\mathbf{J}$ denotes the eddy-current density, then the power loss in the object is given by

$$P_{ed} = \frac{1}{V}\int_V dv \frac{1}{T}\int_0^T \mathrm{Re}\left[\mathbf{J}^*\mathbf{E}\right] dt, \tag{2.18}$$

where P_{ed} is the eddy-current loss expressed as time-averaged power loss per unit volume. Assuming **J** and **E** are steady-state sinusoidal time-varying functions, and performing the time integral in eq. (2.18), we obtain

$$P_{ed} = \frac{1}{2V}\int_V \mathrm{Re}\left[\mathbf{J}^*\mathbf{E}\right] dv. \tag{2.19}$$

2.5 Hysteresis Loss

2.5.1 Definition of Hysteresis Loss

The analysis of magnetic loss into its constituent parts is difficult and still a matter of some debate. A conventional approach is that the overall magnetic loss is divided into two principal parts: hysteresis loss and eddy-current loss. The hysteresis loss is determined from the area enclosed by the so-called *static hysteresis loop*. This separation of losses is based on the assumption that there is something fundamental about the static hysteresis loss. However, this assumption is not necessarily true, because the loop is not completely static and the shape and area of the loop depend on the way in which the applied field changes with time. If the drive field changes sinusoidally and its frequency increases slowly from a very low value with a constant field-amplitude, the shape and area of the loop change.

The current view of magnetic loss is that virtually all observed losses in alternating magnetization are due to eddy currents. Any field change over time, such as the change caused by the domain wall motion and magnetization rotation, accompanies eddy currents that cause the power loss. This view implies that the so-called *static hysteresis loss* is due to the same cause, that no matter how slowly the loop is traversed, irreversible changes in magnetization occur and these changes generate eddy currents. In other words, the overall magnetic loss given by eq. (2.15) is precisely equal to the eddy-current loss in the current interpretation. However, since the term *hysteresis loss* is still widely used, we propose an improvement of the conventional approach, as explained in the following paragraph.

In this approach, the overall magnetic loss is divided into two parts: the hysteresis loss, which is no longer static but changes with the frequency, and the so-called *classical eddy-current loss*. In order to apply classical electromagnetic theory, the latter is calculated on the assumption that the magnetization is microscopic and distributed homogeneously. The word “classical” in “classical eddy-current loss” is hereafter omitted for simplicity. The hysteresis loss defined here is equivalent to the loop area of

the *B-H* loop in which H and B are the magnetic field intensity and the magnetic flux density within the object, both of which vary with the frequency and position. This hysteresis loss is distinct from the overall magnetic loss that is defined as the loop area of the *B-H* loop in which H is the magnetic field in the medium before introducing the object, and B is the magnetic flux density within the object. Defined this way, for a known, simple field distribution, the eddy-current loss and hysteresis loss can be calculated separately; otherwise, it is extremely difficult to measure them separately even for a simple field distribution.

2.5.2 Hysteresis Loss Equation

As defined above, the time-averaged hysteresis loss per unit volume, P_h, of a magnetic object in a magnetic field is given by

$$P_h = \frac{1}{2V}\int_V \mathrm{Re}\left[\mathbf{H}_2^* \frac{\partial \mathbf{B}_2}{\partial t}\right] dv, \tag{2.20}$$

where $\mathbf{H}_2$ and $\mathbf{B}_2$ are the magnetic field intensity and magnetic flux density, respectively, within the object. Provided that $\mathbf{H}_2$ and $\mathbf{B}_2$ reflect all of the magnetization mechanisms functioning in the object, eq. (2.20) represents all types of magnetic loss arising from each mechanism. If the magnetic power loss definition given above is correct, the sum of P_h in eq. (2.20) and P_{ed} in eq. (2.19) must agree with P_m in eq. (2.15), that is,

$$P_m = P_h + P_{ed}. \tag{2.21}$$

Since these three types of losses can be calculated separately for a flat magnetic sheet, under the simplified conditions given in the next chapter, we verify eq. (2.21) in the following chapters.

Likewise, the hysteresis loss per cycle per unit volume of a magnetic object, $P_{h,c}$, is represented by

$$P_{h,c} = \frac{T}{2V}\int_V \mathrm{Re}\left[\mathbf{H}_2^* \frac{\partial \mathbf{B}_2}{\partial t}\right] dv. \tag{2.22}$$

The area inside a *B-H* loop displayed on an oscilloscope corresponds to the overall magnetic loss, not solely the hysteresis loss. If the *B-H* loop is traced as frequency increases, we observe that a coercive field H_c increases, the loop becomes more rounded, and the loop area increases until it reaches a maximum at a specific frequency (see Chapter 7). This behavior is, of course, attributed to the eddy current induced in the object by the rapid change in magnetic flux. We will see in Chapters 3 and 7 that the hysteresis loss decreases with an increase in the frequency, even when the overall

magnetic loss increases. This is because as frequency increases, both the magnetic field intensity and the magnetic flux density within the sheet diminish due to the eddy-current effect. However, it is shown in Chapter 7 that the Q-value defined by the hysteresis loss, Q_h, is always equal to the intrinsic Q-value Q_0, which does not depend on frequency, as long as the frequency is within a nondispersive region.

Incidentally, the word "hysteresis" is Greek, meaning "a coming late," and is today applied to almost any phenomenon in which the effect lags behind the cause. Its first scientific use was by J. A. Ewing in 1881, referring to the magnetic behavior of iron. Incidentally, Ewing was a professor at the University of Tokyo from 1878 to 1883. During his five-year tenure at the university, he introduced his students to research on magnetism, and Japanese research in this field has flourished ever since [89].

2.6 *Q*-Value of Magnetic Materials

In the materials-engineering field, a so-called *loss factor* or *loss tangent* has usually been used as a measure of a material's quality. It is defined by the ratio of the imaginary part of the complex permeability of a material to its real part and is customarily referred to as $\tan\delta$, where δ is sometimes called the *loss angle*. In electrical engineering, a quality factor Q, which is often referred to as the Q-value, has traditionally been used as a figure of merit of an oscillating system, such as a resonant circuit. It is defined by the ratio of the stored energy to the energy dissipated in one radian of an oscillation. Most proton-ring RF cavities are loaded with magnetic cores to make the cavity length short and to provide a means of dynamically tuning the cavity. Hence, it is advantageous to express the quality of the core by the Q-value, because cavity loss and core loss can then be treated in a unified manner. In Chapter 7, we demonstrate using an orthodox method that the Q-value of a material is exactly equal to the reciprocal of its loss factor, $1/\tan\delta$.

On the basis of the above definition, we can obtain the overall Q-value of a magnetic object, Q_e, from the stored magnetic energy W (given in eq. (2.7)) and the time-averaged overall magnetic loss P_m (given in eq. (2.15)) as follows:

$$Q_e = \frac{\omega W}{P_m}. \tag{2.23}$$

A magnetic object, subjected to a high magnetic field at a high frequency can have several types of losses from different mechanisms. The Q-value can be defined for each loss mechanism. If there are a number of loss mechanisms in the magnetic object whose stored energy is W, the overall Q-value is defined as

$$\frac{1}{Q_e} = \frac{\sum_n P_n}{\omega W} = \frac{P_1 + P_2 + P_3 + \cdots\cdots}{\omega W} = \sum_n \frac{1}{Q_n}, \tag{2.24}$$

with

$$Q_n = \frac{\omega W}{P_n}, \tag{2.25}$$

where P_n ($n = 1, 2, 3, \cdot$) denotes the power loss due to each mechanism and Q_n the corresponding Q-value. Equation (2.24) indicates that for Q-values obtained separately, the overall Q-value is obtained through their combination. However, it is very difficult to experimentally separate a power loss caused by one mechanism from those caused by other mechanisms. Theoretically, eq.(2.15) gives the overall magnetic loss and does not provide any way of distinguishing one mechanism from another. Nevertheless, as mentioned before, the eddy-current loss and the hysteresis loss can be calculated separately provided the field distribution is simple and easy to handle. It should be noted that hysteresis loss generally includes several types of losses arising from separate magnetization mechanisms and eq.(2.20) gives the sum of those losses.

Let Q_h represent the Q-value defined by the hysteresis loss and Q_{ed} represent the Q-value defined by the eddy-current loss. Then, in our present model, in which the overall magnetic loss consists of the hysteresis loss and the eddy-current loss, the overall Q-value Q_e is given (from eq.(2.24)) by

$$\frac{1}{Q_e} = \frac{1}{Q_h} + \frac{1}{Q_{ed}}. \tag{2.26}$$

If we know the stored energy, the hysteresis loss, and the eddy-current loss, we can obtain Q_h and Q_{ed} from eq.(2.25) and then Q_e from eq.(2.26). Equation (2.26) can therefore be used as an expression for cross-checking the value of Q_e obtained from eq. (2.23).

If a device is comprised of several components, its Q-value is determined by the energy stored in the device and the sum of the power loss of each component. For RF cavities for proton rings, the power loss of the magnetic core is much higher than the cavity wall loss and the losses of other components. As a result, the Q-value of the cavity is almost equal to that of the magnetic core.

2.7 Permeability

The magnetic characterization of a magnetic object is based on the measurement of **B** as a function of **H**. The permeability μ, which is defined by the ratio of **B** to **H**, is the slope of a line from the origin to a particular point on the *B*-*H* curve shown in Fig.2.1.

Therefore, it varies continuously as **H** increases from zero. Two special values of μ are the initial permeability and the maximum permeability. The initial permeability μ_i is the limit approached by the permeability as **B** and **H** are decreased toward zero. The maximum permeability μ_m is the highest value of permeability obtained by varying the amplitude of **H**, as illustrated in Fig. 2.1.

We are interested in an alternating magnetic field $\mathbf{H}_{ac}$ swinging about the origin or about some operating point set on a *B-H* curve by applying a biasing field. A closed curve traced on the *B-H* plane by this field variation is sometimes referred to as a *minor loop*. If the swing is small, the *incremental permeability* μ_Δ, defined by $\mathbf{B}_{ac}/\mathbf{H}_{ac}$, where $\mathbf{B}_{ac}$ is the magnetic flux density created by $\mathbf{H}_{ac}$, can be regarded as a constant value. As the permeability we use in this paper is exclusively the incremental permeability, the word "incremental" and the subscript Δ are omitted for simplicity. Incidentally, it is a simple matter to show that if the incremental permeability is a constant, a minor loop takes the shape of an exact ellipse.

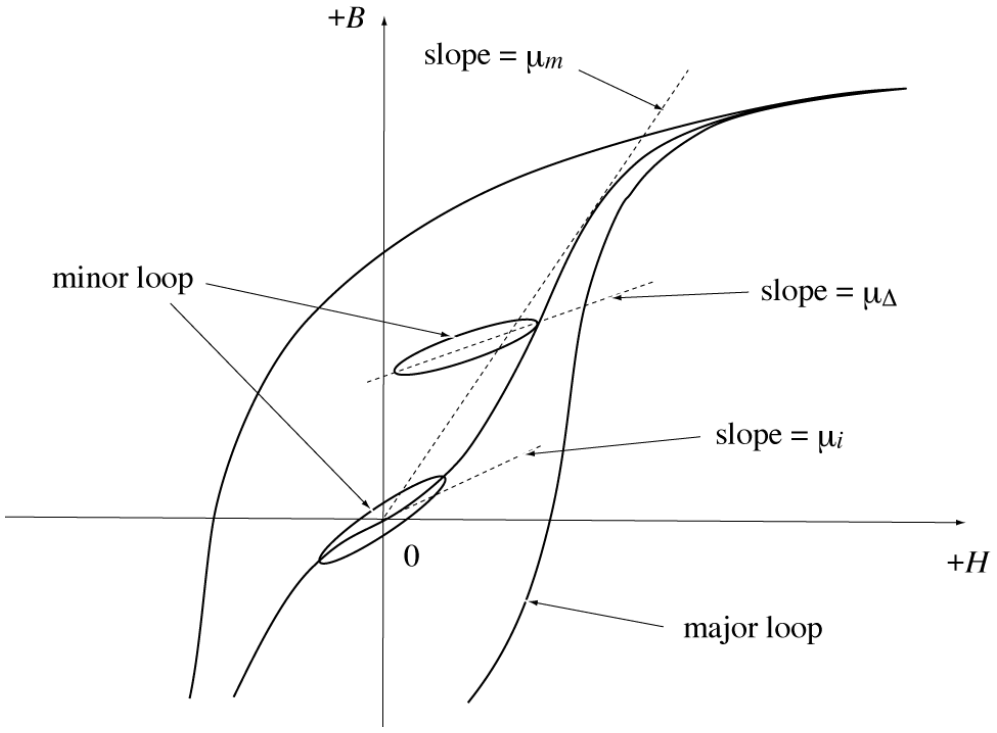

Figure 2.1 Virgin induction curve, part of a hysteresis loop and two minor loops. Three kinds of permeability (μ_i, μ_m, and μ_Δ) are also illustrated.

In this paper, we use two definitions of permeability: *intrinsic permeability* and *effective permeability*. The intrinsic permeability $\mu\,(=\mu'-j\mu'')$ is the permeability that is inherent in magnetization mechanisms and characterizes the local relationship between **B** and **H**. It is a material constant and does not depend on the geometry of a magnetic object, but is a function of the frequency because of the presence of some dispersion mechanisms. The frequency behavior of intrinsic permeability is briefly reviewed in Chapter 5.

The permeability definition we usually use is the effective permeability, which is defined by the ratio of the average magnetic flux density within the object to the applied magnetic field strength. Thus, it characterizes the macroscopic magnetic properties of the object and is expressed by $\mu_e\,(=\mu_e'-j\mu_e'')$. The effective permeability is related to the intrinsic permeability by a *demagnetizing factor*, which is defined as the ratio of the demagnetizing field to the magnetization (see Section 6.2). While the demagnetizing factor essentially depends on the geometry of a magnetic object, if the object is somewhat conductive and used in an alternating magnetic field, it also depends on the eddy current. In particular, when the conductive object is used at high frequencies, eddy currents virtually determine the demagnetizing field and, consequently, the effective permeability.

We can easily measure the applied magnetic field $\mathbf{H}_{appl}$ and can obtain the average magnetic flux density within an object, $\mathbf{B}_{av}$, by measuring, for example, the inductance of the object. Then, by taking the ratio $\mathbf{B}_{av}/\mathbf{H}_{appl}$, we can obtain the effective permeability μ_e. In Chapter 6, the expression of the effective permeability of magnetic sheet is derived using the magnetic field distribution obtained in Chapter 4.

3. Low-Frequency Properties of Magnetic Sheet

3.1 Introduction

Most applications use magnetic materials in an alternating magnetic field, because of which their magnetic properties in such applications differ from those they exhibit in a quasistatic state. In this chapter, we discuss the magnetic properties of a plane magnetic sheet in an alternating magnetic field applied at a low frequency. There are three reasons for deriving the approximate expressions applicable only to the low-frequency regions. First, the obtained expressions are sufficiently useful in low-frequency applications up to 10 [kHz] or even 100 [kHz], depending on the values of the material constants and thickness of the sheet. Second, since the expressions are simple and easily understood, they can help us interpret the behavior of magnetic materials when used in an alternating magnetic field. Third, these expressions can be used as references to which the expressions derived in the following chapters without any frequency assumptions must reduce when the frequency is much lower than RFs. This is a necessary condition for the accuracy of the expressions.

3.2 Assumptions

Figure 3.1 shows a cross section of a flat magnetic sheet of thickness d which extends infinitely in both x and z directions. Assume a sinusoidal, time-varying, uniform magnetic field of small to moderate amplitude is applied in the z direction, parallel to the sheet surface. The applied magnetic field induces some eddy currents, which hinder its penetration into the interior of the sheet. However, as long as the frequency is very low, the field can penetrate fairly well into the sheet, such that both the field nonuniformity and the eddy-current loss are very small. In this chapter, we deal with the case where the magnetic field is applied at such a low frequency (that is, the ratio of the sheet thickness to the skin depth is very small) that the effect of the eddy currents is quite weak.

To summarize, the analyses in this chapter are based on the following assumptions:

(1) the magnetic sheet is flat and extends infinitely in both x and z directions,
(2) the intrinsic permeability of the sheet is linear and isotropic, and
(3) the frequency of the applied magnetic field is low enough to cause only very minor eddy currents.

Assume that the applied magnetic field $\mathbf{H}_{z0}$ is given by

$$\mathbf{H}_{z0} = H_0 e^{j\omega t}. \tag{3.1}$$

The magnetic field intensity $\mathbf{H}_z$ and the magnetic flux density $\mathbf{B}_z$ within the sheet are written as

$$\mathbf{H}_z = \mathbf{H}(y)\, e^{j\omega t} \quad \text{and} \quad \mathbf{B}_z = \mu \mathbf{H}_z = \left(\mu' - j\,\mu''\right) \mathbf{H}(y)\, e^{j\omega t}, \tag{3.2}$$

where $\mu\,(=\mu'-j\mu'')$ is the intrinsic permeability. It is important to distinguish between the intrinsic permeability and the effective permeability, although at low frequencies, the two are very similar because the eddy-current effect is weak.

3.3 Approximate Field Distribution

To obtain the low-frequency magnetic properties of the sheet, we require the field distribution within the sheet in this frequency range. Even at low frequencies, the time-varying magnetic flux creates small eddy currents, which cause the field intensity to diminish slightly and the field phase to lag slightly behind the surface phase. As a result of this phase lag, the magnetic field has a small imaginary part in addition to a real part whose magnitude is slightly less than that of the applied field. Thus, $\mathbf{H}_z$ is represented in the complex form by the real part Re[$\mathbf{H}_z$] and the imaginary part Im[$\mathbf{H}_z$]:

$$\mathbf{H}_z = \mathbf{H}(y)\, e^{j\omega t} = \left\{ \mathrm{Re}\left[\mathbf{H}_z\right] + j\,\mathrm{Im}\left[\mathbf{H}_z\right] \right\} e^{j\omega t}. \tag{3.3}$$

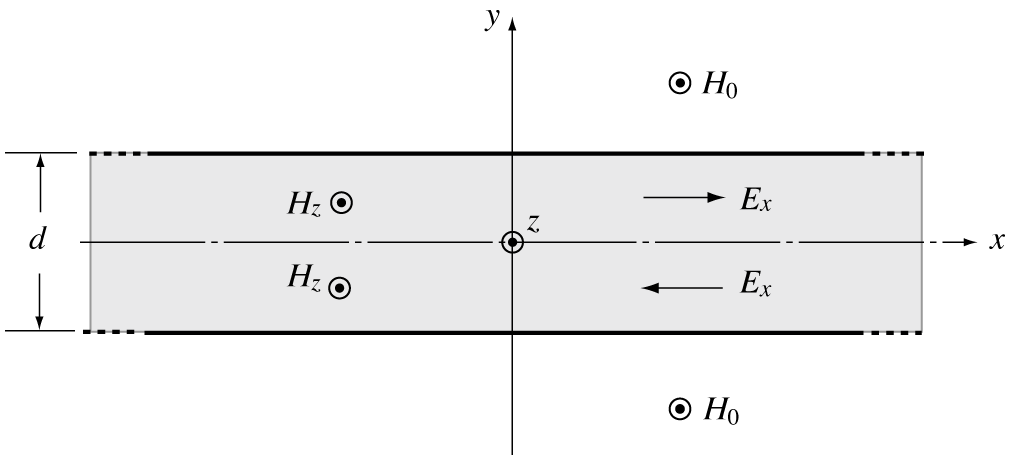

Figure 3.1 Field components in Cartesian coordinates in a flat magnetic sheet extending infinitely in both x and z directions.

The next step is to understand how the low-frequency approximations of Re[$\mathbf{H}_z$] and Im[$\mathbf{H}_z$] are expressed in terms of the frequency and the thickness and material constants of the sheet. Fortunately, we have obtained the exact expressions of magnetic field distribution (next chapter), from which we can obtain the low-frequency approximations. Then, we only need to reduce the exact expressions to approximate forms on the assumption that the field is applied at a low frequency.

The expressions of the field distribution are written as a function of θ, which is defined as

$$\theta \equiv \frac{d}{\delta_s}, \tag{3.4}$$

where d is the thickness of the sheet and δ_s is the skin depth given by

$$\delta_s = \sqrt{\frac{2}{\omega \mu' \sigma}}, \tag{3.5}$$

with σ being the conductivity of the sheet material. The skin depth is discussed at some length in Chapter 4. The real and imaginary parts of the magnetic field given in eqs. (4.29) and (4.30) are expressed in terms of trigonometric and hyperbolic functions, both of which can be expanded into a power series of θ. The expansions are written in a series of even powers of θ, $a_0 + \Sigma a_{2n}\theta^{2n}$, where a_0 is a constant, n is a positive integer ($n = 1, 2, 3, \cdots$), and a_{2n} is a coefficient of the $(n+1)$th term. Under the low frequency assumption, we take only the first and second terms from the expansions of Re[$\mathbf{H}_z$] and Im[$\mathbf{H}_z$] and ignore the other terms. Then, Re[$\mathbf{H}_z$] and Im[$\mathbf{H}_z$] can be approximately written as

$$\mathrm{Re}[\mathbf{H}_z] \simeq \left[1 - \frac{1}{4}\theta^2 \tan\delta + \theta^2 \tan\delta \left(\frac{y}{d} \right)^2 \right] H_0, \tag{3.6}$$

and

$$\mathrm{Im}[\mathbf{H}_z] \simeq \left[-\frac{1}{4}\theta^2 + \theta^2 \left(\frac{y}{d} \right)^2 \right] H_0, \tag{3.7}$$

where $\tan\delta$ is the intrinsic loss factor given by μ''/μ'. It follows from eqs. (3.6) and (3.7) that at the surface of the sheet ($y = d/2$ or $y = -d/2$),

$$\frac{\mathrm{Re}[\mathbf{H}_z]}{H_0} = 1 \quad \text{and} \quad \frac{\mathrm{Im}[\mathbf{H}_z]}{H_0} = 0, \tag{3.8}$$

and in the middle of the sheet ($y = 0$),

$$\frac{\mathrm{Re}[\mathbf{H}_z]}{H_0} \simeq 1 - \frac{1}{4}\theta^2 \tan\delta \qquad \text{and} \qquad \frac{\mathrm{Im}[\mathbf{H}_z]}{H_0} \simeq -\frac{1}{4}\theta^2. \tag{3.9}$$

In the following sections of this chapter, we use the approximate field distribution given in eqs. (3.6) and (3.7).

3.4 Stored Magnetic Energy

The average density of the stored magnetic energy W of a magnetic object when it is placed in a magnetic field is given by eq. (2.7). In the present case, the magnetic field $\mathbf{H}_{z0}$ is applied parallel to a sheet surface of infinite width, and consequently, the magnetization of the sheet does not affect the field in the medium outside the sheet. Therefore, the field intensity in the medium remains unchanged regardless of the presence or absence of the sheet. As a result, $\mathbf{H}_1$ in eq. (2.7) is replaced with $\mathbf{H}_{z0}$, and $\mathbf{B}_2$ is replaced with $\mathbf{B}_z$. Then, W is written as

$$W = \frac{1}{2V}\int_V \mathrm{Re}\left[\mathbf{H}_{z0}^{*}\mathbf{B}_z\right] dv. \tag{3.10}$$

Figure 3.2 shows the rectangular parallelepiped over which the volume integral in eq. (3.10) is performed. The length of the sides are l_0 in the x direction, d in the y direction, and one unit length in the z direction, so that the volume V is equal to $l_0 d$.

From eqs. (3.2) and (3.3), the magnetic flux density $\mathbf{B}_z$ is given by

$$\begin{aligned}\mathbf{B}_z = \mu\mathbf{H}_z &= \left(\mu' - j\,\mu''\right)\left\{\mathrm{Re}\left[\mathbf{H}_z\right] + j\,\mathrm{Im}\left[\mathbf{H}_z\right]\right\} e^{j\omega t} \\ &= \left\{\mathrm{Re}\left[\mathbf{B}_z\right] + j\,\mathrm{Im}\left[\mathbf{B}_z\right]\right\} e^{j\omega t}.\end{aligned} \tag{3.11}$$

Substituting $\mathrm{Re}[\mathbf{H}_z]$ from eq. (3.6) and $\mathrm{Im}[\mathbf{H}_z]$ from eq. (3.7) into eq. (3.11) yields the approximate expressions of $\mathrm{Re}[\mathbf{B}_z]$ and $\mathrm{Im}[\mathbf{B}_z]$:

$$\mathrm{Re}[\mathbf{B}_z] = \mu'\mathrm{Re}\left[\mathbf{H}_z\right] + \mu''\mathrm{Im}\left[\mathbf{H}_z\right] \simeq \left[\mu' - \frac{1}{2}\mu''\theta^2 + 2\mu''\theta^2\left(\frac{y}{d}\right)^2\right] H_0, \tag{3.12}$$

and

$$\begin{aligned}\mathrm{Im}[\mathbf{B}_z] &= \mu'\mathrm{Im}\left[\mathbf{H}_z\right] - \mu''\mathrm{Re}\left[\mathbf{H}_z\right] \\ &\simeq \left[-\mu'' - \frac{1}{4}\mu'\theta^2\left(1-\tan^2\delta\right) + \mu'\theta^2\left(1-\tan^2\delta\right)\left(\frac{y}{d}\right)^2\right] H_0.\end{aligned} \tag{3.13}$$

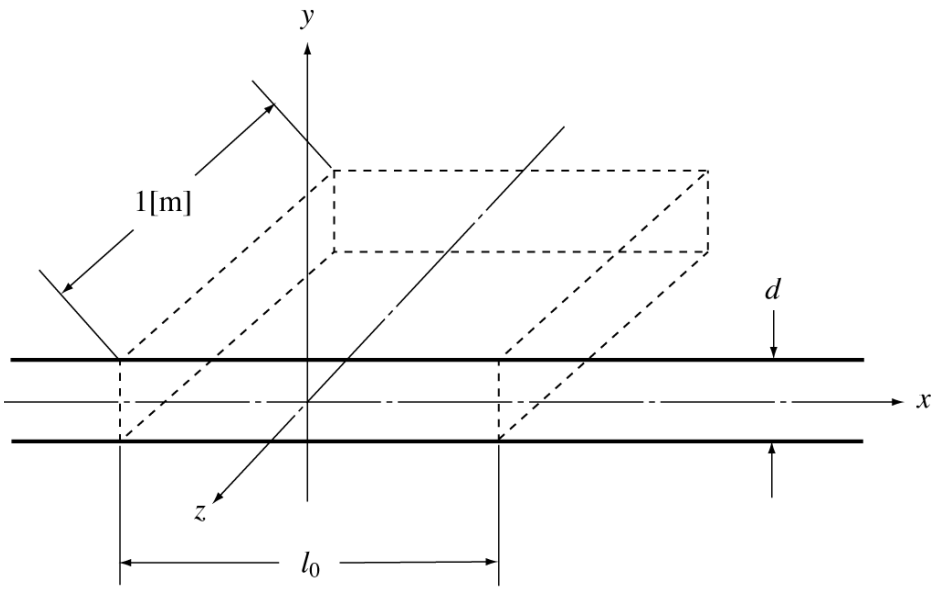

Figure 3.2 Rectangular parallelepiped over which the volume integral is performed.

The real part of $\mathbf{H}_{z0}^{*}\mathbf{B}_z$ is then given by

$$\mathrm{Re}\left[\mathbf{H}_{z0}^{*}\mathbf{B}_z\right] = \mathrm{Re}\left[H_0\, e^{-j\omega t}\left\{\mathrm{Re}\left[\mathbf{B}_z\right] + j\,\mathrm{Im}\left[\mathbf{B}_z\right]\right\} e^{j\omega t}\right] = \mathrm{Re}\left[\mathbf{B}_z\right] H_0$$

$$\simeq \left[\mu' - \frac{1}{2}\mu''\theta^2 + 2\mu''\theta^2\left(\frac{y}{d}\right)^2\right] H_0^2. \tag{3.14}$$

Replacing $\mathrm{Re}[\mathbf{H}_{z0}^{*}\mathbf{B}_z]$ in eq. (3.10) with eq. (3.14) gives

$$W \simeq \frac{1}{2V}\int_V \left[\mu' - \frac{1}{2}\mu''\theta^2 + 2\mu''\theta^2\left(\frac{y}{d}\right)^2\right] H_0^2\, dv. \tag{3.15}$$

Performing the integration over the volume V and dividing the result by V, we find

$$W \simeq \frac{1}{2}\left(\mu' - \frac{1}{3}\mu''\theta^2\right) H_0^2 = \frac{1}{2}\mu'\left(1 - \frac{1}{3}\theta^2\tan\delta\right) H_0^2. \tag{3.16}$$

If the magnetic field varies quasistatically or at a very low frequency, the second term in parentheses can be ignored, and thus, W reduces to a familiar form of stored magnetic energy:

$$W_0 = \frac{1}{2}\mu' H_0^2. \tag{3.17}$$

From eqs. (3.16) and (3.17), the ratio of W to W_0 is given by

$$\frac{W}{W_0} \simeq 1 - \frac{1}{3}\theta^2 \tan\delta. \tag{3.18}$$

Equation (3.18) clearly shows that the stored energy decreases as θ or the frequency increases. This is attributed to the diminished magnetic field intensity due to the eddy-current effect.

3.5 Overall Magnetic Loss

The time-averaged overall magnetic loss per unit volume, P_m, of a magnetic object placed in a magnetic field is given by eq. (2.15). As mentioned in the previous section, $\mathbf{H}_1$ and $\mathbf{B}_2$ are replaced with $\mathbf{H}_{z0}$ and $\mathbf{B}_z$, respectively, and then P_m is written as

$$P_m = \frac{1}{2V}\int_V \mathrm{Re}\left[\mathbf{H}_{z0}^* \frac{\partial \mathbf{B}_z}{\partial t}\right] dv. \tag{3.19}$$

From $\mathbf{B}_z$ given in eq. (3.11), $\partial\mathbf{B}_z/\partial t$ becomes

$$\frac{\partial \mathbf{B}_z}{\partial t} = \left\{-\omega \mathrm{Im}\left[\mathbf{B}_z\right] + j\omega \mathrm{Re}\left[\mathbf{B}_z\right]\right\} e^{j\omega t}. \tag{3.20}$$

It follows from $\mathbf{H}_{z0}$ in eq. (3.1), $\partial\mathbf{B}_z/\partial t$ in eq. (3.20), and $\mathrm{Im}[\mathbf{B}_z]$ in eq. (3.13) that we can obtain the real part of $\mathbf{H}_{z0}^*(\partial\mathbf{B}_z/\partial t)$,

$$\begin{aligned}\mathrm{Re}\left[\mathbf{H}_{z0}^* \frac{\partial \mathbf{B}_z}{\partial t}\right] &= \mathrm{Re}\left[H_0 e^{-j\omega t}\left\{-\omega \mathrm{Im}\left[\mathbf{B}_z\right] + j\omega \mathrm{Re}\left[\mathbf{B}_z\right]\right\} e^{j\omega t}\right] = -\omega \mathrm{Im}\left[\mathbf{B}_z\right] H_0 \\ &\simeq \omega\left[\mu'' + \frac{1}{4}\mu'\theta^2\left(1-\tan^2\delta\right) - \mu'\theta^2\left(1-\tan^2\delta\right)\left(\frac{y}{d}\right)^2\right] H_0^2.\end{aligned} \tag{3.21}$$

Substituting eq. (3.21) for $\mathrm{Re}[\mathbf{H}_{z0}^*(\partial\mathbf{B}_z/\partial t)]$ in eq. (3.19), performing the integration over the volume V, and dividing the result by V, we obtain

$$\begin{aligned}P_m &\simeq \frac{1}{2}\omega\left[\mu'' + \frac{1}{6}\mu'\theta^2\left(1-\tan^2\delta\right)\right] H_0^2 \\ &= \frac{1}{2}\omega\mu''\left[1 + \frac{1}{6}\theta^2\left(\frac{1}{\tan\delta} - \tan\delta\right)\right] H_0^2.\end{aligned} \tag{3.22}$$

If the magnetic field varies at a very low frequency, P_m reduces to

$$P_{m0} = \frac{1}{2}\omega\mu'' H_0^2. \tag{3.23}$$

From eqs. (3.22) and (3.23), the ratio P_m/P_{m0} is given by

$$\frac{P_m}{P_{m0}} \simeq 1 + \frac{1}{6}\theta^2\left(\frac{1}{\tan\delta} - \tan\delta\right), \tag{3.24}$$

which increases with an increase in θ when $\tan\delta$ is lower than 1.0 and decreases when $\tan\delta$ is higher than 1.0. The magnetic loss is often expressed as the energy loss in one hysteresis cycle, $P_{m,c}$, which is given in eq. (2.16). Let us replace $\mathbf{H}_1$ and $\mathbf{B}_2$ in eq. (2.16) with $\mathbf{H}_{z0}$ and $\mathbf{B}_z$, respectively, and substitute eq. (3.21) for $\mathrm{Re}[\mathbf{H}_{z0}^*(\partial\mathbf{B}_z/\partial t)]$ in eq. (2.16). Then, performing the integration in eq. (2.16) over volume V, we obtain

$$P_{m,c} \simeq \pi\mu''\left[1 + \frac{1}{6}\theta^2\left(\frac{1}{\tan\delta} - \tan\delta\right)\right] H_0^2. \tag{3.25}$$

The loss $P_{m,c}$ can also be obtained by dividing P_m given in eq. (3.22) by the frequency f.

3.6 Eddy-Current Loss

3.6.1 Electric Field Distribution

The time-averaged eddy-current loss per unit volume, P_{ed}, is given by eq. (2.19). As shown in Fig. 3.1, the magnetic field exists only in the z direction, and accordingly, the electric field and current are induced only in the x direction. Therefore, P_{ed} is given by

$$P_{ed} = \frac{1}{2V}\int_V \mathrm{Re}\left[\mathbf{J}_x^*\mathbf{E}_x\right] dv, \tag{3.26}$$

where $\mathbf{J}_x$ and $\mathbf{E}_x$ denote the electric current density and the electric field intensity in the x direction, respectively. To evaluate the eddy-current loss of the sheet, we require the distribution of $\mathbf{J}_x$ and $\mathbf{E}_x$ in y, which can be obtained from the distribution of $\mathbf{B}_z$ using Faraday's law.

Figure 3.3 shows a closed path c in an x-y cross section of the sheet. The path is composed of two segments of length l_0 in the x direction and two segments of length $2y_0$ in the y direction. We apply Faraday's law, given in eq. (2.17), to this path c and the surface S enclosed by the path. Supposing that the operation of the derivative with respect to t and the operation of the surface integral can be interchanged, we can write

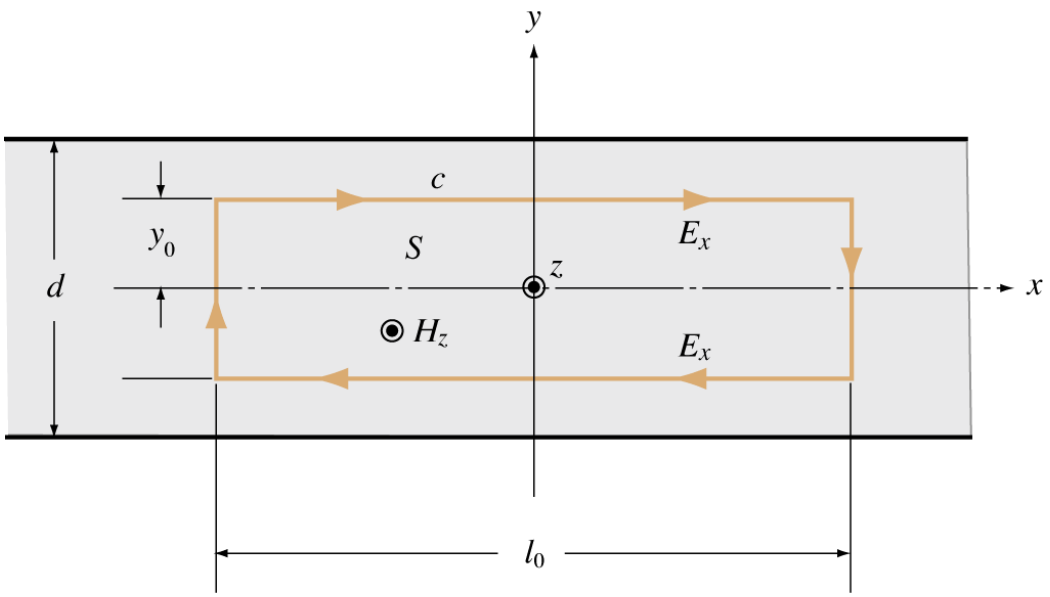

Figure 3.3 Closed path c and surface S enclosed by c in x-y cross section of the sheet. Line integrals of E_x along c and surface integral of $\partial \mathbf{B}_z/\partial t$ over S are performed to obtain E_x at $y = y_0$.

$$\oint_c \mathbf{E}_x \cdot d\mathbf{s} = -\int_S \frac{\partial \mathbf{B}_z}{\partial t} \cdot \mathbf{n}\, da. \tag{3.27}$$

First, we perform the line integral of $\mathbf{E}_x$ along the closed path c. It is clear from the configuration shown in Fig. 3.1 that the induced $\mathbf{E}_x$ is antisymmetric with respect to the x axis. To be more precise, the operation of replacing y with $-y$ reverses the sign of $\mathbf{E}_x$ but does not change the magnitude of $\mathbf{E}_x$. Since $\mathbf{E}_x$ at $y = +y_0$ or $y = -y_0$ is independent of position x, the left-hand side of eq. (3.27) is given by

$$\oint_c \mathbf{E}_x \cdot d\mathbf{s} = 2 l_0 \mathbf{E}_x. \tag{3.28}$$

Next, we perform the surface integral of $\partial \mathbf{B}_z/\partial t$ over the area S $(= 2y_0 l_0)$. Making use of $\partial \mathbf{B}_z/\partial t$ given in eq. (3.20), we can write the right-hand side of eq. (3.27) as

$$-\int_S \frac{\partial \mathbf{B}_z}{\partial t} \cdot \mathbf{n}\, da = -2 l_0 \omega \int_0^{y_0} \left\{ -\mathrm{Im}\left[\mathbf{B}_z\right] + j\, \mathrm{Re}\left[\mathbf{B}_z\right] \right\} dy\, e^{j\omega t}, \tag{3.29}$$

where $\mathrm{Re}[\mathbf{B}_z]$ and $\mathrm{Im}[\mathbf{B}_z]$ are given in eqs. (3.12) and (3.13). Performing the integral of eq. (3.29), we obtain

$$-\int_S \frac{\partial \mathbf{B}_z}{\partial t}\cdot\mathbf{n}\,da \simeq -2l_0 y_0 \omega H_0 \left(Re + j\,Im\right) e^{j\omega t}, \tag{3.30}$$

where

$$Re \simeq \mu'' + \mu'\theta^2\left(1-\tan^2\delta\right)\left[\frac{1}{4} - \frac{1}{3}\left(\frac{y_0}{d}\right)^2\right] \tag{3.31}$$

and

$$Im \simeq \mu' - \mu''\theta^2\left[\frac{1}{2} - \frac{2}{3}\left(\frac{y_0}{d}\right)^2\right]. \tag{3.32}$$

Substituting eqs. (3.28) and (3.30) into eq. (3.27) yields the $\mathbf{E}_x$ induced at $y = y_0$:

$$\mathbf{E}_x \simeq -y_0 \omega H_0 \left(Re + j\,Im\right) e^{j\omega t}. \tag{3.33}$$

3.6.2 Calculations of Eddy-Current Loss

The current density $\mathbf{J}_x$ induced by $\mathbf{E}_x$ is written as

$$\mathbf{J}_x = \sigma \mathbf{E}_x = \frac{\mathbf{E}_x}{\rho} \simeq -\frac{y_0 \omega H_0 \left(Re + j\,Im\right)}{\rho} e^{j\omega t}, \tag{3.34}$$

where σ is the conductivity and $\rho\,(=1/\sigma)$ is the resistivity of the sheet material. Then, $\mathbf{J}_x$ in eq. (3.26) is replaced with $\mathbf{J}_x$ from eq. (3.34) to give

$$P_{ed} = \frac{1}{2\rho V}\int_V \left|\mathbf{E}_x\right|^2 dv, \tag{3.35}$$

where

$$\left|\mathbf{E}_x\right|^2 = \mathbf{E}_x^* \mathbf{E}_x \simeq y_0^2\,\omega^2 H_0^2 \left(Re^2 + Im^2\right). \tag{3.36}$$

By expanding $(Re^2 + Im^2)$ in a power series of θ and taking only the first two terms, that is, the constant term and the θ^2 term, the following approximate expression is obtained from eq. (3.36):

$$\left|\mathbf{E}_x\right|^2 \simeq \omega^2 H_0^2 \alpha \left[\left(\mu'^2 - \frac{1}{2}\mu'\mu''\theta^2\right) y_0^2 - \frac{2}{3}\frac{\mu'\mu''\theta^2}{d^2} y_0^4\right] \tag{3.37}$$

with

$$\alpha = 1 + \frac{\mu''^2}{\mu'^2} = 1 + \tan^2\delta = 1 + \frac{1}{Q_0^2}, \tag{3.38}$$

where Q_0 is the intrinsic Q-value defined by $1/\tan\delta$. Substituting $|\mathbf{E}_x|^2$ given in eq. (3.37) into eq. (3.35) and performing the integral extending over the whole volume of the

rectangular parallelepiped shown in Fig. 3.2, we obtain

$$P_{ed} \simeq \frac{d^2 \mu'^2 \alpha}{24 \rho} \omega^2 \left(1 - \frac{2}{5} \theta^2 \tan\delta \right) H_0^2 . \tag{3.39}$$

3.6.3 Discussions on Eddy-Current Loss

Equation (3.39) clearly shows how each parameter is related to the eddy-current loss in the low-frequency range. The most important result is the strong dependence of P_{ed} on the frequency ω and the sheet thickness d as well as on the applied field intensity H_0. First, the eddy-current loss is proportional to ω^2. This is because the induced field $\mathbf{E}_x$ is proportional to ω, as shown in eq. (3.33), and the power loss P_{ed} is proportional to $|\mathbf{E}_x|^2$, as given in eq. (3.35). In most cases, ω and H_0 cannot be chosen freely because they are usually determined by each application's requirements and operational conditions.

The parameters d, ρ, and $\mu'^2\alpha$ can, in principle, be controlled to reduce the eddy-current loss. The most important parameter among them is d, because the eddy-current loss is proportional to d^2. Fortunately, reducing d in manufacturing processes is not difficult as long as the amount of reduction is within an allowable limit. On the other hand, ρ is intrinsically connected with the manufacturing method itself and therefore cannot be controlled in ordinary manufacturing processes. Note that if ρ is anisotropic, it is ρ in the direction of the tape width (x in Fig. 3.1) that is important for the eddy-current loss, not ρ in the direction of the tape length (z in Fig. 3.1). This is because the eddy current flows perpendicularly to the magnetic flux that flows along the tape.

Another factor determining the eddy-current loss is $\mu'^2\alpha$, which is given (from eq. (3.38)) by

$$\mu'^2 \alpha = \mu'^2 + \mu''^2 . \tag{3.40}$$

If a magnetic sheet is used in a low-frequency range, or more precisely, if $\alpha \simeq 1$ ($\mu' \gg \mu''$), only the real part μ' is responsible for the eddy-current loss. The eddy-current loss depends heavily on μ' because the magnetic flux Φ is proportional to μ', and therefore, a high μ' creates a large Φ, which in turn produces large eddy currents. Although lowering the value of μ' clearly helps to reduce eddy-current loss, it is not realistic because a higher μ' is desirable in most cases and a top priority in many applications. The adverse effect of a high μ' value on the eddy-current loss must be compensated for by reducing the thickness of the sheet. If a magnetic sheet is used in a dispersive frequency region, the imaginary part μ'' might increase considerably, which might contribute to an increase in eddy-current loss. Note that μ'' is the intrinsic permeability free from dispersion due to eddy currents and that for most sheet materials,

μ'' is much lower than μ' as long as the magnetic sheet is used in a frequency region well below the lowest relaxation frequency (see Chapter 5).

The above discussions can be summarized as follows. It is desirable, but very difficult, to increase ρ by improving manufacturing methods and processes. It is important to avoid a reduction in μ' in order to retain the advantage of the very high μ' property of magnetic alloys. The only practical way of reducing the eddy-current loss is to make the thickness of the sheet as thin as possible while preserving the appropriate sheet strength.

The eddy-current loss given in eq. (3.39) can be rewritten by using θ from eq. (3.4) and the skin depth δ_s from eq. (3.5) as follows:

$$P_{ed} \simeq \frac{1}{12}\omega\alpha\mu'\theta^2 H_0^2\left(1-\frac{3}{5}\theta^2\tan\delta\right) \simeq \frac{1}{12}\omega\alpha\mu'\theta^2 H_0^2$$
$$= \frac{1}{12}\omega\mu''\theta^2\left(\frac{1}{\tan\delta}+\tan\delta\right)H_0^2, \tag{3.41}$$

where the θ^4 term is ignored. It follows from eqs. (3.23) and (3.41) that the ratio of P_{ed} to P_{m0} is given by

$$\frac{P_{ed}}{P_{m0}} \simeq \frac{1}{6}\theta^2\left(\frac{1}{\tan\delta}+\tan\delta\right). \tag{3.42}$$

Equation (3.42) shows that in a low-frequency region P_{ed}/P_{m0} is proportional to θ^2 or ω. This is because P_{ed} is proportional to ω^2 while P_{m0} is proportional to ω.

3.7 Hysteresis Loss

The time-averaged hysteresis loss per unit volume, P_h, of a magnetic object placed in a magnetic field is given by eq. (2.20). In the present case, $\mathbf{H}_2$ and $\mathbf{B}_2$ are replaced with $\mathbf{H}_z$ and $\mathbf{B}_z$, respectively, and then P_h is written as

$$P_h = \frac{1}{2V}\int_V \mathrm{Re}\left[\mathbf{H}_z^*\frac{\partial\mathbf{B}_z}{\partial t}\right]dv. \tag{3.43}$$

It follows from $\mathbf{H}_z$ in eq. (3.3) and $\partial\mathbf{B}_z/\partial t$ in eq. (3.20) that $\mathrm{Re}[\mathbf{H}_z^*(\partial\mathbf{B}_z/\partial t)]$ is represented by

$$\mathrm{Re}\left[\mathbf{H}_z^*\frac{\partial\mathbf{B}_z}{\partial t}\right] = \omega\left\{-\mathrm{Re}\left[\mathbf{H}_z\right]\mathrm{Im}\left[\mathbf{B}_z\right]+\mathrm{Im}\left[\mathbf{H}_z\right]\mathrm{Re}\left[\mathbf{B}_z\right]\right\}. \tag{3.44}$$

Substituting eqs. (3.6), (3.7), (3.12), and (3.13) into eq. (3.44) leads to the low-frequency

approximation of $\mathrm{Re}[\mathbf{H}_z^*(\partial \mathbf{B}_z/\partial t)]$ given by

$$\mathrm{Re}\left[\mathbf{H}_z^* \frac{\partial \mathbf{B}_z}{\partial t}\right] \simeq \omega\mu''\left[\left(1-\frac{1}{2}\theta^2\tan\delta\right)+2\theta^2\tan\delta\left(\frac{y}{d}\right)^2\right]H_0^2. \tag{3.45}$$

Replacing $\mathrm{Re}[\mathbf{H}_z^*(\partial \mathbf{B}_z/\partial t)]$ in eq. (3.43) with eq. (3.45), performing the integration over the volume V shown in Fig. 3.2, and dividing the result by V, we finally obtain

$$P_h \simeq \frac{1}{2}\omega\mu''\left(1-\frac{1}{3}\theta^2\tan\delta\right)H_0^2. \tag{3.46}$$

We see from eq. (3.46) that in a very low frequency region where the θ^2 term can be ignored, P_h is exactly proportional to ω. Equation (3.46) also shows that the second term in parentheses makes P_h shift slightly below the linear increase with an increase in ω. This is, of course, attributed to the eddy current, which slightly reduces both the magnetic field and the magnetic flux density and, as a result, causes a slight decrease in hysteresis loss. From eqs. (3.23) and (3.46), the ratio of P_h to P_{m0} is written as

$$\frac{P_h}{P_{m0}} \simeq 1-\frac{1}{3}\theta^2\tan\delta. \tag{3.47}$$

It is worth noting that P_h/P_{m0} given in eq. (3.47) is identical to W/W_0 given in eq. (3.18). Taking the sum of P_h from eq. (3.46) and P_{ed} from eq. (3.41) yields

$$\begin{aligned} P_h + P_{ed} &\simeq \frac{1}{2}\omega\mu''\left(1-\frac{1}{3}\theta^2\tan\delta\right)H_0^2+\frac{1}{12}\omega\alpha\mu'\theta^2H_0^2 \\ &= \frac{1}{2}\omega\mu''\left[1+\frac{1}{6}\theta^2\left(\frac{1}{\tan\delta}-\tan\delta\right)\right]H_0^2. \end{aligned} \tag{3.48}$$

The result is exactly the same as the overall magnetic loss P_m given in eq. (3.22). This verifies the accuracy of eq. (2.21) in the low-frequency region.

3.8 Q-Value

The overall Q-value of the magnetic sheet, Q_e, is obtained by introducing the stored magnetic energy W from eq. (3.16) and the overall magnetic loss P_m from eq. (3.22) into eq. (2.23) as follows:

$$Q_e = \frac{\omega W}{P_m} \simeq \frac{\mu' - \frac{1}{3}\mu''\theta^2}{\mu'' + \frac{1}{6}\mu'\theta^2\left(1-\tan^2\delta\right)} = \frac{1-\frac{1}{3}\theta^2\tan\delta}{\tan\delta + \frac{1}{6}\theta^2\left(1-\tan^2\delta\right)}. \quad (3.49)$$

Now, let Q_h be the Q-value defined by the hysteresis loss. Substituting W and the hysteresis loss P_h from eq. (3.46) into eq. (2.25) gives

$$Q_h = \frac{\omega W}{P_h} \simeq \frac{\mu' - \frac{1}{3}\mu''\theta^2}{\mu'' - \frac{1}{3}\mu'\theta^2\tan^2\delta} = \frac{\mu'}{\mu''} = \frac{1}{\tan\delta} = Q_0. \quad (3.50)$$

It is interesting that Q_h is determined solely by the intrinsic permeabilities μ' and μ'' and is independent of θ. This can be explained mathematically by the behavior of W and P_h as θ changes. W and P_h vary with θ in exactly the same manner, and consequently, their dependence on θ is canceled out when W is divided by P_h. We will see in Chapter 7 that the equation $Q_h = Q_0$ applies not only to low-frequency regions but to any frequency region.

Likewise, let Q_{ed} be the Q-value defined by the eddy-current loss. Substituting W and the eddy-current loss P_{ed} from eq. (3.41) into eq. (2.25) yields

$$\begin{aligned} Q_{ed} = \frac{\omega W}{P_{ed}} &\simeq \frac{6\left(\mu' - \frac{1}{3}\mu''\theta^2\right)}{\alpha\mu'\theta^2} \\ &= \frac{6}{\theta^2\left(1+\tan^2\delta\right)}\left(1-\frac{1}{3}\theta^2\tan\delta\right). \end{aligned} \quad (3.51)$$

This can also be written as

$$Q_{ed} \simeq \frac{12}{\omega\mu'\sigma d^2\left(1+\tan^2\delta\right)}\left(1-\frac{1}{6}\omega\mu'\sigma d^2\tan\delta\right). \quad (3.52)$$

Equation (3.52) shows that as the frequency decreases toward zero, Q_{ed} approaches infinity. This corresponds to the behavior of the eddy-current loss, which decreases toward zero when the frequency approaches zero, as shown in eq. (3.39).

The overall Q-value of the magnetic sheet is also obtained from eq. (2.26) using Q_h from eq. (3.50) and Q_{ed} from eq. (3.51):

$$\frac{1}{Q_e} = \frac{1}{Q_h} + \frac{1}{Q_{ed}} \simeq \frac{\mu''}{\mu'} + \frac{\theta^2\left(1+\tan^2\delta\right)}{6\left(1-\frac{1}{3}\theta^2\tan\delta\right)} = \frac{\tan\delta + \frac{1}{6}\theta^2\left(1-\tan^2\delta\right)}{1-\frac{1}{3}\theta^2\tan\delta}. \quad (3.53)$$

The result is consistent with eq. (3.49). If the frequency is very low, Q_{ed} becomes high enough to satisfy the condition $Q_{ed} \gg Q_h$ so that Q_e becomes almost equal to Q_h.

3.9 Expressions in Terms of Effective Permeability

In Chapter 6, the accurate expression of the effective permeability of the sheet, μ_e, is derived and given in eqs. (6.19) and (6.22). If the frequency is low, the real part μ_e' and the imaginary part μ_e'' are approximated by

$$\mu_e' \simeq \mu' - \frac{1}{3}\mu''\theta^2, \quad (3.54)$$

and

$$\mu_e'' \simeq \mu'' + \frac{1}{6}\mu'\theta^2\left(1-\tan^2\delta\right). \quad (3.55)$$

By using these equations, we can rewrite W in eq. (3.16), P_m in eq. (3.22), and the Q-value in eq. (3.49) as

$$W \simeq \frac{1}{2}\mu_e' H_0^2, \qquad P_m \simeq \frac{1}{2}\omega\mu_e'' H_0^2, \qquad \text{and} \qquad Q_e \simeq \frac{\mu_e'}{\mu_e''}, \quad (3.56)$$

all of which are reasonable and expected results. Likewise, P_{ed} in eq. (3.41) and P_h in eq. (3.46) can be rewritten as

$$P_{ed} \simeq \frac{1}{2}\omega\mu_e' H_0^2\left(\tan\delta_e - \tan\delta\right), \quad (3.57)$$

and

$$P_h \simeq \frac{1}{2}\omega\mu_e' H_0^2\tan\delta, \quad (3.58)$$

where $\tan\delta_e$ is the effective loss factor of the sheet given by μ_e''/μ_e'.

3.10 Numerical Examples

Figure 3.4 shows W/W_0 as a function of θ $(=d/\delta_s)$ for four values of $\tan\delta$, where W is the stored magnetic energy and W_0 is that at very low frequencies. The results obtained from the approximate expression in eq. (3.18) are represented as dotted lines, and those from the accurate expression in eq. (7.9) as solid lines. As seen from Fig. 3.4, W/W_0 decreases as θ increases because of the reduced magnetic field intensity due to the eddy

current. W/W_0 decreases faster for higher values of $\tan\delta$ because the field within the sheet diminishes more rapidly when $\tan\delta$ is higher, as will be shown in the next chapter. For $\tan\delta = 0.5$, the approximate plot almost overlaps with the accurate one throughout the range of θ shown in the figure. As mentioned in Section 3.7, the ratio P_h/P_{m0}, where P_h is the hysteresis loss and P_{m0} is the overall magnetic loss at very low frequencies, is identical to the ratio W/W_0.

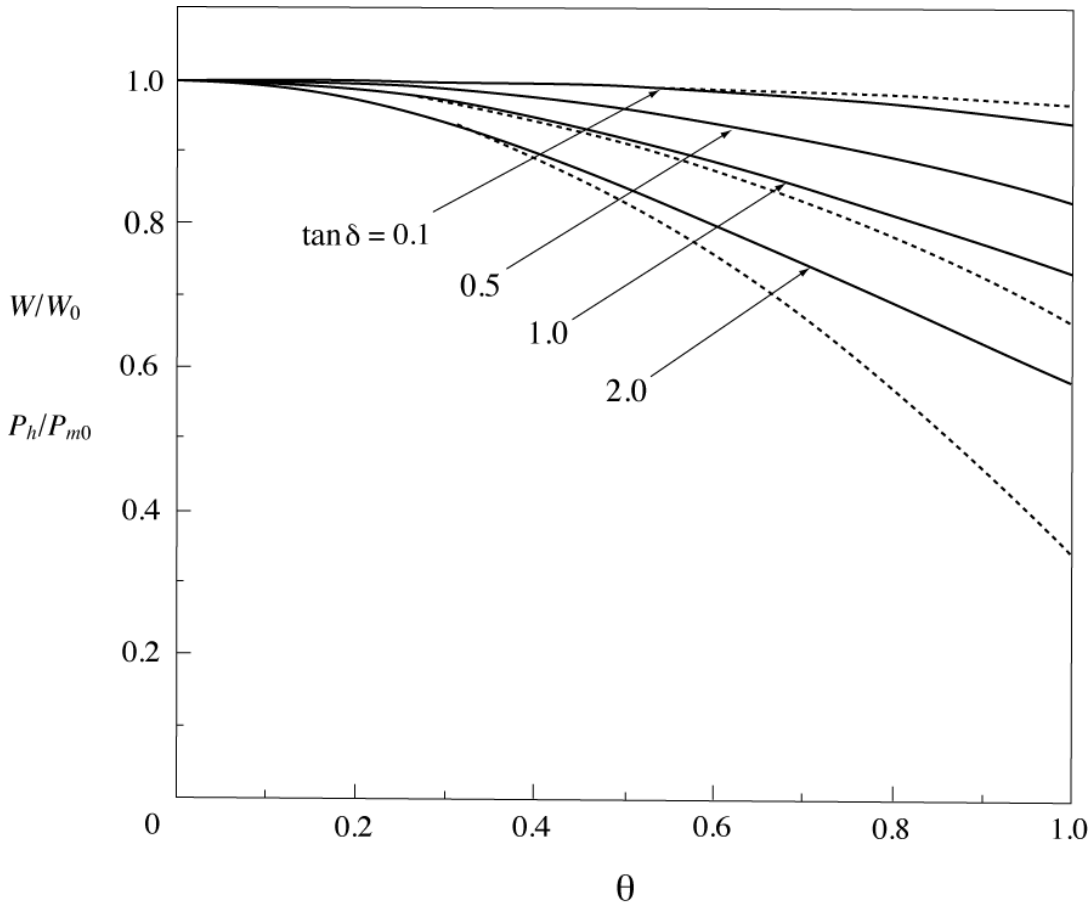

Figure 3.4 Normalized stored energy W/W_0 versus θ $(=d/\delta_s)$ for four values of $\tan\delta$. The dotted lines show the low-frequency approximations obtained from eq. (3.18), and the solid lines show the accurate results obtained from eq. (7.9). Normalized hysteresis loss P_h/P_{m0} is equal to W/W_0.

Figure 3.5 illustrates the normalized eddy-current loss P_{ed}/P_{m0} versus θ for four values of $\tan\delta$. The dotted lines show the low-frequency approximations obtained from eq.(3.42), and the solid lines show the accurate results obtained from eq.(7.35). P_{ed}/P_{m0} behaves in a rather complex manner when $\tan\delta$ changes, and the reason for this can be mathematically explained using eqs.(3.42) and (7.35), both of which include the factor $(1/\tan\delta + \tan\delta)$. For $\tan\delta = 0.1$, the factor is quite large due to the predominance of the term $1/\tan\delta$, and consequently, P_{ed}/P_{m0} also becomes large. As $\tan\delta$ is increased from 0.1, the factor continuously decreases until $\tan\delta$ reaches 1.0, where it reaches a minimum value of 2.0. If $\tan\delta$ increases beyond 1.0, the factor starts to increase, and therefore, the approximate P_{ed}/P_{m0} begins to increase as well. However, as the figure shows, the accurate P_{ed}/P_{m0} hardly increases when $\tan\delta$ increases beyond 1.0, because

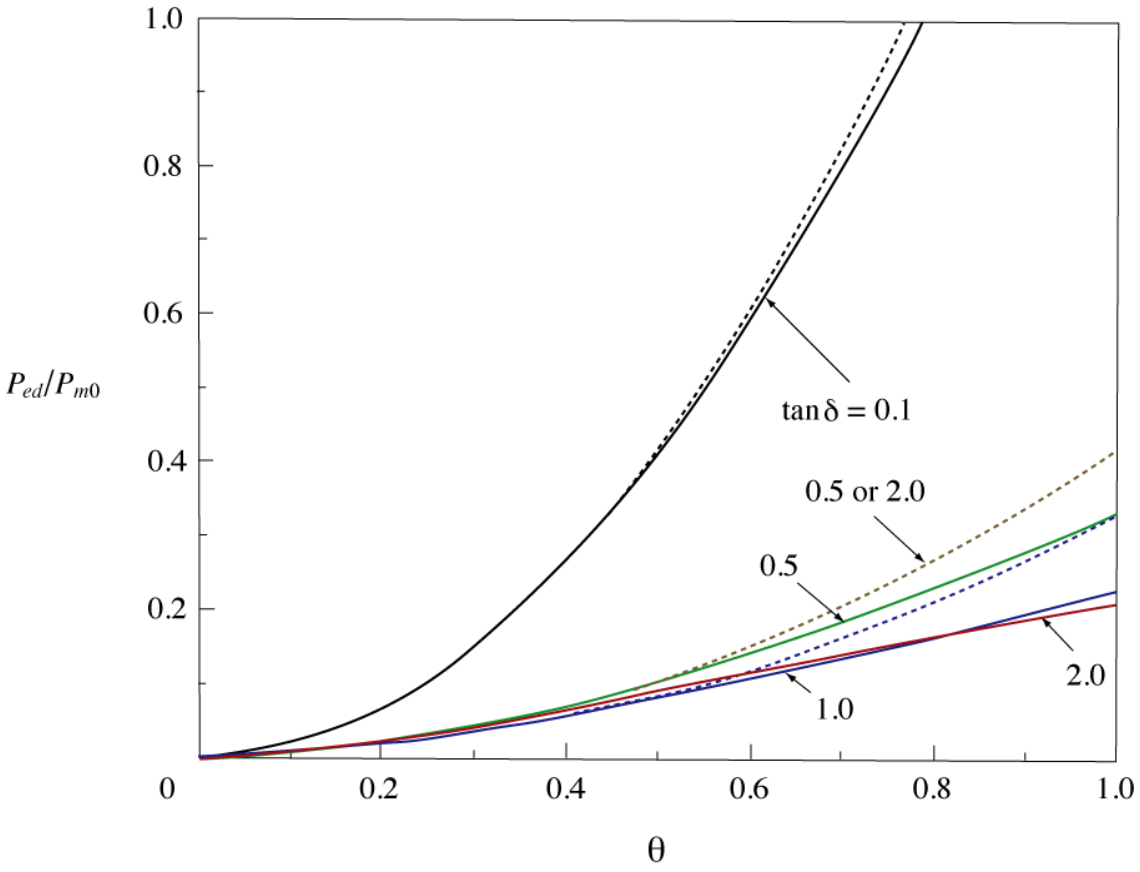

Figure 3.5 Normalized eddy-current loss P_{ed}/P_{m0} versus θ for four values of $\tan\delta$. The dotted lines show the low-frequency approximations obtained from eq. (3.42), and the solid lines show the accurate results obtained from eq.(7.35).

eq. (7.35) includes a factor, $g(\theta,\varphi)$, which decreases rapidly with an increase in $\tan\delta$, as will be demonstrated in Fig. 6.2.

Figure 3.6 shows the normalized overall magnetic loss P_m/P_{m0} as a function of θ for four values of $\tan\delta$. The dotted lines show the low-frequency approximations obtained from eq. (3.24), and the solid lines show the accurate results obtained from eq. (7.17). Note that the ordinate in Fig. 3.6 starts at 0.6. We know from Figs. 3.4 and 3.5 that as θ increases, the normalized hysteresis loss P_h/P_{m0} decreases, whereas the normalized eddy-current loss P_{ed}/P_{m0} increases. Since P_m/P_{m0} is given by the sum of these two normalized losses, the behavior of P_m/P_{m0} shown in Fig. 3.6 must be explained by the behavior of these two losses. When $\tan\delta$ is lower than 1.0, the increase rate of eddy-current loss exceeds the decrease rate of hysteresis loss, so that P_m/P_{m0} increases as θ increases. When $\tan\delta$ is higher than 1.0, the decrease rate of hysteresis loss exceeds

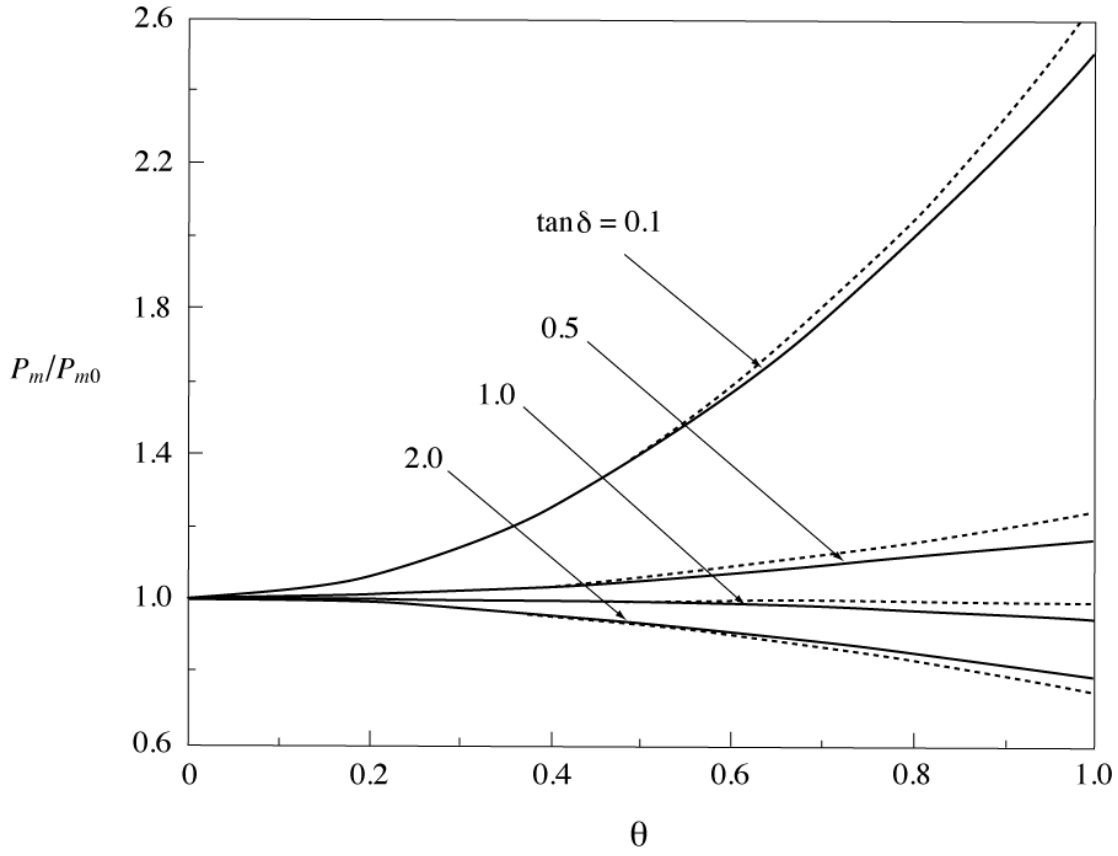

Figure 3.6 Normalized overall magnetic loss P_m/P_{m0} versus θ for four values of $\tan\delta$. The dotted lines show the low-frequency approximations obtained from eq. (3.24), and the solid lines show the accurate results obtained from eq. (7.17).

the increase rate of eddy-currnt loss and consequently P_m/P_{m0} decreases as θ inceases.

The dotted lines in Fig. 3.7 show Q_e/Q_0 as a function of θ for four values of $\tan\delta$, where Q_e is the approximate overall Q-value given in eq. (3.49) and Q_0 is the intrinsic Q-value given by μ'/μ''. The solid lines show the accurate Q_e/Q_0 obtained from Q_e given in eq. (7.51). Since Q_e/Q_0 is equal to the ratio of W/W_0 to P_m/P_{m0} $((W/W_0)/(P_m/P_{m0}) = (W/P_m)/(W_0/P_{m0}) = Q_e/Q_0)$, the behavior of Q_e/Q_0 shown in Fig. 3.7 can be interpreted from the behavior of W/W_0 shown in Fig. 3.4 and that of P_m/P_{m0} in Fig. 3.6. For example, consider the case of $\tan\delta = 0.1$. While W/W_0 decreases very slowly as θ increases, P_m/P_{m0} increases rather sharply. As a result, Q_e/Q_0 decreases appreciably with an increase in θ.

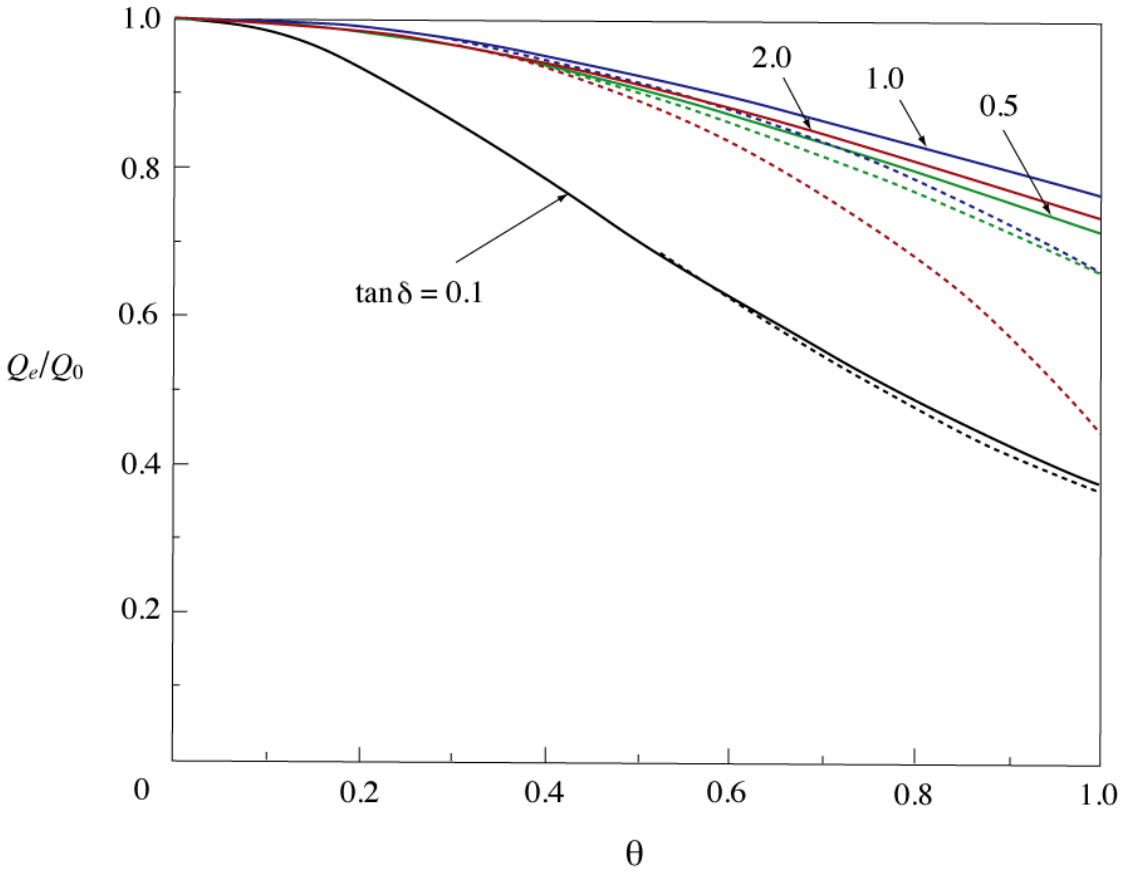

Figure 3.7 Normalized overall Q-value Q_e/Q_0 versus θ for four values of $\tan\delta$. The dotted lines show the low-frequency approximations obtained from the ratio of eq. (3.49) to Q_0, and the solid lines show the accurate results obtained from the ratio of eq. (7.51) to Q_0.

3.11 Frequency Range of Application

We can easily determine the range of θ for which the approximate expressions obtained in this chapter are applicable. Close study of the figures in the previous section show that the approximate plots agree quite well with the accurate ones, at least up to $\theta \simeq 0.4$. If $\tan\delta$ is lower than 0.1, the range in which the plots are in good agreement may be extended. Now, we are particularly interested in the frequency range in which θ is less than 0.4. It follows from eqs.(3.4) and (3.5) that the frequency at which θ is equal to 0.4 is given by

$$f_{\theta=0.4} = \frac{0.16}{\pi d^2 \mu' \sigma}, \tag{3.59}$$

where d is the thickness of the sheet; μ', the real part of the intrinsic permeability ($=\mu'_r\mu_0$, where μ'_r is the relative permeability); and σ, the conductivity. Let us consider a numerical example: if $d = 18$ [μm], $\mu'_r = 10{,}000$, and $\sigma = 1\times10^6$ [S/m], then $f_{\theta=0.4}$ is 12.5[kHz]. If μ'_r decreases to 1,000 while the other parameters remain the same, $f_{\theta=0.4}$ becomes 125 [kHz].

4. Field Distribution within Magnetic Sheet

4.1 Introduction

In Chapter 3, the magnetic properties of a plane magnetic sheet were discussed on the assumption that the magnetic field is applied at a low frequency. In this low-frequency range, the magnetic field distribution within the sheet is not much different from the uniform one. However, as the frequency increases, the eddy currents become more noticeable and more influential in altering the field distribution. In this chapter, the low frequency assumption is removed and the expressions useful for any frequency range are derived.

First, we derive a field equation that governs the magnetic field in the interior of the sheet and solve it to obtain the magnetic field distribution. In the following chapters, the field distribution obtained here will be used to derive the expressions for the effective permeability and other RF magnetic properties of the sheet, such as the magnetic power loss and the Q-value.

Effects of eddy currents on the magnetic properties of the sheet usually fall into one of three categories:

(1) the intensity of the field diminishes and the phase of the field lags behind that at the surface,
(2) the effective permeability of the sheet changes, and
(3) the energy loss of the sheet increases.

Category (1) is discussed in this chapter and categories (2) and (3) are discussed in Chapters 6 and 7, respectively.

4.2 Assumptions

Ferromagnetic materials are usually magnetized by the movement of magnetic walls, by the rotation of magnetic domains, or both. In fact, both mechanisms produce the same result because the spins in a region swept out by a moving wall have their orientation rotated through a definite angle. When studying the magnetic properties of a ferromagnetic material, we generally must take into account the domain structure of the material.

As regards materials for RF cavity applications, we are presently interested in magnetic alloys, such as the fine-structured soft magnetic alloys and the amorphous alloys. The fine-structured soft magnetic alloys, such as IRNC, are composed of nanometer-size, single-domain, crystalline grains in an amorphous phase. The amorphous alloys are noncrystalline materials and do not have definite rectilinear

domain walls. In both the fine-structured alloys and the amorphous alloys, the domain structure is less important and the magnetization is considered to be microscopic and distributed homogeneously. For this reason, it may be safe to assume that the magnetization can be regarded as a subject to which a standard method of classical electromagnetic theory is applied.

In the present and following chapters, we remove assumption (3) from Section 3.2, which states that a low-frequency field is applied and consequently the eddy-current effects are quite weak. However, assumptions (1) and (2), given below, remain, because these assumptions facilitate the calculation of the way in which the magnetic field decreases with depth below the surface:

(1) the magnetic sheet is flat and infinitely wide in both x and z directions, and

(2) the intrinsic permeability of the sheet is linear and isotropic.

4.3 Field Equation

Maxwell's equations expressed in differential form are given in Appendix B (eqs. (B.1), (B.2), and (B.3)). We start with Maxwell's equations written in Cartesian coordinates and composed of eight equations for six field components ($\mathbf{E}_x$, $\mathbf{E}_y$, $\mathbf{E}_z$, $\mathbf{H}_x$, $\mathbf{H}_y$, and $\mathbf{H}_z$). Because of the assumption that the uniform magnetic field is applied in the z direction, as shown in Fig. 3.1, only the two field components $\mathbf{E}_x$ and $\mathbf{H}_z$ have nonzero values, while the other four components are zero. Likewise, only the two field gradients $\partial\mathbf{E}_x/\partial y$ and $\partial\mathbf{H}_z/\partial y$ have nonzero values, while the other four field gradients are zero, that is,

$$\mathbf{E}_y = \mathbf{E}_z = \mathbf{H}_x = \mathbf{H}_y = 0 \quad \text{and} \quad \frac{\partial \mathbf{E}_x}{\partial x} = \frac{\partial \mathbf{E}_x}{\partial z} = \frac{\partial \mathbf{H}_z}{\partial x} = \frac{\partial \mathbf{H}_z}{\partial z} = 0. \tag{4.1}$$

As a result, only the following two equations are significant:

$$\begin{cases} \dfrac{\partial \mathbf{E}_x}{\partial y} = \mu \dfrac{\partial \mathbf{H}_z}{\partial t}, & (4.2) \\ \dfrac{\partial \mathbf{H}_z}{\partial y} = \varepsilon \dfrac{\partial \mathbf{E}_x}{\partial t} + \sigma \mathbf{E}_x = \sigma \left(1 + \dfrac{j\omega\varepsilon}{\sigma}\right) \mathbf{E}_x, & (4.3) \end{cases}$$

where ε and σ are the permittivity and the conductivity, respectively, of a sheet material. Since we are assuming that the electromagnetic fields vary sinusoidally in time, it is convenient to represent all field quantities as complex vectors with a time dependence $e^{j\omega t}$. The second equation of eq. (4.3) is obtained by assuming this time dependence. In this paper, $e^{j\omega t}$ is sometimes omitted for the sake of simplicity.

For conductive materials, even if the conductivity is not as high as that of copper,

we can show that the condition $\omega\varepsilon/\sigma \ll 1$ is satisfied over a wide frequency range up to at least microwave frequencies. For instance, σ/ε of a magnetic alloy with $\sigma \simeq 1\times10^6$ [S/m] is in the order of 10^{17} [s^{-1}], which is much higher than the frequencies we are interested in for particle acceleration. Hence, the displacement current in the magnetic sheet, $\varepsilon(\partial \mathbf{E}_x/\partial t)$, is negligible compared to the conducting current $\sigma \mathbf{E}_x$. Therefore, from eq. (4.3), we obtain

$$\mathbf{E}_x = \frac{1}{\sigma}\frac{\partial \mathbf{H}_z}{\partial y}. \tag{4.4}$$

Substituting eq. (4.4) into eq. (4.2) eliminates $\mathbf{E}_x$ to give the second-order differential equation for $\mathbf{H}_z$ as follows:

$$\frac{\partial^2 \mathbf{H}_z}{\partial y^2} = \mu\sigma\frac{\partial \mathbf{H}_z}{\partial t}. \tag{4.5}$$

This can also be written as

$$\frac{\partial^2 \mathbf{H}_z}{\partial y^2} - j\omega\mu\sigma\mathbf{H}_z = 0. \tag{4.6}$$

We use the complex intrinsic permeability μ given by

$$\mu = \mu' - j\mu''. \tag{4.7}$$

Replacing μ in eq. (4.6) with eq. (4.7) leads to

$$\frac{\partial^2 \mathbf{H}_z}{\partial y^2} - j\omega\left(\mu' - j\mu''\right)\sigma\mathbf{H}_z = 0. \tag{4.8}$$

Now, we take a square root of the coefficient of $\mathbf{H}_z$ from eq. (4.8) and denote it by γ:

$$\gamma = \sqrt{j\omega\left(\mu' - j\mu''\right)\sigma} = \sqrt{\omega\mu'\sigma\left(\tan\delta + j\right)}$$

$$= \frac{\sqrt{2}}{\delta_s}\alpha^{1/4}e^{j\phi}, \tag{4.9}$$

where

$$\tan\delta = \frac{\mu''}{\mu'} = \frac{1}{Q_0}, \tag{4.10}$$

$$\delta_s = \sqrt{\frac{2}{\omega\mu'\sigma}}, \tag{3.5}$$

$$\alpha = 1 + \tan^2 \delta, \tag{3.38}$$

and

$$\phi = \frac{1}{2} \tan^{-1}\left(\frac{1}{\tan \delta}\right) + m\pi = \frac{1}{2} \tan^{-1}\left(Q_0\right) + m\pi. \tag{4.11}$$
$$\left(m = 0,\ 1\right)$$

In this paper, $\tan\delta$ and Q_0 are referred to as the *intrinsic loss factor* and *intrinsic quality factor*, respectively. The word "intrinsic" is derived from the term "intrinsic permeability," which was introduced in Section 2.7 and will be described in further detail in Chapter 5. The skin depth δ_s, defined by eq. (3.5), is customarily used as a measure of penetration of the applied magnetic field into the interior of a magnetic object. It is the distance at which the amplitude of the field decays to $1/e$ of its surface value. However, δ_s is not applicable to all magnetic materials, because it does not include the imaginary part of the permeability μ''. It is considered to be the skin depth of a conductor or a magnetic material whose $\tan\delta$ is much lower than 1.0. In this chapter, we introduce a new expression for the skin depth of magnetic sheet, which includes μ'' and is therefore applicable to all magnetic sheets. When the distinction between these two definitions is necessary, we call δ_s, defined by eq. (3.5), the *conductor skin depth*.

By using γ given in eq. (4.9), we can rewrite eq. (4.8) as

$$\frac{\partial^2 \mathbf{H}_z}{\partial y^2} - \gamma^2 \mathbf{H}_z = 0. \tag{4.12}$$

This is recognized as a homogeneous linear differential equation with a complex number coefficient.

4.4 Solution of Equation

We can express the general solution of eq. (4.12) by

$$\mathbf{H}_z = C_1 e^{\gamma y} + C_2 e^{-\gamma y}, \tag{4.13}$$

where C_1 and C_2 are the constants of complex numbers, chosen to satisfy the boundary conditions. With reference to Fig. 3.1, let the applied magnetic field be $H_0 e^{j\omega t}$ (eq. (3.1)); then, the boundary conditions to be satisfied at both surfaces of the sheet, that is, at $y = +d/2$ or at $y = -d/2$, are

$$\mathbf{H}_z = H_0 \qquad \text{at} \qquad y = +\frac{d}{2} \quad \text{or} \quad y = -\frac{d}{2}. \tag{4.14}$$

By applying these boundary conditions to eq. (4.13), we can determine C_1 and C_2:

$$C_1 = C_2 = \frac{H_0}{2\cosh\left(\frac{\gamma d}{2}\right)}. \tag{4.15}$$

Substituting C_1 and C_2 into eq. (4.13) leads to the solution

$$\mathbf{H}_z = \frac{H_0}{\cosh\left(\frac{\gamma d}{2}\right)} \cosh(\gamma y). \tag{4.16}$$

Next, we transform eq. (4.16) into a form more suitable for calculating the field distribution. Let θ denote the ratio of the sheet thickness d to the skin depth δ_s,

$$\theta \equiv \frac{d}{\delta_s}; \tag{3.4}$$

then, γ given in eq. (4.9) can be written as

$$\gamma = \frac{\sqrt{2}\,\alpha^{1/4}}{d}\,\theta\, e^{j\phi}. \tag{4.17}$$

It can also be expressed in an explicit complex form

$$\gamma = a_1 + jb_1, \tag{4.18}$$

with
$$a_1 = \frac{\sqrt{2}\,\alpha^{1/4}}{d}\,\theta\cos\phi = \pm\frac{\left(\alpha^{1/2} + \tan\delta\right)^{1/2}}{d}\,\theta \tag{4.19-1}$$

and
$$b_1 = \frac{\sqrt{2}\,\alpha^{1/4}}{d}\,\theta\sin\phi = \pm\frac{\left(\alpha^{1/2} - \tan\delta\right)^{1/2}}{d}\,\theta. \tag{4.19-2}$$

The plus sign in the last terms of eq. (4.19) is for $m=0$, and the minus sign is for $m=1$ (see eq. (4.11)). We can also write

$$\frac{\gamma d}{2} = a_2 + jb_2, \tag{4.20}$$

with
$$a_2 = \frac{\alpha^{1/4}}{\sqrt{2}}\,\theta\cos\phi = \pm\frac{\left(\alpha^{1/2} + \tan\delta\right)^{1/2}}{2}\,\theta \tag{4.21-1}$$

and $$b_2 = \frac{\alpha^{1/4}}{\sqrt{2}}\,\theta\sin\phi = \pm\frac{\left(\alpha^{1/2} - \tan\delta\right)^{1/2}}{2}\,\theta. \tag{4.21-2}$$

Using these expressions leads to another expression of $\mathbf{H}_z$ with the time factor $e^{j\omega t}$:

$$\mathbf{H}_z = \frac{H_0}{\cosh\left(\dfrac{\alpha^{1/4}}{\sqrt{2}}\,\theta\, e^{j\phi}\right)}\cosh\left(\frac{\sqrt{2}\,\alpha^{1/4}}{d}\,\theta\, e^{j\phi} y\right) e^{j\omega t}$$

$$= H_0\,\frac{\cosh\left(a_1 y + j b_1 y\right)}{\cosh\left(a_2 + j b_2\right)}\, e^{j\omega t}. \tag{4.22}$$

The complex field $\mathbf{H}_z$ can be expressed as a combination of the amplitude $|\mathbf{H}_z|$ and the phase θ_z:

$$\mathbf{H}_z = \left|\mathbf{H}_z\right| e^{\,j\left(\omega t + \theta_z\right)}, \tag{4.23}$$

where $$\left|\mathbf{H}_z\right| = H_0\left[\frac{\cosh\left(2a_1 y\right) + \cos\left(2b_1 y\right)}{\cosh\left(2a_2\right) + \cos\left(2b_2\right)}\right]^{1/2} \tag{4.24}$$

and $$\theta_z = \tan^{-1}\left[\tanh\left(a_1 y\right)\tan\left(b_1 y\right)\right] - \tan^{-1}\left[\tanh\left(a_2\right)\tan\left(b_2\right)\right]. \tag{4.25}$$

Equation (4.24) gives the relationship between the *amplitude of the interior field* $|\mathbf{H}_z|$ and the *amplitude of the surface field* H_0. The maximum values of these two amplitudes are reached at different times due to a time lag or a phase lag of the field, which is given by eq. (4.25). Fig. 4.2 shows an example of the difference between $|\mathbf{H}_z|/H_0$ and the instantaneous $\mathbf{H}_z/H_0$ at the instant when the surface field reaches its maximum. The phase lag θ_z is closely related to the eddy-current loss as will be seen later.

If the intrinsic $\tan\delta$ given in eq. (4.10) is zero or $\mu'' = 0$, then eqs. (4.24) and (4.25) reduce to

$$\left|\mathbf{H}_z\right| = H_0\left[\frac{\cosh\left(\dfrac{2\theta}{d}\,y\right) + \cos\left(\dfrac{2\theta}{d}\,y\right)}{\cosh\left(\theta\right) + \cos\left(\theta\right)}\right]^{1/2} \tag{4.26}$$

and

$$\theta_z = \tan^{-1}\left[\tanh\left(\frac{\theta}{d}\,y\right)\tan\left(\frac{\theta}{d}\,y\right)\right] - \tan^{-1}\left[\tanh\left(\frac{\theta}{2}\right)\tan\left(\frac{\theta}{2}\right)\right]. \tag{4.27}$$

These expressions agree with those given in some textbooks on ferromagnetism [89] [90].

4.5 Real and Imaginary Part of the Field

Instead of expressing $\mathbf{H}_z$ by the amplitude and phase, it is often convenient to express it by a combination of the real and the imaginary parts as follows:

$$\mathbf{H}_z = H_0 \frac{\cosh\left(a_1 y + j b_1 y\right)}{\cosh\left(a_2 + j b_2\right)} e^{j\omega t} = \left\{ \mathrm{Re}\left[\mathbf{H}_z\right] + j\,\mathrm{Im}\left[\mathbf{H}_z\right] \right\} e^{j\omega t}, \quad (4.28)$$

where

$$\mathrm{Re}\left[\mathbf{H}_z\right] = H_0 \frac{\cosh\left(a_1 y + a_2\right)\cos\left(b_1 y - b_2\right) + \cosh\left(a_1 y - a_2\right)\cos\left(b_1 y + b_2\right)}{\cosh\left(2a_2\right) + \cos\left(2b_2\right)} \quad (4.29)$$

and

$$\mathrm{Im}\left[\mathbf{H}_z\right] = H_0 \frac{\sinh\left(a_1 y + a_2\right)\sin\left(b_1 y - b_2\right) + \sinh\left(a_1 y - a_2\right)\sin\left(b_1 y + b_2\right)}{\cosh\left(2a_2\right) + \cos\left(2b_2\right)}. \quad (4.30)$$

If $\tan\delta = 0$, then eqs. (4.29) and (4.30) reduce to

$$\mathrm{Re}\left[\mathbf{H}_z\right] = H_0 \frac{\cosh\left(\frac{\theta}{d} y + \frac{\theta}{2}\right)\cos\left(\frac{\theta}{d} y - \frac{\theta}{2}\right) + \cosh\left(\frac{\theta}{d} y - \frac{\theta}{2}\right)\cos\left(\frac{\theta}{d} y + \frac{\theta}{2}\right)}{\cosh\left(\theta\right) + \cos\left(\theta\right)} \quad (4.31)$$

and

$$\mathrm{Im}\left[\mathbf{H}_z\right] = H_0 \frac{\sinh\left(\frac{\theta}{d} y + \frac{\theta}{2}\right)\sin\left(\frac{\theta}{d} y - \frac{\theta}{2}\right) + \sinh\left(\frac{\theta}{d} y - \frac{\theta}{2}\right)\sin\left(\frac{\theta}{d} y + \frac{\theta}{2}\right)}{\cosh\left(\theta\right) + \cos\left(\theta\right)}. \quad (4.32)$$

In Chapters 6 and 7, the complex field representation given in eqs. (4.28), (4.29), and (4.30) is used to derive the expressions for various magnetic properties of the sheet.

4.6 Skin Depth from Field Distribution

In the present and the following sections, we consider the behavior of the magnetic field in a frequency region where the skin depth is much smaller than the thickness of the sheet. In other words, we consider the case where the condition $\theta \gg 1.0$ is satisfied. In this frequency range, the amplitude of the field near the surface can be approximated from eq. (4.24) by

$$\frac{|\mathbf{H}_z|}{H_0} \approx \left[\frac{\cosh(2a_1 y)}{\cosh(2a_2)}\right]^{1/2} \approx \left[\frac{e^{2a_1 y}}{e^{2a_2}}\right]^{1/2} = e^{a_1 y - a_2}. \tag{4.33}$$

We use the inequalities, $\cosh(2a_1 y) \gg \cos(2b_1 y)$ and $\cosh(2a_2) \gg \cos(2b_2)$, which are valid under the condition, $\theta \gg 1.0$. Using a_1 and a_2 from eqs. (4.19) and (4.21), we can rewrite eq. (4.33) as

$$\frac{|\mathbf{H}_z|}{H_0} \approx \exp\left\{\left(y - \frac{d}{2}\right) \Bigg/ \left[\frac{\delta_s}{\left(\alpha^{1/2} + \tan\delta\right)^{1/2}}\right]\right\}. \tag{4.34}$$

Then, replacing the axis y with Y, which is given by

$$Y = \frac{d}{2} - y, \tag{4.35}$$

we obtain

$$\frac{|\mathbf{H}_z|}{H_0} \approx e^{-\frac{Y}{\delta_{s,m}}}, \tag{4.36}$$

where

$$\delta_{s,m} = \frac{\delta_s}{\left(\alpha^{1/2} + \tan\delta\right)^{1/2}} = \frac{1}{\left(\alpha^{1/2} + \tan\delta\right)^{1/2}} \sqrt{\frac{2}{\omega \mu' \sigma}}. \tag{4.37}$$

Note that Y is the distance from the surface, whereas y is the distance from the middle of the sheet. Equation (4.36) shows that the amplitude of the field decays exponentially with the distance from the surface and at the depth of $\delta_{s,m}$ below the surface, it becomes $1/e$ or 0.368 of the amplitude at the surface. The length $\delta_{s,m}$ given in eq. (4.37) is hereafter referred to as the *skin depth*, while as mentioned before, the commonly used δ_s given by eq. (3.5) is called the *conductor skin depth*. We can see from eq. (4.37) that the skin depth $\delta_{s,m}$ is somewhat shorter than the conductor skin depth δ_s depending on the value of intrinsic $\tan\delta$. It is quite evident that if $\tan\delta = 0$, $\delta_{s,m}$ reduces to δ_s.

A similar approximation can be applied to the phase lag θ_z. Provided that $a_1 y \gg 1.0$ and $a_2 \gg 1.0$ (these conditions are equivalent to $y/\delta_s \gg 1.0$ and $\theta \gg 1.0$, respectively), we can use approximate expressions, $\tanh(a_1 y) \simeq 1.0$ or -1.0 and $\tanh(a_2) \simeq 1.0$ or -1.0. The sign of plus or minus depends on the value of m given in eq. (4.11). As a result of the approximations, θ_z, given in eq. (4.25), simplifies to

$$\theta_z \approx \tan^{-1}\left[\tan\left(b_1 y\right)\right] - \tan^{-1}\left[\tan\left(b_2\right)\right] = b_1 y - b_2$$
$$= -\frac{Y}{\delta_s \Big/ \left(\alpha^{1/2} - \tan\delta\right)^{1/2}}. \tag{4.38}$$

Equation (4.38) shows that the phase of the field lags linearly with respect to Y and at a depth of $\delta_s/(\alpha^{1/2}-\tan\delta)^{1/2}$, the phase is exactly 1.0 [rad] behind the phase at the surface. It should be emphasized that this distance is somewhat greater than the skin depth $\delta_{s,m}$. If $\tan\delta = 0$, the depth at which the phase lag reaches 1.0 [rad] is exactly the same as the depth at which the amplitude decays to $1/e$.

The general expression of the skin depth for conductive magnetic materials should include the complex permeability and the complex conductivity. As noted in Section 4.3, in the frequency range of interest, the imaginary part of the effective conductivity is much smaller than the real part and can be completely ignored. It is therefore safe to say that the skin depth given in eq. (4.37), that includes μ', μ'', and σ, is the general expression for conductive magnetic sheets. The commonly used definition given by eq. (3.5) is the skin depth of a conductor or a magnetic material whose intrinsic $\tan\delta$ is much less than 1.0.

4.7 Skin Depth from Wave Number

We consider the skin depth again from the viewpoint of damped-wave propagation. Equation (4.12) is the general wave or Helmholtz equation for $\mathbf{H}_z$ in a lossy (or conductive) material. It is only when the material is much less conductive and hence the displacement current is much higher than the conducting current that we obtain true wave propagation with less attenuation. However, in a magnetic sheet of moderate conductivity, a considerable amount of damping occurs during wave propagation. We can obtain the skin depth (eq. (4.37)) and phase lag (eq. (4.38)) more easily by solving eq. (4.12) under the condition $\theta \gg 1.0$.

Using the axis Y from eq. (4.35) as the distance measured from the surface, eq. (4.12) can be written as

$$\frac{\partial^2 \mathbf{H}_z}{\partial Y^2} - \gamma^2 \mathbf{H}_z = 0, \tag{4.39}$$

where γ is given in eq. (4.9) and often referred to as the *wave number*, meaning the number of cycles per unit length. If $\theta \gg 1.0$, a wave entering from the opposite surface is attenuated to a negligible value when it propagates through the sheet. Therefore, the solution of eq. (4.39) is simplified to

$$\mathbf{H}_z \simeq H_0 e^{j\omega t - \gamma Y}, \tag{4.40}$$

where H_0 is the field intensity at the surface. Since γ is a complex number, eq. (4.40) indicates a propagating wave whose amplitude dampens with the distance from the surface.

Now, we must only express the real and imaginary parts of γ in terms of δ_s and $\tan\delta$ to obtain the skin depth and phase lag. It follows from eq.(4.9) that γ is written as

$$\gamma = \gamma_r + j\gamma_i, \tag{4.41}$$

where

$$\gamma_r = \frac{\sqrt{2}}{\delta_s}\alpha^{1/4}\cos\phi \qquad \text{and} \qquad \gamma_i = \frac{\sqrt{2}}{\delta_s}\alpha^{1/4}\sin\phi. \tag{4.42}$$

Taking the plus sign in eq. (4.19), we can write

$$\cos\phi = \frac{1}{\sqrt{2}\,\alpha^{1/4}}\left(\alpha^{1/2} + \tan\delta\right)^{1/2} \tag{4.43}$$

and

$$\sin\phi = \frac{1}{\sqrt{2}\,\alpha^{1/4}}\left(\alpha^{1/2} - \tan\delta\right)^{1/2}. \tag{4.44}$$

Substituting eqs. (4.43) and (4.44) into eq. (4.42) gives

$$\gamma_r = \frac{\left(\alpha^{1/2} + \tan\delta\right)^{1/2}}{\delta_s} \qquad \text{and} \qquad \gamma_i = \frac{\left(\alpha^{1/2} - \tan\delta\right)^{1/2}}{\delta_s}. \tag{4.45}$$

The obtained γ_r and γ_i are consistent with eqs. (4.37) and (4.38), respectively. It follows from eq. (4.40) that the ratio $\mathbf{H}_z/H_0$ is given by

$$\frac{\mathbf{H}_z}{H_0} \simeq e^{j\omega t - (\gamma_r + j\gamma_i)Y} = \frac{|\mathbf{H}_z|}{H_0} e^{j(\omega t + \theta_z)}, \tag{4.46}$$

where

$$\frac{|\mathbf{H}_z|}{H_0} \simeq e^{-\gamma_r Y} = e^{-\frac{Y}{\delta_{s,m}}} \qquad \text{and} \qquad \theta_z \simeq -\gamma_i Y. \tag{4.47}$$

Figure 4.1 shows the approximate amplitude $|\mathbf{H}_z|/H_0$ and phase θ_z as a function of the normalized distance Y/δ_s for several values of $\tan\delta$. The amplitude diminishes exponentially and the phase lags linearly with respect to the distance from the surface. For higher values of $\tan\delta$, the amplitude diminishes faster, whereas the phase lags slower.

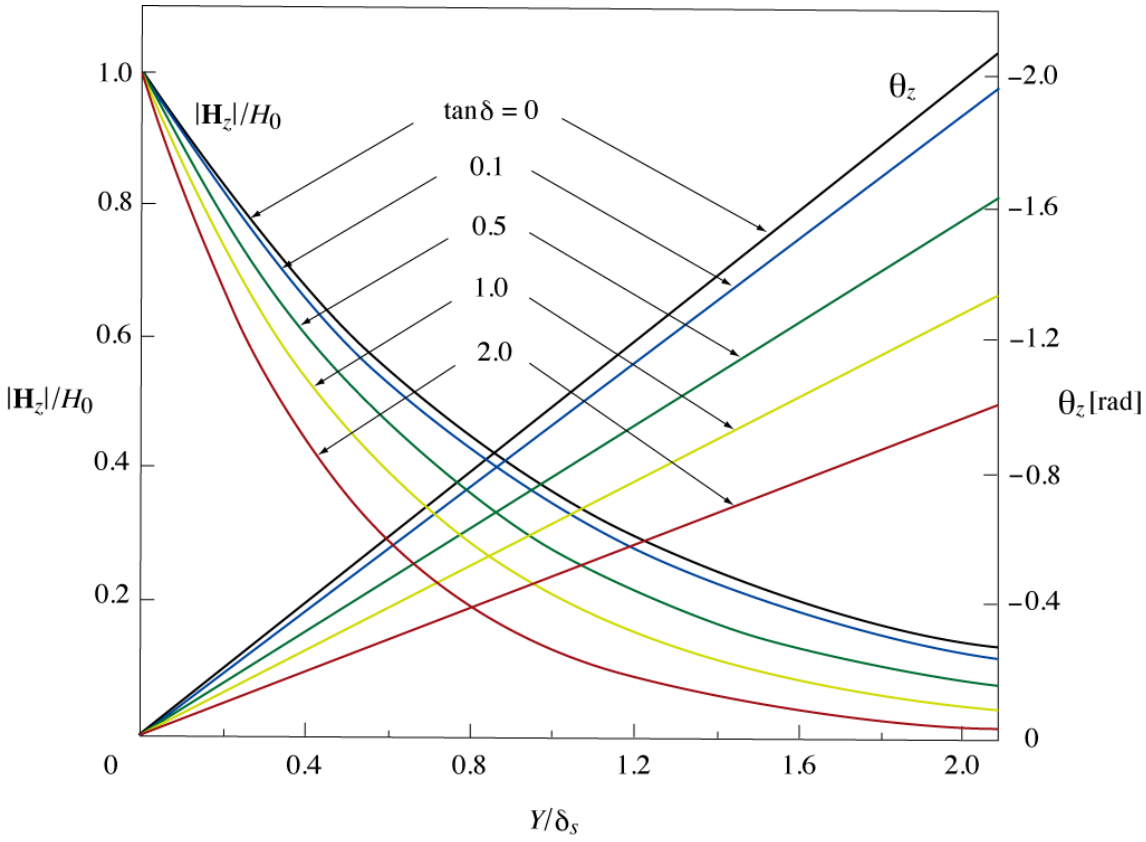

Figure 4.1 Approximate normalized amplitude $|\mathbf{H}_z|/H_0$ and phase θ_z of the field as a function of normalized distance Y/δ_s for several values of $\tan\delta$. Y is the distance measured from the surface and δ_s is the conductor skin depth given by eq. (3.5).

4.8 Numerical Examples

4.8.1 Amplitude and Phase of the Field

(a) $|\mathbf{H}_z|/H_0$ and θ_z versus y/d

First, we consider the case where the imaginary part of the intrinsic permeability μ'' is zero, that is, the intrinsic loss factor $\tan\delta$ is zero. Figure 4.2 shows the normalized amplitude $|\mathbf{H}_z|/H_0$ and the phase θ_z obtained from eqs. (4.24) and (4.25) for several values of θ. The abscissa is the normalized distance from the middle of the sheet y/d, where d is the thickness of the sheet. Therefore, $y/d = 0$ refers to the middle and $y/d = 0.5$ to the surface of the sheet. The parameter θ is, as given in eq. (3.4), the normalized thicknesses given by the ratio of the sheet thickness d to the conductor skin depth δ_s as follows:

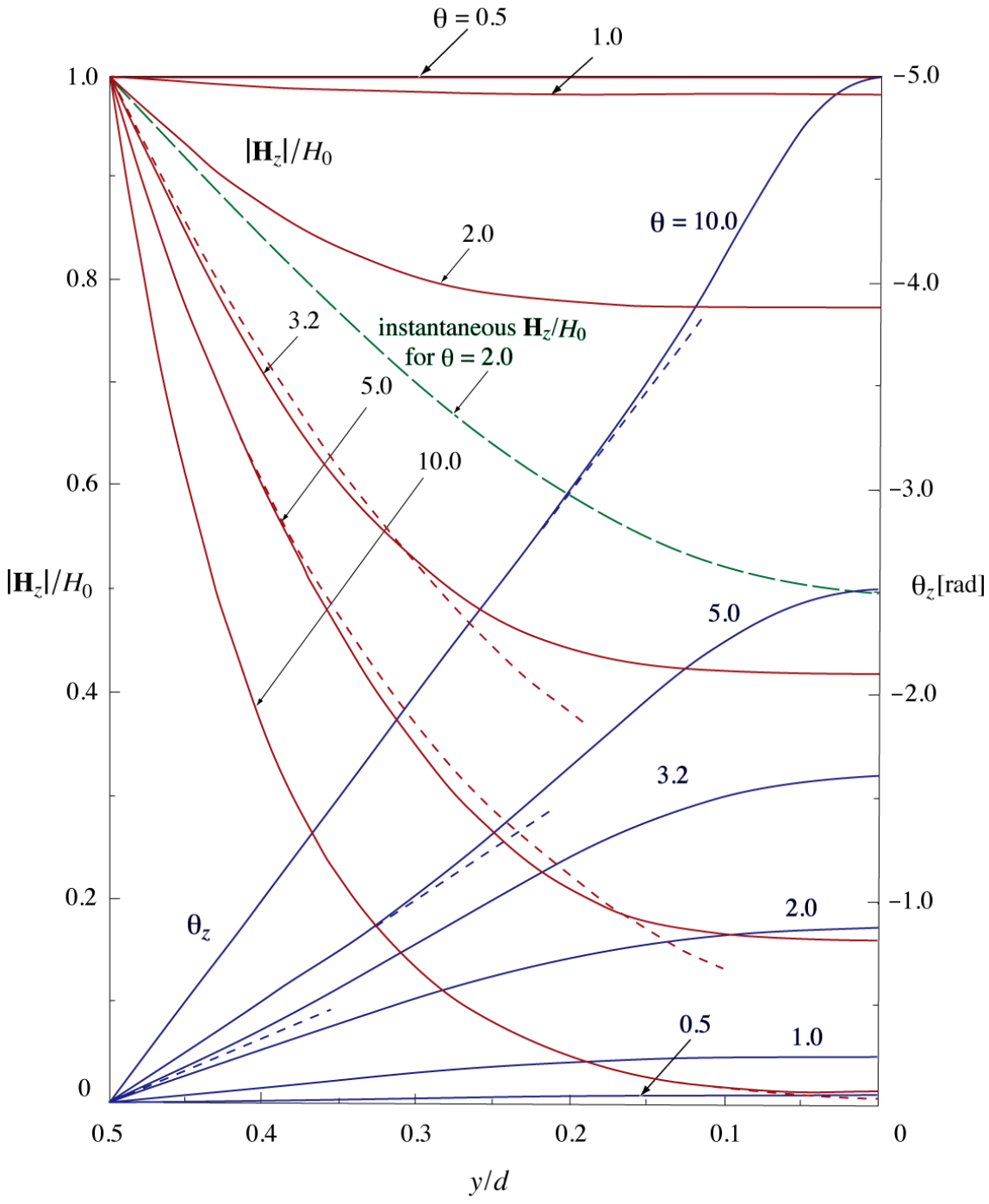

Figure 4.2 Normalized amplitude $|\mathbf{H}_z|/H_0$ and phase θ_z of the field versus y/d for several values of θ in the case of $\tan\delta = 0$. $y/d = 0$ refers to the middle and $y/d = 0.5$ to the surface of the sheet. Dotted lines show the approximate $|\mathbf{H}_z|/H_0$ and θ_z obtained from eqs.(4.36) and (4.38). Green broken line represents the instantaneous $\mathbf{H}_z/H_0$ at the instant when the surface field reaches its maximum.

$$\theta = \frac{d}{\delta_s} = d\sqrt{\frac{\omega\mu'\sigma}{2}}. \tag{4.48}$$

Equation (4.48) shows that θ is proportional to the sheet thickness d, the square root of the product of the frequency ω, the real part of the intrinsic permeability μ', and conductivity σ.

Figure 4.2 clearly shows the magnetic field distribution formed within the sheet when a uniform alternating magnetic field is continuously applied to the sheet, parallel to its surface. The amplitude of the field $|\mathbf{H}_z|$ diminishes and the phase of the field θ_z lags with the distance from the surface. For a larger value of θ, $|\mathbf{H}_z|$ decreases more rapidly and θ_z lags faster.

The dotted lines in Fig. 4.2 show the approximate values of $|\mathbf{H}_z|/H_0$ and θ_z obtained from eqs. (4.36) and (4.38) for $\theta = 3.2$, 5.0, and 10.0. Figure 4.2 shows that provided the skin depth is much smaller than the sheet thickness ($\theta \gg 1.0$) and the position is near the surface, the approximate and accurate results are in good agreement. For $\theta = 10.0$, the approximation is valid even in the interior of the sheet.

Formation of the magnetic field distribution can be explained in two ways. One is a quasistationary field view, in which the field distribution is formed as the result of superposition of the uniformly distributed applied magnetic field on the opposite-phase equilibrium magnetic field, which is produced by eddy currents, with its amplitude reaching a maximum in the middle of the sheet. The other is a propagating damped-wave view, in which the secondary magnetic fields created by multireflections at both surfaces are superimposed on the primary fields created by the waves that enter the sheet through both surfaces and propagate toward the opposite surfaces while attenuating.

As noted below eq. (4.25), $|\mathbf{H}_z|/H_0$ shown in Fig. 4.2 gives the ratio of the amplitude of the interior field to the amplitude of the surface field. Because of the phase lag, the field in the interior of the sheet reaches a maximum value at a different time from when the surface field reaches its maximum. The green broken line in Fig. 4.2 represents the instantaneous value of $\mathbf{H}_z/H_0$ for $\theta = 2.0$ at the instant when the surface field reaches its maximum.

Next, we examine the way in which the field distribution depends on the intrinsic $\tan\delta$. Figure 4.3 shows $|\mathbf{H}_z|/H_0$ and θ_z as a function of y/d for five values of θ. Fig. 4.3 (a), (b), (c), (d), and (e) illustrate the results for $\theta = 0.5$, 1.0, 2.0, 3.2, and 5.0, respectively, each showing the field distribution for $\tan\delta = 0.1$, 0.5, 1.0, and 2.0. Note that the scale of $|\mathbf{H}_z|/H_0$ is common to all figures, but the scale of θ_z is different from

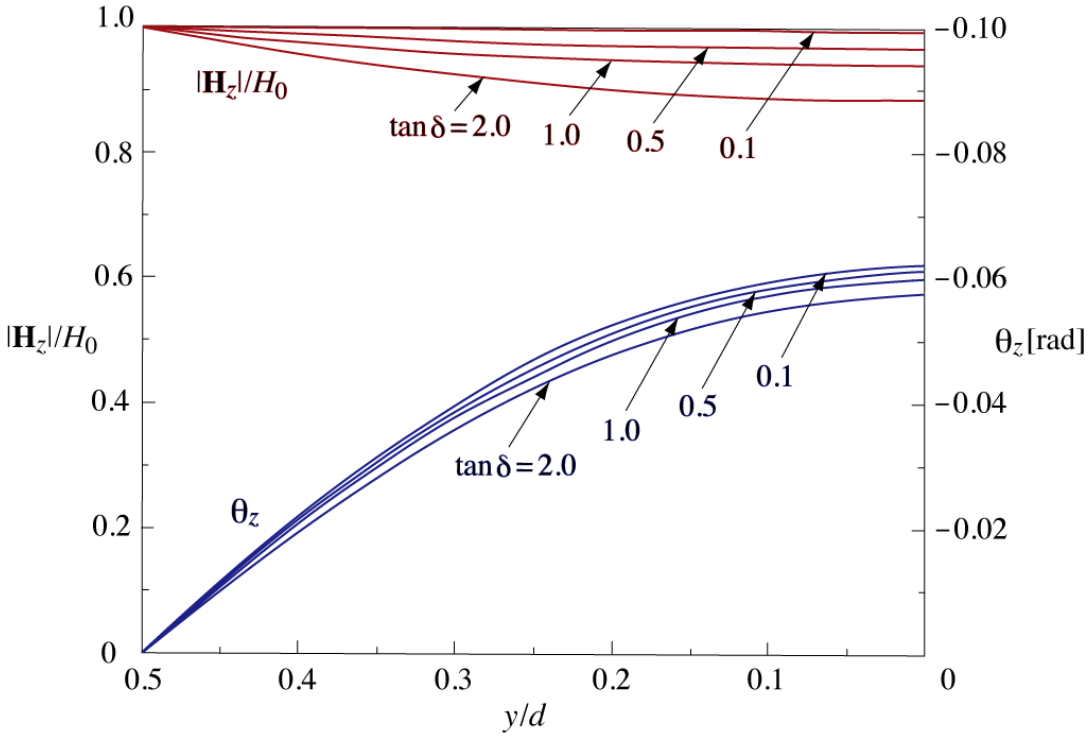

Figure 4.3 (a) Normalized amplitude $|\mathbf{H}_z|/H_0$ and phase θ_z of the field versus y/d for $\theta = 0.5$ and four values of $\tan\delta$.

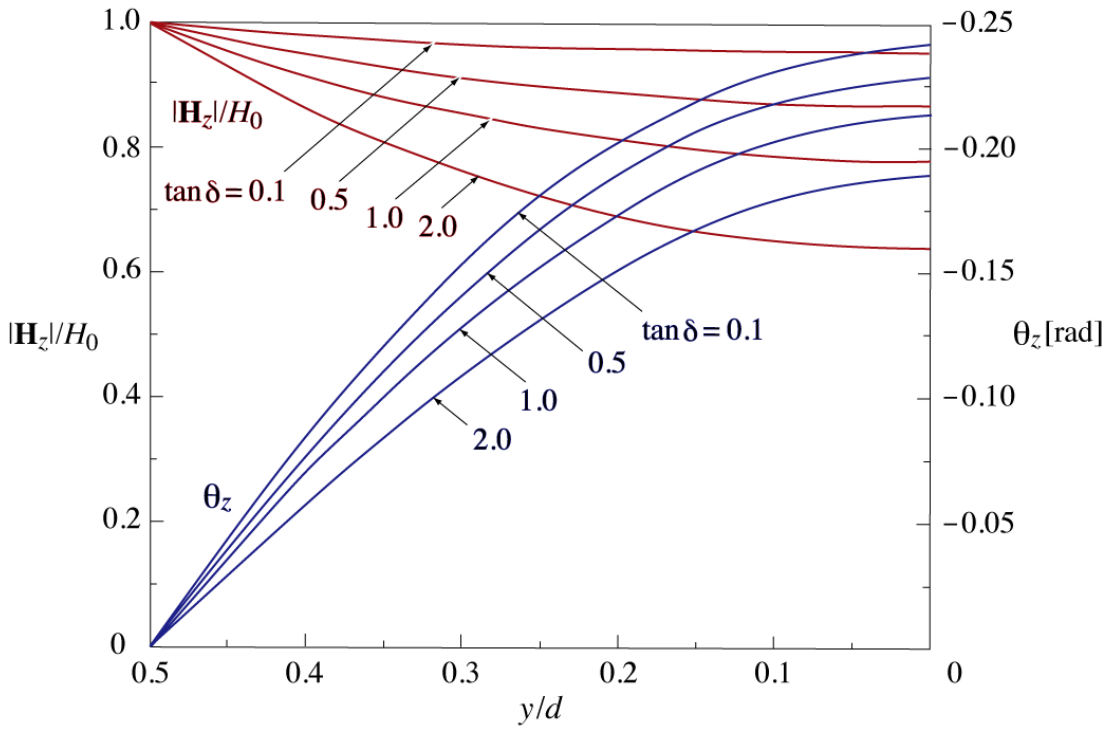

Figure 4.3 (b) Normalized amplitude $|\mathbf{H}_z|/H_0$ and phase θ_z for $\theta = 1.0$.

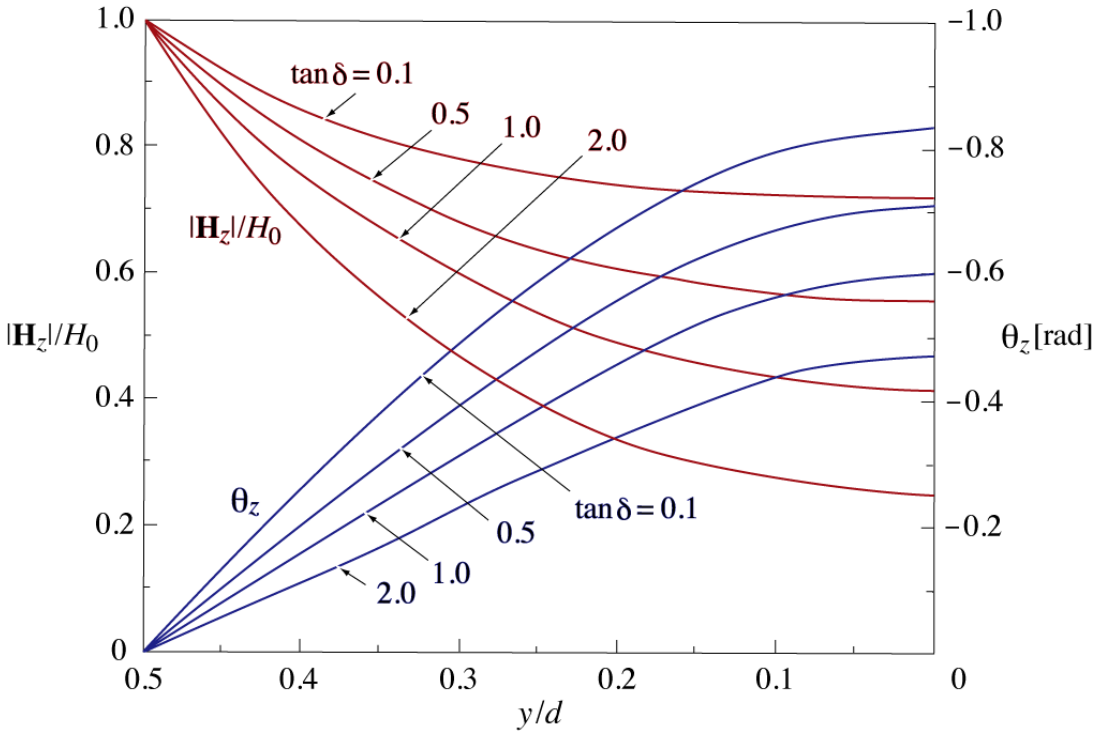

Figure 4.3 (c) Normalized amplitude $|\mathbf{H}_z|/H_0$ and phase θ_z for θ=2.0.

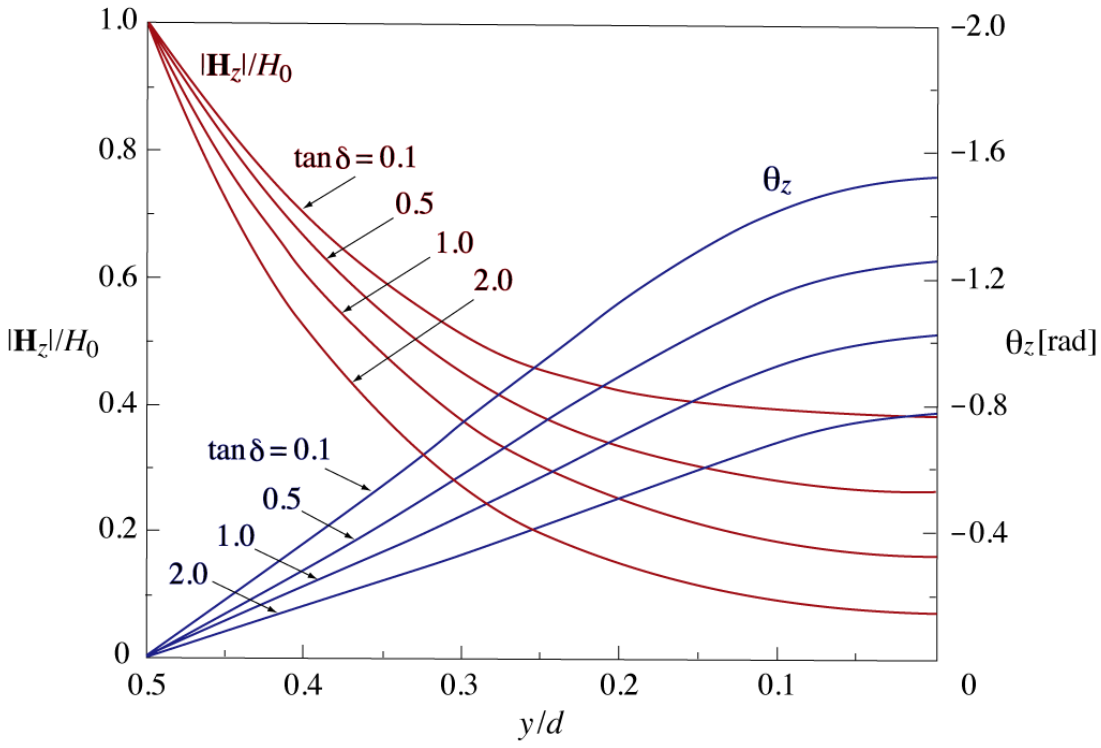

Figure 4.3 (d) Normalized amplitude $|\mathbf{H}_z|/H_0$ and phase θ_z for θ=3.2.

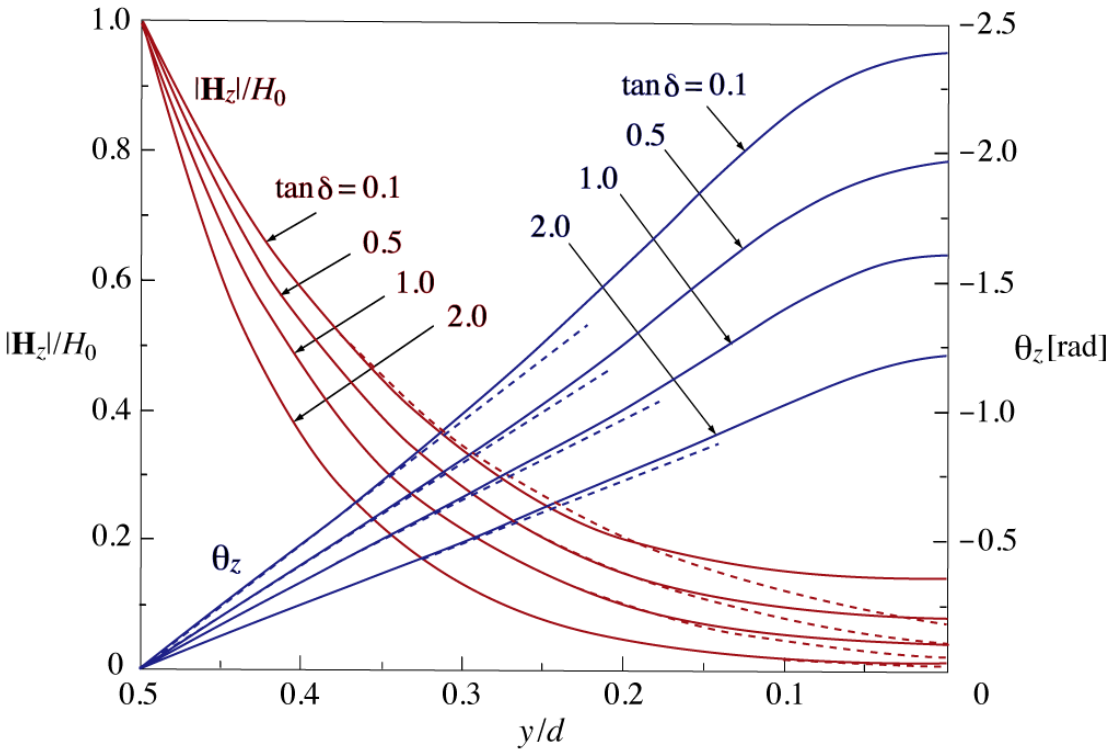

Figure 4.3 (e) Normalized amplitude $|\mathbf{H}_z|/H_0$ and phase θ_z of the field for $\theta = 5.0$. Dotted lines show approximate $|\mathbf{H}_z|/H_0$ and θ_z obtained from eqs. (4.36) and (4.38).

figure to figure. It is clear from the figures that as $\tan\delta$ increases, the field amplitude diminishes more rapidly, whereas the phase lags more slowly. The dotted lines in Fig. 4.3(e) show the approximate $|\mathbf{H}_z|/H_0$ and θ_z obtained from eqs. (4.36) and (4.38). We see that in the case of $\theta = 5.0$, the approximate curves agree quite well with the accurate ones up to approximately the halfway point between the surface and the middle of the sheet.

(b) $|\mathbf{H}_z|/H_0$ and θ_z versus θ

Now, we would like to know how the amplitude and phase of the field at a fixed position behave as θ is changed over a wide range. Figure 4.4 shows $|\mathbf{H}_z|/H_0$ and θ_z as a function of θ for five values of $\tan\delta$. Fig. 4.4 (a) gives the results at $y/d = 0.4$, a position near the surface, and Fig. 4.4 (b) shows the results at $y/d = 0.1$, a position near the middle of the sheet. The figures clearly show that at the deeper position (y/d = 0.1) the amplitude diminishes more rapidly and the phase lags faster as θ increases.

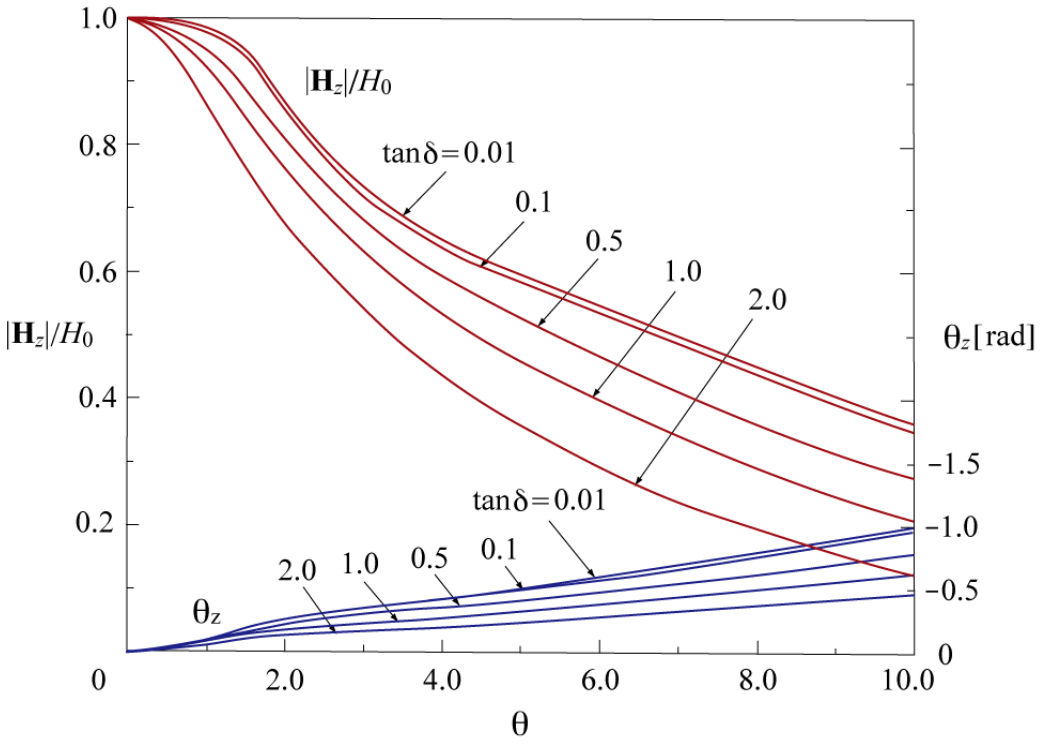

Figure 4.4 (a) Normalized amplitude $|\mathbf{H}_z|/H_0$ and phase θ_z versus θ at $y/d=0.4$ for five values of $\tan\delta$.

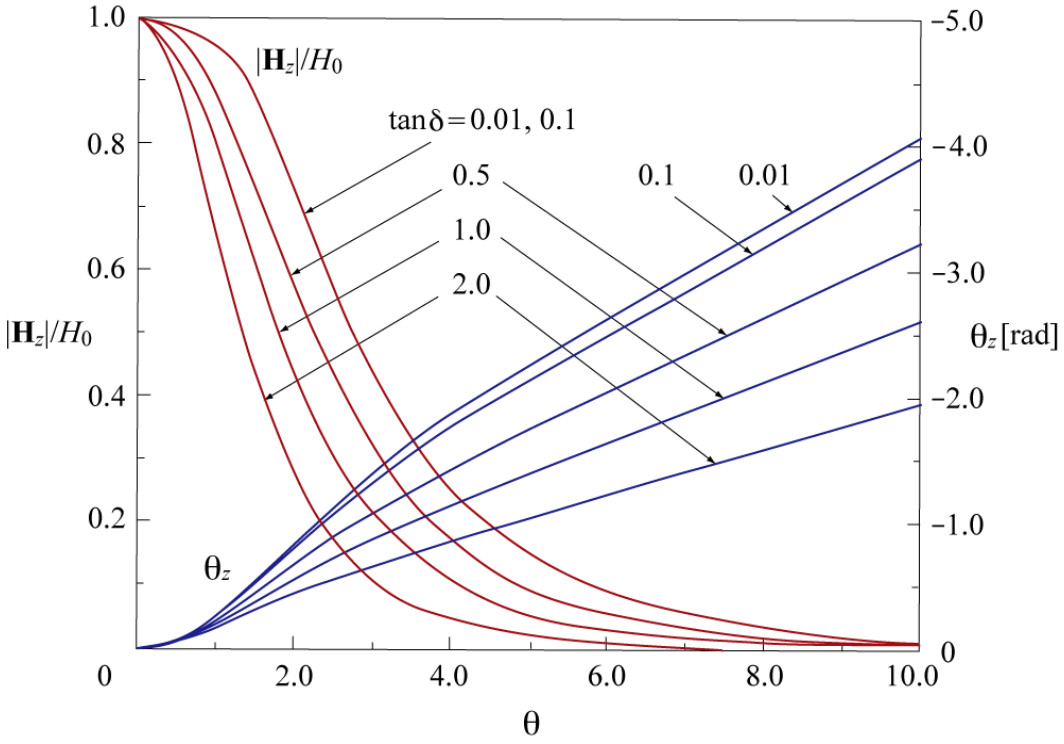

Figure 4.4 (b) Normalized amplitude $|\mathbf{H}_z|/H_0$ and phase θ_z versus θ at $y/d=0.1$.

4.8.2 Real Part and Imaginary Part of the Field

In Chapters 6 and 7, we will use the complex field representation given in eq. (4.28) to derive expressions for the magnetic properties of the sheet. We will show that integrating and averaging Re[$\mathbf{H}_z$] and Im[$\mathbf{H}_z$] over the cross section of the sheet are the essential parts of the calculations. The distribution of Re[$\mathbf{H}_z$] and Im[$\mathbf{H}_z$] within the sheet and how the fields at a fixed position vary as θ changes may be helpful in understanding the high-frequency behavior of the sheet. Here we show some numerical examples of Re[$\mathbf{H}_z$]/H_0 and Im[$\mathbf{H}_z$]/H_0 as a function of y/d or as a function of θ.

(a) Re[$\mathbf{H}_z$]/H_0 and Im[$\mathbf{H}_z$]/H_0 versus y/d

Figure 4.5 shows Re[$\mathbf{H}_z$]/H_0 and Im[$\mathbf{H}_z$]/H_0 as a function of y/d for five values of $\tan\delta$. Fig. 4.5 (a) gives the results for $\theta = 0.5$ and Fig. 4.5 (b) the results for $\theta = 2.0$. As the amplitude of the field $|\mathbf{H}_z|$ is given by $|\mathbf{H}_z| = (\mathrm{Re}^2[\mathbf{H}_z] + \mathrm{Im}^2[\mathbf{H}_z])^{1/2}$ and the phase θ_z by $\theta_z = \tan^{-1}(\mathrm{Im}[\mathbf{H}_z]/\mathrm{Re}[\mathbf{H}_z])$, the behavior of $|\mathbf{H}_z|$ and θ_z is directly related to that of Re[$\mathbf{H}_z$] and Im[$\mathbf{H}_z$]. Therefore, to better understand the behavior of $|\mathbf{H}_z|$ and θ_z, it is worth comparing Fig. 4.5 (a) with Fig. 4.3 (a) for $\theta = 0.5$ and Fig. 4.5 (b) with Fig. 4.3 (c) for $\theta = 2.0$.

(b) Re[$\mathbf{H}_z$]/H_0 and Im[$\mathbf{H}_z$]/H_0 versus θ

Figure 4.6 shows Re[$\mathbf{H}_z$]/H_0 and Im[$\mathbf{H}_z$]/H_0 as a function of θ for five values of $\tan\delta$. Fig. 4.6 (a) gives the results at $y/d = 0.4$, a position near the surface, and Fig. 4.6 (b) gives the results at $y/d = 0.1$, deep in the interior of the sheet. For the same reason as in Section 4.8.2 **(a)**, it is worthwhile to compare Fig. 4.6 (a) with Fig. 4.4 (a) for $y/d = 0.4$ and Fig. 4.6 (b) with Fig. 4.4 (b) for $y/d = 0.1$. For example, although Im[$\mathbf{H}_z$]/H_0 at $y/d = 0.4$ in Fig. 4.6 (a) becomes almost flat in the region where θ is greater than approximately 2.0, the phase θ_z in Fig. 4.4 (a) continues to lag as θ increases. This can be understood from the behavior of Re[$\mathbf{H}_z$]/H_0, which decreases rapidly as θ increases, as shown in Fig. 4.6 (a).

Figure 4.6 (b) shows the typical behavior of Re[$\mathbf{H}_z$]/H_0 and Im[$\mathbf{H}_z$]/H_0 at a position deep in the interior of the sheet. One of the noticeable features is that Re[$\mathbf{H}_z$]/H_0 becomes negative when θ exceeds approximately 3.0. This is closely related to the behavior of the phase θ_z that lags continuously as θ increases. Since Im[$\mathbf{H}_z$]/H_0 is negative up to approximately $\theta = 8.0$, the phase θ_z passes $-\pi/2$[rad] when Re[$\mathbf{H}_z$]/H_0 crosses zero from positive to negative. In this way, the continuous increase in θ_z with further increases in θ is closely related to the alternating changes in sign of Re[$\mathbf{H}_z$]/H_0 and Im[$\mathbf{H}_z$]/H_0.

The other noticeable feature shown in Fig. 4.6 (b) is that Im[$\mathbf{H}_z$]/H_0 reaches a maximum at approximately $\theta = 2.0$ and decreases thereafter. The behavior of Im[$\mathbf{H}_z$]/H_0

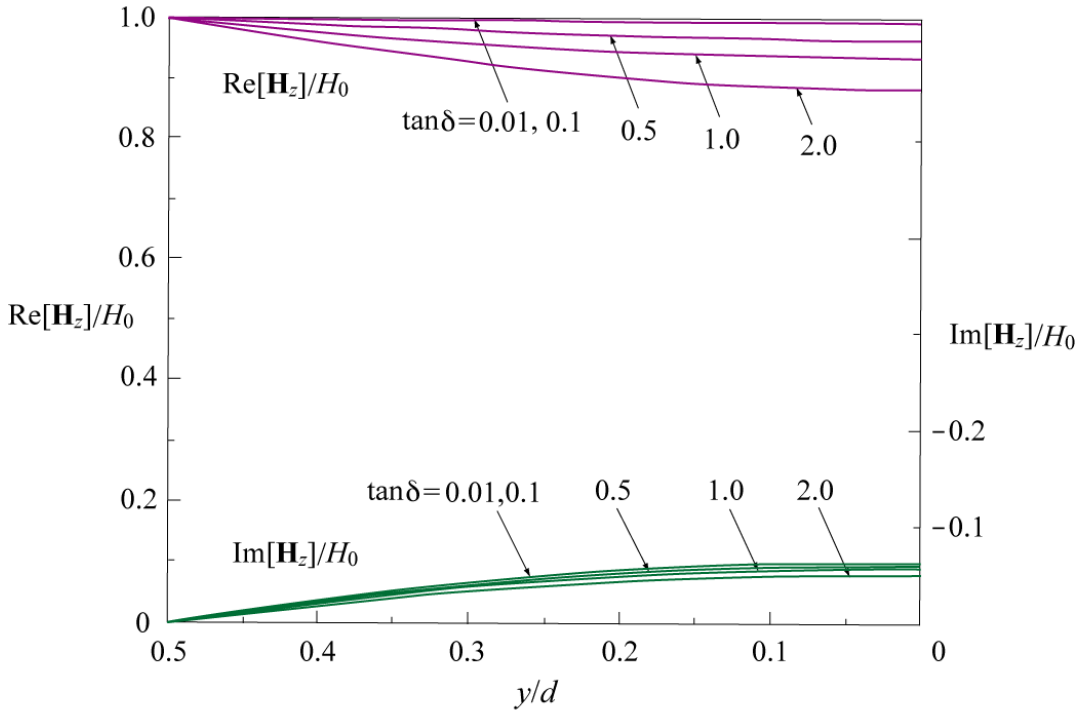

Figure 4.5 (a) Normalized real Re[**H**$_z$]/H_0 and imaginary Im[**H**$_z$]/H_0 parts of the field as functions of y/d for θ=0.5 and five values of tanδ.

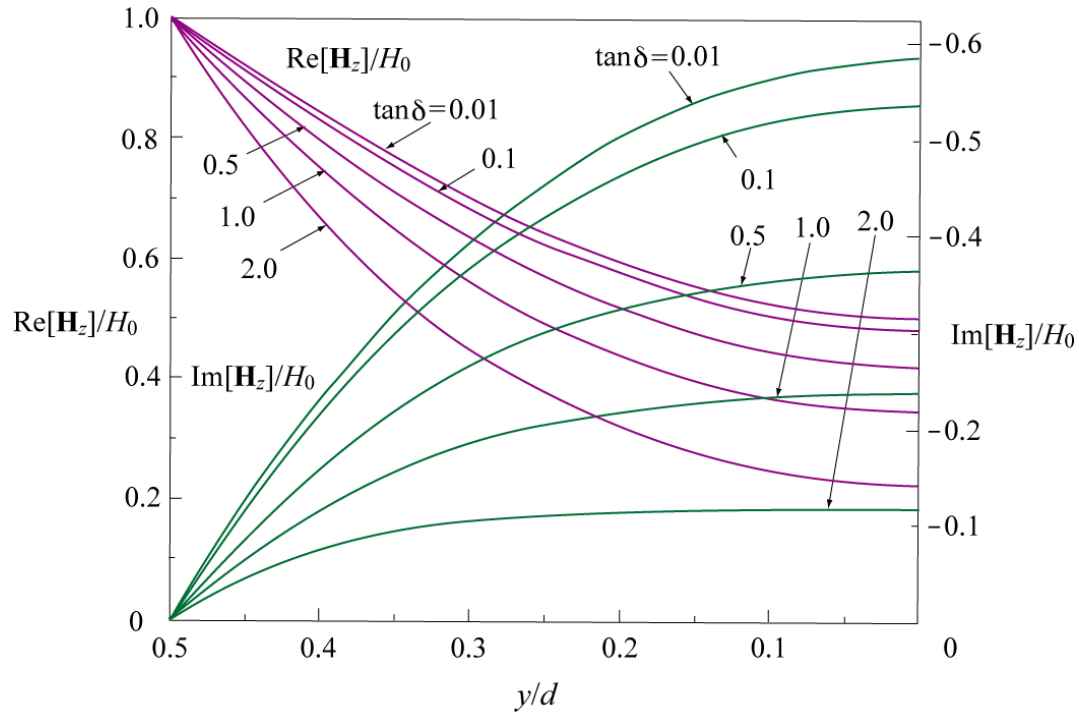

Figure 4.5 (b) Re[**H**$_z$]/H_0 and Im[**H**$_z$]/H_0 versus y/d for θ=2.0.

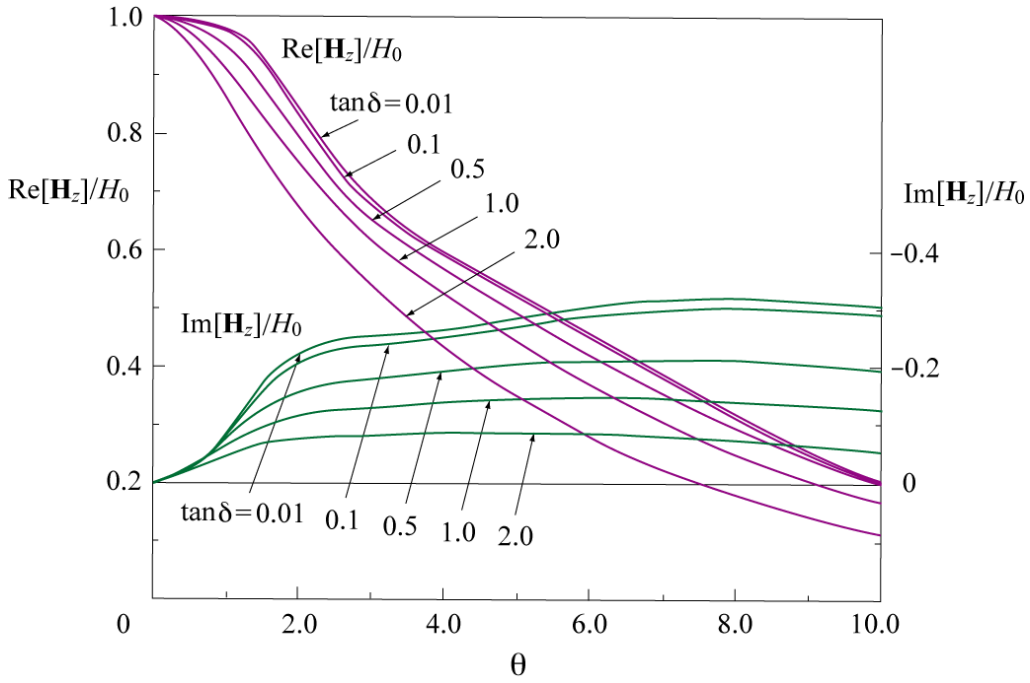

Figure 4.6 (a) Normalized real $\mathrm{Re}[\mathbf{H}_z]/H_0$ and imaginary $\mathrm{Im}[\mathbf{H}_z]/H_0$ parts of the field as functions of θ at $y/d = 0.4$ for five values of $\tan\delta$.

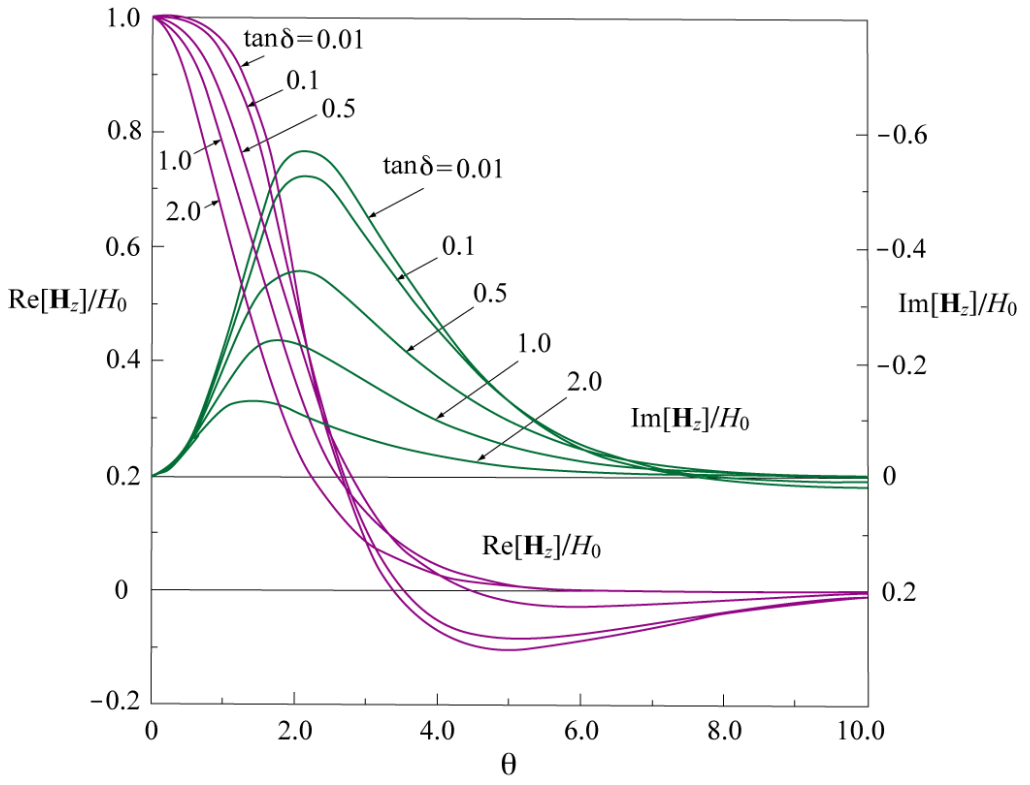

Figure 4.6 (b) $\mathrm{Re}[\mathbf{H}_z]/H_0$ and $\mathrm{Im}[\mathbf{H}_z]/H_0$ versus θ at $y/d = 0.1$.

is closely related with the phase lag of the field as well as with the diminution of the field amplitude. In the region where θ is small, the effect of the phase lag prevails over the effect of the diminishing amplitude, so that $\mathrm{Im}[\mathbf{H}_z]/H_0$ increases as θ increases. However, after a certain point, depending on the value of $\tan\delta$, the diminishing amplitude effect surpasses the phase-lag effect, and consequently, $\mathrm{Im}[\mathbf{H}_z]/H_0$ decreases monotonously.

In Chapter 6, we will introduce a factor, $g(\theta,\varphi)$, which is proportional to the average value of $\mathrm{Im}[\mathbf{H}_z]$ ($[\mathrm{Im}[\mathbf{H}_z]]_{av}$). In Chapter 7, we will show that the eddy-current loss P_{ed} is also closely associated with $[\mathrm{Im}[\mathbf{H}_z]]_{av}$. Hence, the characteristic pattern of $\mathrm{Im}[\mathbf{H}_z]/H_0$ shown in Fig 4.6(b) appears on the curves of $g(\theta,\varphi)$ in Fig. 6.2 and those of P_{ed} in Fig. 7.2.

4.8.3 Interpretation of Phase Behavior

As shown in Fig. 4.3, for a higher value of $\tan\delta$, the field amplitude $|\mathbf{H}_z|/H_0$ diminishes more rapidly as the distance from the surface Y is increased, whereas the phase of the field, θ_z, lags more slowly with Y. A similar dependence on $\tan\delta$ is also seen in Fig. 4.4, in which $|\mathbf{H}_z|/H_0$ and θ_z are given as a function of θ. One can readily understand that a high $\tan\delta$ corresponds to a high loss, but may not easily understand the reason why the phase lag of the field decreases with an increase in $\tan\delta$. We now examine the way in which phase behaves as $\tan\delta$ is varied by using a phasor diagram. Figure 4.7 shows

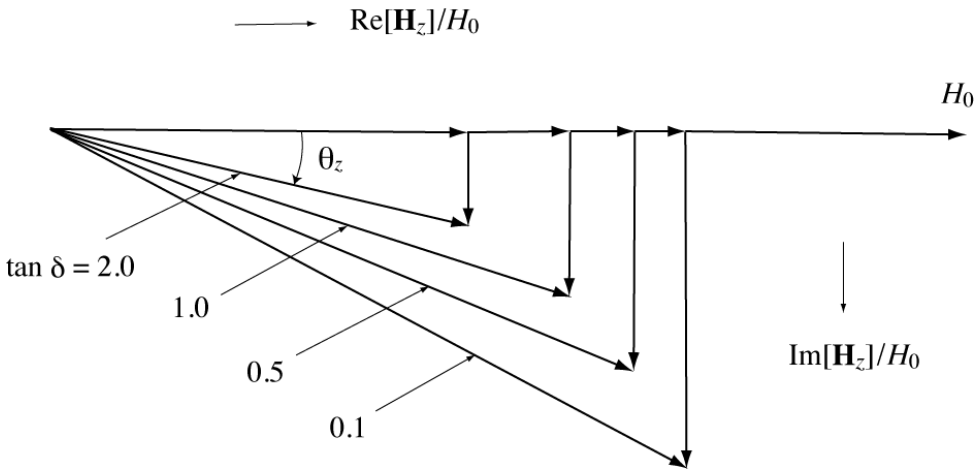

Figure 4.7 Phasor diagram of the field $\mathbf{H}_z$ constructed using the values of $\mathrm{Re}[\mathbf{H}_z]/H_0$ and $\mathrm{Im}[\mathbf{H}_z]/H_0$ calculated at $y/d=0.3$ for θ=2.0 and four values of $\tan\delta$ (Fig. 4.3(c)).

the phasor diagrams of the field $\mathbf{H}_z$, constructed using numerical values of Re[$\mathbf{H}_z$]/H_0 and Im[$\mathbf{H}_z$]/H_0 calculated at $y/d = 0.3$ for $\theta = 2.0$ and four values of $\tan\delta$ (Fig. 4.3(c)). The figure shows that both the imaginary and real parts of the field decrease as $\tan\delta$ increases. Studying the figures more closely, we see that Im[$\mathbf{H}_z$]/H_0 decreases more rapidly than Re[$\mathbf{H}_z$]/H_0, which results in a decrease in θ_z.

5. Frequency Characteristics of Intrinsic Permeability

5.1 Introduction

In Section 2.7, we explained that we use two kinds of permeability in this paper, the intrinsic permeability μ and the effective permeability μ_e. The intrinsic permeability is inherent in magnetization mechanisms and accordingly it is a material constant. On the other hand, the effective permeability is affected by demagnetizing fields (see Section 6.2) and consequently depends on the frequency as well as the geometry of the magnetic object. The effective permeability of magnetic sheet will be fully discussed in Chapter 6.

In this chapter, we survey the frequency characteristics of the intrinsic permeability [89]-[104]. We are primarily interested in the magnetization processes that influence the intrinsic permeability in the relatively low RF range where most RF cavities for proton rings operate. In particular, two important processes are reviewed here at some length, that is, the relaxation in orientation of magnetic moments and the resonance of domain wall motion.

5.2 Fundamentals of Magnetization

It is well known that spin plays a central role in magnetism and that a wide range of magnetic phenomena is associated primarily with magnetic moments due to the spins of electrons and orbital effects. A ferromagnetic material is divided into a number of small regions termed *magnetic domains* or simply *domains*, each consisting of many atoms whose magnetic moments are aligned in parallel with each other. As a result, each domain spontaneously magnetizes to the saturation value, but the directions of magnetization of the various domains are such that the object as a whole has no net magnetization. The shape and dimensions of domains in thermodynamic equilibrium are determined by the minimum free energy condition of the ferromagnetic substance. At domain boundaries, there are transition layers where spins gradually change their direction from one domain to the other to decrease the exchange energy of spin pairs. These transition layers are called *domain walls* or occasionally *Bloch walls*.

When a magnetic object is subjected to an increasing external magnetic field, its magnetization increases and finally reaches magnetization saturation. For an object with no domain structure, the magnetization processes are dominated by the orientation of magnetic moments of particles and the rotation of the vector of spontaneous magnetization as a whole. If a domain structure exists, the magnetization process is governed by motion of the domain walls and rotation of the domain magnetization. The former is associated with a change in the volume of the domain by movement of its

boundaries and the latter is associated with a rotation of the magnetization vector in a domain of fixed volume. In some objects and in certain field ranges, only one mechanism, either the domain wall motion or magnetization rotation, is operative; in others, both are operative. In most cases, the rotation process is characteristic of the change in magnetization in relatively high fields. The magnetization process in soft magnetic alloys may be characterized less by domain wall motion and more by magnetization rotation [91].

Considering the intrinsic permeability further, on a minute scale, the local permeability inside a magnetic specimen is not homogeneous. This is because the magnetic flux distribution within a domain is not uniform during the process of magnetization by the domain wall motion and/or the domain rotation. For example, in the case of a field applied parallel to a 180° boundary, the local relative permeability is almost unity away from the boundary, but assumes extremely high values within the boundary. The intrinsic permeability that can be measured at the quasistatic state is the macroscopic one averaged over the entire volume of the specimen. Analyses in this paper are carried out solely on the assumption that the macroscopic intrinsic permeability is distributed uniformly throughout the specimen.

When an alternating magnetic field is applied to a specimen and its frequency is swept, dispersion appears in the frequency response of the permeability. Since we are discussing the intrinsic permeability, the dispersion due to eddy-current effects is not considered. The dispersion of the intrinsic permeability arises mainly from the relaxation and resonance absorption associated with magnetization processes. If the frequency is beyond $1/\tau$, where τ is the relaxation time defined in the next section, the magnetization can no longer follow the applied field, and as a result, we obtain a permeability dispersion. In addition, when the frequency approaches a natural resonance frequency of magnetic processes, dispersion arises from the resonant power absorption.

5.3 Relaxation

First, we examine how relaxation in the orientation of magnetic moments affects the frequency behavior of the intrinsic permeability.

5.3.1 Relaxation Equation

The magnetization $\mathbf{M}(t)$ is given by

$$\mathbf{M}(t) = \chi \mathbf{H}(t), \tag{5.1}$$

where χ is the magnetic susceptibility and $\mathbf{H}(t)$ is an external magnetic field. The magnetic flux density $\mathbf{B}(t)$ is related to $\mathbf{H}(t)$ through the intrinsic permeability μ as

follows:

$$\boldsymbol{B}(t) = \mu_0\left[\mathbf{H}(t)+\mathbf{M}(t)\right] = \mu_0\left[\mathbf{H}(t)+\chi\mathbf{H}(t)\right] = \mu_0(1+\chi)\mathbf{H}(t)$$
$$= \mu_0\,\mu_r\mathbf{H}(t) = \mu\mathbf{H}(t). \tag{5.2}$$

Equation (5.2) shows that the relationship between the relative permeability μ_r and χ is given by $\mu_r = 1+\chi$.

Consider a magnetic object where M_s denotes its magnetization saturation value. Assume that M_s is determined by two contributors:

$$M_s = M_{os} + M_w, \tag{5.3}$$

where M_{os} is the saturation magnetization by orientation of magnetic moments and M_w is the magnetization by a fast mechanism with a response time much faster than τ. In general, when such an object is suddenly exposed to an external static magnetic field, a certain length of time is required for the magnetization by orientation to build up to its final value M_{os}, whereas M_w is reached instantaneously on the relaxation time scale.

The relaxation is characterized by a response time or relaxation time τ, which is the time required for the magnetization to fall from the equilibrium value to $1/e$ of the that value, after the field is switched off. Figure 5.1 illustrates the time dependence of the total magnetization $\mathbf{M}(t)$ after a sudden application of a static magnetic field at $t=0$. The instantaneous increase to M_w is associated with fast magnetization, and the orientation of the magnetic moments then causes a slow increase in magnetization to the static value M_s. In the figure, $\mathbf{M}_o(t)$ denotes the time-dependent magnetization due to orientation of the magnetic moments.

Assuming the relaxation time of orientation is τ, we can write $\mathbf{M}(t)$ as

$$\mathbf{M}(t) = \mathbf{M}_o(t) + M_w = M_{os}\left(1-e^{-\frac{t}{\tau}}\right) + M_w. \tag{5.4}$$

Differentiating both sides of eq. (5.4) with respect to t leads to

$$\frac{d\mathbf{M}_o(t)}{dt} = \frac{1}{\tau}M_{os}\,e^{-\frac{t}{\tau}}. \tag{5.5}$$

From eqs. (5.3), (5.4), and (5.5) we obtain the differential equation for $\mathbf{M}_o(t)$,

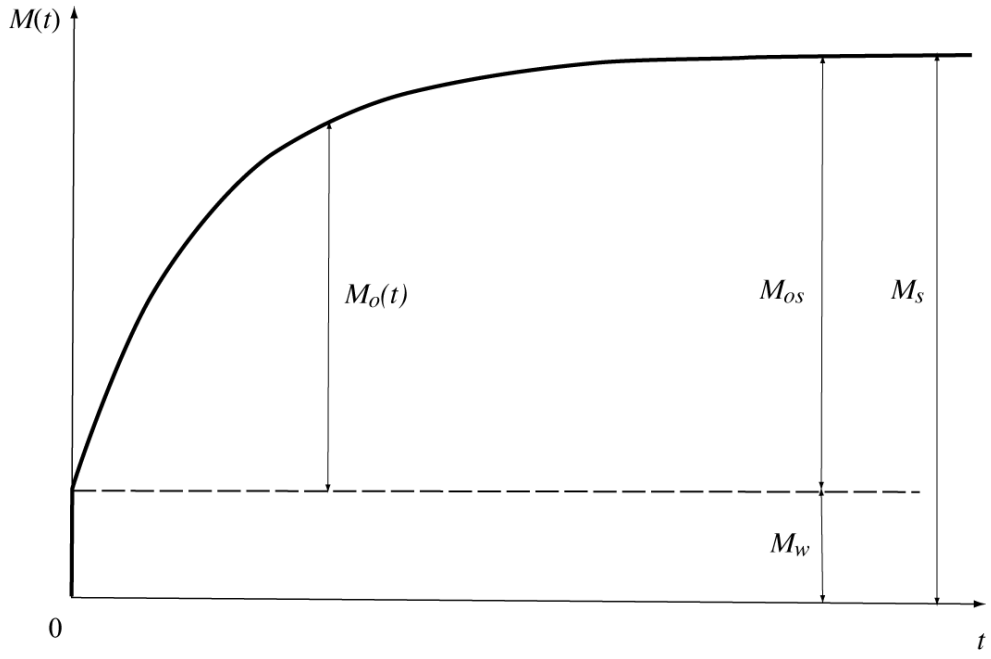

Figure 5.1 Time dependence of magnetization $\mathbf{M}(t)$ after sudden application of a static magnetic field to a magnetic object. M_w is the fast-mechanism magnetization.

$$\frac{d\mathbf{M}_o(t)}{dt} + \frac{1}{\tau}\mathbf{M}_o(t) = \frac{1}{\tau}\left(M_s - M_w\right). \tag{5.6}$$

When an alternating magnetic field

$$\mathbf{H}(t) = H_0 e^{j\omega t} \tag{5.7}$$

is applied, eq. (5.6) can be employed if we make the following changes [105]. We replace M_s with a function of time $\mathbf{M}_s(t)$, which represents the saturation value obtained in a static field equivalent to the instantaneous value $\mathbf{H}(t)$. Likewise, we replace M_w with $\mathbf{M}_w(t)$. Then, eq. (5.6) is written as

$$\frac{d\mathbf{M}_o(t)}{dt} + \frac{1}{\tau}\mathbf{M}_o(t) = \frac{1}{\tau}\left[\mathbf{M}_s(t) - \mathbf{M}_w(t)\right], \tag{5.8}$$

where $\mathbf{M}_s(t)$ and $\mathbf{M}_w(t)$ are given by

$$\mathbf{M}_s(t) = \chi_s H_0 e^{j\omega t} \qquad \text{and} \qquad \mathbf{M}_w(t) = \chi_w H_0 e^{j\omega t}. \tag{5.9}$$

Here, χ_s is the static susceptibility and χ_w is the fast-magnetization susceptibility.

5.3.2 Dispersion of Permeability due to Relaxation

The next step is to solve eq. (5.8) to obtain the frequency characteristics of $\mathbf{M}_o(t)$, from which we can derive the frequency response of the intrinsic permeability influenced by the relaxation in orientation.

A solution of eq. (5.8), $\mathbf{M}_o(t)$, is given by a combination of the general solution to the homogeneous equation, in which the term on the right-hand side is zero, and a particular solution to the inhomogeneous equation:

$$\mathbf{M}_o(t) = \mathbf{A}(\omega)e^{-\frac{t}{\tau}} + \frac{\chi_s - \chi_w}{1 + j\omega\tau} H_0 e^{j\omega t}. \tag{5.10}$$

The first term is the general solution with the complex amplitude $\mathbf{A}(\omega)$, which depends on the initial conditions, and the second term is the particular solution. If we assume that $\mathbf{M}_o(t)=0$ at $t=0$, eq. (5.10) becomes

$$\mathbf{M}_o(t) = -\frac{\chi_s - \chi_w}{1 + j\omega\tau} H_0 e^{-\frac{t}{\tau}} + \frac{\chi_s - \chi_w}{1 + j\omega\tau} H_0 e^{j\omega t}. \tag{5.11}$$

Since we are presently not interested in transient behavior, the first term on the right-hand side is omitted, resulting in

$$\mathbf{M}_o(t) = \frac{\chi_s - \chi_w}{1 + j\omega\tau} H_0 e^{j\omega t}. \tag{5.12}$$

It follows from eqs. (5.4), (5.9), and (5.12) that the total magnetization $\mathbf{M}(t)$ can be written as

$$\mathbf{M}(t) = \mathbf{M}_o(t) + \mathbf{M}_w(t) = \left(\frac{\chi_s - \chi_w}{1 + j\omega\tau} + \chi_w \right) H_0 e^{j\omega t}. \tag{5.13}$$

The magnetic flux density $\mathbf{B}(t)$ is then given by

$$\mathbf{B}(t) = \mu_0 \left[\mathbf{H}(t) + \mathbf{M}(t) \right] = \mu_0 \left(1 + \chi_w + \frac{\chi_s - \chi_w}{1 + j\omega\tau} \right) H_0 e^{j\omega t}. \tag{5.14}$$

The susceptibilities χ_w and χ_s are given by $\chi_w = \mu_w - 1$ and $\chi_s = \mu_s - 1$, where μ_w is the relative permeability due to fast magnetization and μ_s is the static relative permeability. Equation (5.14) is then expressed as

$$\mathbf{B}(t) = \mu_0 \left(\mu_w + \frac{\mu_s - \mu_w}{1 + j\omega\tau} \right) H_0 \, e^{j\omega t}. \tag{5.15}$$

We then obtain the frequency-dependent relative permeability $\mu_r(\omega)$ given by

$$\mu_r(\omega) = \mu_w + \frac{\mu_s - \mu_w}{1 + j\omega\tau} = \mu_r'(\omega) - j\,\mu_r''(\omega), \tag{5.16}$$

where

$$\mu_r'(\omega) = \mu_w + \frac{\mu_s - \mu_w}{1 + \omega^2\tau^2}, \tag{5.17}$$

and

$$\mu_r''(\omega) = \frac{(\mu_s - \mu_w)\,\omega\tau}{1 + \omega^2\tau^2}. \tag{5.18}$$

The real part originates from oscillations in phase with the external field, whereas the imaginary part is attributed to oscillations 90° out of phase with the field. Equations (5.17) and (5.18) are equivalent to those for the dielectric constant, which are frequently referred to as the *Debye equations*. Studying eq. (5.17), we find that the real part is nearly equal to μ_s for very low frequencies ($\omega\tau \ll 1$), and nearly equal to μ_w for very high frequencies ($\omega\tau \gg 1$). This is consistent with the definition of χ_s and χ_w given in eq. (5.9).

We can normalize $\mu_r'(\omega)$ and $\mu_r''(\omega)$ as

$$\mu_r'(\omega)\big|_n = \frac{\mu_r'(\omega) - \mu_w}{\mu_s - \mu_w} = \frac{1}{1 + \omega^2\tau^2} \tag{5.19}$$

and

$$\mu_r''(\omega)\big|_n = \frac{\mu_r''(\omega)}{\mu_s - \mu_w} = \frac{\omega\tau}{1 + \omega^2\tau^2}. \tag{5.20}$$

Figure 5.2 illustrates $\mu_r'(\omega)|_n$ and $\mu_r''(\omega)|_n$ as a function of $\omega\tau$. We see simple relaxation behavior as the frequency increases from low values where the magnetization follows the applied field variations to high values where it can no longer follow the field variations. To explain the behavior more specifically, when ω is considerably less than $1/\tau$, the orientation of the moments can follow the field variations and contribute their full share to the magnetization, but when ω is greater than $1/\tau$, the orientation can no longer follow the field variations and consequently the magnetization decreases rapidly as the frequency increases. We can also see from the Fig. 5.2 that the imaginary part $\mu_r''(\omega)|_n$, to which the magnetic loss is proportional, exhibits a maximum at the frequency $1/\tau$, around which there is a rather sharp drop in the real part $\mu_r'(\omega)|_n$.

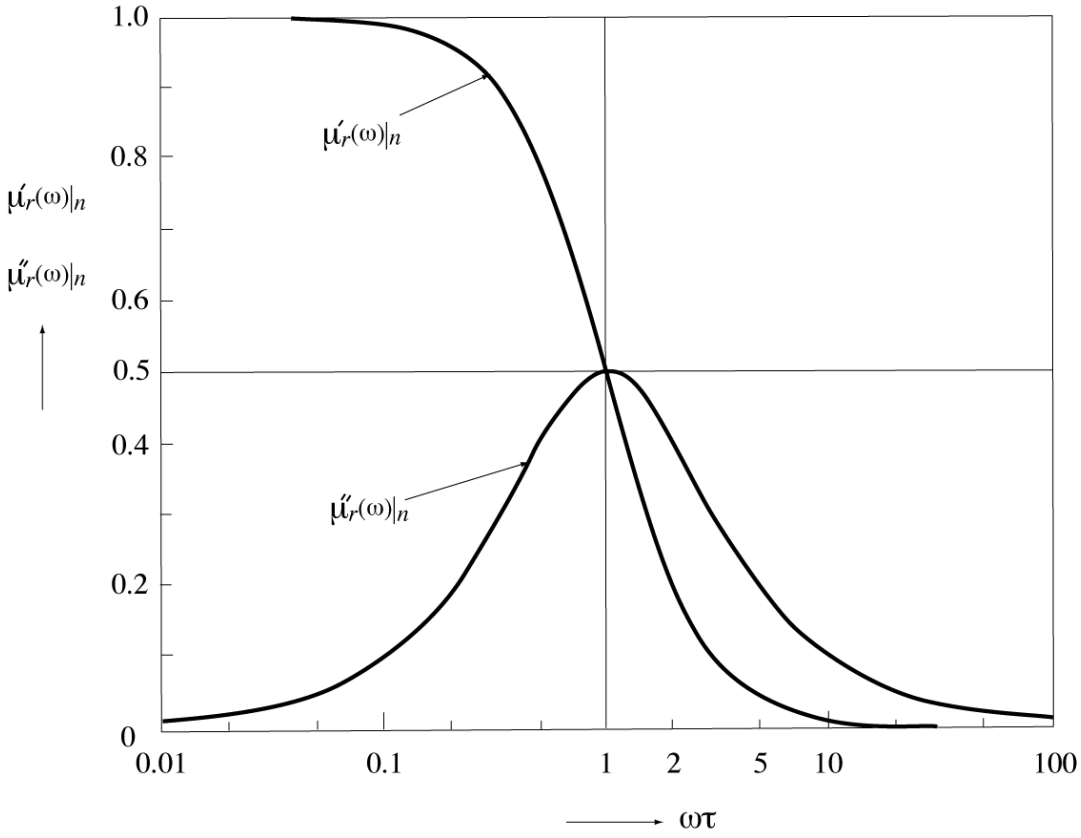

Figure 5.2 Real part and imaginary part of normalized relative permeability obtained from eqs.(5.19) and (5.20) as a function of $\omega\tau$, where ω is the angular frequency and τ is the relaxation time.

Dispersion of permeability due to the relaxation in orientation is found to occur in many kinds of ferrites [92].

5.4 Resonances in Low RF Range

In this section, we outline three types of resonances, which occur in a relatively low RF range and therefore might influence the performance of magnetic-core-loaded RF cavities.

5.4.1 Resonance of Magnetization Rotation

If a ferromagnetic material contains either no domain walls or only immobile domain walls, it can only be magnetized by rotation of the domain magnetization. This mechanism was already mentioned in Section 5.2 and is called *magnetization rotation*. Figure 5.3 shows the typical permeability spectra at room temperatures measured on

Ni-Zn ferrites of various compositions [106]. The general characteristic of the spectra is that μ_r' (μ' in the figure) remains constant in a certain frequency range, while at higher frequencies, after a small rise, it drops fairly rapidly to a very small value. Snoek explained this in terms of the resonance of magnetization rotation under the action of the anisotropic field [107]. Another experiment on a Ni-Zn ferrite was in agreement with this view [108]. This phenomenon is sometimes called *natural resonance*. In Fig. 5.3, the resonance feature does not appear as striking due to the use of the logarithmic scale.

Figure 5.3 also shows that the maximum of μ_r'' (μ'' in the figure) appears at a lower frequency when μ_r' (μ' in the figure) is higher in the low-frequency region. This is well

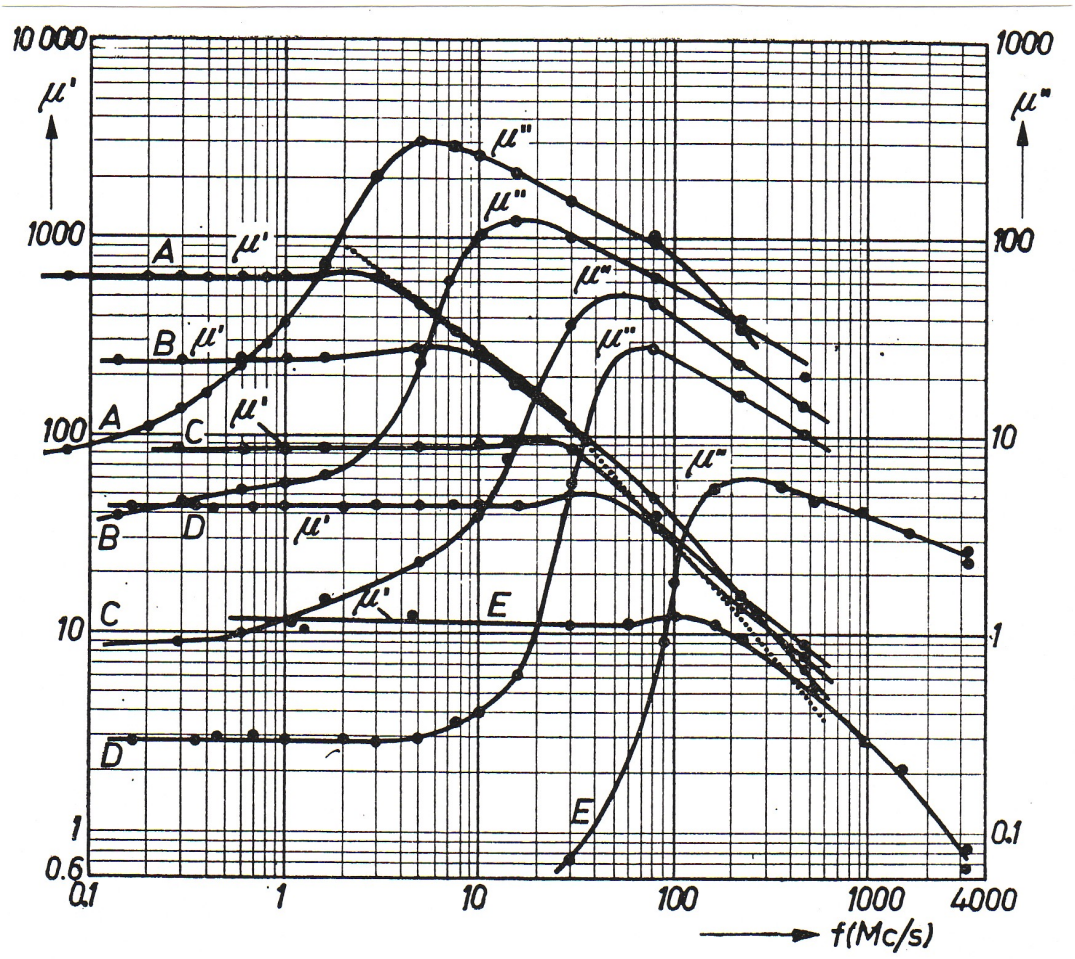

Figure 5.3 Frequency dependence of real part and imaginary part of relative permeability (μ' and μ'' in the figure) measured on Ni-Zn ferrites of various compositions [106]. The dashed line, which represents the *Snoek limit*, connects the points where μ' drops to half its low-frequency value.

described by the following relationship between the resonance frequency f_r, at which absorption and dispersion set in, and the relative permeability before resonance μ_r':

$$f_r\left(\mu_r' - 1\right) = \frac{1}{3\pi\mu_0}\gamma_g M_s. \tag{5.21}$$

Here, μ_0 is the permeability of a vacuum; γ_g, the gyromagnetic constant; and M_s, the spontaneous saturation magnetization. Equation (5.21) shows that for materials having approximately the same value of M_s, the frequency f_r is inversely proportional to μ_r'. The dashed line in Fig. 5.3 was drawn by connecting the points where μ_r' drops to half its low-frequency value. This line is called the *Snoek limit*, which expresses a limitation in the frequency performance of ferrites. Ferrites cannot have a permeability higher than the Snoek limit, as long as cubic magnetocrystalline anisotropy is present [93]. Subsequently, it was discovered that this limit could be overcome by using a special magnetocrystalline anisotropy. If the anisotropy in the *c*-plane is small, magnetization rotation in this plane can occur. Let the anisotropy field for this magnetization rotation be H_{a1}, while that for rotation out of this plane be H_{a2}. In this case, the relationship between f_r and μ_r' becomes [109]

$$f_r\left(\mu_r' - 1\right) = \frac{1}{3\pi\mu_0}\gamma_g M_s\left(\frac{1}{2}\sqrt{\frac{H_{a1}}{H_{a2}}} + \frac{1}{2}\sqrt{\frac{H_{a2}}{H_{a1}}}\right). \tag{5.22}$$

The value inside the parentheses on the right-hand side is always greater than 1.0 because H_{a2} is much greater than H_{a1}, which means this limit is much higher than the Snoek limit given in eq. (5.21). One of the materials that satisfy this condition is a magnetoplumbite-type hexagonal crystal called *Ferroxplana* [110].

5.4.2 Domain Wall Resonance

A domain wall is a boundary between two adjacent magnetic domains and its movement does not accompany any actual mass displacement. However, Döring found that a moving wall exhibits inertia and has an apparent mass [111]. Therefore, when an alternating field is applied, the wall oscillates back and forth about its initial position, just like a mass on a spring acted on by an alternating force. When the frequency of the applied magnetic field coincides with a natural oscillatory frequency of the wall, resonance occurs which enhances the oscillation amplitude. Figure 5.4 shows the frequency spectra of $\mu_r' - 1$ ($\mu_1 - 1$ in the figure) measured on Mg-ferrites, in which two dispersion regions are observed [112]. The dispersion at lower frequencies is attributed to the domain wall resonance and the one at higher frequencies to the magnetization rotation resonance [113][114]. Dispersion of intrinsic permeability due to domain wall

resonance is reviewed in Section 5.5.

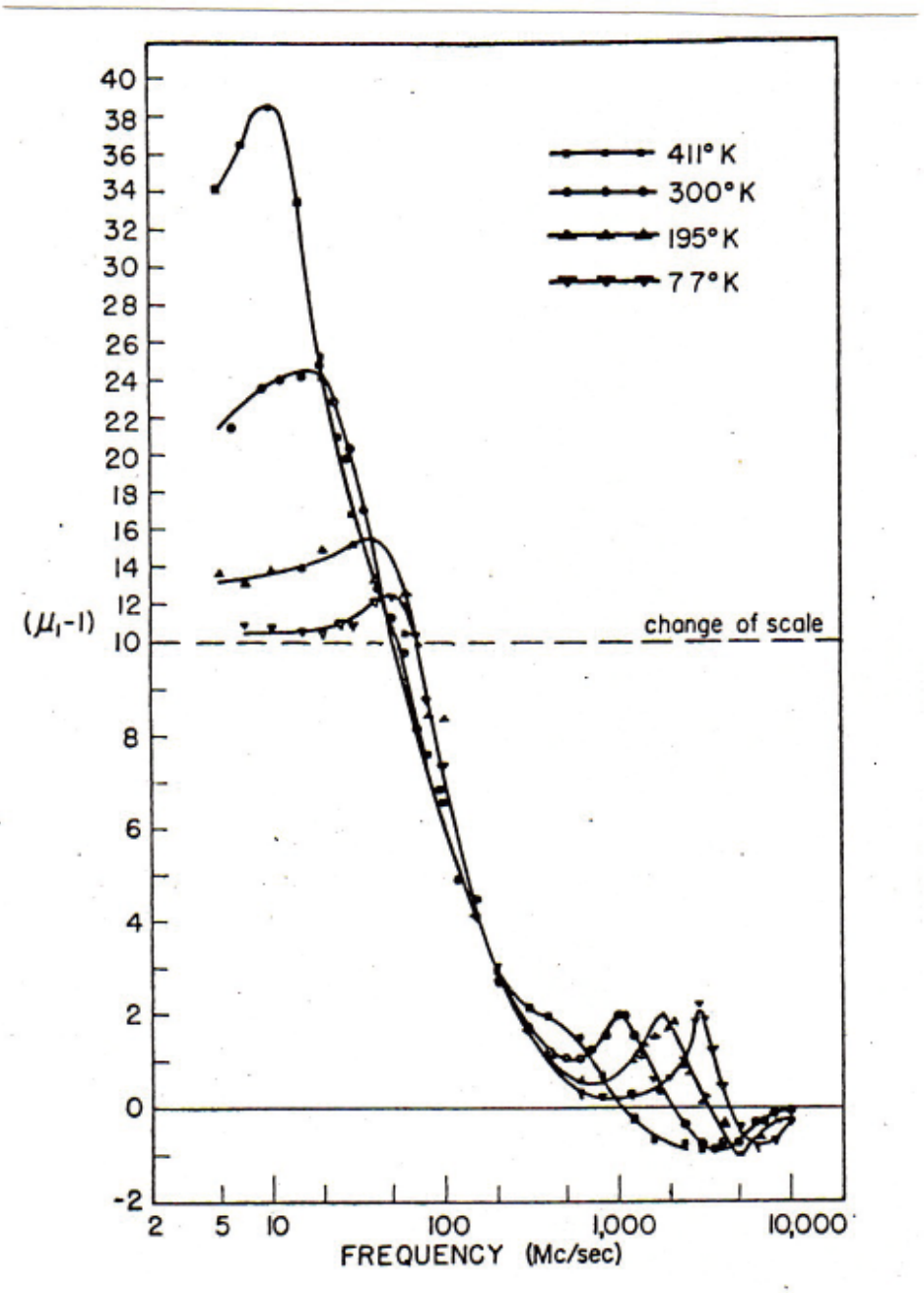

Figure 5.4 Relative permeability spectra of Mg-ferrites, showing two resonances [112]: the resonance at lower frequencies is attributed to domain wall resonance and the one at higher frequencies is due to magnetization rotation resonance [113][114].

5.4.3 Dimensional Resonance

Dimensional resonance is a type of resonance observed in low RF regions. This resonance is not intrinsic to magnetic materials but is discussed here because of its importance in applications of magnetic materials to RF accelerating cavities.

Assuming the relative permittivity and relative permeability of a material are ε_r and μ_r, respectively, the velocity of an electromagnetic wave is reduced by a factor $(\varepsilon_r \mu_r)^{-1/2}$ as compared to that in a vacuum. Therefore, the wavelength in the material λ is given by

$$\lambda = \frac{c}{f\sqrt{\varepsilon_r \mu_r}}, \tag{5.23}$$

where c is the velocity of light in a vacuum and f is the wave frequency. If one of the

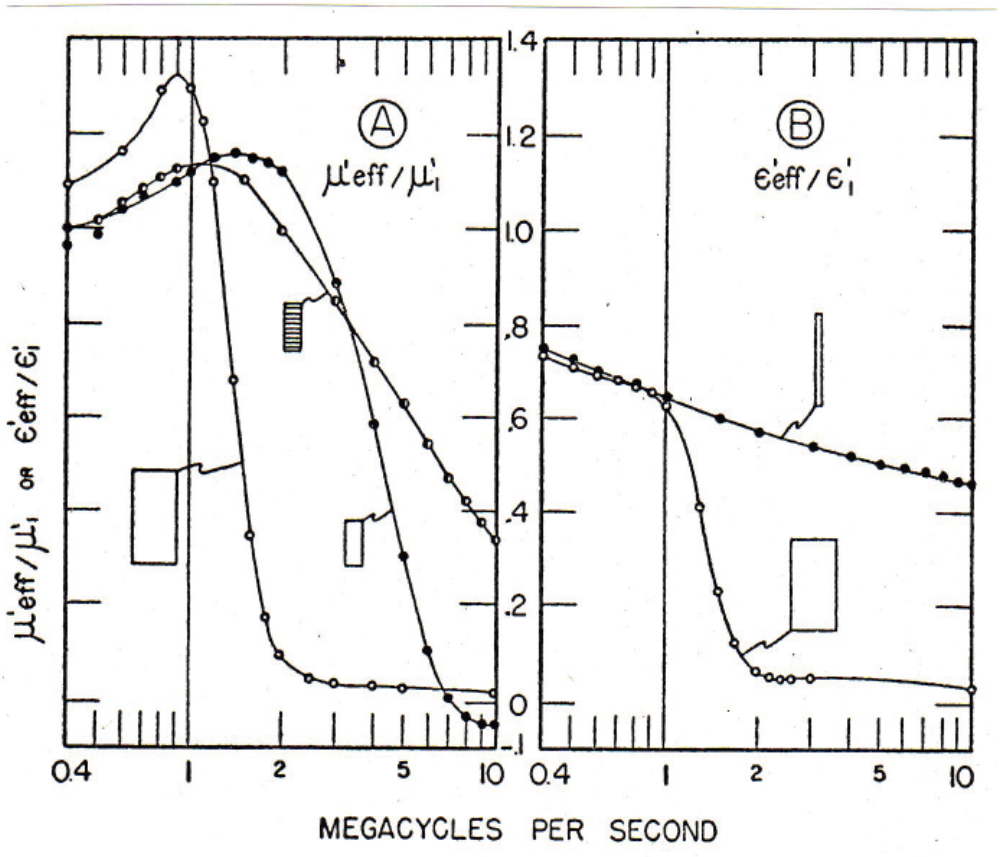

Figure 5.5 Dependence of the real part of relative permeability μ_r' (μ_{eff}' in the figure) on the dimensions of a sample of Mg-Zn ferrites. Sample cross sections are to scale for each curve. The ordinate is normalized to the value at 1 [kHz], μ_1' [115].

dimensions of a sample is very close to an integer multiple of the half wavelength $\lambda/2$, the electromagnetic wave resonates within the sample, giving rise to a standing wave. This phenomenon is called *dimensional resonance* and was first observed by F. G. Brockman et al. in samples of Mn-Zn ferrites with different dimensions [115]. Their results are plotted on the left side of Fig. 5.5, in which sample cross sections are shown to scale for each curve. The figure shows that the frequency response of permeability exhibits a resonance feature and μ_r' (μ_{eff}' in the figure) drops sharply between 1 and 2 [MHz] for a core with cross-sectional dimensions of 1.25×2.5 [cm^2]. This drop in μ_r' is shifted to a higher frequency when the size of the cross section is reduced.

When designing a magnetic-core-loaded cavity, one has to avoid the dimensional resonance by choosing appropriate material constants and size of the core.

5.5 Domain Wall Resonance

5.5.1 Equation of Domain Wall Motion

In this section, we examine the domain wall motion, emphasizing on the resonance of the domain wall oscillations. The equation of motion of the wall per unit area is given by

$$m\frac{d^2\mathbf{z}(t)}{dt^2} + \beta\frac{d\mathbf{z}(t)}{dt} + k\mathbf{z}(t) = 2M_s\mathbf{H}(t), \tag{5.24}$$

where $\mathbf{z}(t)$ is the displacement of the wall from its equilibrium position; m, the apparent mass of the wall per unit area and a measure of its inertia; β, the viscous damping parameter; k, the restoring coefficient; M_s, a spontaneous saturation magnetization of the material; and $\mathbf{H}(t)$, the applied magnetic field given by eq. (5.7). The first term in this equation, the product of the mass m and its acceleration, is the inertial term. This represents the resistance of the spins to sudden rotation. The second term proportional to velocity $d\mathbf{z}(t)/dt$ and represents a resistance to wall motion. The third term represents a force due to crystal imperfections such as residual microstress and inclusions, which hinder the motion of domain walls. The term on the right-hand side of the equation represents the pressure acting on the $180°$ wall and should be replaced with $\sqrt{2}M_s\mathbf{H}(t)$ for a $90°$ wall.

Provided that n represents the number of walls per unit volume, a change in magnetization produced when all the domain walls are displaced by $\mathbf{z}(t)$ is given by $M_s n\mathbf{z}(t) \equiv \mathbf{M}_w(t)$. Multiplying both sides of eq. (5.24) by $M_s n$ leads to

$$m\frac{d^2\mathbf{M}_w(t)}{dt^2} + \beta\frac{d\mathbf{M}_w(t)}{dt} + k\mathbf{M}_w(t) = 2M_s^2 n\mathbf{H}(t). \tag{5.25}$$

This can be rewritten in the form

$$\frac{d^2\mathbf{M}_w(t)}{dt^2} + \gamma \frac{d\mathbf{M}_w(t)}{dt} + \omega_0^2 \mathbf{M}_w(t) = \frac{2M_s^2 n}{m} \mathbf{H}(t), \tag{5.26}$$

with $$\gamma = \frac{\beta}{m} \quad \text{and} \quad \omega_0^2 = \frac{k}{m}, \tag{5.27}$$

where γ is the damping coefficient and ω_0 is the natural resonance frequency of the domain walls. We are primarily interested in the equilibrium state or the steady state solution of eq. (5.26). Assuming the form

$$\mathbf{M}_w(t) = \mathbf{M}_1 e^{j\omega t}, \tag{5.28}$$

and substituting it into eq. (5.26), we obtain

$$\mathbf{M}_1 = \frac{2M_s^2 n}{m} \frac{\left(\omega_0^2 - \omega^2\right) - j\gamma\omega}{\left(\omega_0^2 - \omega^2\right)^2 + \gamma^2\omega^2} H_0. \tag{5.29}$$

5.5.2 Dispersion of Permeability due to Domain Wall Resonance

Now, we write the magnetization $\mathbf{M}(t)$ as

$$\mathbf{M}(t) = \mathbf{M}_h(t) + \mathbf{M}_w(t) \quad \text{with} \quad \mathbf{M}_h(t) = \chi_h H_0 e^{j\omega t}, \tag{5.30}$$

where $\mathbf{M}_h(t)$ and χ_h are the magnetization and the susceptibility for frequencies much higher than ω_0, respectively. Then, the magnetic flux density $\mathbf{B}(t)$ is given by

$$\mathbf{B}(t) = \mu_0\left[\mathbf{H}(t) + \mathbf{M}(t)\right] = \mu_0\left[\mathbf{H}(t) + \mathbf{M}_h(t) + \mathbf{M}_w(t)\right]$$

$$= \mu_0\left(1 + \chi_h + \frac{2M_s^2 n}{m} \frac{\omega_0^2 - \omega^2}{\left(\omega_0^2 - \omega^2\right)^2 + \gamma^2\omega^2} - j\frac{2M_s^2 n}{m} \frac{\gamma\omega}{\left(\omega_0^2 - \omega^2\right)^2 + \gamma^2\omega^2}\right) H_0 e^{j\omega t}. \tag{5.31}$$

The expression inside the parentheses corresponds to the complex relative permeability as a function of frequency, which means that eq. (5.31) can be expressed as

$$\mathbf{B}(t) = \mu_0\left[\mu_r'(\omega) - j\mu_r''(\omega)\right] H_0 e^{j\omega t}, \tag{5.32}$$

where $$\mu_r'(\omega) = \mu_h + \frac{2M_s^2 n}{m} \frac{\omega_0^2 - \omega^2}{\left(\omega_0^2 - \omega^2\right)^2 + \gamma^2\omega^2} \tag{5.33}$$

and $$\mu_r''(\omega) = \frac{2M_s^2 n}{m} \frac{\gamma\omega}{\left(\omega_0^2 - \omega^2\right)^2 + \gamma^2\omega^2}, \tag{5.34}$$

with $\mu_h = 1 + \chi_h$. It follows from eqs. (5.33) and (5.34) that for frequencies much lower than ω_0,

$$\mu_r'(\omega) \approx \mu_h + \frac{2M_s^2 n}{m\omega_0^2} \equiv \mu_w \quad \text{and} \quad \mu_r''(\omega) \approx 0, \tag{5.35}$$

and for frequencies much higher than ω_0,

$$\mu_r'(\omega) \approx \mu_h, \quad \text{and} \quad \mu_r''(\omega) \approx 0. \tag{5.36}$$

We can see from eqs. (5.35) and (5.36) that the difference between the real parts of the relative permeability at very low and very high frequencies is given by

$$\mu_w - \mu_h \approx \frac{2M_s^2 n}{m\omega_0^2}. \tag{5.37}$$

We can normalize $\mu_r'(\omega)$ and $\mu_r''(\omega)$ as

$$\mu_r'(\omega)\big|_n = \frac{\mu_r'(\omega) - \mu_h}{2M_s^2 n/m\omega_0^2} = \frac{1 - (\omega/\omega_0)^2}{\left[1 - (\omega/\omega_0)^2\right]^2 + (1/Q^2)(\omega/\omega_0)^2} \tag{5.38}$$

and $$\mu_r''(\omega)\big|_n = \frac{\mu_r''(\omega)}{2M_s^2 n/m\omega_0^2} = \frac{(1/Q)(\omega/\omega_0)}{\left[1 - (\omega/\omega_0)^2\right]^2 + (1/Q^2)(\omega/\omega_0)^2}, \tag{5.39}$$

where Q is given by

$$Q = \frac{\omega_0}{\gamma} = \frac{\sqrt{mk}}{\beta}. \tag{5.40}$$

Equation (5.40) is equivalent to a quality factor used in various kinds of resonance systems. In this case, a high Q-value means a large dispersion of μ_r' and high energy absorption.

Figure 5.6 shows the normalized relative permeability obtained from eqs. (5.38) and (5.39) as a function of ω/ω_0 for three values of Q. We can see that when the frequency of the applied field is very different from the natural resonance frequency ω_0, the real part $\mu_r'(\omega)|_n$ is approximately constant relative to frequency and the imaginary part $\mu_r''(\omega)|_n$ is virtually zero. In contrast, when the frequency is close to ω_0, there are sudden

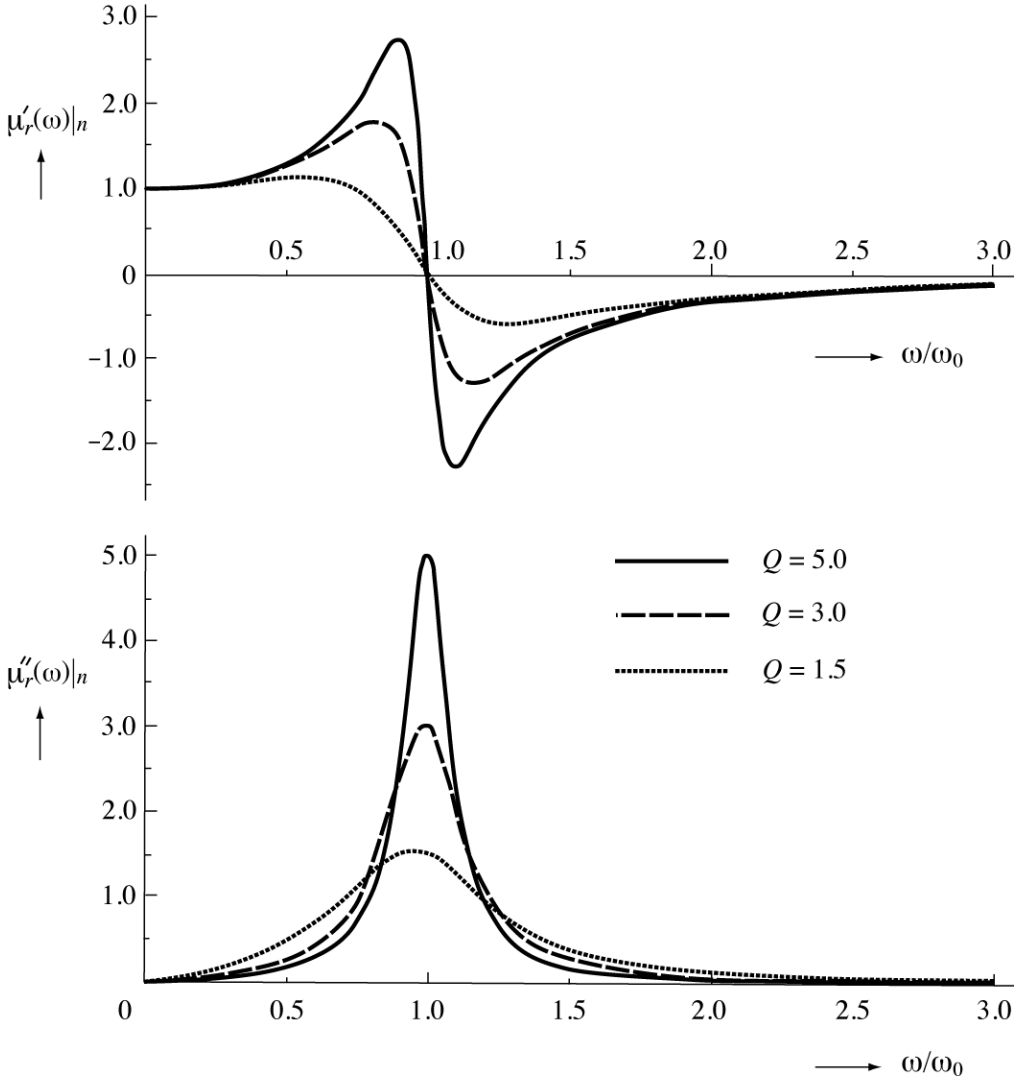

Figure 5.6 Real and imaginary parts of normalized relative permeability obtained from eqs. (5.38) and (5.39) as a function of ω/ω_0 for three values of Q.

changes in both the real and imaginary parts. The sharp peak in the imaginary part reflects the resonance absorption of energy that occurs in the proximity to ω_0. $|\mu_r'(\omega)|_n|$ is larger at low frequencies ($\omega < \omega_0$) than at high frequencies ($\omega > \omega_0$) because the amplitude of in-phase domain wall oscillations below resonance is much larger than the amplitude of 180° out-of-phase oscillations above resonance.

If the inertia of the wall is very small or the value of the apparent mass m is such that the first term on the left-hand side of eq. (5.25) is negligible, the equation reduces to a relaxation equation similar to eq. (5.8). Then, the characteristic rapid change in μ_r' near the resonance disappears and is replaced by a rather slow change.

5.6 Illustration of Typical Frequency Response of Permeability

Different sources of magnetization contribute to the intrinsic permeability in different frequency regimes. Figure 5.7 is a typical frequency response of relative intrinsic permeability, which is helpful in summarizing this section. The figure shows the relative contributions of two different dispersion mechanisms: relaxation and resonance. Since relaxation is a comparatively slow process, its contribution to the permeability generally disappears at a lower frequency than the contribution from resonance. Therefore, as the frequency of the external field is increased from a very low value, first there is a rather slow drop in μ_r' around the relaxation frequency $1/\tau (= \omega_{rel})$, followed by a characteristic change in μ_r' around the resonance frequency ω_0.

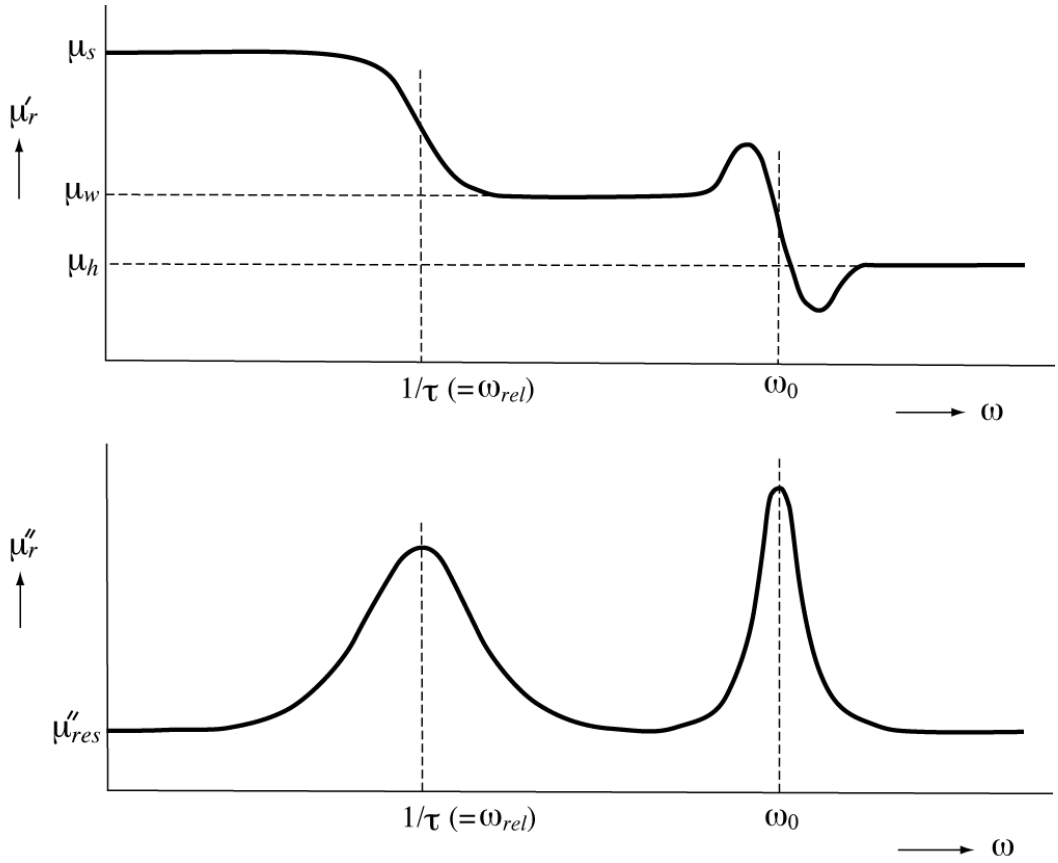

Figure 5.7 Schematic of real and imaginary parts of relative intrinsic permeability as a function of frequency for a magnetic material with a single relaxation at $1/\tau$ and a single resonance at ω_0. μ_{res}'' corresponds to residual losses.

The bottom of Fig. 5.7 shows a schematic of μ_r'', in which μ_{res}'' represents the imaginary part of the permeability corresponding to residual losses.

In general, the frequency behavior of permeability for any particular mechanism in which there is an equilibrium configuration of magnetic moment can be described by a driven damped-oscillator equation such as eq. (5.24). The resonant absorption belongs to this type of mechanism. On the other hand, a freely rotating magnetic moment has no equilibrium configuration and accordingly shows relaxation dynamics.

For most magnetic alloys with moderate conductivity, eddy currents become influential at a lower frequency than the lowest relaxation frequency of magnetic moments. In this case, the dispersion due to relaxation and resonance should be completely masked by the dispersion due to the eddy currents, and as a result, the frequency response of the effective permeability (not intrinsic permeability) depends mainly on eddy currents. This is only speculation, and hence, it would be worthwhile comparing measured values with estimated ones that include the effect of eddy currents, such as estimations obtained from the expressions derived in the next chapter.

6. Effective Permeability

6.1 Introduction

In Chapter 4, we used the intrinsic permeability μ $(=\mu'-j\mu'')$ to obtain the magnetic field distribution in the interior of the sheet. The reason for using μ is that it originates in magnetization mechanisms and hence determines the local relationship between **B** and **H**. Measurement of the intrinsic permeability of a conductive magnetic material is extremely difficult, if not impossible, because the measurement unavoidably involves the eddy-current effects unless the frequency is very low. However, note that although knowing the intrinsic permeability is essential for materials scientists and engineers, it is not necessarily important for most users of magnetic materials. Users are primarily interested in the apparent or macroscopic properties of a magnetic object, not in the fundamental and microscopic properties. Therefore, they need another definition of permeability appropriate for characterizing the magnetic properties of an object as a whole. This definition of permeability must establish a relationship between the applied magnetic field and the average magnetic flux density of the object, both of which can be measured either directly or indirectly. This permeability is referred to as the *effective* or *apparent permeability*. Earlier, we termed this the effective permeability and denoted it by μ_e $(=\mu_e'-j\mu_e'')$. To obtain accurate expressions of μ_e, the fields **H** and **B** are integrated and averaged over the whole volume of the object. In this chapter, we derive the expressions for effective permeability of the magnetic sheet on the assumption that the local relationship of **B** to **H** is determined by the intrinsic permeability that is not influenced by the presence of eddy currents.

6.2 Definition of Effective Permeability

In most cases, it should not be a problem if we are unaware of whether we are using the intrinsic or the effective permeability. However, in some cases, such as the one we are currently dealing with, we must distinguish between intrinsic and effective. We consulted several dictionaries and textbooks for the definition of permeability. *A New Dictionary of Physics* [116] states that permeability is "the ratio of the magnetic flux density in an object or medium to the external magnetic field strength inducing it." This is a typical definition appearing in most physics dictionaries and ferromagnetism textbooks. However, to clarify the definition, we also need to define the term *magnetic flux density*. A statement on the distinction between the intrinsic permeability and the effective permeability is found in the *Encyclopedic Dictionary of Condensed Matter Physics*[117]. It states that the effective permeability of an object depends on its geometry and is related to the intrinsic permeability by the *demagnetizing factor*. In

some textbooks, demagnetizing factor is defined as "when an object of finite size is magnetized by an external magnetic field, the magnetic free poles appear on its ends, which then produce a demagnetizing field directed opposite to the magnetization." The ratio of the demagnetizing field to the magnetization is called the *demagnetizing factor*, which depends on the geometry of the object. This is the term used in the definition of the effective permeability given above.

Here, we extend the definition of the effective permeability to the case where an alternating magnetic field is applied to a conductive magnetic object. The eddy currents induced inside the object produce a magnetic field whose direction is opposite to the applied field. This demagnetizing field is added to the field produced by the magnetic free poles and contributes to the demagnetizing factor and consequently to the effective permeability. In the present model, the magnetic sheet extends infinitely and is magnetized parallel to its surface; therefore, the demagnetizing field due to magnetic free poles is zero. As a result, the demagnetizing factor comes exclusively from the eddy currents. Note that in our treatment, the demagnetizing effect due to eddy currents is naturally included in the expressions of **H** and **B** and does not explicitly appear as a demagnetizing factor. It is quite reasonable to define the effective permeability of the sheet as the ratio of the average magnetic flux density to the applied magnetic field that induces it.

6.3 Relationship between μ and μ_e

In Chapter 4, we discussed how the magnetic field $\mathbf{H}_z$ varies with the depth under the sheet surface. The magnetic flux density within the sheet, $\mathbf{B}_z$, is locally related to $\mathbf{H}_z$ by $\mathbf{B}_z=\mu\mathbf{H}_z$, where μ is the intrinsic permeability. Hence, the amplitude and phase of $\mathbf{B}_z$ vary with the distance from the surface in the same manner as those of $\mathbf{H}_z$.

Now, let H_0 be the amplitude of the applied magnetic field, and let $[\mathbf{H}_z]_{av}$ and $[\mathbf{B}_z]_{av}$ be the magnetic field intensity and magnetic flux density averaged over the cross section of the sheet, respectively. Then, from $\mathbf{B}_z(y)=\mu\mathbf{H}_z(y)$, which holds for any value of y, we can write the following relationship between the effective permeability μ_e and the intrinsic permeability μ:

$$\left[\mathbf{B}_z\right]_{av} = \mu\left[\mathbf{H}_z\right]_{av} = \mu_e H_0 . \tag{6.1}$$

This important equation forms the basis for the derivation of the effective permeability. It is worthwhile emphasizing that μ_e expresses the relationship between H_0 and $[\mathbf{B}_z]_{av}$, whereas μ expresses the relationship between $[\mathbf{H}_z]_{av}$ and $[\mathbf{B}_z]_{av}$. Provided that the values of H_0 and μ are given and $[\mathbf{H}_z]_{av}$ is known, we can obtain μ_e from eq. (6.1).

In the next section, using the field distribution obtained in Chapter 4, we derive the

expression for $[\mathbf{H}_z]_{av}$, and in the following section, we use it to obtain μ_e.

6.4 Average Magnetic Field Calculations

For the calculations in this section, we use the complex representation of $\mathbf{H}_z$ given in eq. (4.28), from which the average magnetic field $[\mathbf{H}_z]_{av}$ is expressed by

$$\left[\mathbf{H}_z\right]_{av} = \left[\mathrm{Re}\left[\mathbf{H}_z\right]\right]_{av} + j\left[\mathrm{Im}\left[\mathbf{H}_z\right]\right]_{av}, \tag{6.2}$$

where $[\mathrm{Re}[\mathbf{H}_z]]_{av}$ and $[\mathrm{Im}[\mathbf{H}_z]]_{av}$ represent the average values of the real and imaginary parts of the field, respectively. The average fields are obtained by integrating $\mathrm{Re}[\mathbf{H}_z]$ and $\mathrm{Im}[\mathbf{H}_z]$ over the cross section of the sheet S $(=l_0\times d)$ shown in Fig. 3.2. The integration of $\mathrm{Re}[\mathbf{H}_z]$ is then written as

$$\begin{aligned}\int_S \mathrm{Re}\left[\mathbf{H}_z\right] da &= 2l_0 \int_0^{\frac{d}{2}} \mathrm{Re}\left[\mathbf{H}_z\right] dy \\ &= \frac{2l_0 H_0}{\cosh\left(2a_2\right) + \cos\left(2b_2\right)} \times \\ &\quad \int_0^{\frac{d}{2}} \left[\cosh\left(a_1 y + a_2\right)\cos\left(b_1 y - b_2\right) + \cosh\left(a_1 y - a_2\right)\cos\left(b_1 y + b_2\right)\right] dy.\end{aligned} \tag{6.3}$$

Performing the integration, we obtain

$$\begin{aligned}\int_S \mathrm{Re}\left[\mathbf{H}_z\right] da &= \frac{\sqrt{2}\, l_0 d\, H_0}{\alpha^{1/4}\theta} \frac{\cos(\phi)\sinh\left(2a_2\right) + \sin(\phi)\sin\left(2b_2\right)}{\cosh\left(2a_2\right) + \cos\left(2b_2\right)} \\ &= l_0 d\, H_0\, f(\theta,\phi),\end{aligned} \tag{6.4}$$

where

$$f(\theta,\phi) = \frac{\sqrt{2}}{\alpha^{1/4}\theta} \frac{\cos(\phi)\sinh\left(2a_2\right) + \sin(\phi)\sin\left(2b_2\right)}{\cosh\left(2a_2\right) + \cos\left(2b_2\right)}. \tag{6.5}$$

Substituting a_2 and b_2 from eq. (4.21) into eq. (6.5) yields another form of $f(\theta,\varphi)$,

$$f(\theta,\phi) = \frac{1}{\alpha^{1/2}\theta} \frac{M\sinh(M\theta) + N\sin(N\theta)}{\cosh(M\theta) + \cos(N\theta)}, \tag{6.6}$$

with

$$M = \pm\left(\alpha^{1/2} + \tan\delta\right)^{1/2} \quad \text{and} \quad N = \pm\left(\alpha^{1/2} - \tan\delta\right)^{1/2}, \tag{6.7}$$

where the plus sign is for $m=0$ from eq. (4.11) and the minus sign is for $m=1$. The average real part $[\mathrm{Re}[\mathbf{H}_z]]_{av}$ is obtained from eq. (6.4) by dividing it by the cross-sectional area S:

$$\left[\mathrm{Re}\left[\mathbf{H}_z\right]\right]_{av} = \frac{1}{S}\int_S \mathrm{Re}\left[\mathbf{H}_z\right] da = \frac{1}{l_0 d}\int_a \mathrm{Re}\left[\mathbf{H}_z\right] dv$$

$$= H_0\, f(\theta,\phi). \tag{6.8}$$

Likewise, the integration of $\mathrm{Im}[\mathbf{H}_z]$ over the cross section of the sheet is performed:

$$\int_S \mathrm{Im}\left[\mathbf{H}_z\right] da = 2l_0 \int_0^{\frac{d}{2}} \mathrm{Im}\left[\mathbf{H}_z\right] dy$$

$$= -\frac{\sqrt{2}\, l_0 d\, H_0}{\alpha^{1/4}\theta}\, \frac{\sin(\phi)\sinh(2a_2) - \cos(\phi)\sin(2b_2)}{\cosh(2a_2) + \cos(2b_2)}$$

$$= -l_0 d\, H_0\, g(\theta,\phi), \tag{6.9}$$

where

$$g(\theta,\phi) = \frac{\sqrt{2}}{\alpha^{1/4}\theta}\, \frac{\sin(\phi)\sinh(2a_2) - \cos(\phi)\sin(2b_2)}{\cosh(2a_2) + \cos(2b_2)}. \tag{6.10}$$

This can also be written as

$$g(\theta,\phi) = \frac{1}{\alpha^{1/2}\theta}\, \frac{N\sinh(M\theta) - M\sin(N\theta)}{\cosh(M\theta) + \cos(N\theta)}. \tag{6.11}$$

Dividing eq. (6.9) by the cross-sectional area S, we obtain the average imaginary part:

$$\left[\mathrm{Im}\left[\mathbf{H}_z\right]\right]_{av} = \frac{1}{S}\int_S \mathrm{Im}\left[\mathbf{H}_z\right] da = \frac{1}{l_0 d}\int_S \mathrm{Im}\left[\mathbf{H}_z\right] da$$

$$= -H_0\, g(\theta,\phi). \tag{6.12}$$

It follows from eqs. (6.8) and (6.12) that $[\mathbf{H}_z]_{av}$ in eq. (6.2) is represented by

$$\left[\mathbf{H}_z\right]_{av} = H_0\left[f(\theta,\phi) - j\, g(\theta,\phi)\right]. \tag{6.13}$$

In the remainder of this paper, we will frequently see expressions including $f(\theta,\varphi)$ and/or $g(\theta,\varphi)$. Equation (6.13) shows that the average real part of the field is proportional to $f(\theta,\varphi)$ and the average imaginary part is proportional to $g(\theta,\varphi)$. Remembering this when we see expressions including $f(\theta,\varphi)$ and/or $g(\theta,\varphi)$ will help us understand the meaning of the expressions.

If $\tan\delta = 0$, then $f(\theta,\varphi)$ and $g(\theta,\varphi)$ are reduced to

$$f(\theta) = \frac{1}{\theta}\,\frac{\sinh(\theta) + \sin(\theta)}{\cosh(\theta) + \cos(\theta)}, \tag{6.14}$$

and

$$g(\theta) = \frac{1}{\theta}\,\frac{\sinh(\theta) - \sin(\theta)}{\cosh(\theta) + \cos(\theta)}. \tag{6.15}$$

These expressions agree with those in the ferromagnetism textbook [90]. In the textbook, $f(\theta)$ is used to express the ratio of the inductance of a coil to that at very low frequencies and $g(\theta)$ is used in the expression of the AC resistance of the coil caused by eddy currents. This clearly shows that the coil inductance is related to the real part of the magnetic field and that the coil AC resistance or eddy-current loss is related to the imaginary part of the field.

6.5 Derivation of Effective Permeability

Now that the average magnetic field inside the sheet is known, we are ready to derive the effective permeability μ_e. From eq. (6.1), the average magnetic flux density $[\mathbf{B}_z]_{av}$ is given by

$$\left[\mathbf{B}_z\right]_{av} = \mu_e H_0 = \left(\mu_e' - j\mu_e''\right) H_0. \tag{6.16}$$

We see from eqs. (6.1) and (6.2) that $[\mathbf{B}_z]_{av}$ can also be written as

$$\begin{aligned}\left[\mathbf{B}_z\right]_{av} &= \mu\left[\mathbf{H}_z\right]_{av} = \left(\mu' - j\mu''\right)\left\{\left[\mathrm{Re}\left[\mathbf{H}_z\right]\right]_{av} + j\left[\mathrm{Im}\left[\mathbf{H}_z\right]\right]_{av}\right\} \\ &= \left\{\mu'\left[\mathrm{Re}\left[\mathbf{H}_z\right]\right]_{av} + \mu''\left[\mathrm{Im}\left[\mathbf{H}_z\right]\right]_{av}\right\} - j\left\{-\mu'\left[\mathrm{Im}\left[\mathbf{H}_z\right]\right]_{av} + \mu''\left[\mathrm{Re}\left[\mathbf{H}_z\right]\right]_{av}\right\}.\end{aligned} \tag{6.17}$$

Letting the real part of eq. (6.17) be equal to that of eq. (6.16), we have

$$\mu_e' H_0 = \mu'\left[\mathrm{Re}\left[\mathbf{H}_z\right]\right]_{av} + \mu''\left[\mathrm{Im}\left[\mathbf{H}_z\right]\right]_{av}. \tag{6.18}$$

Replacing $[\mathrm{Re}[\mathbf{H}_z]]_{av}$ and $[\mathrm{Im}[\mathbf{H}_z]]_{av}$ in eq. (6.18) with eqs. (6.8) and (6.12), we obtain the real part of the effective permeability:

$$\mu_e' = \mu' f(\theta,\phi) - \mu'' g(\theta,\phi). \tag{6.19}$$

Dividing both sides of eq. (6.19) by μ' gives

$$\frac{\mu_e'}{\mu'} = f(\theta,\phi) - g(\theta,\phi)\tan\delta. \tag{6.20}$$

In the same manner, equating the imaginary part of eq. (6.17) with that of eq. (6.16), we obtain

$$\mu_e'' H_0 = -\mu'\left[\mathrm{Im}\left[\mathbf{H}_z\right]\right]_{av} + \mu''\left[\mathrm{Re}\left[\mathbf{H}_z\right]\right]_{av}. \tag{6.21}$$

Substituting $[\mathrm{Re}[\mathbf{H}_z]]_{av}$ from eq. (6.8) and $[\mathrm{Im}[\mathbf{H}_z]]_{av}$ from eq. (6.12) into eq. (6.21) yields the imaginary part of the effective permeability:

$$\mu_e'' = \mu'' f(\theta,\phi) + \mu' g(\theta,\phi). \tag{6.22}$$

This can also be written as

$$\frac{\mu_e''}{\mu''} = f(\theta,\phi) + g(\theta,\phi)\frac{1}{\tan\delta}. \tag{6.23}$$

From the expressions of μ_e' and μ_e'' together with those of $f(\theta,\varphi)$ and $g(\theta,\varphi)$, we see that the effective permeability is determined by the frequency ω, the sheet thickness d, the intrinsic permeability μ, and the conductivity σ.

It follows from eqs. (6.1) and (6.13) that the relationship between the average magnetic field within the sheet $[\mathbf{H}_z]_{av}$ and the applied magnetic field H_0 is given by

$$\frac{\left[\mathbf{H}_z\right]_{av}}{H_0} = \frac{\mu_e}{\mu} = f(\theta,\phi) - j\, g(\theta,\phi). \tag{6.24}$$

Expanding $f(\theta,\varphi)$ and $g(\theta,\varphi)$ into a power series of θ and taking only the first term of a fixed number and the second term of θ^2, we obtain the low-frequency approximations of $f(\theta,\varphi)$ and $g(\theta,\varphi)$, which are given by

$$f(\theta,\phi) \simeq 1 - \frac{1}{6}\theta^2\tan\delta \quad \text{and} \quad g(\theta,\phi) \simeq \frac{1}{6}\theta^2. \tag{6.25}$$

Then, μ_e' from eq. (6.19) and μ_e'' from eq. (6.22) are approximately written as

$$\mu_e' \simeq \mu' - \frac{1}{3}\mu''\theta^2, \tag{6.26}$$

and $$\mu_e'' \simeq \mu'' + \frac{1}{6}\mu'\theta^2\left(1-\tan^2\delta\right). \tag{6.27}$$

These low-frequency approximations were already shown in Chapter 3 in eqs.(3.54) and (3.55).

6.6 Permeability as a Function of Frequency

In practice, it is advantageous to write the permeability in terms of the frequency f instead of θ, because the measured permeability is usually given as a function of f. We can rewrite $f(\theta,\varphi)$ from eq.(6.5) and $g(\theta,\varphi)$ from eq.(6.10) as

$$F(f,\phi) = \frac{k_0}{\sqrt{f}}\frac{\cos(\phi)\sinh\left(2k_1\sqrt{f}\right)+\sin(\phi)\sin\left(2k_2\sqrt{f}\right)}{\cosh\left(2k_1\sqrt{f}\right)+\cos\left(2k_2\sqrt{f}\right)} \tag{6.28}$$

and $$G(f,\phi) = \frac{k_0}{\sqrt{f}}\frac{\sin(\phi)\sinh\left(2k_1\sqrt{f}\right)-\cos(\phi)\sin\left(2k_2\sqrt{f}\right)}{\cosh\left(2k_1\sqrt{f}\right)+\cos\left(2k_2\sqrt{f}\right)}, \tag{6.29}$$

with $$k_0 = \frac{2^{1/2}}{\alpha^{1/4}d\left(\pi\mu'\sigma\right)^{1/2}}, \tag{6.30}$$

$$k_1 = \frac{d}{2}\left[\left(\alpha^{1/2}+\tan\delta\right)\pi\mu'\sigma\right]^{1/2}, \tag{6.31}$$

and $$k_2 = \frac{d}{2}\left[\left(\alpha^{1/2}-\tan\delta\right)\pi\mu'\sigma\right]^{1/2}, \tag{6.32}$$

where φ is a function of $\tan\delta$ given in eq.(4.11), d is the thickness, and σ is the conductivity of the sheet. Using eqs.(6.28) and (6.29), we can rewrite μ_e' given in eq. (6.19) and μ_e'' in eq. (6.22) in the forms

$$\mu_e' = \mu' F(f,\phi) - \mu'' G(f,\phi) \tag{6.32}$$

and $$\mu_e'' = \mu'' F(f,\phi) + \mu' G(f,\phi). \tag{6.33}$$

6.7 Numerical Examples

Figure 6.1 shows $f(\theta,\varphi)$ versus θ for four values of $\tan\delta$. We see from the figure that $f(\theta,\varphi)$ is nearly equal to 1.0 in the region where $\theta \ll 1.0$, and decreases rapidly as θ

increases. Since $f(\theta,\varphi)$ is proportional to the average real part of the field $[\mathrm{Re}[\mathbf{H}_z]]_{av}$, this behavior can be inferred from the typical pattern of $\mathrm{Re}[\mathbf{H}_z]$ shown in Fig. 4.6.

Figure 6.2 plots $g(\theta,\varphi)$ against θ for four values of $\tan\delta$, showing that $g(\theta,\varphi)$ is nearly equal to zero when θ is very small, gradually increases as θ increases, reaches its maximum at $\theta=1.3-2.3$, and then decreases afterward. When $\tan\delta$ is rather high, the value of θ at which $g(\theta,\varphi)$ reaches a maximum depends on the value of $\tan\delta$. However, if $\tan\delta$ is reduced to less than 0.1, the maximum always occurs when θ is approximately 2.254, at which $f(\theta,\varphi)$ is approximately 0.58. The reason why $g(\theta,\varphi)$, shown in Fig. 6.2, is similar to $\mathrm{Im}[\mathbf{H}_z]/H_0$, shown in Fig. 4.6(b), is that $g(\theta,\varphi)$ is proportional to the average imaginary part of the field $[\mathrm{Im}[\mathbf{H}_z]]_{av}$. The difference between Fig. 6.2 and Fig. 4.6(b) is that Fig. 4.6(b) shows $\mathrm{Im}[\mathbf{H}_z]/H_0$ at a fixed position and not for the average value within the sheet. We will see in Chapter 7 that $g(\theta,\varphi)$ is actually closely related to

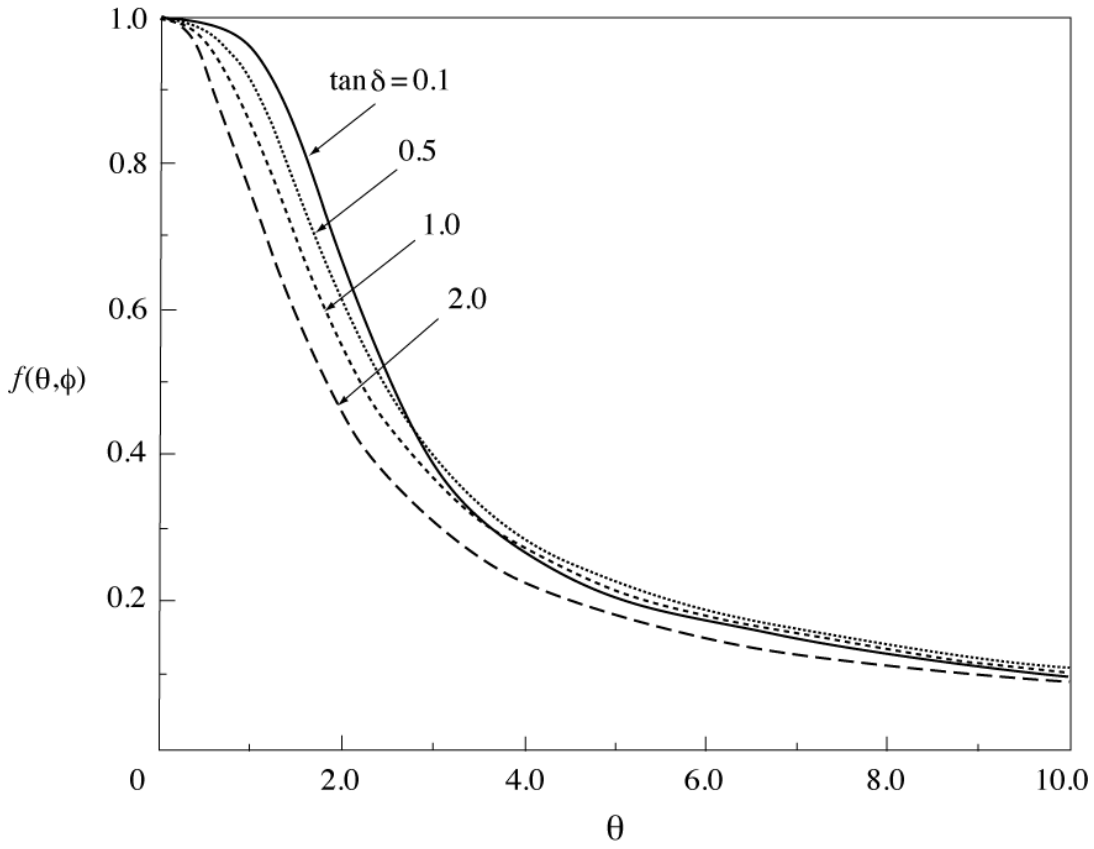

Figure 6.1 $f(\theta,\varphi)$ obtained from eq.(6.5) versus θ for four values of $\tan\delta$. $f(\theta,\varphi)$ is proportional to the average real part of the magnetic field inside the sheet.

the eddy-current loss.

As mentioned above, if θ decreases toward 0, $f(\theta,\varphi)$ approaches 1.0 and $g(\theta,\varphi)$ decreases toward 0. As a result, μ_e' in eq.(6.19) and μ_e'' in eq.(6.22) reduce to μ' and μ'', respectively. Thus, we have a natural consequence that in a very low frequency range, the effective permeability, μ_e $(=\mu_e' - j\mu_e'')$, reduces to the intrinsic permeability, μ $(=\mu' - j\mu'')$.

Figure 6.3 shows the plots of μ_e'/μ' as a function of θ for four values of $\tan\delta$. The behavior of μ_e'/μ' is similar to that of $f(\theta,\varphi)$ shown in Fig.6.1, because the main factor determining μ_e'/μ' is $f(\theta,\varphi)$, as given in eq.(6.20). In particular, when $\tan\delta$ is very small, μ_e'/μ' is almost equal to $f(\theta,\varphi)$.

Figure 6.4 shows plots of μ_e''/μ'' versus θ for four values of $\tan\delta$. When $\tan\delta$ is very low, the second term on the right-hand side of eq.(6.23) is dominant over the first

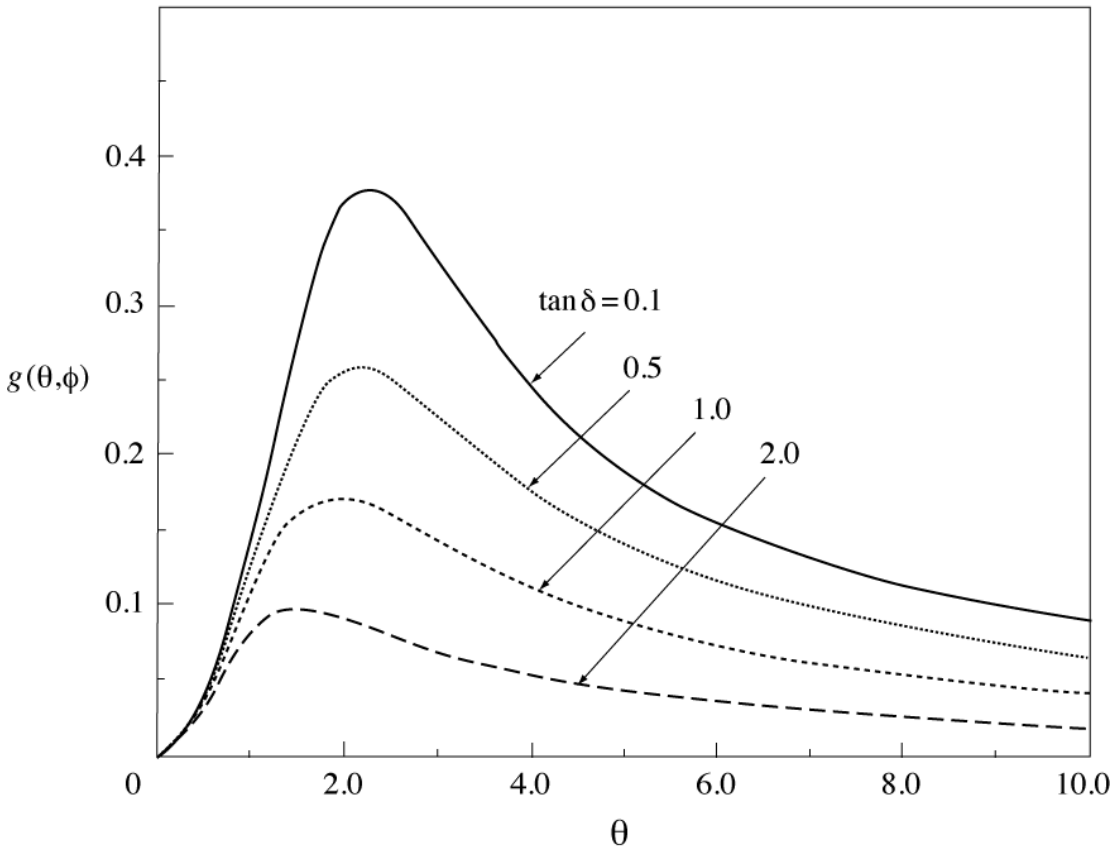

Figure 6.2 $g(\theta,\varphi)$ obtained from eq.(6.10) versus θ for four values of $\tan\delta$. $g(\theta,\varphi)$ is proportional to the average imaginary part of the magnetic field inside the sheet.

term, and consequently, the dependence of μ_e''/μ'' is nearly the same as that of $g(\theta,\varphi)$. We can also see this feature by comparing Fig. 6.4 with Fig. 6.2 for the case of $\tan\delta = 0.1$. As $\tan\delta$ increases from a very low value, the influence of $g(\theta,\varphi)$ gradually decreases and instead $f(\theta,\varphi)$ becomes the dominant factor determining μ_e''/μ''.

We assume in all of the numerical examples that the intrinsic $\tan\delta$ is independent of θ, although it is generally a function of θ or frequency f as discussed in Chapter 5. Because of this assumption, the behaviors of $f(\theta,\varphi)$, $g(\theta,\varphi)$, μ_e'/μ', and μ_e''/μ'' described above are solely attributed to the effect of eddy currents. However, since the analyses given in this paper do not rule out variations in $\tan\delta$, if the frequency response of $\tan\delta$ is known and included in the calculations, we can obtain more a realistic θ dependence of these variables.

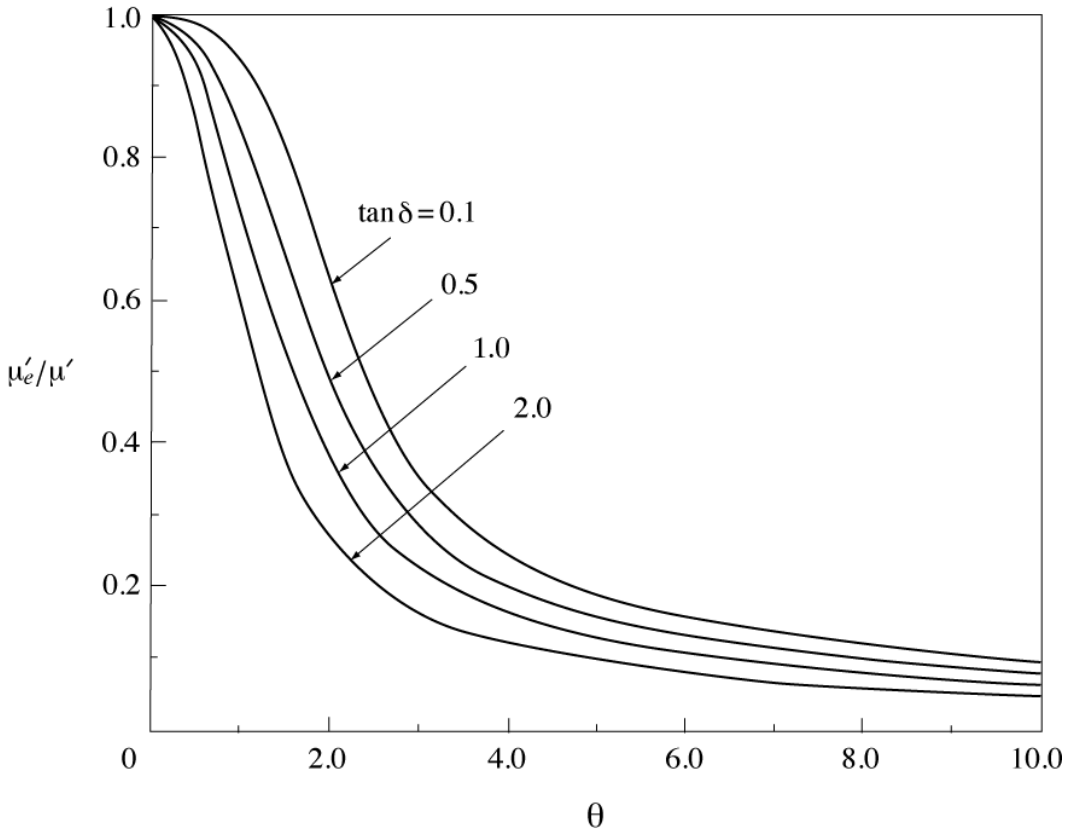

Figure 6.3 μ_e'/μ' obtained from eq.(6.20) versus θ for four values of $\tan\delta$.

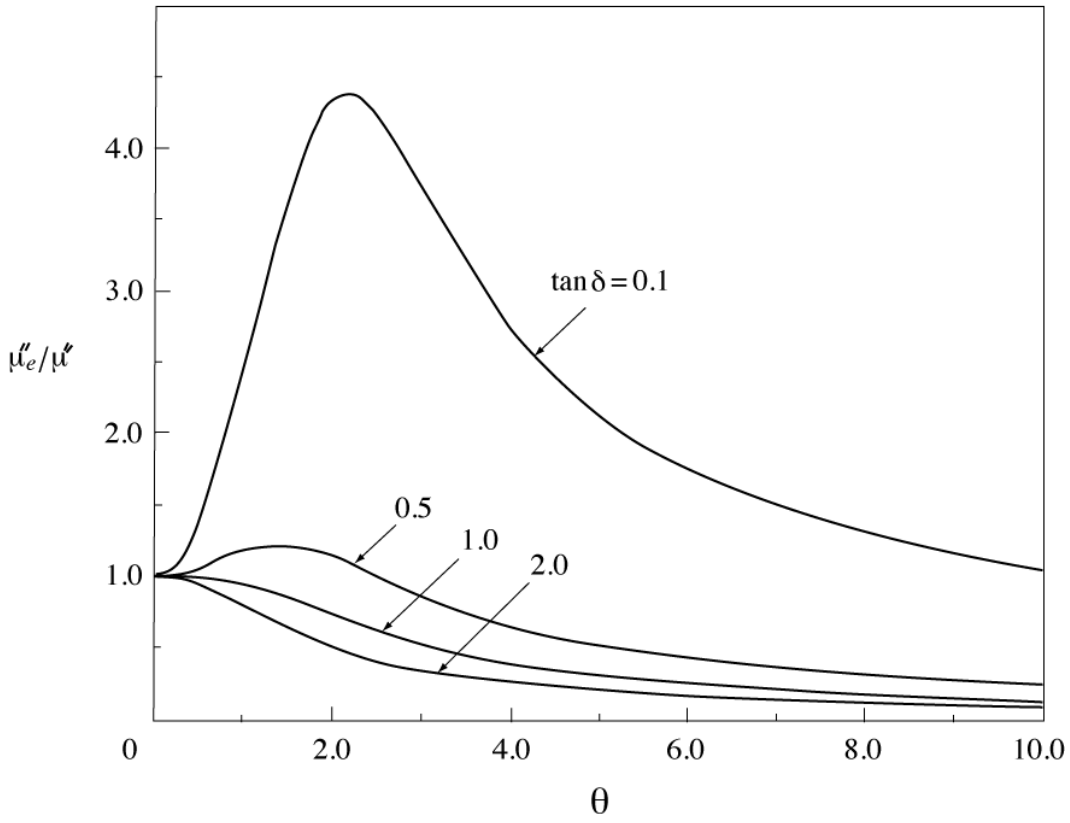

Figure 6.4 μ_e''/μ'' obtained from eq.(6.23) versus θ for four values of $\tan\delta$.

7. RF Properties of Magnetic Sheet

7.1 Introduction

In Chapter 3, we obtained the approximate expressions for the AC magnetic properties of the sheet, which are useful in low-frequency applications. We found in Chapter 4 that as the frequency of the applied magnetic field increases, the induced eddy currents become increasingly influential in changing the distribution of the magnetic field in the interior of the sheet. The change in the field distribution results in a change in the effective permeability as shown in Chapter 6. As a natural consequence, it also causes a change in other magnetic properties of the sheet. In this chapter, we derive the accurate expressions of the stored magnetic energy, overall magnetic loss, eddy-current loss, hysteresis loss, and Q-value of the sheet by fully utilizing the field distributions obtained in Chapter 4 and its integrations given in Chapter 6. The obtained expressions are useful for estimating AC properties of magnetic sheets used in applications in a wide frequency range from very low to RF frequencies.

7.2 Stored Magnetic Energy

The applied magnetic field $\mathbf{H}_{z0}$ is given by

$$\mathbf{H}_{z0} = H_0 e^{j\omega t}. \tag{7.1}$$

The average density of the stored magnetic energy W of the sheet, when it is placed in the magnetic field $\mathbf{H}_{z0}$ is given in eq. (3.10) and is written here again:

$$W = \frac{1}{2V} \int_V \mathrm{Re}\left[\mathbf{H}_{z0}^* \mathbf{B}_z\right] dv, \tag{7.2}$$

where $\mathbf{B}_z$ is the magnetic flux density within the sheet.

Making use of the real and imaginary parts of the field Re[$\mathbf{H}_z$] and Im[$\mathbf{H}_z$], respectively, given in eqs. (4.29) and (4.30), together with the intrinsic permeability μ ($=\mu' - j\mu''$), we can write $\mathbf{B}_z$ as

$$\begin{aligned}\mathbf{B}_z &= \mu \mathbf{H}_z = \left(\mu' - j\,\mu''\right)\left\{\mathrm{Re}\left[\mathbf{H}_z\right] + j\,\mathrm{Im}\left[\mathbf{H}_z\right]\right\} e^{j\omega t} \\ &= \left\{\left[\mu'\,\mathrm{Re}\left[\mathbf{H}_z\right] + \mu''\,\mathrm{Im}\left[\mathbf{H}_z\right]\right] + j\left[\mu'\,\mathrm{Im}\left[\mathbf{H}_z\right] - \mu''\,\mathrm{Re}\left[\mathbf{H}_z\right]\right]\right\} e^{j\omega t}. \end{aligned} \tag{7.3}$$

It follows from $\mathbf{H}_{z0}$ in eq. (7.1) and $\mathbf{B}_z$ in eq. (7.3) that the real part of $\mathbf{H}_{z0}^* \mathbf{B}_z$ is given by

$$\mathrm{Re}\left[\mathbf{H}_{z0}^* \mathbf{B}_z\right] = H_0 \left\{\mu'\,\mathrm{Re}\left[\mathbf{H}_z\right] + \mu''\,\mathrm{Im}\left[\mathbf{H}_z\right]\right\}, \tag{7.4}$$

where the time factors $e^{j\omega t}$ in $\mathbf{B}_z$ and $e^{-j\omega t}$ in $\mathbf{H}_{z0}^*$ cancel each other out. Substituting eq. (7.4) into eq. (7.2) leads to

$$W = \frac{H_0}{2V}\left[\mu' \int_V \mathrm{Re}\left[\mathbf{H}_z\right] dv + \mu'' \int_V \mathrm{Im}\left[\mathbf{H}_z\right] dv\right]. \tag{7.5}$$

The surface integrals of Re[$\mathbf{H}_z$] and Im[$\mathbf{H}_z$] extended over the cross section of the sheet $l_0 \times d$ shown in Fig. 3.2 were performed in Chapter 6 and the results are given in eqs. (6.4) and (6.9). The volume integrals over the rectangular parallelepiped shown in Fig. 3.2 give the same expressions, because $\mathbf{H}_z$ does not change in the z direction and the length of the side in the z direction is the unit length. Then, substituting eqs. (6.4) and (6.9) into eq. (7.5), we have

$$W = \frac{1}{2} H_0^2 \left[\mu' f(\theta,\phi) - \mu'' g(\theta,\phi)\right]. \tag{7.6}$$

The expression inside the brackets is equal to the real part of the effective permeability μ_e' given in eq. (6.19). Thus, we finally obtain the simple and expected result:

$$W = \frac{1}{2} \mu_e' H_0^2. \tag{7.7}$$

If the magnetic field is applied at a very low frequency such that $f(\theta,\varphi)$ is nearly equal to 1.0 and $g(\theta,\varphi)$ is nearly equal to zero (see Figs. 6.1 and 6.2), W reduces to

$$W_0 = \frac{1}{2} \mu' H_0^2, \tag{7.8}$$

which is consistent with eq. (3.17) in Chapter 3. From eqs. (7.7), (7.8), and (6.20), the ratio of W to W_0 is

$$\frac{W}{W_0} = \frac{\mu_e'}{\mu'} = f(\theta,\phi) - g(\theta,\phi)\tan\delta. \tag{7.9}$$

7.3 Overall Magnetic Loss

The time-averaged overall magnetic loss per unit volume, P_m, of the sheet placed in the magnetic field $\mathbf{H}_{z0}$ is given by eq. (3.19), which is written as

$$P_m = \frac{1}{2V} \int_V \mathrm{Re}\left[\mathbf{H}_{z0}^* \frac{\partial \mathbf{B}_z}{\partial t}\right] dv. \tag{7.10}$$

From $\mathbf{B}_z$ in eq. (7.3), $\partial \mathbf{B}_z / \partial t$ can be expressed by

$$\frac{\partial \mathbf{B}_z}{\partial t} = \omega \left\{ \left[\mu'' \operatorname{Re}\left[\mathbf{H}_z\right] - \mu' \operatorname{Im}\left[\mathbf{H}_z\right] \right] + j \left[\mu' \operatorname{Re}\left[\mathbf{H}_z\right] + \mu'' \operatorname{Im}\left[\mathbf{H}_z\right] \right] \right\} e^{j\omega t}. \tag{7.11}$$

Using $\mathbf{H}_{z0}$ from eq. (7.1) and $\partial \mathbf{B}_z / \partial t$ from eq. (7.11), we have

$$\operatorname{Re}\left[\mathbf{H}_{z0}^{*} \frac{\partial \mathbf{B}_z}{\partial t} \right] = \omega H_0 \left\{ \mu'' \operatorname{Re}\left[\mathbf{H}_z\right] - \mu' \operatorname{Im}\left[\mathbf{H}_z\right] \right\}. \tag{7.12}$$

Substituting eq. (7.12) into eq. (7.10) leads to

$$P_m = \frac{\omega H_0}{2V} \left[\mu'' \int_V \operatorname{Re}\left[\mathbf{H}_z\right] dv - \mu' \int_V \operatorname{Im}\left[\mathbf{H}_z\right] dv \right]. \tag{7.13}$$

In the same manner that eq. (7.6) was obtained, substituting the integrations of $\operatorname{Re}[\mathbf{H}_z]$ and $\operatorname{Im}[\mathbf{H}_z]$ from eqs. (6.4) and (6.9) into eq. (7.13) yields

$$P_m = \frac{\omega H_0^2}{2} \left[\mu'' f(\theta, \phi) + \mu' g(\theta, \phi) \right]. \tag{7.14}$$

We see that the expression inside the brackets in eq. (7.14) is the imaginary part of the effective permeability μ_e'' given in eq. (6.22). Thus, P_m is also expressed by

$$P_m = \frac{1}{2} \omega \mu_e'' H_0^2. \tag{7.15}$$

This is the simple and expected expression of the overall magnetic loss.

For very low frequencies, P_m reduces to

$$P_{m0} = \frac{1}{2} \omega \mu'' H_0^2, \tag{7.16}$$

which is identical to eq. (3.23) in Chapter 3. Then, P_m normalized by P_{m0} is given by

$$\frac{P_m}{P_{m0}} = \frac{\mu_e''}{\mu''} = f(\theta, \phi) + g(\theta, \phi) \frac{1}{\tan \delta}. \tag{7.17}$$

The overall magnetic loss per cycle per unit volume, $P_{m,c}$, is given by eq. (2.16). Since we already have P_m from eq. (7.15), instead of using eq. (2.16), we can readily obtain $P_{m,c}$ from P_m by dividing it by the frequency f:

$$P_{m,c} = \pi \mu_e'' H_0^2. \tag{7.18}$$

7.4 Eddy-Current Loss

7.4.1 Distribution of Electric Field and Current Density

Time-averaged eddy-current loss per unit volume of the sheet P_{ed} is given by eq. (3.26), which is written as

$$P_{ed} = \frac{1}{2V}\int_V \mathrm{Re}\left[\mathbf{J}_x^* \mathbf{E}_x\right] dv, \tag{7.19}$$

where $\mathbf{J}_x$ is the electric current density and $\mathbf{E}_x$ is the electric field intensity in the x direction. In the present model, these are the only current and field components that can exist within the sheet. If we know the distribution of $\mathbf{J}_x$ and $\mathbf{E}_x$ along the y axis (see Fig. 3.3), we can derive the expression of the eddy-current loss from eq. (7.19). Since we already know the distribution of $\mathbf{B}_z$, we can obtain the distribution of $\mathbf{J}_x$ and $\mathbf{E}_x$ from Faraday's law, in which $\mathbf{E}_x$ has a close relationship with $\mathbf{B}_z$, as given below.

Faraday's law, which states the relationship between the time rate of change in magnetic flux and the induced voltage, is given by

$$\oint_c \mathbf{E}_x \cdot d\mathbf{s} = -\int_S \frac{\partial \mathbf{B}_z}{\partial t} \cdot d\mathbf{a}. \tag{7.20}$$

We perform the closed line integral along the path c, shown in Fig. 3.3, and the surface integral over the area S $(=2y_0 l_0)$ enclosed by path c. Since the sheet extends infinitely in the x direction, $\mathbf{E}_x$ at $y=y_0$ is independent of position x, and $\mathbf{E}_y=0$ at every point over the cross section. Then, the left-hand side of eq. (7.20) becomes

$$\oint_c \mathbf{E}_x \cdot d\mathbf{s} = 2\, l_0 \mathbf{E}_x. \tag{7.21}$$

Next, using $\partial \mathbf{B}_z/\partial t$ from eq. (7.11), we write the right-hand side of eq. (7.20) as

$$-\int_S \frac{\partial \mathbf{B}_z}{\partial t} \cdot d\mathbf{a} = -2\, l_0\, \omega \times \int_0^{y_0} \left\{ \left[\mu'' \mathrm{Re}\left[\mathbf{H}_z\right] - \mu' \mathrm{Im}\left[\mathbf{H}_z\right]\right] + j\left[\mu' \mathrm{Re}\left[\mathbf{H}_z\right] + \mu'' \mathrm{Im}\left[\mathbf{H}_z\right]\right] \right\} dy\, e^{j\omega t}. \tag{7.22}$$

Substituting eqs. (7.21) and (7.22) into eq. (7.20) leads to the following expression of the electric field $\mathbf{E}_x$, induced at $y=y_0$:

$$\mathbf{E}_x = -\omega \int_0^{y_0} \left\{ \left[\mu'' \mathrm{Re}\left[\mathbf{H}_z\right] - \mu' \mathrm{Im}\left[\mathbf{H}_z\right]\right] + j\left[\mu' \mathrm{Re}\left[\mathbf{H}_z\right] + \mu'' \mathrm{Im}\left[\mathbf{H}_z\right]\right] \right\} dy\, e^{j\omega t}. \tag{7.23}$$

The integrations of $\mathrm{Re}[\mathbf{H}_z]$ and $\mathrm{Im}[\mathbf{H}_z]$ are performed along the y axis from 0 to y_0

with the result being

$$\mathbf{E}_x = \frac{\omega H_0 d}{\sqrt{2}\,\alpha^{1/4}\theta\left[\cosh(2a_2)+\cos(2b_2)\right]}\left(R + jI\right)e^{j\omega t}, \tag{7.24}$$

where R and I denote the expressions given in Appendix D.

7.4.2 Eddy-Current Loss Calculations

The current density $\mathbf{J}_x$ induced by $\mathbf{E}_x$ is given by

$$\mathbf{J}_x = \sigma\,\mathbf{E}_x = \frac{1}{\rho}\mathbf{E}_x. \tag{7.25}$$

Substituting eq. (7.25) into eq. (7.19) gives

$$P_{ed} = \frac{1}{2\rho V}\int_V \left|\mathbf{E}_x\right|^2 dv. \tag{7.26}$$

From eq. (7.24), we can write

$$\begin{aligned}\left|\mathbf{E}_x\right|^2 &= \mathbf{E}_x^*\,\mathbf{E}_x \\ &= \frac{\omega^2 H_0^2 d^2}{2\,\alpha^{1/2}\theta^2\left[\cosh(2a_2)+\cos(2b_2)\right]^2}\left(R^2 + I^2\right).\end{aligned} \tag{7.27}$$

After various calculations to reduce $|\mathbf{E}_x|^2$ to a simpler form, we obtain

$$\left|\mathbf{E}_x\right|^2 = \frac{\omega^2 H_0^2 d^2 \mu'^2 \alpha^{1/2}}{2\theta^2\left[\cosh(2a_2)+\cos(2b_2)\right]}\left[\cosh\left(2a_1 y_0\right) - \cos\left(2b_1 y_0\right)\right]. \tag{7.28}$$

If $\tan\delta$ is very small, eq. (7.28) can be approximated by

$$\left|\mathbf{E}_x\right|^2 = \frac{\omega^2 H_0^2 d^2 \mu'^2}{2\theta^2\left[\cosh(\theta)+\cos(\theta)\right]}\left[\cosh\left(\frac{2\theta}{d}y_0\right) - \cos\left(\frac{2\theta}{d}y_0\right)\right]. \tag{7.29}$$

Substituting $|\mathbf{E}_x|^2$ from eq. (7.28) into eq. (7.26) leads to

$$P_{ed} = \frac{\omega^2 H_0^2 d\,\mu'^2 \alpha^{1/2}}{2\theta^2\rho\left[\cosh(2a_2)+\cos(2b_2)\right]}\int_0^{\frac{d}{2}}\left[\cosh\left(2a_1 y\right) - \cos\left(2b_1 y\right)\right]dy, \tag{7.30}$$

where a volume integral over the rectangular parallelepiped shown in Fig. 3.2 is reduced to a single integral with respect to y because $\mathbf{E}_x$ varies only in the y direction. From the beginning of this section to eq. (7.29), the symbol y_0 has been used to denote a fixed position at which the expression of $\mathbf{E}_x$ is derived. However, in eq. (7.30) it is now used as an integral variable and the symbol is changed accordingly from y_0 to y. The integration in eq. (7.30) is performed to give

$$P_{ed} = \frac{\omega^2 H_0^2 d^2 \mu'^2 \alpha^{1/4}}{2\sqrt{2}\,\theta^3 \rho \sin(2\phi)} \frac{\sin(\phi)\sinh(2a_2) - \cos(\phi)\sin(2b_2)}{\cosh(2a_2) + \cos(2b_2)}. \tag{7.31}$$

By using $g(\theta,\varphi)$ from eq. (6.10), the following expression of P_{ed} is obtained:

$$P_{ed} = \frac{\omega^2 H_0^2 d^2 \mu'^2 \alpha^{1/2}}{4\,\theta^2 \rho \sin(2\phi)} g(\theta,\phi). \tag{7.32}$$

Equation (7.32) shows that $g(\theta,\varphi)$, which is proportional to the average imaginary part of the field as given in eq. (6.12), is the important factor determining P_{ed}. Equation (7.32) should be the generalized expression of eq. (3.39) obtained in Chapter 3. We can easily show that if we expand $g(\theta,\varphi)$ into a power series of θ and take only the lowest term of θ, eq. (7.32) reduces to eq. (3.39).

Equation (7.32) can be expressed in a simpler form by using θ from eq. (3.4) and δ_s from eq. (3.5):

$$P_{ed} = \frac{1}{2} \omega H_0^2 \alpha \mu' g(\theta,\phi). \tag{7.33}$$

This can also be rewritten as

$$P_{ed} = \frac{1}{2} \omega \mu'' H_0^2 \frac{\alpha}{\tan\delta} g(\theta,\phi). \tag{7.34}$$

It follows from eqs. (7.16) and (7.34) that the ratio of P_{ed} to P_{m0} is given by

$$\frac{P_{ed}}{P_{m0}} = \frac{\alpha}{\tan\delta} g(\theta,\phi) = \left(\frac{1}{\tan\delta} + \tan\delta\right) g(\theta,\phi). \tag{7.35}$$

In this paper, we assume the magnetization of the sheet is microscopic and distributed homogeneously as mentioned in Section 4.2. The expressions of eddy-current loss given above are derived on the basis of this assumption, which allows us to apply the classical electromagnetic theory. The loss calculated by this approach is sometimes referred to as the *classical eddy-current loss*. It has been reported that materials whose magnetization process is determined by domain wall displacements

exhibit much higher eddy-current losses (typically two to three times as high as the classical eddy-current loss) due to the so-called *anomalous eddy-current contribution* [89][91][92] [95]. The reason for this large loss is that the change in magnetization due to eddy currents is not uniform inside domains but is concentrated near the domain walls [118][119][120][121]. Essentially, the magnetic response of the material away from the domain wall is very weak and almost all the flux change is concentrated in the narrow region of inhomogeneous magnetization that defines the wall.

7.5 Hysteresis Loss

Time-averaged hysteresis loss per unit volume, P_h, of the sheet placed in the magnetic field $\mathbf{H}_{z0}$ is given by

$$P_h = \frac{1}{2V}\int_V \mathrm{Re}\left[\mathbf{H}_z^* \frac{\partial \mathbf{B}_z}{\partial t}\right] dv, \tag{7.36}$$

where $\mathbf{H}_z$ and $\mathbf{B}_z$ are the magnetic field intensity and the magnetic flux density within the sheet. It follows from $\mathbf{H}_z$ given in eq. (4.28) and $\partial\mathbf{B}_z/\partial t$ in eq. (7.11) that the real part of $\mathbf{H}_z^*(\partial\mathbf{B}_z/\partial t)$ is written as

$$\mathrm{Re}\left[\mathbf{H}_z^* \frac{\partial \mathbf{B}_z}{\partial t}\right] = \omega\mu''\left\{\mathrm{Re}^2\left[\mathbf{H}_z\right] + \mathrm{Im}^2\left[\mathbf{H}_z\right]\right\} = \omega\mu''\left|\mathbf{H}_z\right|^2, \tag{7.37}$$

where $|\mathbf{H}_z|$ is the amplitude of the field given in eq. (4.24). Replacing $\mathrm{Re}[\mathbf{H}_z^*(\partial\mathbf{B}_z/\partial t)]$ in eq. (7.36) with eq. (7.37) leads to

$$P_h = \frac{\omega\mu'' H_0^2}{d}\int_0^{\frac{d}{2}} \frac{\cosh(2a_1 y)+\cos(2b_1 y)}{\cosh(2a_2)+\cos(2b_2)}\, dy, \tag{7.38}$$

where the volume V is replaced with $l_0 \times d \times 1$ (see Fig. 3.2), and the volume integral is reduced to a single integral with respect to y. Performing the integration yields

$$P_h = \frac{\omega\mu'' H_0^2}{\sqrt{2}\,\alpha^{1/4}\theta\,\sin(2\phi)} \frac{\sinh(2a_2)\sin(\phi) + \sin(2b_2)\cos(\phi)}{\cosh(2a_2)+\cos(2b_2)}. \tag{7.39}$$

After more calculations, this is expressed in a simpler form:

$$\begin{aligned} P_h &= \frac{\omega\mu'' H_0^2}{2\mu'}\left[\mu' f(\theta,\phi) - \mu'' g(\theta,\phi)\right] \\ &= \frac{1}{2}\omega\mu_e' H_0^2 \tan\delta. \end{aligned} \tag{7.40}$$

It can also be written as

$$P_h = W\,\omega \tan\delta, \tag{7.41}$$

where W is the stored magnetic energy per unit volume given in eq. (7.7). Note that P_h is proportional to W and $\tan\delta$. The hysteresis loss normalized by P_{m0} is

$$\frac{P_h}{P_{m0}} = \frac{\mu_e'}{\mu'}. \tag{7.42}$$

Comparing eq. (7.42) with eq. (7.9), we see that P_h/P_{m0} is identical to W/W_0.

7.6 Verification of $\mathbf{P}_{ed} + \mathbf{P}_h = \mathbf{P}_m$

Having obtained the expressions for the eddy-current loss P_{ed} and the hysteresis loss P_h, we are now ready to verify that the sum of P_{ed} and P_h equals the overall magnetic loss P_m. Before calculating the sum, we transform eq. (7.33) into a more suitable form for summation. The factor $\alpha\mu' g(\theta,\varphi)$ in eq. (7.33) can be rewritten in terms of μ_e', $\tan\delta_e$, and $\tan\delta$:

$$\begin{aligned}
\alpha\,\mu' g(\theta,\phi) &= \left(\mu' + \mu'' \tan\delta\right) g(\theta,\phi) \\
&= \mu' g(\theta,\phi) - \tan\delta\left[\mu_e' - \mu' f(\theta,\phi)\right] \\
&= \mu_e' \left(\tan\delta_e - \tan\delta\right),
\end{aligned} \tag{7.43}$$

with $$\tan\delta_e = \frac{\mu_e''}{\mu_e'} \quad \text{and} \quad \tan\delta = \frac{\mu''}{\mu'}, \tag{7.44}$$

where $\tan\delta_e$ is the effective loss factor of the sheet. This is the loss factor that we regularly use and can obtain by ordinary measurements of magnetic properties of the sheet. Using eq. (7.43), we can express eq. (7.33) by

$$P_{ed} = \frac{1}{2}\,\omega\,\mu_e' H_0^2 \left(\tan\delta_e - \tan\delta\right). \tag{7.45}$$

Then, the sum of P_h from eq. (7.40) and P_{ed} from eq. (7.45) is

$$\begin{aligned}
P_h + P_{ed} &= \frac{1}{2}\,\omega\,\mu_e' H_0^2 \tan\delta + \frac{1}{2}\,\omega\,\mu_e' H_0^2 \left(\tan\delta_e - \tan\delta\right) \\
&= \frac{1}{2}\,\omega\,\mu_e' H_0^2 \tan\delta_e = \frac{1}{2}\,\omega\,\mu_e'' H_0^2.
\end{aligned} \tag{7.46}$$

The result agrees exactly with the overall magnetic loss P_m given in eq. (7.15).

7.7 Relationships between P_m, P_h, and P_{ed}

The relationships between P_m, P_h, and P_{ed} can be derived from eqs. (7.15), (7.40), and (7.45). From eqs. (7.15) and (7.45), we obtain

$$\frac{P_{ed}}{P_m} = 1 - \frac{\tan\delta}{\tan\delta_e}. \tag{7.47}$$

Likewise, from eqs. (7.15) and (7.40), we have

$$\frac{P_h}{P_m} = \frac{\tan\delta}{\tan\delta_e}. \tag{7.48}$$

These two equations lead to the following natural consequence:

$$\frac{P_{ed}}{P_m} + \frac{P_h}{P_m} = 1. \tag{7.49}$$

The ratio of P_{ed} to P_h is given by

$$\frac{P_{ed}}{P_h} = \frac{\tan\delta_e}{\tan\delta} - 1. \tag{7.50}$$

7.8 Q-value

In the previous sections, we obtained expressions for the stored magnetic energy, the overall magnetic loss, the eddy-current loss, and the hysteresis loss. Making use of these expressions, we can readily obtain the Q-value of the magnetic sheet.

We obtain the overall Q-value Q_e by substituting the stored magnetic energy W from eq.(7.6) and the overall magnetic loss P_m from eq.(7.14) into the definition of the Q-value given by eq. (2.23):

$$\begin{aligned} Q_e &= \frac{\omega W}{P_m} \\ &= \frac{\mu' f(\theta,\phi) - \mu'' g(\theta,\phi)}{\mu'' f(\theta,\phi) + \mu' g(\theta,\phi)} = \frac{Q_0 f(\theta,\phi) - g(\theta,\phi)}{f(\theta,\phi) + Q_0 g(\theta,\phi)}, \end{aligned} \tag{7.51}$$

where Q_0 is the intrinsic Q-value given by μ'/μ''. The expression of Q_e can also be obtained by substituting W from eq. (7.7) and P_m from eq. (7.15) into eq. (2.23):

$$Q_e = \frac{\mu_e'}{\mu_e''} = \frac{1}{\tan\delta_e}. \tag{7.52}$$

This widely used definition of the Q-value of a magnetic object is given by the ratio of the real part of the effective permeability to the imaginary part and is equal to the reciprocal of the effective loss factor. The derivation of eq. (7.52) is based on the primary definition of the Q-value given in eq. (2.23), into which we introduce the derived expressions of the stored magnetic energy and the overall magnetic loss. Thus, we have demonstrated the validity of this popular definition of the Q-value using a very orthodox method.

Next, let Q_h be the Q-value defined by the hysteresis loss. It follows directly from W given in eq. (7.7) and P_h in eq. (7.40) that Q_h is given by

$$Q_h = \frac{\omega W}{P_h} = \frac{1}{\tan\delta} = Q_0. \tag{7.53}$$

Equation (7.53) is exactly equal to eq. (3.50) from Chapter 3, which was derived on the assumption that the field is applied at a low frequency. This result clearly shows that Q_h is determined solely by $\tan\delta$, in any frequency region, not only in low frequency regions. However, it should be noted that Q_h is not necessarily constant, because the intrinsic permeability is only constant when the frequency is considerably lower than a lowest dispersion region as described in Chapter 5.

Likewise, let Q_{ed} be the Q-value defined by the eddy-current loss. Then, using W and P_{ed} from eq. (7.45), we obtain

$$Q_{ed} = \frac{\omega W}{P_{ed}} = \frac{1}{\tan\delta_e - \tan\delta}. \tag{7.54}$$

The overall Q-value of the magnetic sheet is also obtained from eq. (2.26) as a combination of Q_h from eq. (7.53) and Q_{ed} from eq. (7.54):

$$\frac{1}{Q_e} = \frac{1}{Q_h} + \frac{1}{Q_{ed}} = \tan\delta_e. \tag{7.55}$$

This is consistent with the expression of Q_e given in eq. (7.52).

7.9 Low-Frequency Approximation

As discussed in Section 6.5, if the frequency of the applied magnetic field is fairly low, the effective permeability μ_e' and μ_e'' reduce to eqs. (6.26) and (6.27), respectively. They can also be written as

$$\mu_e' \simeq \mu' \left(1 - \frac{1}{3}\theta^2 \tan\delta\right), \tag{7.56}$$

and

$$\mu_e'' \simeq \mu'' \left[1 + \frac{1}{6}\theta^2 \left(\frac{1}{\tan\delta} - \tan\delta\right)\right]. \tag{7.57}$$

Using this low-frequency approximation of the effective permeability, we can reduce the accurate expressions obtained in this chapter to approximate forms that can be used only in low frequency regions.

Substituting μ_e' from eq. (7.56) into eq. (7.7) leads to the approximate form of the stored magnetic energy:

$$W \simeq \frac{1}{2}\mu' \left(1 - \frac{1}{3}\theta^2 \tan\delta\right) H_0^2. \tag{7.58}$$

Using eq. (7.15) and eq. (7.57), the approximate overall magnetic loss P_m is written as

$$P_m \simeq \frac{1}{2}\omega\mu'' \left[1 + \frac{1}{6}\theta^2 \left(\frac{1}{\tan\delta} - \tan\delta\right)\right] H_0^2. \tag{7.59}$$

By using the approximate forms of $g(\theta,\varphi)$ given in eq. (6.25) and μ_e' in eq. (7.56), we can reduce the eddy-current loss P_{ed} given in eq. (7.33) and the hysteresis loss P_h in eq. (7.40) to approximate forms:

$$P_{ed} \simeq \frac{1}{12}\omega\alpha\mu'\theta^2 H_0^2 = \frac{1}{12}\omega\mu''\theta^2 \left(\frac{1}{\tan\delta} + \tan\delta\right) H_0^2 \tag{7.60}$$

and

$$P_h \simeq \frac{1}{2}\omega\mu'' \left(1 - \frac{1}{3}\theta^2 \tan\delta\right) H_0^2. \tag{7.61}$$

Equations (7.56) and (7.57) are introduced into the first equation of eq. (7.52) to give the approximate form of Q_e:

$$Q_e \simeq \frac{1 - \frac{1}{3}\theta^2 \tan\delta}{\tan\delta + \frac{1}{6}\theta^2 \left(1 - \tan^2\delta\right)}. \tag{7.62}$$

We obtain the approximate Q_{ed} by substituting W from eq. (7.58) and P_{ed} from eq. (7.60) into eq. (2.25):

$$Q_{ed} \simeq \frac{6}{\theta^2\left(1+\tan^2\delta\right)}\left(1-\frac{1}{3}\theta^2\tan\delta\right). \tag{7.63}$$

Likewise, it follows from W and P_h given in eq. (7.61) that the approximate Q_h is given by

$$Q_h = \frac{\mu'}{\mu''} = \frac{1}{\tan\delta}. \tag{7.64}$$

All of the approximate expressions obtained above agree precisely with those given in Chapter 3, which were derived by assuming that the field was applied at a low frequency. This agreement is a necessary condition for the accuracy of the expressions obtained in this chapter and in Chapter 3.

7.10 Magnetic Properties as a Function of Frequency

The magnetic properties obtained in this chapter are expressed as a function of θ. We can rewrite these expressions in terms of the frequency f by using $F(f,\varphi)$ given in eq. (6.28) and $G(f,\varphi)$ in eq. (6.29). The results are as follow

$$W = \frac{1}{2}H_0^2\left[\mu' F(f,\phi) - \mu'' G(f,\phi)\right], \tag{7.65}$$

$$P_m = \frac{1}{2}\omega H_0^2\left[\mu'' F(f,\phi) + \mu' G(f,\phi)\right], \tag{7.66}$$

$$P_{ed} = \frac{1}{2}\omega H_0^2\,\alpha\mu' G(f,\phi), \tag{7.67}$$

$$P_h = \frac{1}{2}\omega H_0^2\tan\delta\left[\mu' F(f,\phi) - \mu'' G(f,\phi)\right], \tag{7.68}$$

and

$$Q_a = \frac{\mu' F(f,\phi) - \mu'' G(f,\phi)}{\mu'' F(f,\phi) + \mu' G(f,\phi)}. \tag{7.69}$$

7.11 Numerical Examples

Figure 7.1 shows the normalized stored energy W/W_0 as a function of θ for four values of $\tan\delta$. In Section 7.5, we found that W/W_0 is equal to P_h/P_{m0}, where P_h is the hysteresis loss and P_{m0} is the overall magnetic loss at a very low frequency. Both W/W_0 and P_h/P_{m0} are equivalent to μ_e'/μ', which is shown in the plots in Fig. 6.3. Chapter 6 shows that μ_e'/μ' is mainly dependent on $f(\theta,\varphi)$, which is proportional to the average real part of

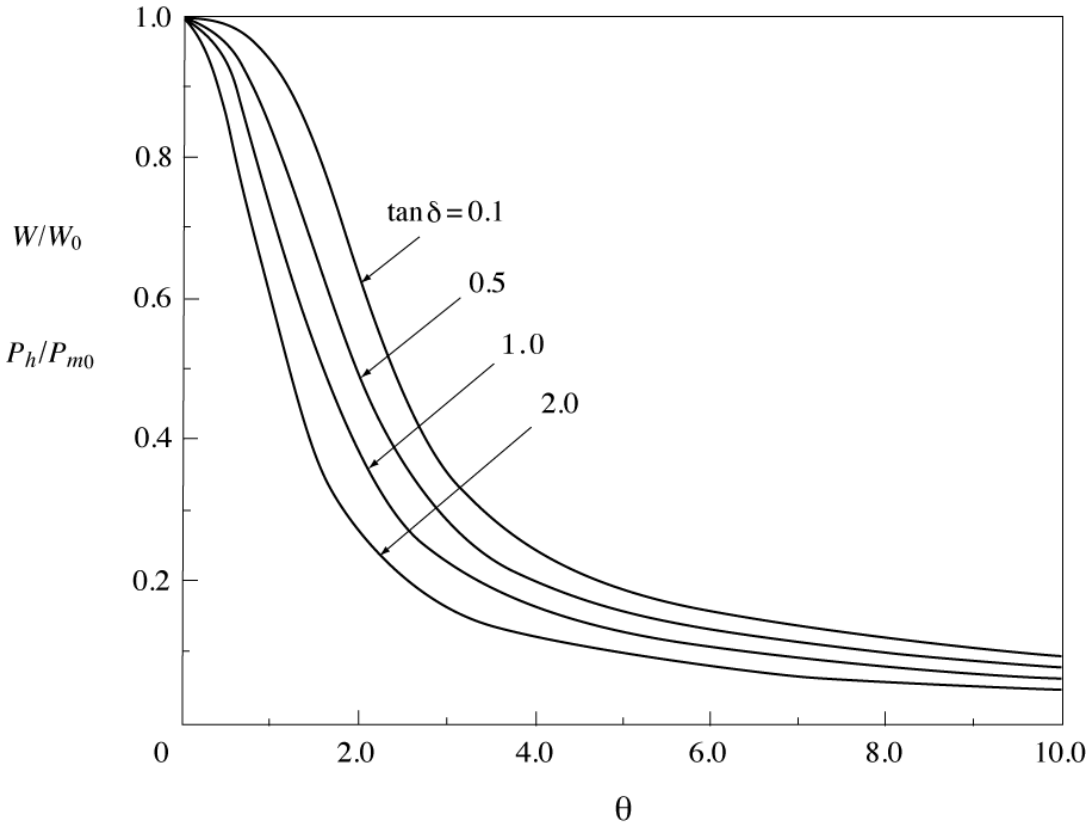

Figure 7.1 Normalized stored energy W/W_0 as a function of θ for four values of $\tan\delta$. W_0 is the stored energy at very low frequencies. W/W_0 is identical to P_h/P_{m0}, where P_h is the hysteresis loss and P_{m0} is the overall magnetic loss at very low frequencies. The curves are the same as those of μ_e'/μ' shown in Fig. 6.3.

the magnetic field, $[\mathrm{Re}[\mathbf{H}_z]]_{av}$. Therefore, the behaviors of W/W_0 and P_h/P_{m0} are closely related to the behavior of $[\mathrm{Re}[\mathbf{H}_z]]_{av}$.

Figure 7.2 illustrates the normalized eddy-current loss P_{ed}/P_{m0} as a function of θ for several values of $\tan\delta$. As θ increases from zero, the eddy-current loss increases slowly, reaches a maximum, and then gradually decreases thereafter. The curves are similar to those of the imaginary part of the field $\mathrm{Im}[\mathbf{H}_z]$ shown in Fig.4.6(b) and those of $g(\theta,\varphi)$ shown in Fig. 6.2. This is because the expression of P_{ed}/P_{m0} given in eq. (7.35) includes $g(\theta,\varphi)$, which is proportional to $[\mathrm{Im}[\mathbf{H}_z]]_{av}$, the average imaginary part of the field. From the discussion on $\mathrm{Im}[\mathbf{H}_z]$ in Subsection 4.8.2(b), the behavior of P_{ed}/P_{m0} in Fig. 7.2 can be explained from the two kinds of eddy-current effects: the amplitude diminution and the phase lag of the field.

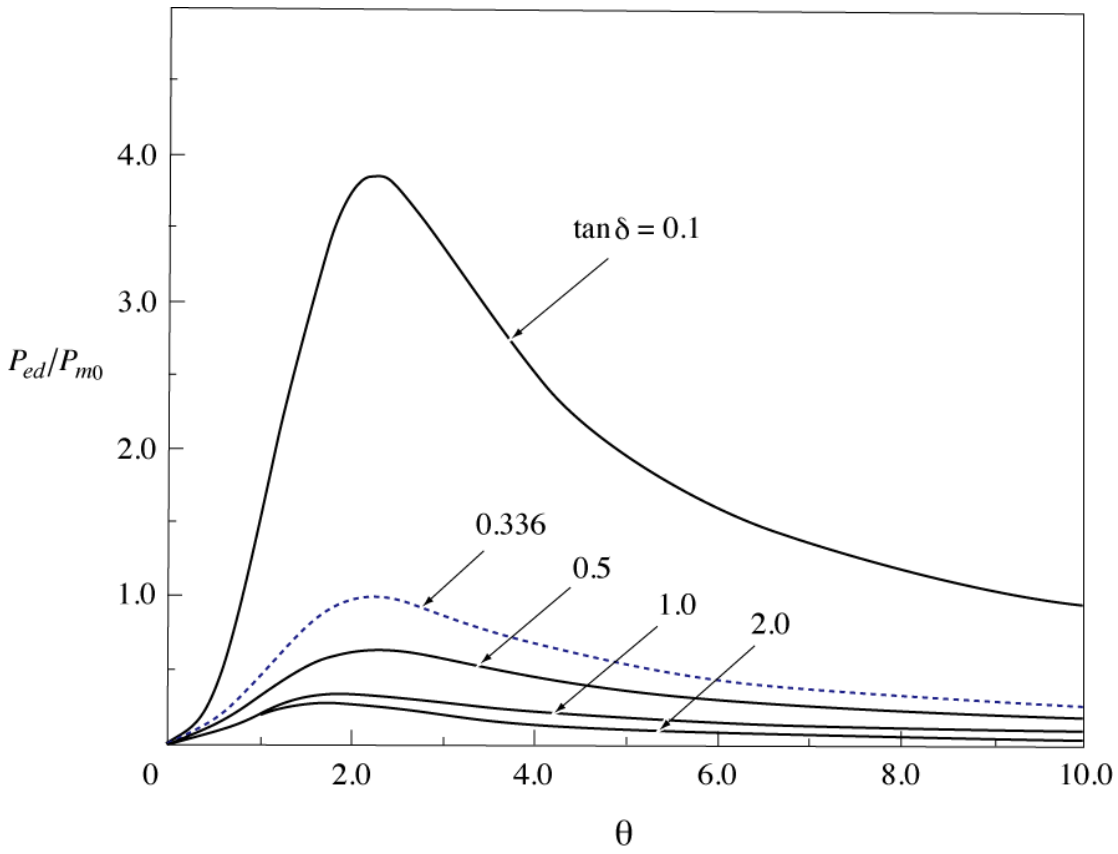

Figure 7.2 Normalized eddy-current loss P_{ed}/P_{m0} as a function of θ for five values of $\tan\delta$.

Fig. 7.2 shows that P_{ed}/P_{m0} is very large for $\tan\delta = 0.1$. This is because the expression of P_{ed}/P_{m0} includes a factor $1/\tan\delta$, which causes P_{ed}/P_{m0} to increase substantially when $\tan\delta$ is much lower than 1.0. The dotted line in Fig. 7.2 shows the case where the maximum value of P_{ed} is equal to P_{m0}, which occurs when $\tan\delta = 0.336$.

Figure 7.3 shows P_m/P_{m0} as a function of θ for four values of $\tan\delta$. As given in eq. (7.17), P_m/P_{m0} is identical to μ_e''/μ'', whose plots have already been shown in Fig. 6.4. Since $P_m = P_h + P_{ed}$, the plots shown in Fig. 7.3 are combinations of the plots of P_h/P_{m0} shown in Fig. 7.1 and the plots of P_{ed}/P_{m0} shown in Fig. 7.2.

Figure 7.4 shows Q_e/Q_0 as a function of θ for four values of $\tan\delta$. It follows from eqs. (7.52) and (7.53) that $Q_e/Q_0 = \tan\delta/\tan\delta_e$. This ratio is equivalent to the ratio of the hysteresis loss to the overall magnetic loss P_h/P_m given in eq. (7.48). Referring to eqs. (7.47), (7.48), and (7.49), we can see that the portion under the curve in Fig. 7.4 is P_h/P_m and the portion above the curve corresponds to P_{ed}/P_m.

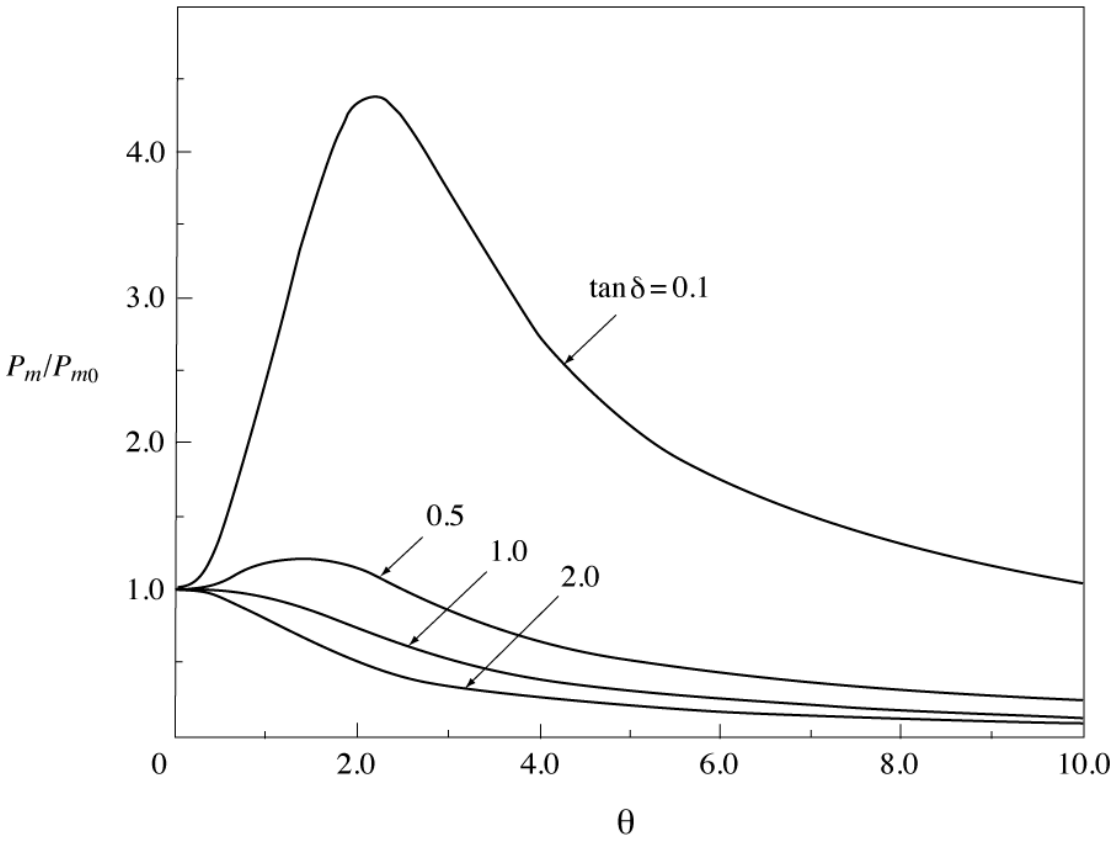

Figure 7.3 Normalized overall magnetic loss P_m/P_{m0} as a function of θ for four values of $\tan\delta$. Curves are identical to those of μ_e''/μ'' shown in Fig. 6.4.

As shown in Fig. 7.4, Q_e/Q_0 is nearly constant in the region where θ is larger than approximately 4.0. This is explained by the behavior of μ_e' and μ_e'' because Q_e/Q_0 is also expressed by $(\mu_e'/\mu_e'')\tan\delta$ and $\tan\delta$ is assumed to be constant. Equations (6.19) and (6.22) show that for values of θ larger than approximately 4.0, the ratio μ_e'/μ_e'' is almost independent of θ and depends only on μ' and μ''.

Figure 7.5 shows $\tan\delta_e/\tan\delta$ as a function of θ for four values of $\tan\delta$. It is obvious from eqs. (7.52) and (7.53) that $\tan\delta_e/\tan\delta$ in Fig. 7.5 is just the reciprocal of Q_e/Q_0 shown in Fig. 7.4.

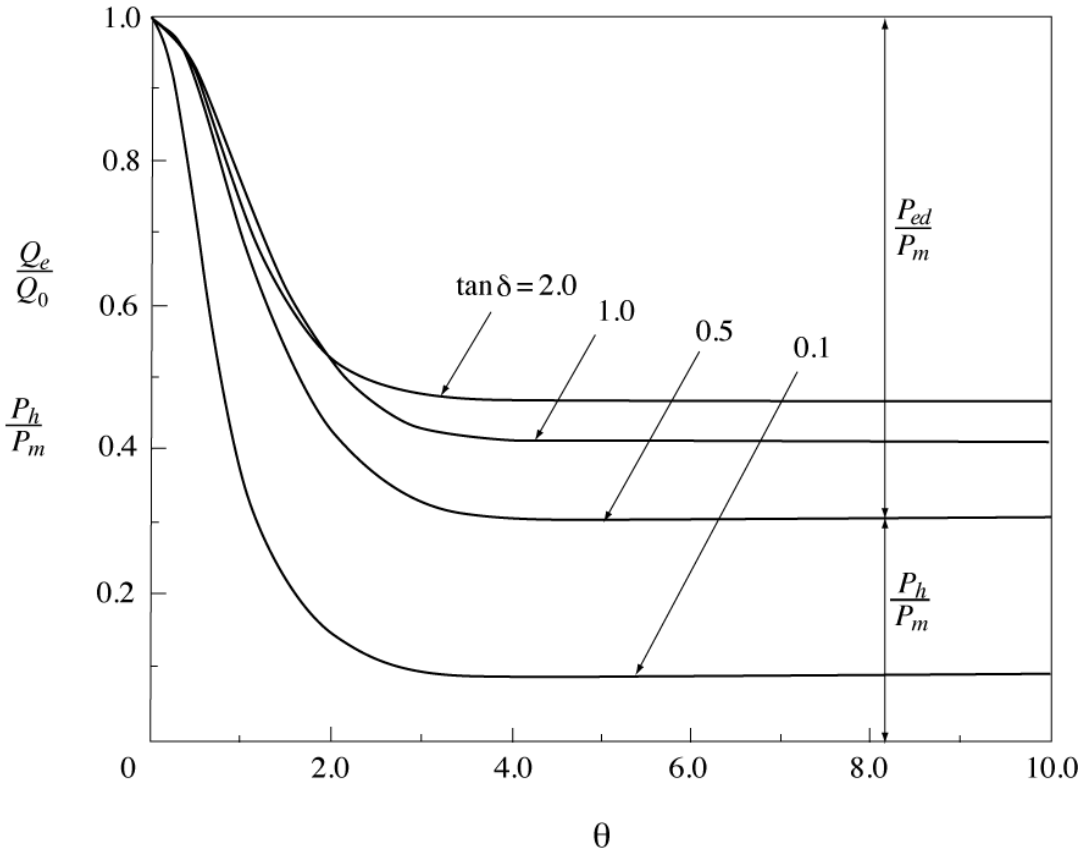

Figure 7.4 Ratio of overall Q-value to intrinsic Q-value Q_e/Q_0 as a function of θ for four values of $\tan\delta$. Q_e/Q_0 is identical to P_h/P_m.

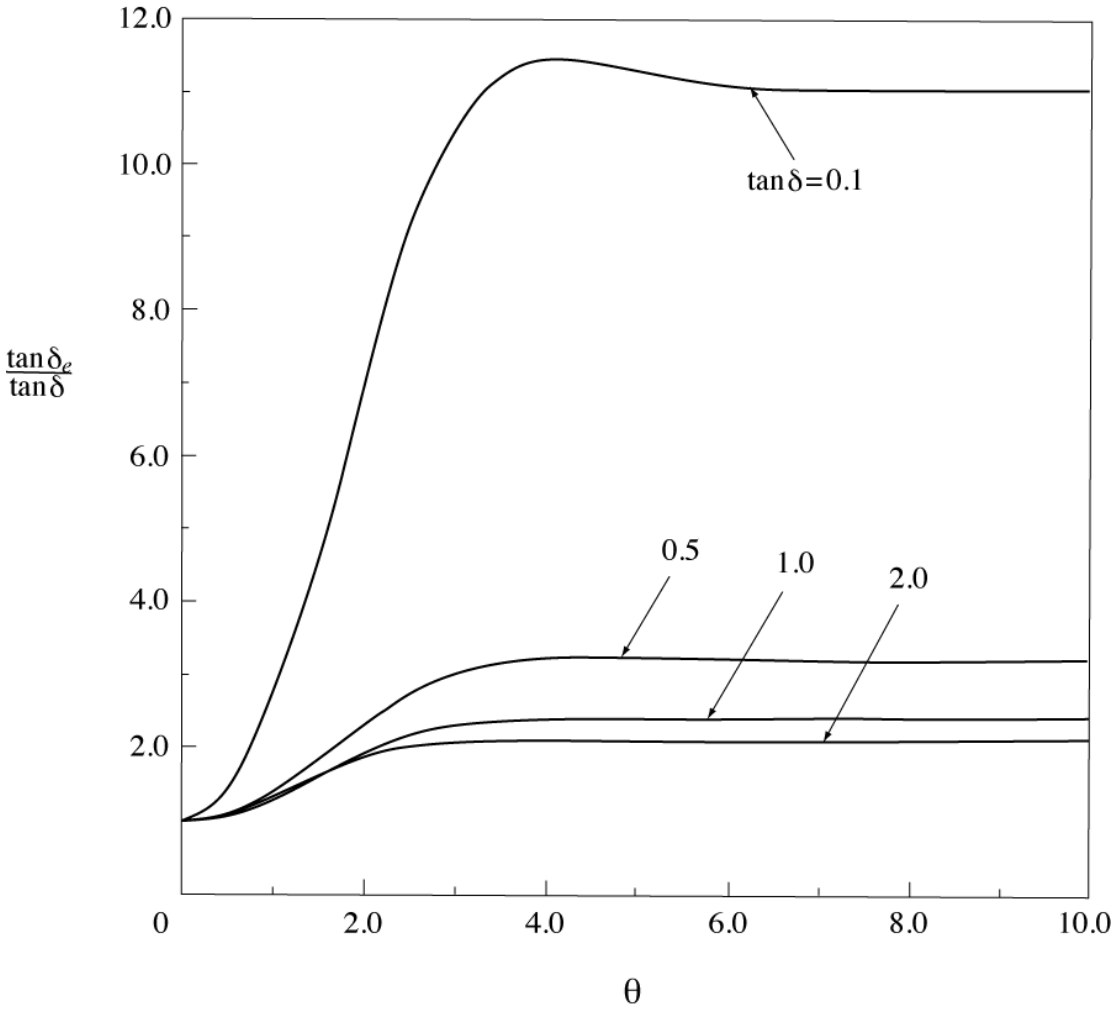

Figure 7.5 Ratio of effective loss factor to intrinsic loss factor $\tan\delta_e/\tan\delta$ as a function of θ for four values of $\tan\delta$. $\tan\delta_e/\tan\delta$ is the reciprocal of Q_e/Q_0.

8. Summary

RF properties of plane magnetic sheet made of lossy material, such as magnetic alloys, were analyzed on the assumption that the sheet is infinitely wide and placed in a uniform magnetic field applied parallel to its surface. Complex permeability and nonzero conductivity were used in the calculations. The following is a summary of our findings.

(1) Field Distribution within the Sheet

Maxwell's equations were used to derive the distribution of the magnetic field within the sheet. Numerical examples showed the distribution's dependence on frequency, thickness, and material constants. The following points apply to the field distribution:

- As the depth under the sheet surface Y increases, the field amplitude diminishes and the phase of the field lags behind the phase at the surface. The field diminishes more and the phase lags more as θ increases, where $\theta = d/\delta_s$ with d being the thickness of the sheet and δ_s, the commonly used skin depth. Hence, θ is proportional to the square root of the frequency.
- When the intrinsic loss factor $\tan\delta$ is higher, the amplitude diminishes more rapidly as Y or θ increases, whereas the phase lags more slowly. The effect of $\tan\delta$ on the amplitude behavior is obvious and the phase behavior can be explained from the way in which the magnitude of the real and imaginary parts of the field vary as Y or θ changes.
- In regions in which $\theta \gg 1$, the field amplitude can be expressed in an approximate form, from which an expression of the skin depth for magnetic sheet can be derived. This definition includes $\tan\delta$, as well as the frequency and conductivity, and consequently is applicable to all magnetic sheets.

(2) Effective Permeability

The complex effective permeability, which characterizes the macroscopic magnetic properties of the sheet, was derived by integrating and then averaging the complex magnetic field over the cross section of the sheet. The following points apply to the effective permeability:

- The average magnetic field within the sheet is proportional to $(f(\theta,\varphi) - jg(\theta,\varphi))$ in which φ is a function of $\tan\delta$. $f(\theta,\varphi)$ and $g(\theta,\varphi)$ are important parameters determining the effective permeability and other magnetic properties of the sheet.
- As θ increases, the real part of the effective permeability μ_e' monotonically decreases, whereas the imaginary part μ_e'' increases at the beginning, reaches a

broad maximum, and then decreases thereafter.

- Both the real and imaginary parts of the effective permeability decrease as $\tan\delta$ increases.

(3) RF Magnetic Properties

The expressions of RF magnetic properties, such as the stored magnetic energy, the magnetic loss, and the Q-value, were derived using the magnetic field distribution within the sheet. The following points apply to the RF magnetic properties:

- The overall magnetic loss is assumed to be composed of the hysteresis loss and the eddy-current loss.
- The hysteresis loss is proportional to $\mu_e' \tan\delta$ and the eddy-current loss is proportional to $(\mu_e'' - \mu_e' \tan\delta)$. This leads to the natural consequence that the overall magnetic loss given by the sum of these two kinds of losses is proportional to μ_e''.
- The above expressions indicate that the hysteresis loss behaves in exactly the same way as μ_e' when θ changes, while the θ dependence of the eddy-current loss is almost equal to that of μ_e'' if $\tan\delta$ is fairly low, as is usually the case for magnetic alloy cavity applications.
- The widely used relationship $Q_e = 1/\tan\delta_e$, where Q_e and $\tan\delta_e$ are the effective Q-value and loss factor of the sheet, respectively, was verified by using a very orthodox method. This method used the primary definition of the Q-value $Q = \omega W/P_m$, where ω is the angular frequency; W, the stored energy; and P_m, the power dissipation.
- The Q-value defined by the hysteresis loss, Q_h, is independent of θ, or the frequency, and is equal to Q_0, the intrinsic Q-value of sheet.

(4) Low-Frequency Approximation

The approximate expressions for the magnetic properties of the sheet were derived on the assumption that the frequency of the applied magnetic field is much less than RF frequencies. The following points apply to the frequency:

- The numerical results obtained from the approximate expressions in the low-θ region were compared with those from the exact expressions. They agree quite well up to $\theta \simeq 0.4$, which corresponds to a frequency range of approximately 10 to 100 [kHz], depending on the thickness and the material constants of the sheet.

Appendix A

Stored Magnetic Energy

In this Appendix, we first review the concept of stored magnetic energy and express it in terms of field quantities. Then, we derive the expression of the magnetic energy stored within an object that is placed in a magnetic field [122]–[128].

A.1 Energy Stored in a Magnetic Field

Consider a closed conducting loop with a current i which is initially zero. In the process of increasing i from zero to a final value I, work is done on the system. This work results in stored energy in the magnetic field surrounding the conductor. If we divide the cross section of the conductor into n distinct current filaments, the magnetic energy in the field around the current loop, W_V, is given by

$$W_V = \frac{1}{2}\sum_{i=1}^{n} I_i \phi_i, \tag{A.1}$$

where I_i is the current of the ith filament (or circuit) and ϕ_i is the flux linking the ith filament due to all the other $(n-1)$ current filaments in the current loop. Equation (A.1) is correct for the magnetic energy of n circuits in a medium for which the relationship of **B** to **H** is linear. Equation (A.1) can be transformed into the following form, which is applicable even when the relationship between **B** and **H** is nonlinear:

$$W_V = \sum_{i=1}^{n} \int_{\phi_{i0}}^{\phi_i} I_i \, \delta\phi_i, \tag{A2}$$

where ϕ_{i0} is the flux linking the ith circuit at the initial instant when all currents are zero.

It is a simple matter to extend eq.(A.2) from a finite number of current filaments to a continuous distribution of current. The increment in magnetic flux, $\delta\phi$, can be expressed by using the vector potential **A** in the form

$$\delta\phi = \int_S \delta\mathbf{B}\cdot d\mathbf{a} = \int_S (\nabla\times\delta\mathbf{A})\cdot d\mathbf{a} = \oint_c \delta\mathbf{A}\cdot d\mathbf{s}. \tag{A.3}$$

We use Stokes's theorem to transform the surface integral of $\nabla\times\delta\mathbf{A}$ over the surface S into the line integral of $\delta\mathbf{A}$ along a closed curve c bounding the surface. The current distribution can be broken up into a network of current loops, with the typical one being

a current tube of cross-sectional area $d\sigma$. For a current tube, we can write $Ids = \mathbf{J}\cdot\mathbf{n}\,dv$, where $\mathbf{J}$ is the current density and $dv\,(=d\sigma ds)$ is the volume of an infinitesimal length (ds) of a current tube. Using this relationship and eq.(A.3), we can transform eq. (A.2) into the expression for a system of distributed currents:

$$W_V = \int\int_{A_0}^{A} \mathbf{J}\cdot\delta\mathbf{A}\,dv. \tag{A.4}$$

This is the work required to set up a continuous current distribution and it is identical to the magnetic energy stored around a current carrying system.

We can obtain an expression involving the magnetic fields rather than $\mathbf{J}$ and $\delta\mathbf{A}$ by using the vector identity

$$\nabla\cdot(\delta\mathbf{A}\times\mathbf{H}) = \mathbf{H}\cdot(\nabla\times\delta\mathbf{A}) - \delta\mathbf{A}\cdot(\nabla\times\mathbf{H}) = \mathbf{H}\cdot\delta\mathbf{B} - \mathbf{J}\cdot\delta\mathbf{A}, \tag{A.5}$$

where we use the relationships $\delta\mathbf{B}=\nabla\times\delta\mathbf{A}$ and $\mathbf{J}=\nabla\times\mathbf{H}$. It follows from eq.(A.5) that

$$\mathbf{J}\cdot\delta\mathbf{A} = \mathbf{H}\cdot\delta\mathbf{B} + \nabla\cdot(\mathbf{H}\times\delta\mathbf{A}). \tag{A.6}$$

Substituting eq. (A.6) into eq. (A.4) and applying the divergence theorem

$$\int_V \nabla\cdot\mathbf{F}\,dv = \int_S \mathbf{F}\cdot\mathbf{n}\,da, \tag{A.7}$$

we obtain

$$W_V = \int_V \int_{B_0}^{B} \mathbf{H}\cdot d\mathbf{B}\,dv + \int_S \int_{A_0}^{A} (\mathbf{H}\times d\mathbf{A})\cdot\mathbf{n}\,da. \tag{A.8}$$

Here, V is any volume bounded by a surface S enclosing all the sources of the field. If we choose S to be a spherical surface at infinity, the second integral of eq. (A.8) disappears, because the integrand diminishes with r^{-3} ($\mathbf{H}\propto r^{-2}$ and $\mathbf{A}\propto r^{-1}$), whereas S grows only with r^2. Therefore, the work done to build up a magnetic field from B_0 to the final value B is represented by the integral

$$W_V = \int_V dv \int_{B_0}^{B} \mathbf{H}\cdot d\mathbf{B}. \tag{A.9}$$

This is the magnetic energy stored in the magnetic fields when they are brought up from B_0 to B. The present form is applicable to all magnetic media or materials, including ferromagnetic substances.

Strictly speaking, the derivation of the result is based on the assumption that the building up of the field takes place so slowly that it might be represented by a succession of stationary states. Therefore, it is essential to determine whether this

expression for the energy density remains valid when the fields vary at an arbitrary rate. In Section B.1, we review the power balance equation known as *Poynting's theorem*, which is valid for any frequency. The theorem supports that the expression of the density of energy stored in the electromagnetic field is the same as that in the stationary or quasistationary regime.

Now, we assume that the relationship of $\mathbf{B}$ to $\mathbf{H}$ is linear and that the medium is isotropic. Then, the relationship can be given by $\mathbf{B}=\mu\mathbf{H}$, where μ is the permeability of the medium and is at most a scalar function of position, which reduces to a constant if the medium is homogeneous. In this case, the relationship

$$d(\mathbf{H}\cdot\mathbf{B}) = d\mathbf{H}\cdot\mu\mathbf{H}+\mathbf{H}\cdot d\mathbf{B} = d\mathbf{B}\cdot\mathbf{H}+\mathbf{H}\cdot d\mathbf{B} = 2\mathbf{H}\cdot d\mathbf{B},$$

holds true, and we can write

$$\mathbf{H}\cdot d\mathbf{B} = \frac{1}{2}d(\mathbf{H}\cdot\mathbf{B}). \tag{A.10}$$

Under these circumstances, W_V in eq. (A.9) is reduced to

$$W_V = \frac{1}{2}\int_V \mathbf{H}\cdot\mathbf{B}\,dv. \tag{A.11}$$

We can assume this energy is distributed throughout the field with a density $(\mathbf{H}\cdot\mathbf{B})/2$, which reduces to $\mu H^2/2$ if μ is a constant. Equation (A.11) is commonly used to calculate the stored energy of magnetic media or materials.

A.2 Energy Stored in Magnetic Object

Our goal is to obtain the energy stored in a magnetic object when it is placed in a magnetic field. We consider the question of the change in a system's energy when a magnetic object is introduced into a magnetic field of fixed current sources. Suppose that initially the magnetic field $\mathbf{H}_1$ has been established in a medium having linear and isotropic permeability μ_1 (Fig. A.1(a)). The energy of the field stored in a volume V (from eq. (A.11)), is given by

$$W_{V1} = \frac{1}{2}\int_V \mathbf{H}_1\cdot\mathbf{B}_1\,dv, \tag{A.12}$$

where $\mathbf{B}_1$ is the magnetic flux density in the medium ($\mathbf{B}_1=\mu_1\mathbf{H}_1$). Then, with the sources fixed in position, a magnetic object is introduced into the field. The object is assumed to be initially unmagnetized but its magnetic properties are otherwise arbitrary. The volume occupied by the object is denoted V_a and the entire region outside is denoted

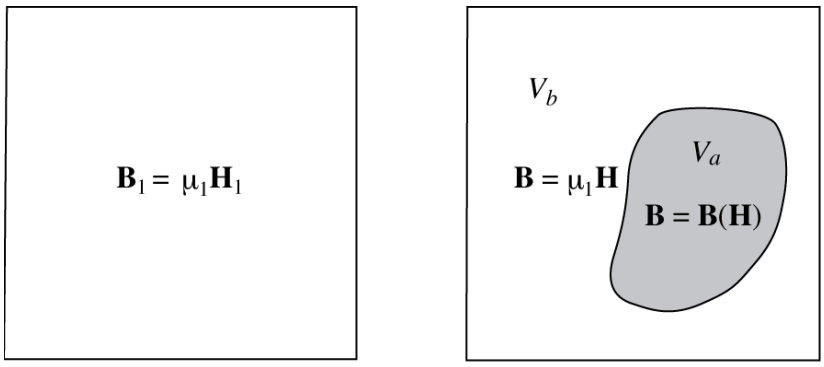

Figure A.1 (a) Fields in a homogeneous medium before introducing a magnetic object. (b) Fields after introducing a magnetic object of volume V_a. The volume of the medium outside the object is V_b.

V_b (Fig. A.1(b)). The energy of the system in this new state is

$$W_{V2} = \frac{1}{2} \int_{V_b} \mathbf{H} \cdot \mathbf{B} \, dv + \int_{V_a} dv \int_0^B \mathbf{H} \cdot d\mathbf{B}. \tag{A.13}$$

The ultimate magnetic flux density in the medium $\mathbf{B}$ differs from the initial magnetic flux density $\mathbf{B}_1$ by an amount, $\mathbf{B} - \mathbf{B}_1$, which arises from the polarization of the matter contained within V_a. The change in energy is

$$\begin{aligned} W_V &= W_{V2} - W_{V1} \\ &= \frac{1}{2} \int_{V_b} \left(\mathbf{H} \cdot \mathbf{B} - \mathbf{H}_1 \cdot \mathbf{B}_1 \right) dv + \int_{V_a} dv \left(\int_0^B \mathbf{H} \cdot d\mathbf{B} - \frac{1}{2} \mathbf{H}_1 \cdot \mathbf{B}_1 \right). \end{aligned} \tag{A.14}$$

This is the work done when introducing the object into the field, which must be equal to the energy stored in the object. The assumption of fixed sources and the use of some vector identities mean that the energy W_V in eq. (A.14) can be expressed in terms of integrals extended over the volume V_a occupied by the object, as follows:

$$W_V = \frac{1}{2} \int_{V_a} \left(\mathbf{H}_1 \cdot \mathbf{B} - \mathbf{H} \cdot \mathbf{B}_1 - \mathbf{H} \cdot \mathbf{B} + 2 \int_0^B \mathbf{H} \cdot d\mathbf{B} \right) dv. \tag{A.15}$$

If the magnetic properties of the material within V_a can be characterized by the permeability μ_2, the relationship $\mathbf{B} = \mu_2 \mathbf{H}$ holds true, and consequently, eq. (A.10),

which can also be written as

$$2\int_0^B \mathbf{H}\cdot d\mathbf{B} \;=\; \mathbf{H}\cdot\mathbf{B}, \tag{A.16}$$

is applicable to this case. Substituting eq. (A.16) into eq. (A.15) leads to

$$\begin{aligned} W_V \;&=\; \frac{1}{2}\int_{V_a}\left(\mathbf{H}_1\cdot\mathbf{B}-\mathbf{H}\cdot\mathbf{B}_1\right)dv \\ &=\; \frac{1}{2}\int_{V_a}\left(\mu_2-\mu_1\right)\mathbf{H}_1\cdot\mathbf{H}\;dv. \end{aligned} \tag{A.17}$$

This can also be written as

$$W_V \;=\; \frac{1}{2}\int_{V_a}\left(1-\frac{\mu_1}{\mu_2}\right)\mathbf{H}_1\cdot\mathbf{B}\;dv. \tag{A.18}$$

It is important to note that $\mathbf{B}$ in eq. (A.18) is the magnetic flux density within the object, whereas $\mathbf{H}_1$ is the magnetic field intensity in the medium before the object is introduced.

In general, in ferromagnetic materials, $\mathbf{B}$ and $\mathbf{H}$ do not have a linear relationship. However, if the amplitude of the alternating magnetic field is not very large, the permeability can usually be assumed to be a constant and then, eq. (A.18) can be used to estimate the stored energy of a magnetic object placed in a magnetic field.

Appendix B

Magnetic Power Loss

In Appendix A, the stored magnetic energy was expressed in terms of integrals of the field vectors from eq.(A.18). The next step is to understand how to express the magnetic power loss in terms of field vectors. We first review Poynting's theorem, which is essentially an energy conservation law that gives the relationship between the change in energy stored in a given volume of space and the flow of energy through the surface enclosing this volume. From this theorem, we obtain the general expression for the magnetic power loss [122]–[128]. Then, taking a magnetic solenoid as an example, we verify that the magnetic power loss of the solenoid, given in terms of **B** and **H**, is exactly equivalent to the product of voltage and current, which is the common definition of power loss.

B.1 Poynting's Theorem

We mentioned at the end of Section A.1 that the energy is expected to be distributed throughout the field. If this hypothesis is tenable, any change in field intensity and energy density must be associated with a flow of energy. The relationship between the rate of change in the energy stored in the field and the energy flow can be deduced as a general integral of Maxwell's field equations, which are given by

$$\nabla \times \mathbf{E} = -\frac{\partial \mathbf{B}}{\partial t}, \tag{B.1}$$

$$\nabla \times \mathbf{H} = \frac{\partial \mathbf{D}}{\partial t} + \mathbf{J}, \tag{B.2}$$

$$\nabla \cdot \mathbf{D} = \rho, \qquad \nabla \cdot \mathbf{B} = 0. \tag{B.3}$$

These four equations form the basis for all classical electromagnetic phenomena.

If there exists a continuous distribution of charge and current, the total rate of work done by the fields in a finite volume V is

$$\int_V \mathbf{E} \cdot \mathbf{J}\, dv. \tag{B.4}$$

This power represents a conversion of electromagnetic energy into mechanical or thermal energy. It must be balanced by a corresponding power decrease in the electromagnetic field within the volume V. To exhibit this conservation law explicitly,

we use Maxwell's equations to express eq. (B.4) in other terms. Solving **J** from eq. (B.2) and substituting it into eq. (B.4) leads to

$$\int_V \mathbf{E}\cdot\mathbf{J}\,dv = \int_V \left[\mathbf{E}\cdot\left(\nabla\times\mathbf{H}\right) - \mathbf{E}\cdot\frac{\partial\mathbf{D}}{\partial t}\right] dv. \tag{B.5}$$

If we employ the vector identity

$$\nabla\cdot\left(\mathbf{E}\times\mathbf{H}\right) = \mathbf{H}\cdot\left(\nabla\times\mathbf{E}\right) - \mathbf{E}\cdot\left(\nabla\times\mathbf{H}\right), \tag{B.6}$$

and use eq. (B.1), the first term in the brackets on the right-hand side of eq. (B.5) is written as

$$\begin{aligned}\mathbf{E}\cdot\left(\nabla\times\mathbf{H}\right) &= -\nabla\cdot\left(\mathbf{E}\times\mathbf{H}\right) + \mathbf{H}\cdot\left(\nabla\times\mathbf{E}\right)\\ &= -\nabla\cdot\left(\mathbf{E}\times\mathbf{H}\right) - \mathbf{H}\cdot\frac{\partial\mathbf{B}}{\partial t}.\end{aligned} \tag{B.7}$$

Substituting eq. (B.7) into eq. (B.5), we obtain

$$\int_V \mathbf{E}\cdot\mathbf{J}\,dv = -\int_V \nabla\cdot\left(\mathbf{E}\times\mathbf{H}\right) dv - \int_V \left(\mathbf{E}\cdot\frac{\partial\mathbf{D}}{\partial t} + \mathbf{H}\cdot\frac{\partial\mathbf{B}}{\partial t}\right) dv. \tag{B.8}$$

Using the divergence theorem given in eq. (A.7), the first term on the right-hand side of eq. (B.8) can be transformed from a volume integral into a surface integral, such that eq. (B.8) becomes

$$\oint_S \left(\mathbf{E}\times\mathbf{H}\right)\cdot d\mathbf{a} + \int_V \mathbf{E}\cdot\mathbf{J}\,dv = -\int_V \left(\mathbf{E}\cdot\frac{\partial\mathbf{D}}{\partial t} + \mathbf{H}\cdot\frac{\partial\mathbf{B}}{\partial t}\right) dv. \tag{B.9}$$

This result was first derived by J. H. Poynting in 1884 and again in the same year by O. Heaviside. The equation is known as Poynting's theorem and is customarily interpreted as follows: Since the term $\mathbf{E}\cdot\mathbf{J}$ has the dimension of power expended per unit volume (watts per cubic meter), the terms on both sides of eq. (B.9) must represent the power or the time rate of change in energy. Hence, the right-hand side of eq. (B.9) represents the rate of decrease in electric and magnetic energy stored within the volume. The term $\mathbf{H}\cdot\partial\mathbf{B}/\partial t$, which represents the density of magnetic power loss, is consistent with the expression of stored magnetic energy given in eq. (A.9) (see Section 2.3). This supports the validity of eq. (A.9) even if the fields vary at an arbitrary rate.

The loss of available stored energy given on the right-hand side of eq. (B.9) must be accounted for by the terms on the left-hand side. Since the second integral on the left-hand side represents the power dissipated in the volume V in Joule heat, then the

first integral must represent the power flow out of the surface S enclosing the volume V. The important consequence is that the integration of

$$\mathbf{E} \times \mathbf{H} \equiv \mathbf{S} \tag{B.10}$$

over an arbitrary closed surface gives the electromagnetic power flow from the inside to the outside of the closed surface. **S** is termed the *Poynting vector*, which is interpreted as the intensity of power flow per unit area whose normal is oriented in the direction of the vector $\mathbf{E} \times \mathbf{H}$.

Incidentally, Poynting's theorem can be rewritten as the power balance equation in the explicit complex form [128] as follows:

$$P_s = P_o + P_l + j2\omega\left(W_{m,j} - W_{e,j}\right). \tag{B.11}$$

Here,

P_s is the complex power delivered by the sources,
P_o is the active or real power transmitted through the closed surface,
P_l is the power lost to heat in the volume enclosed by the surface,
$2\omega(W_{m,j} - W_{e,j})$ is the reactive power,
ω is the angular frequency,
$W_{m,j}$ is the reactive magnetic energy stored in the volume, and
$W_{e,j}$ is the reactive electric energy stored in the volume.

B.2 Power Loss of a Magnetic Solenoid

As mentioned previously, the integrand on the right-hand side of eq.(B.9) represents the density of electric and magnetic power loss, and it is evident that the second term $\mathbf{H} \cdot \partial \mathbf{B}/\partial t$ gives the density of the magnetic power loss. Here, we perform a simple thought experiment to verify that the magnetic power loss expressed in terms of magnetic field quantities is consistent with the commonly used power loss defined by the product of voltage and current.

We consider an infinitely long solenoid, which is a single-layer coil of fine wire wound tightly around a solid magnetic cylinder having a permeability μ (Fig.B.1). A current **i** flowing through the wire produces a uniform magnetic field **H** within the solenoid, which is expressed as

$$\mathbf{H} = n\mathbf{i}, \tag{B.12}$$

where n is the number of turns per unit length. Let $\boldsymbol{\phi}$ denote the interlinkage of magnetic flux of the solenoid in a length l. Then it is written as

$$\boldsymbol{\phi} = \pi a^2 l n \mathbf{B}, \tag{B.13}$$

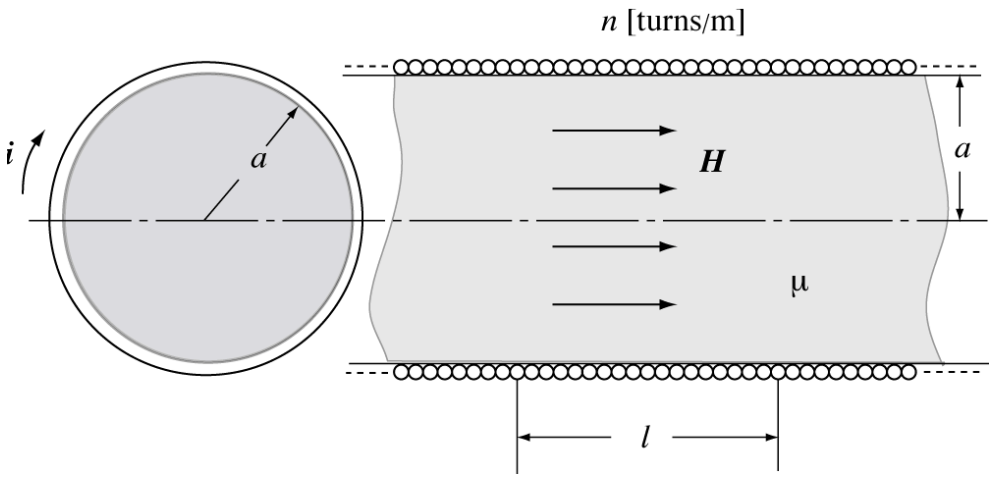

Figure B.1 Infinitely long solenoid made of a single-layer coil of fine wire wound tightly around a solid cylinder of magnetic material.

where a is the radius of the cylinder and $\mathbf{B}$ is the magnetic flux density within the solenoid, which is given by $\mathbf{B}=\mu\mathbf{H}$. The change in ϕ with time induces the voltage $\mathbf{v}$ on the solenoid across the length l such that

$$\mathbf{v} = -\frac{\partial \phi}{\partial t} = -\pi a^2 l n \frac{\partial \mathbf{B}}{\partial t}. \tag{B.14}$$

It is common practice to express the power, or the change in energy per second, as a scalar product of the voltage $\mathbf{v}$ and the current $\mathbf{i}$. Now, we denote the magnetic energy stored in the volume $V\ (=\pi a^2 l)$, by W_V. Then, the time rate of change in W_V must be equal to the power $\mathbf{i}\cdot\mathbf{v}$. Using eqs. (B.12) and (B.14), this is written as

$$\frac{\partial W_V}{\partial t} = \mathbf{i}\cdot\mathbf{v} = -\mathbf{H}\cdot\left(\pi a^2 l\right)\frac{\partial \mathbf{B}}{\partial t}. \tag{B.15}$$

Let W_m be the magnetic energy stored per unit volume, that is, $W_m = W_V/V$. Then, dividing both sides of eq. (B.15) by the volume V, we obtain the time rate of decrease in the magnetic energy stored in a unit volume:

$$\frac{\mathbf{i}\cdot\mathbf{v}}{V} = \frac{\partial W_m}{\partial t} = -\mathbf{H}\cdot\frac{\partial \mathbf{B}}{\partial t}. \tag{B.16}$$

This is exactly the same as the second term in the parentheses on the right-hand side of eq. (B.9).

Next, we consider a capacitor made of two parallel conducting plates that extend infinitely and are maintained at a constant potential difference. Performing a similar thought experiment, we can show that the time rate of decrease in the electric energy stored in a unit volume of the capacitor is given by

$$\frac{\mathbf{i}\cdot\mathbf{v}}{V} = \frac{\partial W_e}{\partial t} = -\mathbf{E}\cdot\frac{\partial \mathbf{D}}{\partial t}, \tag{B.17}$$

which agrees precisely with the first term in the parentheses on the right-hand side of eq. (B.9). In eq. (B.17), $\mathbf{i}$ and $\mathbf{v}$ are the charging current and voltage, respectively, V is the volume of the capacitor, W_e is the electric energy stored per unit volume, and $\mathbf{E}$ and $\mathbf{D}$ are the electric field intensity and electric flux density in the capacitor, respectively.

In conclusion, the average density of magnetic power loss in the volume V is given by

$$P_{m,g} = \frac{1}{V}\int_V \mathbf{H}\cdot\frac{\partial \mathbf{B}}{\partial t}\, dv. \tag{B.18}$$

Appendix C

Field Distribution within a Solid Magnetic Cylinder

In Chapter 4, we discussed the effect of eddy currents on the magnetic field distribution in the interior of the magnetic sheet. The eddy-current effect can also be accurately calculated for a specimen in the form of a solid cylinder. In this appendix, we derive the expressions for the magnetic field distribution within a solid magnetic cylinder. The field distribution is obtained in solving a field equation that governs the magnetic field within the cylinder. Examples are given to show how the field distribution depends on the material parameters and how it varies with the frequency of the applied magnetic field.

C.1 Field Equation

We consider that the specimen is a solid cylinder or a wire made of a magnetic material having complex permeability as well as nonzero conductivity. We assume that the uniform magnetic field

$$\boldsymbol{H}_{z0} = H_0 e^{j\omega t}, \tag{C.1}$$

is applied parallel to the cylinder axis as shown in Fig. C.1. We also assume that

(1) the solid magnetic cylinder is infinitely long, and

(2) the intrinsic permeability μ is linear and isotropic.

On the basis of these assumptions and the configuration shown in Fig. C.1, we derive the field equation, which is then solved to obtain the magnetic field distribution.

We start with Maxwell's equations written in cylindrical coordinates, which are composed of eight equations for six field components $\mathbf{E}_r$, $\mathbf{E}_\phi$, $\mathbf{E}_z$, $\mathbf{H}_r$, $\mathbf{H}_\phi$, and $\mathbf{H}_z$. Under the conditions given above, only the two field components $\mathbf{H}_z$ and $\mathbf{E}_\phi$ have a nonzero value and the other four field components have a value of zero. Likewise, only the two field gradients $\partial\mathbf{E}_\phi/\partial r$ and $\partial\mathbf{H}_z/\partial r$ have a nonzero value and other four field gradients are zero. That is,

$$\mathbf{E}_r = \mathbf{E}_z = \mathbf{H}_r = \mathbf{H}_\phi = 0 \quad \text{and} \quad \frac{\partial \mathbf{E}_\phi}{\partial \phi} = \frac{\partial \mathbf{E}_\phi}{\partial z} = \frac{\partial \mathbf{H}_z}{\partial \phi} = \frac{\partial \mathbf{H}_z}{\partial z} = 0. \tag{C.2}$$

Therefore, only the following two equations remain significant:

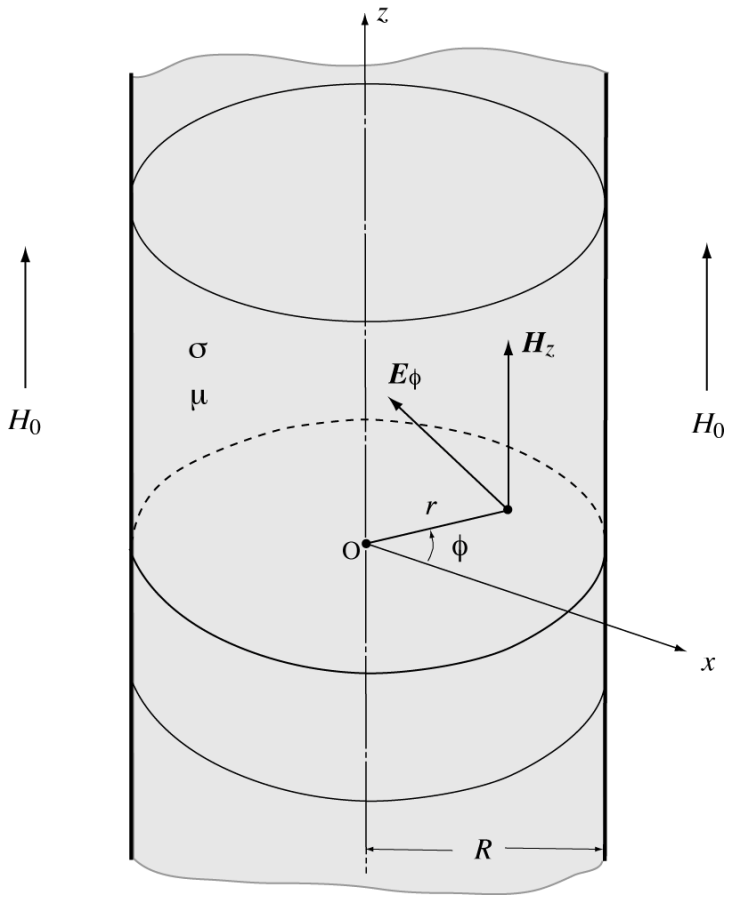

Figure C.1 Geometry and field components of an infinitely long solid cylinder of magnetic material.

$$\frac{1}{r}\frac{\partial}{\partial r}\left(r\mathbf{E}_\phi\right) = -\mu\frac{\partial \mathbf{H}_z}{\partial t}, \tag{C.3}$$

and

$$-\frac{\partial \mathbf{H}_z}{\partial r} = \sigma\mathbf{E}_\phi + \varepsilon\frac{\partial \mathbf{E}_\phi}{\partial t}. \tag{C.4}$$

As mentioned in Section 4.3, the condition $\omega\varepsilon/\sigma \ll 1$ is satisfied over a wide frequency range up to at least microwave frequencies even for moderate conductors, such as steel and magnetic alloys. Therefore, the second term on the right-hand side of eq. (C.4) can be ignored. Solving eq. (C.4) for $\mathbf{E}_\phi$ and substituting it into eq. (C.3), we can eliminate $\mathbf{E}_\phi$ and obtain the second-order differential equation for $\mathbf{H}_z$:

$$\frac{\partial^2 \mathbf{H}_z}{\partial r^2} + \frac{1}{r}\frac{\partial \mathbf{H}_z}{\partial r} - j\omega(\mu' - j\mu'')\sigma \mathbf{H}_z = 0, \tag{C.5}$$

where the time dependence $e^{j\omega t}$ is assumed and μ in eq. (C.3) is replaced with the complex intrinsic permeability $\mu'-j\mu''$.

In order to solve eq. (C.5), which cannot be solved by elementary means, we introduce a dimensionless complex parameter

$$\rho = \gamma_c r, \tag{C.6}$$

where

$$\gamma_c = \sqrt{-j\omega(\mu' - j\mu'')\sigma} = \sqrt{-j}\,\frac{\alpha^{1/4}\theta_c}{\sqrt{2}R}\,e^{-j\phi_c}, \tag{C.7}$$

with

$$\left.\begin{aligned} &\theta_c = \frac{2R}{\delta_s} = \frac{D}{\delta_s}, \qquad \delta_s = \sqrt{\frac{2}{\omega\mu'\sigma}}, \qquad \tan\delta = \frac{\mu''}{\mu'}, \\ &\alpha = 1 + \tan^2\delta, \qquad \text{and} \qquad \phi_c = \frac{1}{2}\tan^{-1}(\tan\delta) - n\pi. \\ &\qquad\qquad\qquad\qquad\qquad\qquad\qquad\qquad (n = 0,\ 1) \end{aligned}\right\} \tag{C.8}$$

Here, R and D denote the radius and diameter of the cylinder, respectively, and $\tan\delta$ is the intrinsic loss factor. In the expression of φ_c, we use the form $\tan^{-1}(\tan\delta)$ instead of δ, because the term $\tan\delta$ is customarily used as a measure of the quality of materials and is often a given parameter. Then, ρ can be written as

$$\rho = \sqrt{-j}\,\frac{\alpha^{1/4}\theta_c}{\sqrt{2}}\,e^{-j\phi_c}\,\frac{r}{R}. \tag{C.9}$$

Changing the independent variable from r to ρ, we rewrite eq. (C.5) as

$$\frac{\partial^2 \mathbf{H}_z}{\partial \rho^2} + \frac{1}{\rho}\frac{\partial \mathbf{H}_z}{\partial \rho} + \mathbf{H}_z = 0, \tag{C.10}$$

which is recognized as a Bessel's differential equation of order zero.

C.2 Solution of Field Equation

There are two independent solutions to eq. (C.10), namely $\mathbf{J}_0(\rho)$ and $\mathbf{N}_0(\rho)$, which are termed the first and second kind of ordinary Bessel function of order zero,

respectively. The general solution is given by a combination of these two functions:

$$\mathbf{H}_z = A\mathbf{J}_0(\rho) + B\mathbf{N}_0(\rho), \tag{C.11}$$

where A and B are the constants of complex numbers, which are chosen to match given boundary conditions. The Bessel function of the second kind, $\mathbf{N}_0(\rho)$, which is often referred to as the Neumann function, becomes infinite at $\rho = 0$. Since in our case, the magnetic field remains finite at $\rho = 0$, the $\mathbf{N}_0(\rho)$ term is physically unacceptable and must be excluded, and therefore, the constant B in eq. (C.11) should be zero.

The boundary condition at the surface of the cylinder requires that $\mathbf{H}_z$ must be equal to the applied field H_0. Then, at $r = R$, eq. (C.11) becomes

$$H_0 = A\mathbf{J}_0(\rho_R), \tag{C.12}$$

where

$$\rho_R = \gamma_c R = \sqrt{-j}\,\frac{\alpha^{1/4}\theta_c}{\sqrt{2}}\,e^{-j\phi_c}. \tag{C.13}$$

Thus, the constant A is determined as

$$A = \frac{H_0}{\mathbf{J}_0(\rho_R)}. \tag{C.14}$$

Substituting eq. (C.14) for A and zero for B in eq. (C.11) and adding the time factor $e^{j\omega t}$, we obtain the solution

$$\mathbf{H}_z = H_0\,\frac{\mathbf{J}_0(\rho)}{\mathbf{J}_0(\rho_R)}\,e^{j\omega t}. \tag{C.15}$$

The function $\mathbf{J}_0(\rho)$ is expressed in a power series of ρ:

$$\mathbf{J}_0(\rho) = \sum_{m=0}^{\infty} \frac{(-1)^m}{2^{2m}\,m!\,\Gamma(m+1)}\,\rho^{2m}. \tag{C.16}$$

Equation (C.15) can be expressed in the explicit complex form by splitting $\mathbf{J}_0(\rho)$ and $\mathbf{J}_0(\rho_R)$ into the real and imaginary parts:

$$\mathbf{H}_z = H_0\,\frac{\mathrm{Re}\left[\mathbf{J}_0(\rho)\right] + j\,\mathrm{Im}\left[\mathbf{J}_0(\rho)\right]}{\mathrm{Re}\left[\mathbf{J}_0(\rho_R)\right] + j\,\mathrm{Im}\left[\mathbf{J}_0(\rho_R)\right]}\,e^{j\omega t}. \tag{C.17}$$

The complex field $\mathbf{H}_z$ can also be represented by a combination of the amplitude $|\mathbf{H}_z|$ and the phase θ_z:

$$\mathbf{H}_z = \left|\mathbf{H}_z\right| e^{j(\omega t+\theta_z)}, \tag{C.18}$$

where $$\left|\mathbf{H}_z\right| = H_0 \left[\frac{\mathrm{Re}^2\left[\mathbf{J}_0(\rho)\right] + \mathrm{Im}^2\left[\mathbf{J}_0(\rho)\right]}{\mathrm{Re}^2\left[\mathbf{J}_0(\rho_R)\right] + \mathrm{Im}^2\left[\mathbf{J}_0(\rho_R)\right]} \right]^{1/2} \tag{C.19}$$

and $$\theta_z = \tan^{-1}\left\{ \frac{\mathrm{Re}\left[\mathbf{J}_0(\rho_R)\right]\mathrm{Im}\left[\mathbf{J}_0(\rho)\right] - \mathrm{Re}\left[\mathbf{J}_0(\rho)\right]\mathrm{Im}\left[\mathbf{J}_0(\rho_R)\right]}{\mathrm{Re}\left[\mathbf{J}_0(\rho)\right]\mathrm{Re}\left[\mathbf{J}_0(\rho_R)\right] + \mathrm{Im}\left[\mathbf{J}_0(\rho)\right]\mathrm{Im}\left[\mathbf{J}_0(\rho_R)\right]} \right\}. \tag{C.20}$$

$\mathrm{Re}[\mathbf{J}_0(\rho)]$ and $\mathrm{Im}[\mathbf{J}_0(\rho)]$ are expanded in a power series of r/R:

$$\mathrm{Re}\left[\mathbf{J}_0(\rho)\right] = \sum_{m=0}^{\infty} \frac{(-1)^m}{\left[(2m)!\right]^2} \left(\frac{\alpha^{1/4}\theta_c}{2\sqrt{2}} \right)^{4m} \cos(4m\phi_c) \left(\frac{r}{R} \right)^{4m} + \sum_{m=0}^{\infty} \frac{(-1)^m}{\left[(2m+1)!\right]^2} \left(\frac{\alpha^{1/4}\theta_c}{2\sqrt{2}} \right)^{2(2m+1)} \sin\left[2(2m+1)\phi_c\right] \left(\frac{r}{R} \right)^{2(2m+1)} \tag{C.21}$$

and

$$\mathrm{Im}\left[\mathbf{J}_0(\rho)\right] = \sum_{m=0}^{\infty} \frac{(-1)^m}{\left[(2m+1)!\right]^2} \left(\frac{\alpha^{1/4}\theta_c}{2\sqrt{2}} \right)^{2(2m+1)} \cos\left[2(2m+1)\phi_c\right] \left(\frac{r}{R} \right)^{2(2m+1)} + \sum_{m=0}^{\infty} \frac{(-1)^{m+1}}{\left[(2m)!\right]^2} \left(\frac{\alpha^{1/4}\theta_c}{2\sqrt{2}} \right)^{4m} \sin\left[4m\phi_c\right] \left(\frac{r}{R} \right)^{4m}. \tag{C.22}$$

The functions at the surface $\mathrm{Re}[\mathbf{J}_0(\rho_R)]$ and $\mathrm{Im}[\mathbf{J}_0(\rho_R)]$ can be obtained by replacing r with R in eqs. (C.21) and (C.22).

If the cylinder material has no imaginary permeability part, in other words, if $\tan\delta = 0$, then $\alpha = 1$ and $\varphi_c = -n\pi$. Hence, eqs. (C.21) and (C.22) reduce to

$$\mathrm{Re}\left[\mathbf{J}_0(\rho)\right] = \mathrm{Re}\left[\mathbf{J}_0(\sqrt{-j}\,x)\right] = \sum_{m=0}^{\infty} \frac{(-1)^m}{\left[(2m)!\right]^2} \left(\frac{x}{2} \right)^{4m} \equiv \mathrm{Ber}_0(x) \tag{C.23}$$

and

$$\mathrm{Im}\left[\mathbf{J}_0(\rho)\right] = \mathrm{Im}\left[\mathbf{J}_0(\sqrt{-j}\,x)\right] = \sum_{m=0}^{\infty} \frac{(-1)^m}{\left[(2m+1)!\right]^2} \left(\frac{x}{2} \right)^{2(2m+1)} \equiv \mathrm{Bei}_0(x), \tag{C.24}$$

where $$x = \frac{\theta_c}{\sqrt{2}} \frac{r}{R}. \tag{C.25}$$

The functions Ber(x) and Bei(x) imply *Bessel real* and *Bessel imaginary functions*, and are sometimes called the Ber and Bei functions of Lord Kelvin, for which many tables exist. The subscript of the Ber and Bei functions indicates the order of the function, which is often omitted if it is zero. Substituting eqs. (C.23) and (C.24) into eqs. (C.19) and (C.20), we obtain the approximate expressions of $|\mathbf{H}_z|$ and θ_z as follows:

$$\left|\mathbf{H}_z\right| = H_0 \left[\frac{\mathrm{Ber}_0^2(x) + \mathrm{Bei}_0^2(x)}{\mathrm{Ber}_0^2(x_R) + \mathrm{Bei}_0^2(x_R)} \right]^{1/2} \tag{C.26}$$

and

$$\theta_z = \tan^{-1} \left\{ \frac{\mathrm{Ber}_0(x_R)\,\mathrm{Bei}_0(x) - \mathrm{Ber}_0(x)\,\mathrm{Bei}_0(x_R)}{\mathrm{Ber}_0(x)\,\mathrm{Ber}_0(x_R) + \mathrm{Bei}_0(x)\,\mathrm{Bei}_0(x_R)} \right\}, \tag{C.27}$$

where

$$x_R = \frac{\theta_c}{\sqrt{2}}. \tag{C.28}$$

These expressions agree with those found in textbooks on electromagnetic theory [127] and ferromagnetism [89] [90] and are applicable to the case where the intrinsic $\tan\delta$ of the cylinder is negligible.

C.3 Numerical Examples

The amplitude $|\mathbf{H}_z|$ and the phase θ_z of the field are calculated from eqs. (C.19) and (C.20), which contain the exact forms of $\mathrm{Re}[\mathbf{J}_0(\rho)]$ and $\mathrm{Im}[\mathbf{J}_0(\rho)]$ given in eqs. (C.21) (C.22).

First, we examine the case where the intrinsic loss factor $\tan\delta$ is zero. Figure C.2 shows the normalized amplitude $|\mathbf{H}_z|/H_0$ and the phase θ_z for several values of θ_c. The abscissa is the normalized distance from the central axis r/D, where D is the diameter of the cylinder. Therefore, the position $r/D=0$ refers to the central axis and $r/D=0.5$ to the surface of the cylinder. The parameter θ_c is given by eq. (C.8) and written as

$$\theta_c = \frac{D}{\delta_s} = D\sqrt{\frac{\omega\mu'\sigma}{2}}. \tag{C.29}$$

This equation shows that θ_c is proportional to the diameter D and is also proportional to the square root of the product of the frequency ω, the real part of intrinsic permeability μ', and the conductivity σ. Figure C.2 clearly shows how the magnetic field is distributed within the cylinder when the uniform alternating magnetic field is continuously applied to the cylinder, parallel to its axis. The normalized amplitude $|\mathbf{H}_z|/H_0$ diminishes and the phase θ_z lags with the distance from the surface. For a larger

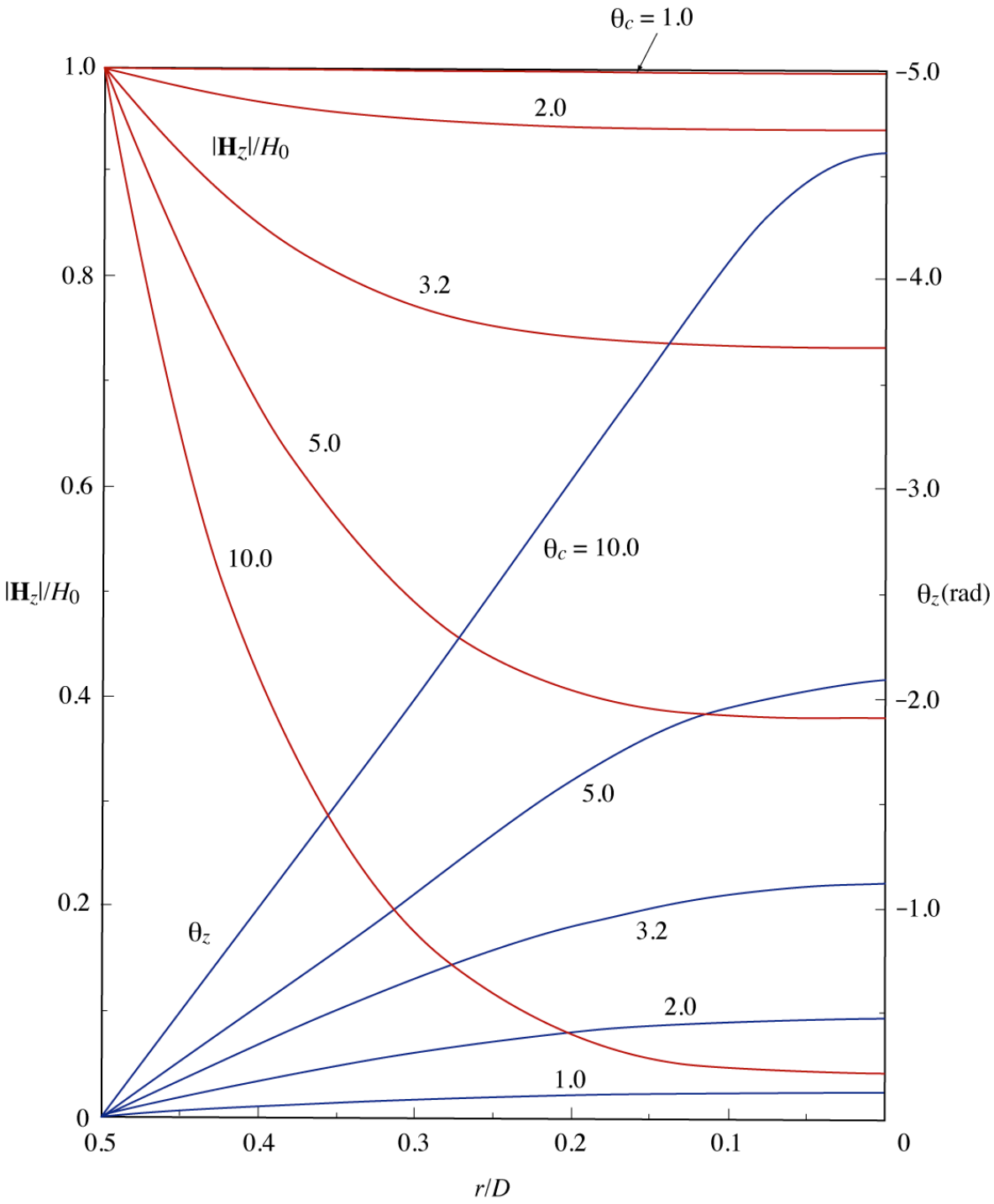

Figure C.2 Normalized amplitude $|\mathbf{H}_z|/H_0$ and phase θ_z of the field inside the solid cylinder versus normalized distance r/D for five values of θ_c in the case of $\tan\delta = 0$. $r/D = 0$ denotes the central axis and $r/D = 0.5$ the surface of cylinder.

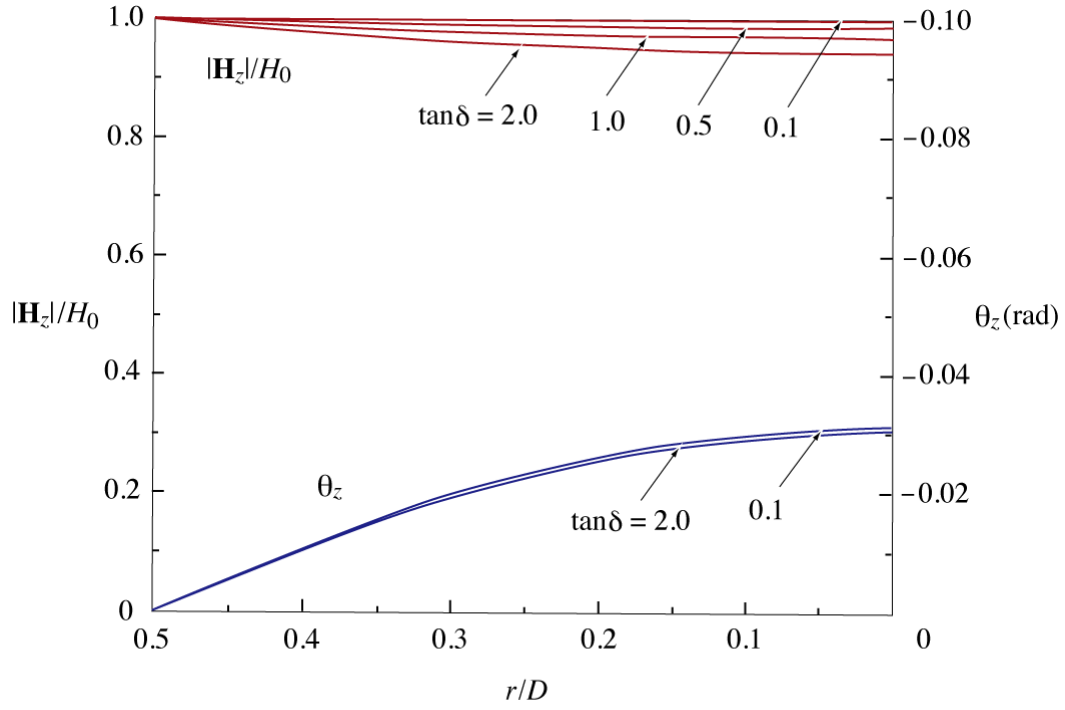

Figure C.3 (a) Normalized amplitude $|\mathbf{H}_z|/H_0$ and phase θ_z of the field inside the solid cylinder versus r/D for $\theta_c = 0.5$ and four values of $\tan\delta$.

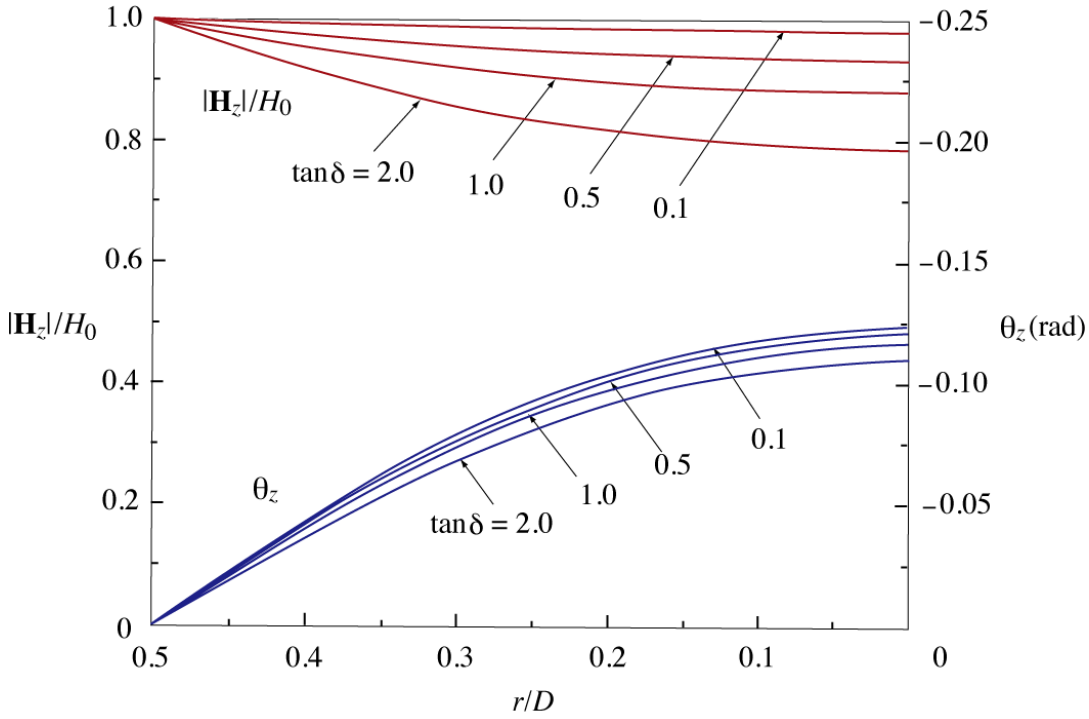

Figure C.3 (b) for $\theta_c = 1.0$.

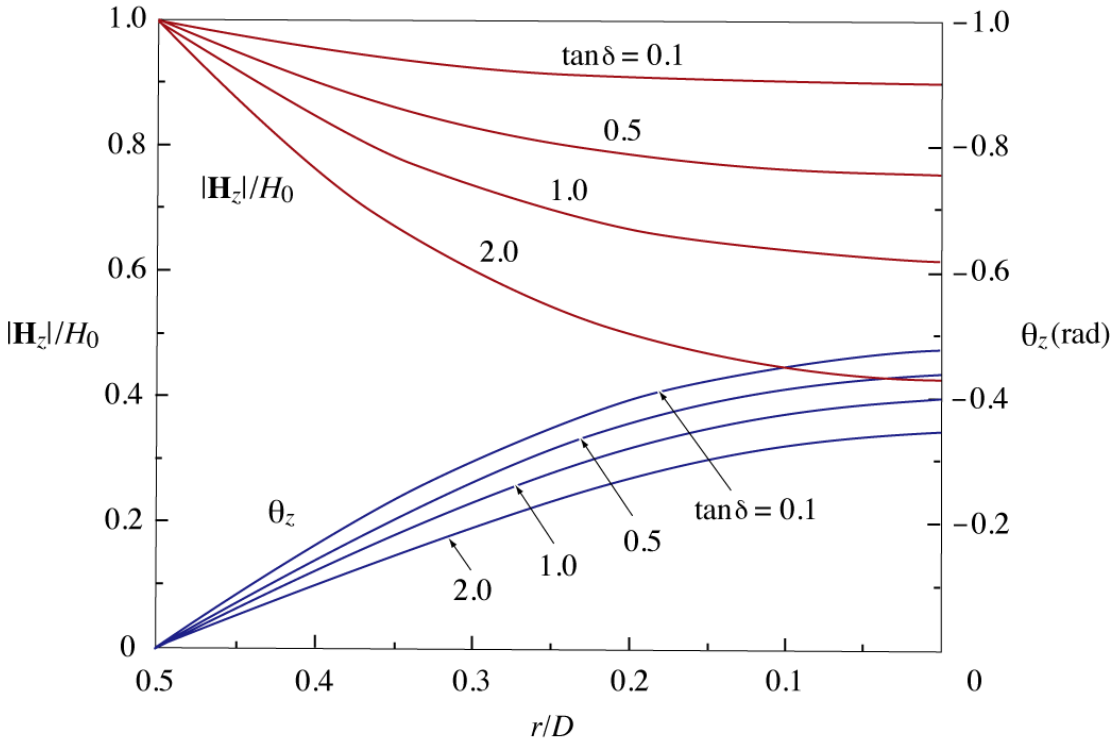

Figure C.3 (c) for $\theta_c = 2.0$.

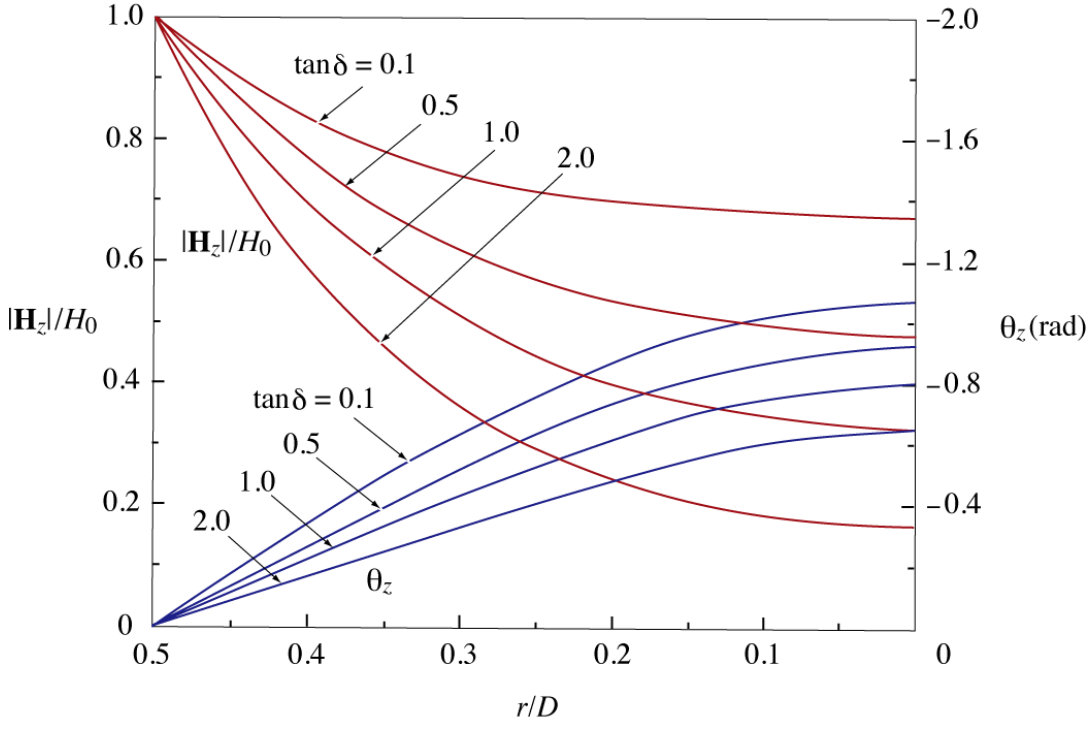

Figure C.3 (d) for $\theta_c = 3.2$.

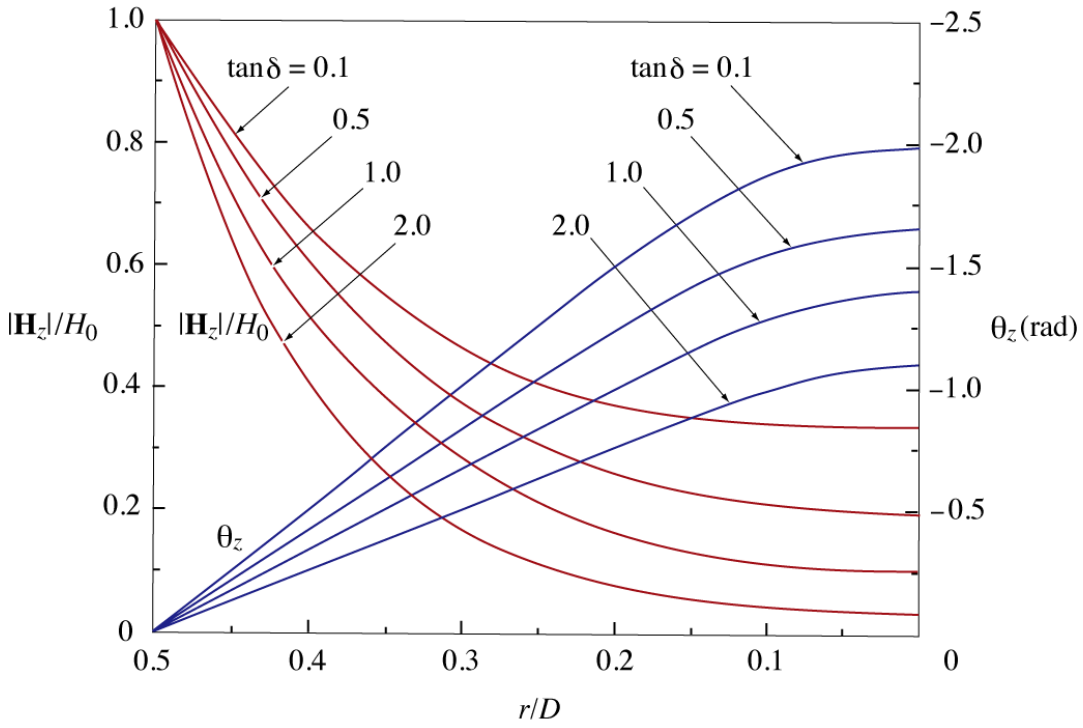

Figure C.3 (e) for $\theta_c = 5.0$.

value of θ_c, $|\mathbf{H}_z|/H_0$ decreases more rapidly and θ_z lags faster.

Next, we examine the way in which the field distribution depends on θ_c and $\tan\delta$. Figure C.3 shows $|\mathbf{H}_z|/H_0$ and θ_z as a function of r/D for five values of θ_c. Fig. C.3 (a), (b), (c), (d), and (e) illustrate the results for $\theta_c = 0.5$, 1.0, 2.0, 3.2, and 5.0, respectively, each showing the field distribution for $\tan\delta = 0.1$, 0.5, 1.0, and 2.0. Note that the scale of $|\boldsymbol{H}_z|/H_0$ is common to all figures, but the scale of θ_z is different from figure to figure. We can see that as $\tan\delta$ increases, the field amplitude diminishes more rapidly, whereas the phase lags more slowly. The reason for this phase behavior was discussed in Subsection 4.8.3, where the behavior was analyzed using the phasor diagrams of $\mathbf{H}_z$.

Appendix D

Electric Field Induced by Time-Varying Magnetic Field

In Section 7.4, we obtained the expression for the electric field $\mathbf{E}_x$, which is induced at $y = y_0$ by the time-varying magnetic flux. It is written as

$$\mathbf{E}_x = \frac{\omega H_0 d}{\sqrt{2}\,\alpha^{1/4}\theta\left[\cosh(2a_2)+\cos(2b_2)\right]}\left(R + jI\right)e^{j\omega t}, \tag{7.24}$$

where R and I are given by

$$R = \mu'\left[(B+D)\cos(\phi)-(A+C)\sin(\phi)\right]-\mu''\left[(A+C)\cos(\phi)+(B+D)\sin(\phi)\right] \tag{D.1}$$

and

$$I = -\mu'\left[(A+C)\cos(\phi)+(B+D)\sin(\phi)\right]-\mu''\left[(B+D)\cos(\phi)-(A+C)\sin(\phi)\right], \tag{D.2}$$

with

$$A = \sinh(a_1y_0+a_2)\cos(b_1y_0-b_2), \tag{D.3}$$

$$B = \cosh(a_1y_0+a_2)\sin(b_1y_0-b_2), \tag{D.4}$$

$$C = \sinh(a_1y_0-a_2)\cos(b_1y_0+b_2), \tag{D.5}$$

and

$$D = \cosh(a_1y_0-a_2)\sin(b_1y_0+b_2). \tag{D.6}$$

References

[1] J. E. Griffin and G. Nicholls, “A Review of Some Dynamic Loss Properties of Ni-Zn Accelerator RF System Ferrite,” *IEEE Transactions on Nuclear Science*, Vol. NS-26, No. 3, pp. 3965–3967 (1979).

[2] C. Fougeron, P. Ausset, J. Peyromaure, “Towards the Construction of an Ultra Short Cavity,” *Proceedings of EPAC 1990*, Nice, France, pp. 961–963 (1990).

[3] C. Fougeron, P. Ausset, D. de Menezes, J. Peyromaure, G. Charruau, “Very Wide Range and Short Accelerating Cavity for MIMAS,” *Proceedings of PAC 1993*, Washington, D.C, pp. 858–861 (1993).

[4] M. Crescenti, G. Primadei, A. Susini, “A New Compact Large Frequency-Swing RF System for Hadron Acceleration: Test Results,” CERN/PS 97-60 (DI) (1997).

[5] M. Crescenti, G. Primadei, A. Susini, “Mechanical Design of the RF Cavity for TERA/PIMMS Medical Synchrotron,” PS/DI/Note 99-13 (Tech.) (1999).

[6] M. Crescenti, A. Susini, G. Primadei, F. J. Etzkorn, A. Schnase, C. Fougeron, “The VITROVAC® Cavity for the TERA/PIMMS Medical Synchrotron,” *Proceedings of EPAC 2000*, Vienna, Austria, pp. 1951–1953 (2000)

[7] T. Uesugi, C. Ohmori, T. Tanabe, Y. Tanabe, H. Nakayama, M. Fujieda, Y. Mori, E. Ezura, A. Takagi, M. Toda, M. Yoshii, “Summary of the Measurement of Magnetic Materials for JHP RF Cavity (1),” *INS Report*, JHP-31, January (in Japanese) (1997).

[8] H. Nakayama, T. Uesugi, E. Ezura, C. Ohmori, Y. Kanai, K. Koba, K. Saito, Y. Sato, M. Souda, A. Takagi, T. Tanabe, Y. Tanabe, M. Toda, M. Fujieda, R. Matsumura, Y. Mori, M. Yamamoto, M. Yoshii, “Summary of the Measurement of Magnetic Materials for JHF RF Cavity (2) − FINEMET,” *KEK Report* 98-13, January (in Japanese) (1999).

[9] M. Fujieda, Y. Mori, H. Nakayama, C. Ohmori, S. Sawada, Y. Tanabe, E. Ezura, A. Takagi, M. Toda, M. Yoshii, T. Tanabe and T. Uesugi, “Studies of Magnetic Cores for JHF Synchrotrons,” *Proceedings of PAC 1997*, Vancouver, B.C., Canada, pp. 2992–2994 (1997).

[10] C. Ohmori, M. Fujieda, S. Machida, Y. Mori, H. Nakayama, K. Saito, S. Sawada, Y. Tanabe, M. Yamamoto, E. Ezura, A. Takagi, M. Toda, M. Yoshii, T. Tanabe, and T. Uesugi, “A Wideband RF Cavity for JHF Synchrotrons,” *Proceedings of PAC 1997*, Vancouver, B.C., Canada, pp. 2995–2997 (1997).

[11] T. Uesugi, E. Ezura, C. Ohmori, K. Koba, K. Saitoh, S. Sawada, A. Takagi, T. Tanabe, Y. Tanabe, M. Toda, H. Nakayama, M. Fujieda, Y. Mori, T. Yan, M. Yamamoto, M. Yoshii, “New Magnetic Material for Proton Synchrotron RF

Cavity," *Proceedings of 11th Symposium on Accelerator Science and Technology*, Ako, Hyogo, Japan, pp. 206–208 (1997).

[12] Y. Tanabe, M. Fujieda, Y. Mori, H. Nakayama, C. Ohmori, K. Saito, Y. Sato, T. Uesugi, M. Yamamoto, T. Yan, E. Ezura, A. Takagi, M. Yoshii, "Evaluation of Magnetic Alloys for JHF RF Cavity," *Proceedings of APAC 1998*, Tsukuba, Japan, pp. 390–392 (1998).

[13] Y. Mori, E. Ezura, M. Fujieda, K. Koba, S. Machida, H. Nakayama, C. Ohmori, K. Saito, S. Sawada, A. Takagi, Y. Tanabe, M. Toda, M. Yamamoto, M. Yoshii, T. Uesugi, "A New Type of RF Cavity for High Intensity Proton Synchrotron," *Proceedings of 11th Symposium on Accelerator Science and Technology*, Ako, Hyogo, Japan, pp. 224–226 (1997).

[14] Y. Mori, M. Fujieda, K. Koba, H. Nakayama, C. Ohmori, K. Saito, Y. Satoh, Y. Tanabe, A. Takagi, M. Toda, T. Uesugi, M. Yamamoto, T. Yan, and M. Yoshii, "A New Type of RF Cavity for High Intensity Proton Synchrotron Using High Permeability Magnetic Alloy," *Proceedings of EPAC 1998*, Stockholm, Sweden, pp. 299–301 (1998).

[15] Y. Yoshizawa, S. Oguma, and K.Yamauchi, "New Fe-Based Soft Magnetic Alloys Composed of Ultrafine Grain Structure," *J. Appl. Phys*. Vol. 64, No. 10, pp. 6044–6046, 15 November (1988).

[16] Y. Yoshizawa, K. Yamauchi, T. Yamane, and H. Sugihara, "Common Mode Choke Cores Using the New Fe-Based Alloys Composed of Ultrafine Grain Structure," *J. Appl. Phys*. Vol. 64, No. 10, pp. 6047–6049, 15 November (1988).

[17] Y. Yoshizawa and K. Yamauchi, "Effects of Magnetic Field Annealing on Magnetic Properties in Ultrafine Crystalline Fe-Cu-Nb-Si-B Alloys," *IEEE Trans. on Magnetics*, Vol. 25, No.5, pp. 3324–3326, September (1989).

[18] T. Misu, A. Sugiura, M. Kanazawa, S. Yamada, K. Sato, K. Katsuki, "Development of Co-Based Amorphous Core for Untuned Broadband RF Cavity," *Proceedings of PAC 2005*, Knoxville, Tennessee, pp. 1511–1513 (2005).

[19] T. Misu, A. Sugiura, M. Kanazawa, S. Yamada, T. Kusaka, K. Sato, K, Katsuki, "High-Permeability Cobalt-Based Amorphous Core for the Use of an Untuned Broadband RF Cavity," *Nucl. Instrum. Methods Phys. Res*., *A*, Vol. 557, pp. 383 –389 (2006).

[20] A. Sugiura, T. Misu, M. Kanazawa, S. Yamada, K. Sato, K. Katsuki, T. Kusaka, "Improvement of Co-Based Amorphous Core for Untuned Broadband RF Cavity," *Proceedings of EPAC 2006*, Edinburgh, Scotland, pp. 1304–1306 (2006).

[21] M. Kanazawa, T. Misu, A. Sugiura, K. Sato, K, Katsuki, T. Kusaka, "RF Cavity with Co-Based Amorphous Core," *Proceedings of EPAC 2006*, Edinburgh, Scotland, pp. 983–985 (2006).

[22] C. Ohmori, K. Hara, A. Takagi, M. Toda, M. Yoshii, K. Hasegawa, M. Nomura, A. Schnase, F. Tamura, M. Yamamoto, "Possible Upgrade Scenario for J-PARC Ring RF," *Proceedings of EPAC 2008*, Genoa, Italy, pp. 799–801 (2008).

[23] C. Ohmori, E. Ezura, K. Hara, K. Hasegawa, A. Takagi, M. Toda, M. Yoshii, M. Nomura, A. Schnase, T. Shimada, H. Suzuki, F. Tamura, M. Yamamoto, A. Koda, Y. Miyake, K. Nishiyama, K. Shimomura, S. Takeshita, M.Miyazaki, K. Kubo, "Design of a New J-PARC RF Cavity for Short Muon Bunch," *Proceedings of PAC 2009*, Vancouver, BC, Canada, pp. 876–878 (2009).

[24] M. Fujieda, S. Machida, Y. Mori, H. Nakayama, C. Ohmori, Y. Sato, Y. Tanabe, T. Uesugi, M. Yamamoto, A. Takagi, M. Toda, M. Yoshii, Y. Iwashita, "MA-Loaded Cavity for Barrier Bucket Experiment," *Proceedings of EPAC 1998*, Stockholm, Sweden, pp. 1796–1798 (1998).

[25] M. Fujieda, Y. Iwashita, Y. Mori, H. Nakayama, C. Ohmori, K. Saito, Y. Sato, S. Sawada, A. Takagi, Y. Tanabe, M. Toda, T. Uesugi, M. Yamamoto, T. Yan, and M. Yoshii, "An RF Cavity for Barrier Bucket Experiment in the AGS," *Proceedings of APAC 1998*, Tsukuba, Japan, pp. 408–410 (1998).

[26] M. Fujieda, Y. Iwashita, A. Noda, Y. Mori, C. Ohmori, Y. Sato, M. Yoshii, M. Blaskiewicz, J. M. Brennan, T. Roser, K. S. Smith, R. Spitz and A. Zaltsman, "Magnetic Alloy Loaded RF Cavity for Barrier Bucket Experiment at the AGS," *Proceedings of PAC 1999*, New York, pp. 857–859 (1999).

[27] M. Blaskiewicz, J. M. Brennan, T. Roser, K. Smith, R. Spitz, A. Zaltsman, M. Fujieda, Y. Iwashita, A. Noda, M. Yoshii, Y. Mori, C. Ohmori, Y. Sato, "Barrier Cavities in the Brookhaven AGS," *Proceedings of PAC 1999*, New York, pp. 2280–2282 (1999).

[28] M. Yoshii, C. Ohmori, Y. Mori, A. Schnase, "MA RF Cavity for the KEK 12 GeV PS," *Proceedings of EPAC 2000*, Vienna, Austria, pp. 984–986 (2000).

[29] M. Yoshii, E. Ezura, Y. Hashimoto, C. Ohmori, Y. Mori, A. Takagi, M. Yamamoto, A. Schnase, "Digital Control for KEK-PS MA Loaded RF System," *Proceedings of PAC 2001*, Chicago, pp. 894–896 (2001).

[30] S. Ninomiya, K. Muto, and M. Toda, "Design Study of Non-Resonant Accelerating System for the KEK PS Booster," *Proceedings of APAC 2001*, Beijing, China, pp. 535–537 (2001).

[31] S. Ninomiya, K. Muto, and M. Toda, "Non-Resonant Accelerating System at the KEK-PS Booster," *Proceedings of EPAC 2004*, Lucerne, Switzerland, pp. 1027–1029 (2004).

[32] R. Garoby, M. Haase, P. Maesen, M. Paoluzzi, C. Rossi, C. Ohmori, "The LEIR RF System," *Proceedings of PAC 2005*, Knoxville, Tennessee, pp. 1619–1621 (2005).

[33] C. Ohmori, M. Hasse, M. Paoluzzi, C. Rossi, R. Garoby, "MA Cavity for I-LHC-LEIR," *Proceedings of the 2nd Annual Meeting of Particle Accelerator Society of Japan and the 30th Linear Accelerator Meeting in Japan*, Tosu, Saga, Japan, pp. 123–125 (in Japanese) (2005).

[34] K. Hanke, et al., "Study of an Energy Upgrade of the CERN PS Booster," CERN-ATS-2011-055 (2011).

[35] C. Ohmori, private communication.

[36] J. Dey, I. Kourbanis, Z. Qian, and D. Wildman, "A Prototype 7.5 MHz Finemet Loaded RF Cavity and 200kW Amplifier for the Fermilab Proton Driver", *Proceedings of PAC 2001*, Chicago, pp. 882–884 (2001).

[37] W. Chou, D. Wildman, A. Takagi, H. Zheng, "Barrier RF System and Applications in Main Injector," *Proceedings of PAC 2005*, Knoxville, Tennessee, pp.1189–1191 (2005).

[38] K. Torikai, K. Koseki, E. Nakamura, Y. Shimosaki, Y. Arakida, T. Kono, T. Toyama, M. Wake, K. Takayama, J. Kishiro, "Induction Accelerating Cavity for a Circular Ring Accelerator," *Proceedings of EPAC 2004*, Lucerne, Switzerland, pp. 704–706 (2004).

[39] K. Takayama, K. Koseki, K. Torikai, A. Tokuchi, E. Nakamura, Y. Arakida, Y. Shimosaki, M. Wake, T. Kouno, K. Horioka, S. Igarashi, T. Iwashita, A. Kawasaki, J. Kishiro, M. Sakuda, H. Sato, M. Shiho, M. Shirakata, T. Sueno, T. Toyama, M. Watanabe, and I. Yamane, "Observation of the Acceleration of a Single Bunch by Using the Induction Device in the KEK Proton Synchrotron," *Phys. Rev. Lett*. 94, 144801 (2005).

[40] K. Torikai, Y. Arakida, K. Otsuka, J. Kishiro, T. Kono, E. Nakamura, Y. Shimosaki, T. Toyama, M. Wake, "POP Experiment (I) of Induction Synchrotron: Induction Acceleration of a Single RF Bunch and Formation of a Superbunch in the KEK-PS," *Proceedings of 2nd Annual Meeting of Particle Accelerator Society of Japan*, Tosu, Saga, Japan, pp. 34–36 (in Japanese) (2005).

[41] K. Takayama, Y. Arakida, T. Dixit, T. Iwashita, T. Kono, E. Nakamura, K. Otsuka, Y. Shimosaki, K. Torikai, and M. Wake, "Experimental Demonstration of the Induction Synchrotron," *Proceedings of 3rd Annual Meeting of Particle Accelerator Society of Japan*, Sendai, Japan, pp. 60–63 (in Japanese) (2006).

[42] K. Takayama, Y. Arakida, T. Dixit, T. Iwashita, T. Kono, E. Nakamura, K. Otsuka, Y. Shimosaki, K. Torikai, and M. Wake, "Experimental Demonstration of the Induction Synchrotron," *Phys. Rev. Lett*. 98, 054801 (2007).

[43] C. Ohmori, E. Ezura, M. Fujieda, Y. Mori, R. Muramatsu, H. Nakayama, Y. Sato, A. Takagi, M. Toda, T. Uesugi, M. Yamamoto, M. Yoshii, M. Kanazawa, and K. Noda, "High Field-Gradient Cavities Loaded with Magnetic Alloys for

Synchrotrons," *Proceedings of PAC 1999*, New York, pp. 413–417 (1999).

[44] R. Muramatsu, M. Fujieda, Y. Mori, H. Nakayama, C. Ohmori, Y. Sato, A. Takagi, T. Uesugi, M. Yamamoto, M. Yoshii, M. Kanazawa, K. Noda, "The First Beam Acceleration Test Using High Gradient Cavity at HIMAC," *Proceedings of PAC 1999*, New York, pp. 798–799 (1999).

[45] Y. Yamamoto, M. Fujieda, Y. Mori, R. Muramatsu, C. Ohmori, Y. Sato, A. Takagi, T. Uesugi, M. Yoshii, M. Kanazawa, and K. Noda, "Multi-Harmonic Acceleration with High Gradient MA Cavity at HIMAC," *Proceedings of PAC 1999*, New York, pp. 863–865 (1999).

[46] M. Umezawa, H. Sakurabata, M. Tadokoro, H. Ootsuka, H. Nishiuchi, K. Saito, K. Matsuda, N. Kosugi, K. Hiramoto, Y. Mori, S. Machida, A. Molodojentsev, Y. Takada, A. Maruhashi, A. Nohtomi, T. Sakae, K. Yasuoka, "Beam Commissioning of the New Proton Therapy System for University of Tsukuba," *Proceedings of PAC 2001*, Chicago, pp. 648–650 (2001).

[47] K. Saito, H. Nishiuchi, H. Sakurabata, M. Katane, K. Kobayashi, K. Moriyama, H. Satomi, K. Masui, "Multi-Harmonic RF Acceleration System for a Medical Proton Synchrotron," *Proceedings of EPAC 2004*, Lucerne, Switzerland, pp.1045–1047 (2004).

[48] K. Matsuda, K. Saito, H. Nishiuchi, M. Umezawa, K. Hiramoto, R. Shinagawa, T. Tonooka, "Beam Commissioning of a Multi-Purpose Compact Ion Synchrotron," *Proceedings of PAC 2001*, Chicago, pp. 2590–2592 (2001).

[49] K. Saito, K. Matsuda, H. Nishiuchi, M. Umezawa, K. Hiramoto, R. Shinagawa, "RF Accelerating System for a Compact Ion Synchrotron," *Proceedings of PAC 2001*, Chicago, pp. 966–968 (2001).

[50] K. Saito, H. Nishiuchi, S. Totake, M. Umezawa, H. Nihongi, H. Sakurabata, K. Moriyama, "Accelerator Development for Advanced Particle Beam Therapy," *Proceedings of EPAC 2008*, Genoa, Italy, pp. 1827–1829 (2008).

[51] A. Takagi, Y. Mori, J. Nakano, T. Uesugi, M. Sugaya, "Radio Frequency Acceleration System for 150 MeV FFAG," *Proceedings of PAC 2003,* Portland, Oregon, pp. 1231–1233 (2003).

[52] S. Machida, Y. Mori, A. Muto, J. Nakano, C. Ohmori, I. Sakai, Y. Sato, A. Takagi, T. Yokoi, M. Yoshii, M. Yoshimoto, Y. Yuasa, M. Matoba, Y. Yonemura, A. Yamazaki, T. Uesugi, M. Aiba, M. Sugaya, "Commissioning of 150 MeV FFAG Synchrotron," *Proceedings of EPAC 2004*, Lucerne, Switzerland, pp. 2643–2645 (2004).

[53] Y. Yonemura, N. Ikeda, M. Matoba, M. Aiba, S. Machida, Y. Mori, A. Muto, J. Nakano, C. Ohmori, K. Okabe, I. Sakai, Y. Sato, A. Takagi, T. Yokoi, M. Yoshii, Y. Yuasa, R. Taki, M. Yoshimoto, A. Yamazaki, T. Uesugi,

"Development of FFAG Accelerator at KEK," *Proceedings of PAC 2005*, Knoxville, Tennessee, pp. 1943–1945 (2005).

[54] M. Aiba, Y. Mori, H. Nakayama, K. Okabe, Y. Sakamoto, A. Takagi, R. Taki, and Y. Yonemura, "Beam Extraction of 150 MeV FFAG," *Proceedings of EPAC 2006*, Edinburgh, Scotland, pp. 1672–1674 (2006).

[55] Y. Yonemura, H. Arima, N. Ikeda, K. Ishibashi, K. Maehata, T. Noro, T. Okai, K. Sagara, N. Shigyo, Y. Uozumi, G. Wakabayashi, H. Ishikawa, H. Nakayama, A. Takagi, S. Fukumoto, Y. Kimura, T. Tomimasu, Y. Mori, "Status of Center for Accelerator and Beam Applied Science of Kyushu University," *Proceedings of EPAC 2008*, Genoa, Italy, pp. 3521–3523 (2008).

[56] T. Fujinaka, et al., "Commissioning of FFAG Accelerator at Kyushu University," *Proceedings of IPAC 2010*, Kyoto, Japan, pp. 543–545 (2010).

[57] M. Tanigaki, K. Mishima, S. Shiroya, Y. Ishi, S. Fukumoto, S. Machida, Y. Mori, M. Inoue, "Construction of FFAG Accelerators in KURRI for ADS Study," *Proceedings of EPAC 2004*, Lucerne, Switzerland, pp. 2673–2675 (2004).

[58] M. Tanigaki, Y. Mori, M. Inoue, K. Mishima, S. Shiroya, Y. Ishi, S. Fukumoto, S. Machida, "Present Status of FFAG Accelerators in KURRI for ADS Study," *Proceedings of EPAC 2006*, Edinburgh, Scotland, pp. 2367–2369 (2006).

[59] J. Collot, Y. Mori, P. Mandrillon, F. Méot, and R. Edgecock, "The Rise of the FFAG," *CERN Courier*, Vol. 48, No. 7, pp. 21–23, September (2008).

[60] Y. Mori, "Development of FFAG Accelerators and Their Applications for Intense Secondary Particle Production," *Nucl. Instrum. Methods Phys. Res*., *A*, Vol. 562, pp. 591–595 (2006).

[61] K. Okabe, M. Muto, Y. Mori, "Development of FFAG-ERIT Ring," *Proceedings of EPAC 2006*, Edinburgh, Scotland, pp. 1675–1677 (2006).

[62] T. Uesugi, Y. Mori, H. Horii, Y. Kuriyama, K. Mishima, A. Osanai, T. Planche, S. Shiroya, M. Tanigaki, K. Okabe, I. Sakai, M. Inoue, Y. Ishi, M. Muto, "FFAGs for the ERIT and ADS Projects at KURRI," *Proceedings of EPAC 2008*, Genoa, Italy, pp. 1013–1015 (2008).

[63] K. Okabe, Y. Mori, and M. Muto, "An Intense Neutron Source with Emittance Recovery Internal Target (ERIT) Using Ionization Cooling," *Proceedings of EPAC 2008*, Genoa, Italy, pp. 3512–3514 (2008).

[64] B. Autin, J. Collot, J. Fourrier, E. Froidefond, F. Martinache, F. Méot, J. Balosso, P. Pommier, J.-L. Lancelot, D. Neuveglise, "The FFAG R&D and Medical Application Project RACCUM," *Proceedings of EPAC 2006*, Edinburgh, Scotland, pp. 2308–2309 (2006).

[65] J. Fourrier, F. Méot, J. Pasternak, M. Conjat, J. Mandrillon, P. Mandrillon, "Variable Energy Protontherapy FFAG Accelerator," *Proceedings of EPAC 2008*,

Genoa, Italy, pp. 1791–1793 (2008).

[66] C. Ohmori, F. Méot, J. Fourrier, J. Pasternak, "High Field Gradient RF System for a Spiral FFAG, RACCAM," *Proceedings of EPAC 2008*, Genoa, Italy, pp. 793–795 (2008).

[67] A. Sato, M. Aoki, Y. Arimoto, Y. Kuno, M. Yoshida, S. Machida, Y. Mori, C. Ohmori, T. Yokoi, K. Yoshimura, Y. Iwashita, S. Ninomiya, "FFAG as Phase Rotator for the PRISM Project," *Proceedings of EPAC 2004*, Lucerne, Switzerland, pp. 713–715 (2004).

[68] Y. Kuriyama, M. Aoki, Y. Arimoto, Y. Kuno, A. Sato, M. Yoshida, C. Ohmori, "RF Development for PRISM-FFAG," *Proceedings of 2nd Annual Meeting of Particle Accelerator Society of Japan*, Tosu, Saga, Japan, pp. 714–716 (in Japanese) (2005).

[69] A. Sato, M. Aoki, Y. Arimoto, T. Itahashi, Y. Kuno, Y. Kuriyama, T. Oki, T. Takayanagi, M. Yoshida, S. Machida, C. Ohmori, T. Yokoi, K. Yoshimura, M. Aiba, Y. Mori, Y. Iwashita, "R&D Status of the High-Intense Monochromatic Low-Energy Muon Source: PRISM," *Proceedings of EPAC 2006*, Edinburgh, Scotland, pp. 2508–2510 (2006).

[70] A. Sato, M. Aoki, S. Araki, Y. Arimoto, Y. Eguchi, K. Hirota, T. Itahashi, Y. Kuno, Y. Nakanishi, M. Yoshida, C. Ohmori, Y. Kuriyama, Y. Mori, Y. Iwashita, A. Kurup, "Six-Sector FFAG Ring to Demonstrate Bunch Rotation for PRISM," *Proceedings of EPAC 2008*, Genoa, Italy, pp. 3389–3391 (2008).

[71] K. Koba, D. Arakawa, M. Fujieda, K. Ikegami, C. Kubota, S. Machida, Y. Mori, C. Ohmori, K. Shinto, S. Shibuya, A. Takagi, T. Toyama, T. Uesugi, T. Watanabe, M. Yamamoto, and M. Yoshii, "Longitudinal Impedance Tuner Using High Permeability Material," *Proceedings of 11th Symposium on Accelerator Science and Technology*, Ako, Hyogo, Japan, pp. 409–411 (1997).

[72] K. Koba, D. Arakawa, M. Fujieda, K. Ikegami, C. Kubota, S. Machida, Y. Mori, C. Ohmori, K. Shinto, S. Shibuya, A. Takagi, T. Toyama, T. Uesugi, T. Watanabe, M. Yamamoto, and M. Yoshii, "Longitudinal Impedance Tuner Using High Permeability Material," *Proceedings of APAC 1998*, Tsukuba, Japan, pp. 450–452 (1998).

[73] K. Koba, D. Arakawa, M. Fujieda, K. Ikegami, Y. Ishi, Y. Kanai, C. Kubota, S. Machida, Y. Mori, C. Ohmori, K. Shinto, S. Shibuya, A. Takagi, T. Toyama, T. Uesugi, T. Watanabe, M. Yamamoto, T. Yokoi, and M. Yoshii, "Longitudinal Impedance Tuner Using High Permeability Material," *Proceedings of PAC 1999*, New York, pp. 1653–1655 (1999).

[74] K. Koba, D. Arakawa, M. Fujieda, K. Ikegami, Y. Ishi, Y. Kanai, C. Kubota, S. Machida, Y. Mori, C. Ohmori, K. Shinto, S. Shibuya, A. Takagi, T. Toyama,

T. Uesugi, T. Watanabe, M. Yamamoto, T. Yokoi, and M. Yoshii, “Longitudinal Impedance Tuner Using New Material FINEMET,” *Rev. Sci. Instrum*., Vol. 70, No. 7, pp. 2988–2992, July (1999).

[75] Y. Mori, M. Muto, C. Ohmori, Y. Shirakabe, A. Takagi, W. Chou, “Fast Beam Chopper with MA Cores,” *Proceedings of EPAC 2000*, Vienna, Austria, pp. 2468–2470 (2000).

[76] C. Ohmori, M. Kanazawa, A. Takagi, K. Noda, T. Uesugi, Y. Shirakabe, A. Sugiura, Y. Mori, M. Muto, W. Chou, “Beam Diagnostics Using a Chopped Beam,” *Nucl. Instrum. Methods Phys. Res*., A, Vol. 526, pp. 215–221 (2004).

[77] M. Watanabe, Y. Chiba, T. Koseki, T. Katayama, Y. Ohshiro, S. Watanabe, “A Broad-Band RF Buncher Cavity Using FINEMET Cut Cores for Ion Beams,” *Proceedings of the 17th International Conf. on Cyclotrons and Their Applications,* Tokyo, pp. 336–338 (2004).

[78] T. Koseki, Y. Chiba, A. Goto, Y. Ohshiro, M. Watanabe, and S. Watanabe, “Development of a Buncher Cavity Using MA Cores,” *Proceedings of 2nd Annual Meeting of Particle Accelerator Society of Japan*, Tosu, Saga, Japan, pp. 329–331 (in Japanese) (2005).

[79] T. Koseki, M. Watanabe, S. Watanabe, Y. Chiba, A. Goto, K. Noda, and Y. Ohshiro, “Broadband Buncher Cavity for Beam Transport Line of HiECR Ion Source,” *Jpn. J. Appl. Phys*., Vol. 45, No. 5A, pp. 4227–4231 (2006).

[80] M. Yoshii, S. Anami, E. Ezura, K. Hara, Y. Hashimoto, C. Ohmori, A. Takagi, M. Toda, K. Haga, K. Hasegawa, M. Nomura, A. Schnase, F. Tamura, M. Yamamoto, “Present Status of J-PARC Ring RF Systems,” *Proceedings of PAC 2007*, Albuquerque, New Mexico, pp. 1511–1513 (2007).

[81] A. Schnase, K. Hasegawa, M. Nomura, F. Tamura, M. Yamamoto, S. Anami, E. Ezura, K. Hara, C. Ohmori, A. Takagi, M. Toda, M. Yoshii, “MA Cavities for J-PARC with Controlled *Q*-value by External Inductor,” *Proceedings of PAC 2007*, Albuquerque, New Mexico, pp. 2131–2133 (2007).

[82] A. Schnase, M. Nomura, F. Tamura, M. Yamamoto, K. Haga, K. Hasegawa, M. Yoshii, C. Ohmori, K. Hara, M. Toda, A. Takagi, S. Anami, E. Ezura, “Status of J-PARC Ring RF Systems,” *Proceedings of 4th Annual Meeting of Particle Accelerator Society of Japan*, Wako, Saitama, Japan, pp. 212–214 (2007).

[83] M. Yamamoto, M. Nomura, A. Schnase, F. Tamura, S. Anami, E. Ezura, K. Hara, Y. Hashimoto, C. Ohmori, A. Takagi, M. Yoshii, “Dual Harmonic Operation with Broadband MA Cavities in J-PARC RCS,” *Proceedings of PAC 2005*, Knoxville, Tennessee, pp. 931–933 (2005).

[84] M. Yoshii, E. Ezura, K. Hara, K. Hasegawa, K. Takata, M. Nomura, C. Ohmori, A. Schnase, T. Shimada, H. Suzuki, A. Takagi, F. Tamura, M. Toda, Y. Yamamoto,

"Recent Status and Future Plan of J-PARC MA Loaded RF Systems," *Proceedings of IPAC 2010*, Kyoto, Japan, pp. 615–617 (2010).

[85] M. Yoshii, E. Ezura, K. Hara, K. Hasegawa, M. Nomura, C. Ohmori, A. Schnase, T. Shimada, A. Takagi, K. Takata, F. Tamura, M. Toda, M. Yamamoto, T. Minamikawa, "Acceleration of High Intensity Proton Beams in the J-PARC Synchrotrons," *Proceedings* of *IPAC 2011*, San Sebastian, Spain, pp. 2502–2504 (2011).

[86] M. Yoshii, E. Ezura, K. Hara, K. Hasegawa, M. Nomura, C. Ohmori, A. Schnase, T. Shimada, A. Takagi, K. Takata, F. Tamura, M. Toda, M. Yamamoto, "Status of the J-PARC ring RF systems," to be presented at IPAC 2012.

[87] Y. Sato, S. Igarashi, K. Ohmi, K. Hara, H. Hotchi, M. Tomizawa, C. Ohmori, T. Koseki, "Beam Dynamics Simulations of J-PARK Main Ring for Upgrade Plan of Fast Extraction Operation," *Proceedings of IPAC 2011*, San Sebastian, Spain, pp. 598–600 (2011).

[88] C. Ohmori, O. Araoka, E. Ezura, K. Hara, K. Hasegawa, A. Koda, Y. Makida, Y. Miyake, R. Muto, K. Nishiyama, M. Nomura, T. Ogitsu, H. Ohhata, K. Shimomura, A. Takagi, T. Shimada, A. Schnase, K. Takata, F. Tamura, K. Tanaka, M. Toda, M. Yamamoto, M. Yoshii, "High Gradient Magnetic Alloy Cavities for J-PARC Upgrade," *Proceedings of IPAC* 2011, San Sebastian, Spain, pp. 2885–2887 (2011).

[89] B. D. Cullity, *Introduction to Magnetic Materials*, Addison-Wesley Publishing Company Inc., Reading, Massachusetts (1972).

[90] R. M. Bozorth, *Ferromagnetism*, D. Van Nostrand Company, Inc., New York (1951).

[91] R. C. O'Handley, *Modern Magnetic Materials − Principles and Applications*, John Wiley & Sons, Inc., New York (2000).

[92] J. Smit and H. P. J. Wijn, translated by G. E. Luton, *Ferrites − Physical Properties of Ferrimagnetic Oxides in Relation to Their Technical Applications*, International Edition, Philips' Technical Library, Eindhoven, Netherlands / Tokyo Electrical Engineering College Press, Tokyo, Japan (1965).

[93] S. Chikazumi, *Physics of Ferromagnetism*, Second Edition, Oxford University Press, Inc., New York (1997).

[94] É. du Trémolet de Lacheisserie, D. Gignoux, and M. Schlenker, Editors, *Magnetism I − Fundamentals*, Kluwer Academic Publishers, Norwell, Massachusetts (2002).

[95] É. du Trémolet de Lacheisserie, D. Gignoux, and M. Schlenker, Editors, *Magnetism II − Materials & Applications*, Kluwer Academic Publishers, Norwell, Massachusetts (2002).

[96] E. P. Wohlfarth, Editor, *Ferromagnetic Materials−A Handbook on the Properties*

of Magnetically Ordered Substances, Vol. 1, Elsevier Science Publishers B. V., Amsterdam (1986).

[97] E. P. Wohlfarth, Editor, *Ferromagnetic Materials−A Handbook on the Properties of Magnetically Ordered Substances*, Vol. 2, Elsevier Science Publishers B. V., Amsterdam (1986).

[98] D. Craik, *Magnetism−Principles and Applications*, John Wiley & Sons, Inc., Chichester (1995).

[99] K. H. J. Buschow, Editor, *Handbook of Magnetic Materials*, Vol. 10, Elsevier Science Publishers B. V., Amsterdam (1997).

[100] J. K. Galt, "Motion of a Ferromagnetic Domain Wall in Fe_3O_4," *Phys. Rev*., Vol. 85, No. 4, pp. 664–669 (1952).

[101] A. J. Dekker, *Solid State Physics*, Prentice-Hall Inc., Englewood Cliffs, N. J. (1957).

[102] J. R. Hook and H. E. Hall, *Solid State Physics*, Second Edition, John Wiley & Sons, Inc., Chichester (1991).

[103] R. Turton, *The Physics of Solids*, Oxford University Press, Inc., New York (2000).

[104] S. R. Elliott, *The Physics and Chemistry of Solids*, John Wiley & Sons, Inc., Chichester (1998).

[105] M. Gevers and F. K. Du Pré, "Power Factor and Temperature Coefficient of Solid (Amorphous) Dielectrics," *Trans. Faraday Soc*., Vol. 42A, pp. 47–55 (1946).

[106] E. W. Gorter, "Some Properties of Ferrites in Connection with Their Chemistry," *Proc. IRE*, Vol. 43, pp. 1945–1973 (1955).

[107] J. L. Snoek, "Dispersion and Absorption in Magnetic Ferrites at Frequencies above One Megacycle," *Physica*, Vol. 14, No. 4, pp. 207–217 (1948).

[108] H. P. J. Wijn, M. Gevers, and C. M. van der Burgt, "Note on the High Frequency Dispersion in Nickel Zinc Ferrites," *Rev. Mod. Phys.*, Vol. 25, No. 1, pp. 91–92 (1953).

[109] K. Ohta, *Foundations for Magnetic Engineering* [II]−*Applications of Magnetism*, Kyoritsu Publishing Company, Inc., Tokyo (in Japanese) (1973).

[110] G. H. Jonker, H. P. J. Wijn and P. B. Braun, "Ferroxplana, Hexagonal Ferromagnetic Iron-Oxide Compounds for Very High Frequencies," *Philips Techn. Rev.*, Vol. 18, No. 6, pp. 145–154 (1956/1957).

[111] W. Döring, "*Uber die Trägheit der Wände zwischen Weiszschen Bezirken*," *Z. Naturforschung*, Vol. 3a, pp. 374–379 (1948).

[112] G. T. Rado, R. W. Wright, W. H. Emerson, and A. Terris, "Ferromagnetism at Very High Frequencies. IV. Temperature Dependence of the Magnetic Spectrum of a Ferrite," *Phys. Rev*., Vol. 88, No. 4, pp. 909–915 (1952).

[113] G. T. Rado, "Magnetic Spectra of Ferrites," *Rev. Mod. Phys.*, Vol. 25, No. 1,

pp. 81–89 (1953).
[114] G. T. Rado, V. J. Folen, and W. H. Emerson, “Effect of Magnetocrystalline Anisotropy on the Magnetic Spectra of Mg-Fe Ferrites,” *Proc. I.E.E.*, Vol. 104, pp. 198–205 (1956).
[115] F. G. Brockman, P. H. Dowling, and W. G. Steneck, “Dimensional Effects Resulting from a High Dielctric Constant Found in a Ferromagnetic Ferrite,” *Phys. Rev.*, Vol. 77, No. 1, pp. 85–93 (1950).
[116] H. J. Gray and Alan Isaacs, Editors, *A New Dictionary of Physics*, Longman Group Limited, London (1975).
[117] C. P. Poole Jr., Editor, *Encyclopedic Dictionary of Condensed Matter Physics*, Vol. 1, Elsevier B. V., Amsterdam (2004).
[118] H. J. Williams, W. Shockley, and C. Kittel, “Studies of the Propagation Velocity of a Ferromagnetic Domain Boundary,” *Phys. Rev.*, Vol. 80, No. 6, pp. 1090−1094 (1950).
[119] R. H. Pry and C. P. Bean, “Calculation of the Energy Loss in Magnetic Sheet Materials Using a Domain Model,” *J. Appl. Phys.*, Vol. 29, No. 3, pp. 532–533 (1958).
[120] G. Brouwer, “Electrical Analog of the Eddy-Current-Limited Domain-Boundary Motion in Ferromagnetics,” *J. Appl. Phys.*, Vol. 26, No. 11, pp. 1297–1301 (1955).
[121] E. W. Lee, “Eddy-Current Losses in Thin Ferromagnetic Sheets,” *Proc. Instn. Elec. Engrs.*, Vol. C105, pp. 337–342 (1958).
[122] J. A. Stratton, *Electromagnetic Theory*, McGraw-Hill Book Company, Inc., New York (1941).
[123] J. D. Jackson, *Classical Electrodynamics*, Third Edition, John Wiley & Sons, Inc., New York (1999).
[124] B. I. Bleaney and B. Bleaney, *Electricity and Magnetism*, Third Edition, Oxford University Press, London (1976).
[125] R. Plonsey and R. E. Collin, *Principles and Applications of Electromagnetic Fields*, McGraw-Hill Book Company, Inc., New York (1961).
[126] D. J. Griffiths, *Introduction to Electrodynamics*, Third Edition, Prentice-Hall International, Inc., New Jersey (1999).
[127] W. R. Smythe, *Static and Dynamic Electricity*, Third Edition, McGraw-Hill Book Company, Inc., New York (1968).
[128] D. M. Pozar, *Microwave Engineering*, Third Edition, John Wiley & Sons, Inc., New York (2005).